Circuit Quantum Electrodynamics with Electrons on Helium

A Dissertation
Presented to the Faculty of the Graduate School
of
Yale University
in Candidacy for the Degree of
Doctor of Philosophy

by
Andreas Arnold Fragner

Dissertation Director: Professor Robert J. Schoelkopf

December 2013

Abstract

Circuit Quantum Electrodynamics with Electrons on Helium

Andreas Arnold Fragner

2013

This thesis describes the theory, design and implementation of a circuit quantum electrodynamics (QED) architecture with electrons floating above the surface of superfluid helium. Such a system represents a solid-state, electrical circuit analog of atomic cavity QED in which the cavity is realized in the form of a superconducting coplanar waveguide resonator and trapped electrons on helium act as the atomic component. As a consequence of the large electric dipole moment of electrons confined in sub-μm size traps, both their lateral motional and spin degrees of freedom are predicted to reach the strong coupling regime of cavity QED, with estimated motional Rabi frequencies of $g/2\pi \sim 20$ MHz and coherence times exceeding 15 μs for motion and tens of milliseconds for spin. The feasibility of the architecture is demonstrated through a number of foundational experiments. First, it is shown how coplanar waveguide resonators can be used as high-precision superfluid helium meters, allowing us to resolve film thicknesses ranging from 30 nm to 20 μm and to distinguish between van-der-Waals, capillary action and bulk films in micro-channel geometries. Taking advantage of the capacitive coupling to submerged electrodes and the differential voltage induced as a result of electron motion driven at a few hundred kHz, we realize the analog of a field-effect transistor on helium at milli-Kelvin temperatures on a superconducting chip and use it to measure and control the density of surface electrons. Finally, the trapping and detection of an electron ensemble in a DC-biased superconducting resonator is reported. The presence of electrons in the resonator mode volume manifests itself as trap-voltage dependent frequency shifts of up to ~ 10 cavity linewidths and increases in cavity loss of up to ~ 45 %.

Contents

List of Figures

List of Tables

Acknowledgements

The work presented in this PhD thesis is the result of collaborations with many amazing people. First I would like to thank my advisor ROB SCHOELKOPF, who offered me a position in his lab at Yale more than five years ago and has been a source of guidance and encouragement ever since. Rob has taught me everything I know about the art of microwave engineering and the importance of developing intuition for an experimental problem and not losing sight of the bigger picture. I am also very grateful for his patience and tolerance with many of my tangential (sometimes orthogonal) pursuits during my time in graduate school.

DAVE SCHUSTER was one of the most influential forces behind this PhD project, first as a post-doc at Yale and later as a professor at the University of Chicago. Dave is one of the smartest and most creative physicists I have had the chance to work with and his influence on me as a scientist runs deep. Many of his ideas, including the one for this PhD project, seem a bit crazy at first but his remarkable intuition is usually a reliable indicator of what can be made to work experimentally. I would like to thank him for sharing his knowledge, insight and enthusiasm for physics and science in general.

I continue to be amazed by MICHEL DEVORET's deep and fundamental understanding of physics and the many connections that exist across quantum mechanics, information theory and computer science. His course on noise and dissipation has been one of the most influential classes of my academic career and has sparked an interest in statistics and information theory that persists to this day. I would also like to thank DAN PROBER for serving on my committee and for his role in building such a great community of scientists in the department of applied physics at Yale. The remarkable community on the 4th floor of Becton center has been much lauded by fellow graduate students in the past and I can only add my appreciation for such a unique, collaborative atmosphere to that. In particular, I am much indebted to LUIGI FRUNZIO for his continuous help in the fabrication of the devices used in this PhD project. Many of the daunting fab challenges I have faced over the last five years ended

up finding straight-forward solutions after a few minutes of discussion with Luigi, whose 'can-do' attitude has saved me from abandoning quite a few promising device designs.

Much gratitude also goes to my collaborators outside Yale, in particular STEVE LYON and his group at Princeton, MARK DYKMAN at Michigan State, DAVE REES at RIKEN and GE YANG at the University of Chicago. I have profited a great deal from their experience and understanding of electrons on helium in the design and implementation of our experiments. I would also like to thank the AUSTRIAN ACADEMY OF SCIENCES for their generous financial support as part of the DOC program.

Most importantly, I would like to thank my parents, ARNOLD and MARIANNE, my brother GEORG and my sister JULIA, who have been a continued source of advice and encouragement in all of my endeavors over the years. None of this would have been possible without their loving support, wisdom and shared passion for science. Lastly, a big thank you goes to my 'second family' in the US, the many amazing friends in New York and New Haven who have made these past five years one of the most fun and personally rewarding periods of my life.

1 Introduction

THE concept of quantum information processing can be traced back three decades ago [1, 2] and it has triggered one of the most exciting research efforts in physics and computer science in recent memory. A computer based on the laws of quantum rather than classical physics holds great promises, offering polynomial or exponential speedup of several important algorithmic tasks such as prime factorization [3], unstructured database search [4], solving linear systems of equations [5] and least-squares fitting [6]. Fundamentally, the power of quantum computing derives from the ability to create superposition states and entanglement among those states. The resulting state space dimensionality is enormous and can be exploited as a powerful computational resource. A classical N-bit register has 2^N distinct possible *states*, while a N quantum bit (qubit) register has a state space of 2^N *dimensions*. The quantum state of such a register is a linear superposition of 2^N classical states, making it possible to take advantage of phenomena such as quantum parallelism and logarithmic-time implementations of the fast Fourier transform.

While its power is conceptually well-understood, the practical implementation of a quantum computer represents a formidable scientific and technological challenge that requires controlling, manipulating and preserving quantum entanglement and coherence in a scalable way. A wide variety of physical systems are being actively explored as possible building blocks of a quantum information processor, including nuclear spins in NMR systems [7, 8], semiconductor quantum dots [9], nitrogen-vacancy centers in diamond [10,11], phosphorous donors in silicon [12], electronic hyperfine states in trapped ions [13–15] and superconducting circuits [16–18], among others. Quantum error correction and feedback control [19–22], a key ingredient for fault-tolerant quantum computing, has so far been demonstrated in Rydberg atoms [23], superconducting circuits [24,25], trapped ions [26,27] and NMR [28]. While progress over the last two decades has been remarkable, it has also started to highlight the inherent limitations of some of these systems in simultaneously achieving scalability, long

coherence times, controlled state preparation and universal gate operations [29]. In this context, the notion of *hybrid quantum systems* which combine and interface different qubit implementations to overcome their individual weaknesses represents a natural extension of experimental efforts so far. This PhD project seeks to lay the theoretical and experimental groundwork for the realization of one such hybrid system, trapped electrons on superfluid helium coupled to superconducting circuits in a solid-state analog of atomic cavity quantum electrodynamics (QED). The two core components of this architecture, superconducting transmission line resonators operated in the microwave regime and electrons levitated above the surface of superfluid helium, are introduced in the following two sections and will be discussed in much detail throughout this thesis.

1.1 Circuit Quantum Electrodynamics

Cavity quantum electrodynamics (QED) studies the interaction of matter and light at the quantum level, making it possible to resolve the coherent exchange of energy between the two in a controlled fashion [30, 31]. 'Light' here means photons in a single-mode electromagnetic field confined to a small volume while 'matter' is represented by a quantum-mechanical two-level system, for example two electronic energy levels in an atom. The interaction of matter and light is reduced to its most fundamental form in such a system. Photons and atoms interact in general very weakly, but the coupling between the two can be strongly enhanced if there is only one precisely-defined photon energy available that matches the relevant transition energy of the atom. This is the case in a cavity where the allowed photon energies are determined by the resonance frequency of the cavity. In addition to enhancement, the decay of the atomic component can also be strongly suppressed if the two energies do not match. In that case, the decay times of the atomic transitions can be greatly increased. The regime where the interaction is so strong that the corresponding coupling rate exceeds all rates of energy loss and decay of the atomic and photonic component is referred to as the *strong coupling regime*, which was first realized experimentally using a beam of cesium atoms and an optical cavity in the early 1990s [32]. In this regime, an atom can emit and reabsorb a single photon many times before the photon escapes or the atom decays irreversibly into the environment. At its core, cavity QED is based on turning an *irreversible* physical process (spontaneous emission in free space) into a *reversible* process (energy oscillations in a single-mode electromagnetic field). Cavity QED represents a fundamental concept. It was origi-

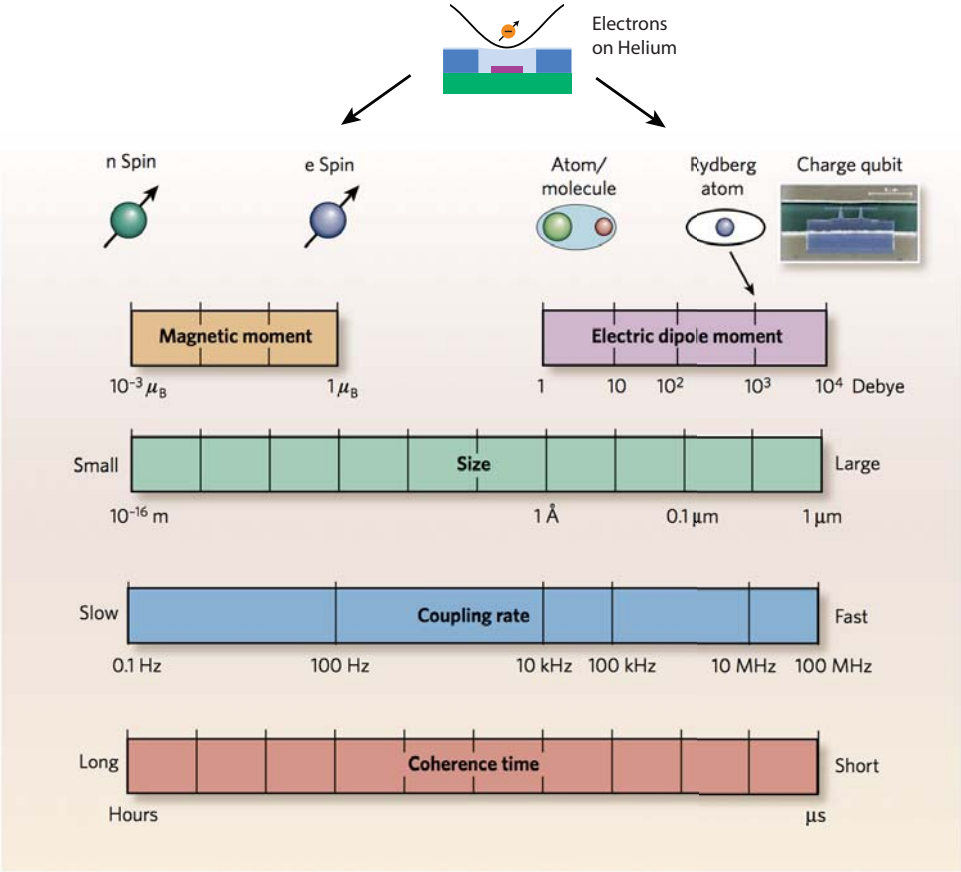

Figure 1.1.: Comparison of different candidate systems for the implementation of a hybrid circuit QED architecture, contrasted with respect to coherence time, coupling rate and transverse size of a cavity required to reach maximal coupling. Fundamental two-level systems based on intrinsic degrees of freedom such as nuclear or electron spins are characterized by long coherence times, partly offsetting their weaker coupling rates which limit the speed of gate operations. Systems with large electric dipole moments such as Rydberg atoms or superconducting qubits exhibit strong coupling, allowing for fast gate operations to overcome their relatively shorter coherence times. Laterally-confined electrons on superfluid helium could potentially be on both ends of the spectrum, promising long spin coherence times while simultaneously offering large electric dipole moments through their lateral quantized motion. For a single 5 GHz photon, the zero-point electric field strength in a transmission line cavity is $E_0 \sim 1 - 2$ V/m, which gives a coupling strength of $g/2\pi \sim 10$ kHz per 1-Debye electric dipole moment. The corresponding zero-point magnetic field strength is $B_0 \sim 0.1$ milli-Gauss with a coupling strength of $g/2\pi \sim 100$ Hz per Bohr magneton. Figure adapted from Ref. [16].

nally developed using alkali atoms and optical cavities formed by two highly reflective mirrors [32–34], but has since been realized using a variety of systems, including Rydberg atoms coupled to microwave cavities [30], semiconductor quantum dots coupled to photonic crystal cavities [35, 36] and superconducting resonators [37], nano-mechanical oscillators [38, 39] as well as spins in nitrogen-vacancy centers in diamond [40, 41]. A particularly successful implementation, called *circuit quantum electrodynamics* (cQED), has been developed at Yale over the last decade [42–44]. Circuit QED can be regarded as an all-electrical, solid-state realization of cavity QED in the microwave regime. In this implementation, atoms are replaced by Josephson junction based superconducting circuits and cavities are realized in the form of quasi two-dimensional transmission line resonators [43, 45] as well as three-dimensional microwave cavities [46, 47]. Many of the cQED system parameters such as photon lifetimes, transition frequencies and atom-photon coupling strengths can be fully engineered using conventional nano- and micro-fabrication techniques. This has allowed for a variety of fascinating on-chip quantum optics experiments, such as resolving photon number states [48], generating single photons on demand [49], observation of multi-photon transitions [50, 51] and the collapse and revival of non-classical states of light [52], to name a few. The intrinsic scalability and the ability to perform quantum non-demolition measurements, together with all-electrical control based on standard microwave and RF engineering methods, has also helped establish cQED as one of the most promising platforms for a future quantum information processor [24, 53–58].

The circuit QED architecture lends itself naturally to the implementation of hybrid quantum systems capable of combining different realizations of the atomic component in cavity QED. Many natural and artificial anharmonic quantum systems have transition frequencies in the microwave frequency range and could be made to couple strongly to photons in a transmission line cavity. For that reason, superconducting transmission line resonators have been considered as mesoscopic electrical interfaces between superconducting circuits and microscopic quantum systems, such as polar molecules and molecular ions [59–61], electron spin ensembles [62–65] and ultracold atoms [66], which typically have smaller couplings but better coherence times than superconducting qubits. Fig. 1.1 contrasts different qubit implementations in terms of coherence times, coupling rates and the required transverse size of a cavity to reach maximal coupling. Systems with large electric dipole moments such as Rydberg atoms or superconducting qubits exhibit strong coupling to the electromagnetic field in a cavity, allowing for fast gate operations on nano-second time scales, but suffer

from relatively short coherence times. Fundamental systems based on intrinsic degrees of freedom such as nuclear or electron spins have weaker coupling due to their small magnetic moments and the small magnetic field, limiting the speed of gate operations, but offer longer coherence times that partly offset this limitation. This thesis explores the coupling of cavity photons to a particularly exotic quantum system, isolated electrons bound to the surface of superfluid helium, which promises large electric dipole moments comparable to those of Rydberg atoms while simultaneously offering long expected spin coherence times of tens of milliseconds or more. This system is introduced in the next section.

1.2 Electrons on Superfluid Helium

Electrons on helium represent a unique type of two-dimensional electron gas (2DEG) formed at the interface of a quantum liquid (superfluid helium) and vacuum [67,68]. The electrons in this system are levitated several nanometers above the surface of liquid helium in vacuum as a result of the combination of a long-range attractive interaction, caused by the image charges electrons induce in the liquid, and a short-range repulsive interaction due to the Pauli exclusion principle. At high densities and low temperatures, electrons on helium form a two-dimensional Coulomb liquid or Wigner crystal, an exotic state of matter known to occur in electrons on helium, semiconductor inversion layers in strong magnetic fields [69] and in the interior of white dwarf stars [70]. Electrons on helium have been actively investigated since the late 1960s [71–73], in large part due to their exceptional transport and coherence properties, which include the highest known mobility of all condensed matter systems [74,75] and spin coherence times possibly exceeding 100 s [76]. However, there have been no observations of quantum-mechanical lateral confinement effects and coherent electron motion so far, partly owing to the fact that it is not possible to make ohmic contact to the floating electrons, which effectively prevents DC transport measurements typically used for probing semiconductor 2DEGs. One of the core ideas of this PhD project is to use electrons on helium to define quantum dots and couple them to superconducting circuits in a cQED architecture. This represents a potentially powerful new way for probing their quantized motional and spin degrees of freedom and allows taking advantage of cavity QED techniques developed in atomic and solid-state systems.

In most traditional semiconductor 2DEGs such as in gallium-arsenide or germanium, the electrons are highly screened by the lattice, forming a degenerate gas of electron-like quasi-

particles with effective masses and dimensionless magnetic moments (g-factors) much less than that of a free electron. Spin coherence is typically limited by the interaction with nuclear spins in the substrate material which create an effective magnetic field for electrons moving in the semiconductor [77]. In contrast, electrons on helium retain their undressed mass and g-factor. Their properties are close to those of free electrons. Decoherence due to spin-orbit interaction is orders of magnitude smaller than in semiconductors as the 'substrate' (superfluid helium) has zero nuclear spin and the electrons are levitated in vacuum, isolating them from any charge impurities and nuclear spins in the substrate below the helium film. The 'undressed' electrons on helium could possibly offer some compelling advantages over semiconductor quantum dots and even ionic or neutral atoms for cavity QED and quantum computing applications. Like superconducting qubits and quantum dots, electrons on helium can be made to strongly interact with lithographically defined gates submerged under the helium, leveraging recent advances in nano- and micro fabrication technology to create complex trapping geometries.

The potential for quantum information processing with electrons on helium has been pointed out early on in one of the first proposals for experimental quantum computing [78,79]. The combination of long-range attractive and short-range repulsive interaction with the superfluid leads to quantization of the vertical motion orthogonal to the helium surface and gives rise to a strongly anharmonic, Rydberg-like energy level spectrum. While these states fulfill many of the criteria required for quantum information processing, their experimentally difficult-to-access transition frequencies (> 100 GHz) and the lack of a non-destructive readout mechanism have so far prevented much progress in this direction. In contrast to those earlier proposals, this PhD project focuses on using lateral quantized states of the electron motion parallel to the helium surface as qubit states. These lateral states can be defined and controlled using electrostatic gates analogous to semiconductor quantum dots.

1.3 Thesis Overview

This thesis describes the theory, design and implementation of a circuit quantum electrodynamics architecture for coupling electrons on superfluid helium to superconducting transmission line resonators. The thesis is structured in a standard way, with the first part focusing on the underlying theory (chapters 2 and 3) and the second part presenting details on

implementation and experimental results (chapters 4 - 7).

Chapter 2 starts with an introduction to electrons on helium that will form the basis for much of the rest of this thesis. Electrons on helium represent a remarkably clean and simple system with some exceptional collective properties. The quantized vertical motion of a single electron above a helium surface is first discussed in section 2.1, together with an early proposal for exploiting this textbook quantum system for information processing purposes. Section 2.2 looks at the physics of many-electron ensembles on helium. These surface states are supported by superfluid helium, a quantum liquid whose unique macroscopic properties arise as a result of microscopic quantum-mechanical effects. Section 2.3 provides a review of the physics of superfluid helium, with particular emphasis on its behavior in micro-channel geometries, which we investigate experimentally in chapter 5.

Chapter 3 develops the theory for circuit QED with trapped electrons on helium. Cavity QED is a quite fundamental and general concept for investigating matter-light interactions with a simple and elegant description in the form of the Jaynes-Cummings hamiltonian. Section 3.1 discusses the Jaynes-Cummings model in the strong coupling regime independent of the physical implementations of the atomic and photonic components. The remainder of chapter 3 then focuses on a cavity QED implementation with superconducting circuits and quantum dots on helium. The cavities used in our experiments are realized in the form of superconducting coplanar waveguide resonators operated in the 1 - 10 GHz range. The modeling and design of those resonators, including various types of terminations, are the subject of section 3.2. In analogy to semiconductors, two-dimensional electron gases on helium can be used to construct single-electron quantum dots using electrostatic gates. This is one of the core ideas behind this thesis and the resulting lateral quantized motional states in such quantum dots are discussed in detail in section 3.3. Section 3.4 then goes on to describe how intradot states can be coupled to coplanar waveguide resonators through dipole interaction, realizing a circuit QED system that is expected to be capable of reaching the strong coupling regime. In addition to its motional degrees of freedom, a trapped electron also has an internal spin degree of freedom that can potentially be used as a highly coherent resource for quantum computing. Unfortunately, the direct coupling of a single electron spin to a cavity is very weak. Section 3.5 therefore describes ways of enhancing the spin-cavity interaction using a form of spin-orbit coupling via the motional degrees of freedom. Reaching the strong coupling regime of cavity QED, where the electron can coherently exchange energy with the cavity, requires sufficiently long lifetimes of the electron states. In addition, long coherence

times are of paramount importance for quantum information processing applications. The various mechanisms of decoherence for both spin and motion in our system are explored in section 3.6. Finally, section 3.7 looks at extended electron traps capable of supporting few-electron states, which will be important for the experiments presented in chapter 7. Much of the work discussed in chapter 3 was carried out together with postdoc Dave Schuster, who originated the main theoretical ideas for this project.

The implementation of a circuit QED setup for electrons on helium experiments requires a combination of a wide variety of techniques and methods, including microwave, RF and DC engineering, nano- and micro-fabrication of superconducting devices and low temperature physics and cryogenics. This is the subject of chapter 4. In addition to the cryogenic measurement setup, particular focus is put on discussing the components developed specifically for electrons on helium experiments such as hermetic sample cells, capillary helium supply lines and thermionic emission sources. Significant effort was put into developing nano- and micro fabrication techniques for single- and many-electron traps, which I summarize in section 4.3.

Chapter 5 moves on to discuss one of the first major experiments carried out for this thesis, which seeks to understand the effects of superfluid helium on the resonance frequencies and quality factors of transmission line cavities. In sections 5.1 and 5.2, I show how superconducting resonators can be used as high precision meters for measuring superfluid thin films and demonstrate how helium-induced frequency shifts help in determining the fill dynamics in micro-channel structures. Using a novel type of DC-biased coplanar waveguide cavity, we then demonstrate in-situ tuning of helium levels in section 5.3.

A key step towards circuit QED experiments with single-electron quantum dots is it to demonstrate that electrons can be generated and trapped on a superconducting chip at sufficiently high densities and milli-Kelvin temperatures. To this end, we have implemented an on-chip submerged electrode geometry, known as a Sommer-Tanner setup, for probing electrons on helium at kHz frequencies. The results of these low-frequency measurements are presented in chapter 6. Section 6.1 discusses the detection method, which takes advantage of the capacitive coupling of surface electrons to the submerged electrodes and the differential voltage they induce as a result of their motion driven at a few hundred kHz. Following a discussion of the device and setup in section 6.2, section 6.3 shows how the on-chip setup can be used to realize the analog of a field-effect transistor on superfluid helium. Electron density measurements are presented in section 6.4.

The final part of this thesis (chapter 7) presents experiments in which an ensemble of electrons is trapped directly inside the gap of a superconducting coplanar waveguide cavity which acts as a large submerged electron trap. There are a variety of ways an electron ensemble in a waveguide gap can couple to the cavity field, including dipole interaction of collective in-plane motional excitations (discussed theoretically in section 3.7), vertical Rydberg states (section 2.1) and combinations thereof. We take advantage of this in our experiments to detect electrons on helium in cavity transmission measurements. The DC-biased center pin design and some numerical simulations of the cavity-ensemble coupling and the electron configurations in the trap are first described in section 7.1. In section 7.2, I present experiments demonstrating how electrons can be trapped in the resonator gap, where their presence manifests itself in the form of trap voltage-dependent shifts in cavity resonance frequency and linewidth. Electron loss, hysteresis and lifetime measurements are presented in section 7.3, showing that the trapped electron ensemble is highly stable and providing a proof of principle for controlled depletion of the trap region. The thesis concludes in chapter 8 with some thoughts on future experiments and the road ahead for circuit QED with electrons on helium.

2 Electrons on Superfluid Helium

ELECTRONS on helium represent a unique type of two-dimensional electron system in which electrons are levitated above the surface of superfluid helium with a bound state spectrum resembling that of a Rydberg atom. Proposed theoretically by Sommer [80, 81], Cole and Cohen [72, 82] and first observed experimentally by Williams et al. [73], these exotic types of surface states are the result of the combination of a long-range attractive interaction due to surface polarization and a short-range repulsive interaction due to the Pauli exclusion principle. Interest in electrons on helium has been historically motivated by their remarkable transport properties, including the highest known mobility of all condensed matter systems [74, 75]. More recently, the focus has shifted towards quantum information processing applications and the possibility of defining quantum dots with electrons on helium where both motional and spin degrees of freedom could be used as long-lived qubit states [64, 76, 78, 79]. In this chapter, the fundamental physics of electronic surface states on superfluid helium are explored, laying the theoretical groundwork for much of chapter 3 and the remaining parts of this thesis. Starting with a discussion of the quantized motion of a single electron perpendicular to the surface of liquid helium, the hydrogen-like energy spectrum and the effects of external electric fields are presented in sections 2.1.1 and 2.1.2, while section 2.1.3 focuses on how the vertical electron motion can be used for quantum computing applications. Extending the single electron case to many-electron systems in section 2.2, the Coulomb liquid, electron gas and Wigner crystal phases are discussed in sections 2.2.1 - 2.2.3. Finally, section 2.3 focuses on the thermodynamic and transport properties of superfluid helium in the thin film regime and provides an introduction to elementary excitations of the liquid such as ripplons.

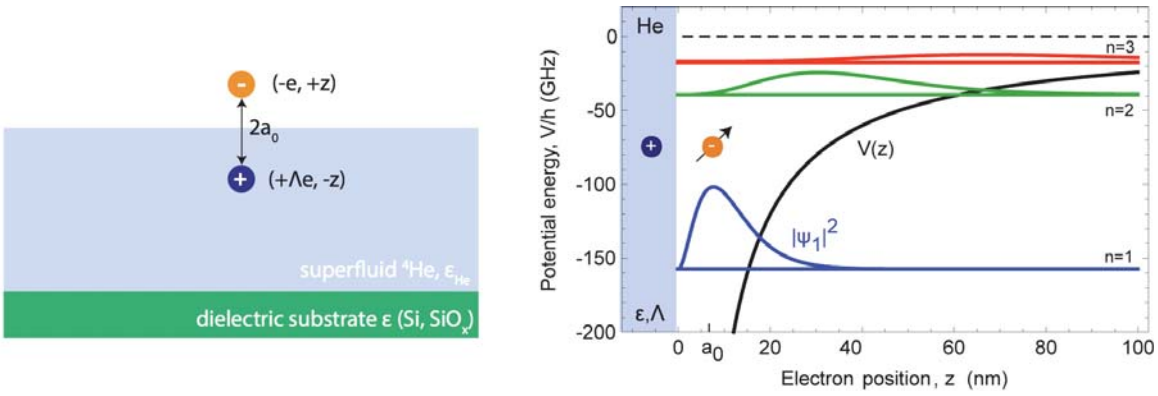

Figure 2.1.: Single electron above the surface of superfluid helium: (a) Illustration of an electron levitated a distance $z \sim a_0$ above the surface, interacting with its image charge $Q = \Lambda e$ at position $-z$. (b) Energy spectrum and wave functions of an electron bound to the surface of liquid helium as a function of electron position above the surface. The lowest three energy levels $n = 1, 2, 3$ are shown together with the probability densities of the wave functions and the image charge potential. The spectrum is strongly anharmonic and resembles that of a hydrogen or Rydberg atom.

2.1 Quantized Vertical Motion

The interaction of a single electron and an isolated ^{4}He atom is governed by a short-range repulsive component and a weakly attractive long-range component [83]. The short-range component is a consequence of the Pauli exclusion principle which requires the additional electron wave function to be orthogonal to the 1s state wavefunctions of ^{4}He, which leads to a substantial energy barrier for the formation of negative helium ions. On the other hand, at distances large compared to typical atomic scales ~ 1 Å, an electron is attracted to a helium atom as a result of polarization. The strength of this interaction is relatively small as a result of the extremely weak polarizability of helium, which has a dielectric constant near unity $\varepsilon_{\mathrm{He}} \simeq 1.0572$ and a measured loss tangent of $< 10^{-11}$ at GHz frequencies [1] [85–87]. The polarization is in fact so weak that an isolated helium atom in three dimensions cannot trap an electron to form a negative ion, an effect commonly referred to as *negative electron affinity*. This, however, need not be the case if an electron interacts with a macroscopic film of liquid ^{4}He.

2.1.1 Rydberg Surface States

The single electron-helium atom interactions carry over to the macroscopic case of the interaction of an electron with a bulk liquid helium film, illustrated in Fig. 2.1 a. The short-range

[1] Theoretical predictions for the loss tangent of superfluid helium are on the order of $\tan\delta < 10^{-25}$ at 3 GHz [84], limited by radiation damping effects.

repulsion manifests itself through the negative work function of liquid helium, leading to an energy barrier for electron injection into the liquid. Calculated values for the barrier energy range from 0.97 - 1.09 eV [88, 89], in good agreement with measured values of 1.02 ± 0.08 eV [90] and 1.3 ± 0.3 eV [80]. As shown below, the mean distance of an electron in the ground state from the liquid-vapor interface is two orders of magnitude larger than typical atomic scales such that the attractive polarization can be described macroscopically by an equivalent induced image charge, as shown schematically in Fig. 2.1 a. While too weak to support binding of an electron to an isolated ^{4}He atom, the polarization effect in bulk helium is strong enough to localize the electron wave function above the surface and support stable bound surface states [72, 82]. Following Refs. [68] and [91], we can approximate the one-dimensional potential of an electron a distance $+z$ above a liquid helium-vapor interface as

$$\Phi_e(z) = \Phi_0 \Theta(-z) - \frac{\Lambda e^2}{4\pi\varepsilon_0(z+z_0)}\Theta(z) \tag{2.1}$$

where $\Theta(\cdot)$ is the Heaviside step function, $\Phi_0 \sim 1$ eV is the injection barrier and

$$\Lambda = \frac{\varepsilon_{\mathrm{He}} - 1}{4(\varepsilon_{\mathrm{He}} + 1)} \approx 0.00696 \quad , \quad \varepsilon_{\mathrm{He}} = 1.05723 \tag{2.2}$$

are the image charge factor and dielectric constant of liquid helium at 1.2 K. The offset parameter z_0 avoids the singularity at the interface boundary and is usually adjusted to fit the bound state spectra obtained from spectroscopy measurements [91] to exact solutions of the Schrödinger equation [92], with a typical value of $z_0 \simeq 1.01$ Å [68]. Note that eq. (2.1) assumes a perfectly flat helium surface, which is a good approximation as corrections accounting for the real density profile of liquid helium have been shown to be small [93]. Since z_0 is two orders of magnitude smaller than the average electron distance from the surface and the injection barrier Φ_0 is three to four orders of magnitude larger than the bound state energies, we can further approximate the potential by

$$\Phi_{\mathrm{e}}(z) = \begin{cases} -\frac{\Lambda e^2}{4\pi\varepsilon_0 z} & , z > 0 \\ +\infty & , z \leq 0 \end{cases} . \tag{2.3}$$

As shown below, this is a very good approximation and typically sufficient to capture most interesting phenomena. While perpendicular motion is limited to $z > 0$, motion parallel to the surface is unconstrained. The three-dimensional Schrödinger equation for an electron

above liquid helium is therefore given by

$$\left[\frac{-\hbar^2}{2m}\left(\frac{\partial^2}{\partial x^2}+\frac{\partial^2}{\partial y^2}+\frac{\partial^2}{\partial z^2}\right)-\frac{\Lambda e^2}{4\pi\varepsilon_0 z}\right]\Psi(\vec{r})=E\Psi(\vec{r}) \tag{2.4}$$

with the boundary condition $\Psi(x,y,z=0)=0\,,\forall x,y$. Eq. (2.4) is trivially separable in Cartesian coordinates with a solution that can be written as the product of a plane wave describing the free electron motion parallel to the surface and a one-dimensional wave function for the vertical motion,

$$\Psi(\vec{r})=\chi(z)\cdot\frac{e^{i\mathbf{k}\cdot\mathbf{r}}}{\sqrt{A_\mathrm{s}}} \tag{2.5}$$

where $\mathbf{k}=(k_x,k_z)$ and $\mathbf{r}=(x,y)$ are two-dimensional vectors and A_s is the surface area under consideration. The total electron energy is given by

$$E=\frac{\hbar^2\mathbf{k}^2}{2m}+E_n \tag{2.6}$$

where E_n is the quantized vertical motional energy to be determined. The vertical wave function $\chi(z)$ in position basis is described by the resulting one-dimensional Schrödinger equation

$$\left[-\frac{\hbar^2}{2m}\frac{\partial^2}{\partial z^2}-\frac{\Lambda e^2}{4\pi\varepsilon_0 z}\right]\chi_n(z)=E_n\chi_n(z) \tag{2.7}$$

with the Dirichlet boundary condition $\lim_{z\to 0}\chi_n(z)\to 0$. Eq. (2.7) is identical to the radial Schrödinger equation for a Hydrogen atom with zero angular momentum and an effective nuclear charge $Z=\Lambda e$.[2] Introducing the effective Bohr Radius and Rydberg constant

$$a_0=\frac{4\pi\varepsilon_0\hbar^2}{m_e e^2\Lambda}\quad,\quad R_y^*=\frac{m_e e^4\Lambda^2}{2\hbar^2(4\pi\varepsilon_0)^2}\quad\to\quad a_0R_y^*=\frac{e^2\Lambda}{8\pi\varepsilon_0} \tag{2.8}$$

and the dimensionless coordinate and energy

$$\xi=z/a_0\quad,\quad \mathcal{E}_n=E_n/R_y^* \tag{2.9}$$

we have

$$\left(-\frac{\partial^2}{\partial\xi^2}-\frac{2}{\xi}\right)\chi_n(\xi)=\mathcal{E}_n\chi_n(\xi) \tag{2.10}$$

[2] The textbook treatment of a Hydrogen atom with separation of variables in spherical coordinates leads to a radial wave function $\Psi(R)=\chi(R)/R$ which requires the boundary condition $\chi(0)=0$ for the solutions to remain finite.

The Rydberg energy of the helium surface is $R_y^* \simeq 0.658\,\text{meV} = 159.123$ GHz or approximately 8 K with a Bohr radius of $a_0 \simeq 76$ Å$= 7.6\,\text{nm}$, much larger than typical atomic scales ~ 1 Å. The regular solutions of (2.10) are given by a confluent hypergeometric series such that the vertical wavefunctions can be written in terms of generalized Laguerre polynomials [94, 95]

$$\chi_n(z) = \langle n|z\rangle = \frac{1}{\sqrt{n^3 a_0}} \frac{2z}{na_0} e^{-z/a_0} \mathcal{L}_{n-1}^{(j)}\left(\frac{2z}{na_0}\right) \tag{2.11}$$

which are related to the *associated* Laguerre polynomials $L_n^{(j)}$ through

$$\mathcal{L}_n^{(j)}(z) = \frac{1}{(-1)^j (n+j)!} L_n^{(j)}(z) \tag{2.12}$$

for $j \in \mathbb{N}$. The corresponding energy spectrum is hydrogen-like and described by a Rydberg formula

$$\mathcal{E}_n = -\frac{1}{n^2} \quad \rightarrow \quad E_\text{n} = -\frac{R_\text{y}^*}{n^2} = -\frac{m_e e^4 \Lambda^2}{8\pi\varepsilon_0 \hbar^2} \frac{1}{n^2} \tag{2.13}$$

The lowest three energy levels and wave functions are shown in Fig. 2.1 b together with the image charge potential. Note the strong natural anharmonicity of the energy spectrum. The average distances from the surface for the ground, first and second excited state are

$$\langle 1|z|1\rangle \simeq 11.42\,\text{nm} \quad , \quad \langle 2|z|2\rangle \simeq 45.66\,\text{nm} \quad , \quad \langle 3|z|3\rangle \simeq 102.73\,\text{nm}$$

which significantly exceeds atomic length scales. The transition frequencies are described by a Balmer series

$$\omega_{mn}/2\pi = \frac{1}{h}\left(|E_m - E_n|\right) = \frac{R_y^*}{h}\left|\frac{1}{m^2} - \frac{1}{n^2}\right| \tag{2.14}$$

For the lowest two transitions we have $\omega_{12}/2\pi \simeq 119.16$ GHz ~ 5.72 K and $\omega_{23}/2\pi \simeq 22.09$ GHz ~ 1.06 K and a natural anharmonicity of $\alpha = (E_{23} - E_{12})/E_{12} = -0.815$. At the typical working temperatures of 20 mK used in the experiments presented in this thesis, the electron is therefore effectively frozen into the ground state of vertical motion.

At this point, it is worthwhile revisiting the various approximations made so far. The details of the surface potential have been neglected in (2.3) and the presence of the helium film only comes into play as a bulk dielectric containing the positive image charge. This is indeed well justified given the large Bohr radius which indicates that the wave function is concentrated far from the surface. Hence we expect the electronic properties to be only weakly sensitive to the details of the surface density profile. A more realistic perturbative

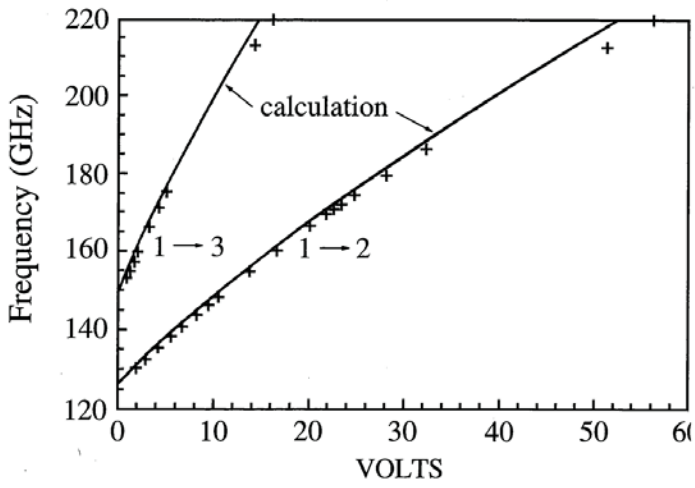

Figure 2.2.: Stark-shifted transition frequencies for vertical motional states as a function of voltage across the experimental cell, as first measured by Grimes et al. [91]. Crosses are spectroscopically measured data points and solid curves are variational calculations using exponentially decaying polynomials as trial wavefunctions. Figure taken from Ref. [68].

treatment by Sanders et al. [96] using expression (2.1) with an interface of non-zero thickness found an effective surface thickness of $z_0 = 0.91$ Å through comparison with spectroscopic data [97]. The error from the hard-core potential assumption (2.3) translates into small deviations from the ideal Hydrogen quantum numbers $n' = n + \delta$ with $\delta = -0.0237$ [96]. Further studies in Refs. [93] and [98] using a general liquid density profile function $\rho(z)$ and Hartree-type potentials confirm that the image potential gives a sufficiently accurate spectrum for most practical applications. Observed transition energies are typically on the order of 7 GHz larger than predicted by the Balmer series (2.14) [91], corresponding to an error of about 5 - 6 %.

2.1.2 Stark Shift and External Fields

Compared to atomic systems, the binding potential between electrons and a liquid helium film is very weak, leading to a large Bohr radius and wave functions that extend far above the helium-vapor interface. An external electric field leads to compression of the wave function and a Stark shift of the bound state energies, similar to the atomic case. Due to the large size of the wave functions, even weak applied electric fields can cause significant compression of the wave function and a sizable Stark shift. The unusually strong Stark effect was used by Grimes et al. in the first spectroscopic measurements to tune the electronic transitions into resonance with applied microwave fields in the range of 100 - 200 GHz [91,97]. The original data from these experiments is reproduced in Fig. 2.2. Understanding the Stark effect for

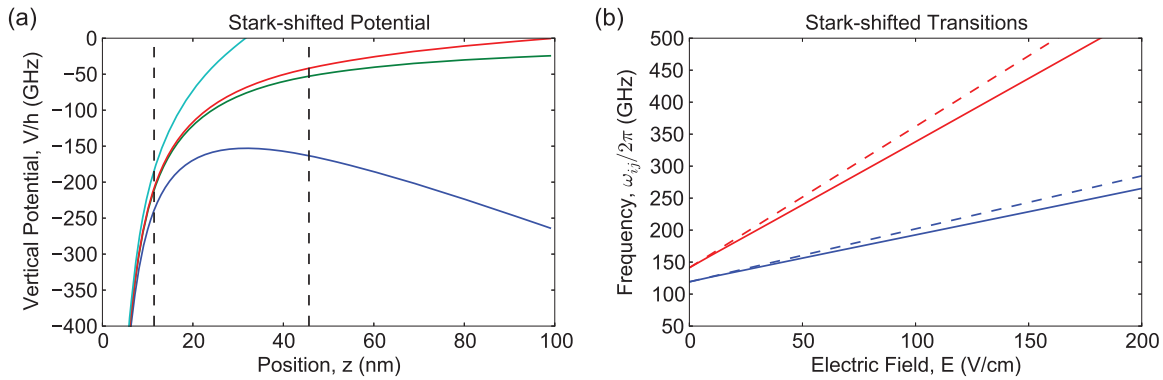

Figure 2.3.: Stark shift for electrons on helium: (a) Electron binding potential for different external fields $E_\perp = -100$ (blue), 0 (green), +10 (red) and +100 V/cm (light blue). For large positive fields, the potential approaches a triangular shape while for negative $E_\perp$ a low ionization barrier forms and excited states can be ionized quickly, see discussion in text. (b) Stark-shifted transition frequencies between ground and first excited $\omega_{12}/2\pi$ (red) and ground and second excited state $\omega_{13}/2\pi$ (blue). Solid lines are results from a numerical diagonalization of the Hamiltonian and dashed lines are first-order perturbation theory results.

electrons on helium will be important later on when coupling to the electromagnetic field in a superconducting transmission line resonator is discussed in chapters 3 and 7.

Using the coordinates (2.9), we can write the dimensionless Hamiltonian of an electron on helium in a uniform external field $E_\perp$ in the z-direction as

$$\mathcal{H} = \frac{\partial^2}{\partial \xi^2} + \frac{2}{\xi} - eE_\perp \xi \left(\frac{a_0}{R_y^*}\right) \tag{2.15}$$

with the original Stark-shifted potential

$$\Phi_e(z) = -\frac{\Lambda e^2}{4\pi\varepsilon_0 z} + eE_\perp z \tag{2.16}$$

The potential $\Phi_e(z)$ is shown in Fig. 2.3 a for several typical electric field strengths $E_\perp = -100, 0, 10$ and 100 V/cm. For large fields, the potential approaches a triangular form as the Stark-shift term dominates the image charge attraction. As the potential becomes steeper for larger positive fields, the ground and excited states are pushed further and further apart in frequency. For negative fields the excited states become very easy to ionize, which is the converse effect of the large Stark tuning rates. For moderate negative field strengths, the potential becomes quite shallow with a small ionization barrier for the lowest excited states, allowing excited surface state electrons to leave the surface via tunneling through the ionization barrier. This forms the basis of the qubit readout mechanism discussed in section 2.1.3.

In the limit of small external fields, the energy correction to the nth vertical state in first-order perturbation theory is given by the linear Stark shift

$$\Delta E_n^{(1)} = eE_\perp \langle n|z|n\rangle = e \cdot a_0 \cdot E_\perp \int_0^\infty \chi_n^*(\xi) \cdot \xi \cdot \chi_n(\xi) d\xi \tag{2.17}$$

where $\chi_n(z)$ are the unperturbed wave functions (2.11). This is in good agreement with experiment for energies $\Delta E_n^{(1)} \ll E_{n+1} - E_n$ [97], giving appreciable linear Stark tuning rates of 0.83 GHz/(V/cm) and 1.38 GHz/(V/cm) for the $1 \rightarrow 2$ and $2 \rightarrow 3$ transitions, respectively. In the limit of large external fields $E_\perp > \Lambda/4\pi\varepsilon_0 a_0^2$, we can ignore the image potential term and replace (2.16) by a triangular-shaped potential with the boundary condition $\lim_{z\to 0} \chi_n(z) = 0$. Exact solutions in terms of Airy functions can be found in this case [68]. For intermediate fields, the ground state wave function can be approximated using a variational method with the unperturbed wave function $\chi_1(z)$ as trial wave function [99, 100], which gives results in good agreement over a wide range of measured shifts [91], see also Fig. 2.2. Alternatively, one can calculate the matrix elements $\mathcal{H}_{ij} = \langle i|\mathcal{H}|j\rangle$ in the basis of the unperturbed states and diagonalize the Hamiltonian numerically taking into account d dimensions of the Hilbert space with $i, j \in [1, d]$. Fig. 2.3 b shows the Stark-shifted transition frequencies for the lowest transitions as functions of applied field, calculated via numerical diagonalization of the Hamiltonian (solid lines) and in first-order perturbation theory (dashed lines). Note that the large Stark shift allows tuning the transitions over hundreds of GHz.

2.1.3 Quantum Information Processing With Vertical States

The strong anharmonicity of the vertical motional spectrum together with the ability to Stark-tune transitions and the relatively weak coupling to the environment make electrons on helium a natural candidate system for quantum information processing applications. In one of the earliest proposals for experimental quantum computing, Platzman and Dykman proposed using the hydrogenic levels of a trapped electron on helium as the computational basis states of a quantum computer [78, 79]. The states of individual electrons are controlled using microwave pulses and information transfer is achieved via nearest-neighbor Coulomb coupling of electrons. In this section we briefly review quantum computing with vertical states and contrast it later on with the lateral motional and spin-based approaches proposed in chapter 3.

Decoherence Mechanisms

The coupling of hydrogenic states of electrons on helium to the environment is generally very weak due to the absence of surface impurities and the atomically smooth superfluid-vapor interface (see section 2.3). In particular, below $T \lesssim 600$ mK the vapor pressure of liquid helium is effectively zero such that scattering by vapor atoms is suppressed. In the absence of external electromagnetic fields, the only substantial coupling to the environment is through thermally excited capillary surface waves, so-called ripplons which are discussed in more detail in section 2.3.5. Ripplons represent quantized propagating height variations $\delta(\mathbf{r}, t)$ with a cubic dispersion relation $\omega^2 = (\sigma/\rho)k^3$ where $\mathbf{r} = (x, y)$ is an in-plane vector and $\rho = 0.154 \times 10^{-3}$ kg/cm^3 and $\sigma = 0.378 \times 10^{-3}$ N/m are the mass density and surface tension of liquid helium, respectively. Quasi-elastic scattering by capillary waves and electron relaxation via ripplon emission are the main decoherence mechanism for hydrogenic electron states. The vertical motion of an electron above the surface couples to these height variations through

$$\mathcal{H}_I = e \cdot E_\perp \cdot \delta(\mathbf{r}, t) \tag{2.18}$$

where $E_\perp$ is the total perpendicular holding field applied to the sample cell. Quasi-elastic scattering by capillary waves is the limiting factor for the mobility of surface-state electrons ($\mu \sim 10^8$ cm^2/Vs [68]) and electron relaxation via ripplon emission sets a limit to achievable energy relaxation times T_1. The size of the transition matrix elements $\langle j|e \cdot E_\perp \cdot \delta(\mathbf{r}, t)|i\rangle$ depends primarily on the size of the ripplon wave vector and the size of the electronic wave function. For a laterally-unconfined electron, coupling to ripplons with matching wave vectors $k \simeq a_0^{-1}$ leads to an energy relaxation rate that can be estimated as [78]

$$\frac{1}{T_1} \simeq \frac{R_y^*}{\hbar}\left(\frac{\delta_{\mathrm{rms}}}{a_0}\right)^2 \quad \rightarrow \quad T_1 \simeq 150\,\mathrm{ns} \tag{2.19}$$

where $\delta_{\mathrm{rms}} = \sqrt{k_B T/\sigma} \sim 2 \times 10^{-9}$ cm is the mean-square height variation at $T = 100$ mK. This looks quite bad at first sight. However, one ripplon decay can be suppressed exponentially by lateral in-plane confinement of the electrons or alternatively by application of a strong perpendicular magnetic field, both of which create a mismatch between the size of the electron wave function and the ripplon wavelength at the same energy [79]. Ripplons are very slow and energy conservation would require too large of a ripplon momentum for an electron to accommodate, as discussed in more detail in section 3.6. The limiting factor in the

confined case are two-ripplon processes, which can lead to energy relaxation via emission of two ripplons of nearly opposite momentum and equal energy. The dominant dephasing mechanism is quasi-elastic scattering of thermally excited ripplons where both one- and two-ripplon coupling contributes [79]. The quasi-elastic scattering of thermal excitations off an electron is different if the electron is in the ground $|1,0,0\rangle$ or first excited vertical state $|2,0,0\rangle$ and therefore randomizes the phase difference between the wave functions without causing any transitions. Other dissipative processes such as spontaneous radiative and non-radiative emission as well as voltage noise can be shown to give only negligible contributions to decoherence, see Ref. [78] and the discussion in section 3.6. Detailed calculations in Ref. [79] predict overall decay and dephasing rates of $\Gamma_1 \sim 10^4$ s^{-1} for two-ripplon decay and $\Gamma_\phi \sim 10^2$ s^{-1} for quasi-elastic one- and two-ripplon dephasing at 10 mK, respectively. In addition, voltage fluctuations in the controlling electrodes (Johnson noise) are predicted to lead to a dephasing rate of $\Gamma_\phi \sim 10^4$ s^{-1} [79].

Qubit Readout

The basic readout mechanism proposed in Ref. [78] is based on destructive, state-selective ionization of electrons from the surface. By applying a weak reverse perpendicular electric field $E_\perp^{(+)}$, the electron tunneling rate for overcoming the ionization barrier, which depends exponentially on the barrier height, becomes strongly state-dependent such that only excited state electrons will leave the surface for certain values of $E_\perp^{(+)}$. The vertical potential in the presence of such a uniform reverse perpendicular holding field of strength -100 V/cm is shown in Fig. 2.3 a. The ionized electrons with kinetic energies of tens of eV are then to be collected on a channel-electrode configuration with good spatial resolution of about $1\,\mu$m, allowing to 'image' the wave function. The main drawback of this approach is its destructive nature as qubits can not be reused for further computational operations.

Qubit Control and Coupling

Single-qubit operations are achieved by application of microwave pulses in the 100 - 200 GHz range, taking advantage of Stark-tuning of the ground to first excited state transition, as discussed in section 2.1.2, which can be done selectively and locally using additional submerged DC electrodes underneath each electron. For microwave field amplitudes of $E_{\mathrm{RF}} \sim 1$ V/cm, the Rabi frequency is approximately $\Omega \simeq eE_{\mathrm{RF}}a_0 \simeq 10^9$ s^{-1}, allowing on the order of $\Omega T_2 \simeq 10^5$ operations for predicted coherence times of $T_2 \simeq 10^{-4}$ s. Coherent

resonant energy transfer between qubits can be achieved through nearest-neighbor Coulomb coupling of individual trapped electrons. As shown in Ref. [79], the Coulomb interaction of two neighboring electrons acquires a positional coupling term

$$V(z_1, z_2) \simeq \frac{e^2}{d^3} z_1 \cdot z_2 \tag{2.20}$$

where $d \simeq 0.5\,\mu$m is the thickness of the helium film. This interaction term leads to a state-dependent energy shift of the neighbor and allows for resonant transfer of energy between nearby electrons.

While vertical motional states should have promising coherence times and a natural strongly anharmonic energy spectrum, the destructive readout together with the experimentally hard-to-access frequency range of > 100 GHz, has so far kept this proposal from being realized experimentally, despite advances in local control of electrons on helium [101, 102].

2.2 Many-Electron States on Helium

A collection of electrons above the surface of superfluid helium can form a two-dimensional electron gas (2DEG), a Coulomb liquid or a Wigner crystal depending on temperature and electron density [67]. Such 2DEGs and solids on liquid helium exhibit some remarkable properties, including long predicted spin coherence times [76], bare electron mass and g factor and the highest known mobility of all condensed matter systems [74, 75]. In this section, the single electron case is extended to the situation of many electrons above the surface and the collective properties of the system and its different phases are explored. Starting with a discussion of the two-dimensional many-electron Hamiltonian and the electrons on helium phase diagram in section 2.2.1, the 2DEG and Coulomb liquid states are discussed and a comparison with traditional semiconductor electron gases is given in section 2.2.2. Wigner crystallization and some important features of this phase are described in section 2.2.3. Much of the physics discussed in this section will be important in the many electron trapping experiments and transport measurements presented in chapters 6 and 7.

2.2.1 Hamiltonian and Phase Diagram

The case of a single electron bound to the surface of liquid helium (section 2.1) can be readily extended to the case of many electrons collected as a two-dimensional sheet floating above

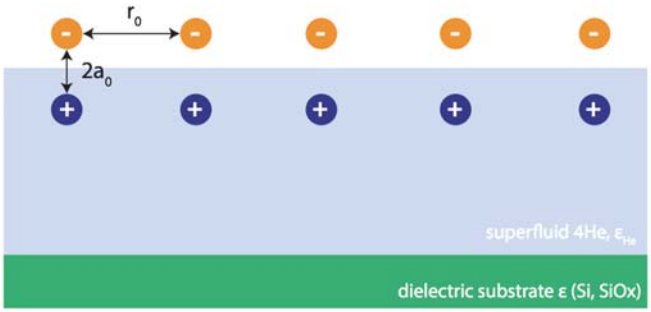

Figure 2.4.: Two-dimensional many-electron system above a superfluid helium film. Electrons are bound to the surface individually through surface polarization, locating them a Bohr radius a_0 above the superfluid-vapor interface. The mean electron separation r_0 is typically several orders of magnitude larger than the Bohr radius, see discussion in text.

the helium surface. The situation is shown schematically in Fig. 2.4. Individual electrons are bound to the surface via their induced image charges and are levitated at distances of $\langle 1|z|1\rangle \sim 11$ nm above the surface in their vertical ground states. Achievable areal electron densities on bulk films are on the order of $n_s \sim 10^7 - 10^9$ cm^{-2} such that the mean electron spacing $r_0 = \sqrt{1/\pi n_s} \sim 0.2 - 2\,\mu$m is orders of magnitude larger than the average distance of the electrons from the helium surface ($r_0 \gg a_0$). Hence, to lowest order we can ignore the interaction of electrons with image charges of their neighboring electrons, which are only a small fraction of the electron charge $Q = \Lambda e \sim 6 \times 10^{-3} e$. Now at temperatures small compared to the vertical excitation energies $T \ll 8$ K, the electrons are effectively frozen into their vertical ground states and the motion orthogonal to the surface can be regarded as eliminated. The characteristic frequencies of the z motion are much higher than for the unconstrained in-plane motion such that the total potential separates, $V(\mathbf{r}) = V(x,y) + V(z)$, to a good approximation. In the absence of any external electromagnetic fields or charge impurities on the surface, the Hamiltonian for motion parallel to the helium surface is given by [103]

$$\mathbf{H} = \sum_{i=1}^{N} \frac{\hbar^2}{2m_e}\Delta_i + \frac{1}{2}\sum_{i\neq j}\frac{e^2}{4\pi\varepsilon_0|\mathbf{r}_i - \mathbf{r}_j|} = \mathbf{H}_{\text{kin}} + \mathbf{H}_{\text{I}} \tag{2.21}$$

where $\mathbf{r}_j = (x_j, y_j)$ are two-dimensional vectors parallel to the helium surface. The neutralizing positive background for electrons on helium is typically provided by a uniform external field generated by macroscopic capacitor plates, as for example in the experiments of chapter 6. Note that the potential and positive charge background provided by the image charges only enters through the z coordinate and does not need to be taken into account again in the 2D Hamiltonian. The effects of neighboring images is negligible due to the large equilibrium

separation.

From (2.21) we see that the phase of the electron system is purely determined by the competition of kinetic energy and electron-electron Coulomb interactions. Due to the absence of any charged impurities in the helium film, electron-electron interactions are therefore the primary mechanism of electron localization in this system. The transition between electron gas, Coulomb liquid and Wigner crystal phases can then be fully characterized by changes in electron density n_s and temperature T. We can parametrize the phase transitions by introducing the dimensionless Bruckner parameter [68]

$$r_s = \frac{r_0}{a_B} \quad , \quad r_0 = \frac{1}{\sqrt{\pi n_s}} \tag{2.22}$$

which is the ratio of mean electron spacing r_0 and the atomic Bohr radius $a_B = 4\pi\varepsilon_0\hbar^2/me^2$. For typical semiconductors we have $n_s \sim 10^{11} - 10^{12}$ cm^{-2} and $r_s \sim 2-6$ [104] while for electrons on helium $r_s \sim 2 \times 10^4$ due to the much lower achievable densities of $n_s \sim 10^7 - 10^8$ cm^{-2}. At small r_s (high densities), electrons on helium form a strongly-correlated Fermi liquid, while at large r_s (low densities) they form a Wigner crystal at sufficiently low temperatures. This transition does not occur in conventional solid state systems under normal conditions where electron-electron Coulomb interactions are strongly screened and have a much shorter range. For electrons on helium, the electron-electron Coulomb interactions are essentially unscreened, which leads to a large restoring force for electron displacement from their equilibrium positions. The long-range nature of the Coulomb interaction is sufficient to localize the electrons in regular lattice sites.

Formally, the characteristic quantity that describes the phase of the electrons on helium system is the plasma parameter $\Gamma^{(\mathrm{pl})} = \overline{V_c}/\overline{K_e}$, the ratio of mean Coulomb to mean kinetic energy. The mean potential energy per electron can be estimated by

$$\overline{V_e} = \frac{e^2}{4\pi\varepsilon_0 r_0} = \frac{e^2\sqrt{\pi n_s}}{4\pi\varepsilon_0} \tag{2.23}$$

while the mean kinetic energy is given by a two-dimensional integral over the Fermi distribution [104]

$$\overline{K_e} = \frac{1}{n_s}\int \frac{d^2p}{2\pi^2}\frac{E_p}{e^{\beta(E_p-\mu)}+1} \tag{2.24}$$

where $E_p = p^2/2m = \hbar^2k^2/2m$, $\beta = 1/k_BT$, μ is the chemical potential and the electron

density is given by

$$n_s = \int \frac{d^2p}{2\pi^2} \frac{1}{e^{\beta(E_p-\mu)}+1} \tag{2.25}$$

In the zero-temperature limit of the Fermi distribution we have

$$\lim_{T\to 0} f(E_p) = 1 \quad \text{if} \quad E_p < \mu = E_F \tag{2.26}$$

where $E_F = \hbar^2 k_F^2/2m$ and $k_F = \sqrt{2\pi n_s}$ are the two-dimensional Fermi energy and wave vector, respectively. In this limit the mean kinetic energy is just half the Fermi energy such that

$$\overline{K_e} = \frac{\varepsilon_F}{2} = \frac{\hbar^2}{2m_e r_0^2} \quad \rightarrow \quad \Gamma^{(\mathrm{pl})} = 2r_s \tag{2.27}$$

and the plasma parameter is equivalent to the Bruckner parameter. In the high-temperature classical regime on the other hand where $\overline{K_e} = k_B T$, we have for non-zero temperatures

$$\Gamma^{(\mathrm{pl})} = \frac{\overline{V_c}}{k_B T} = \frac{e^2\sqrt{\pi n_s}}{4\pi\varepsilon_0 k_B T} = \frac{\hbar^2}{m k_B T}\frac{1}{r_s} \tag{2.28}$$

which has the opposite dependence on the Bruckner parameter. For intermediate temperatures and densities, the integrals (2.24) and (2.25) can be solved analytically [105]. The resulting liquid-solid phase boundary parametrized in terms of critical density and temperature is shown in Fig. 2.5. For $\Gamma^{(\mathrm{pl})} < 1$ (low densities, high temperatures), we expect the kinetic energy to dominate the Coulomb potential and hence a dilute electron gas-like phase. For intermediate densities and temperatures such that $1 \lesssim \Gamma^{(\mathrm{pl})} \lesssim 100$, electron-electron interactions start to dominate electron motion and we expect a strongly-correlated, liquid-like system. Finally, for high densities and low temperatures $\Gamma^{(\mathrm{pl})} \gtrsim 100$, Coulomb interaction completely dominates kinetic energy and the electrons are expected to localize in a regular lattice.

While Fig. 2.5 gives a good qualitative picture, exact determination of the phase boundary and the corresponding critical values of $\Gamma^{(\mathrm{pl})}$ is quite complicated and has been subject of extensive theoretical and experimental research since the 1970s [67, 105–108]. The ability to accurately control the density of electrons on helium over a wide range of values via simple DC voltages has established it as the primary system for studying Wigner crystallization. Experimentally, the measured values for the plasma parameter at melting range from 124 ± 4 to 139 ± 8 [109, 110], The first observation of the phase transition by Grimes et al. [111] gave a value of $\Gamma^{(\mathrm{pl})} > 137 \pm 15$. At fixed density of $n_s = 10^8$ cm^{-2}, the phase transition therefore

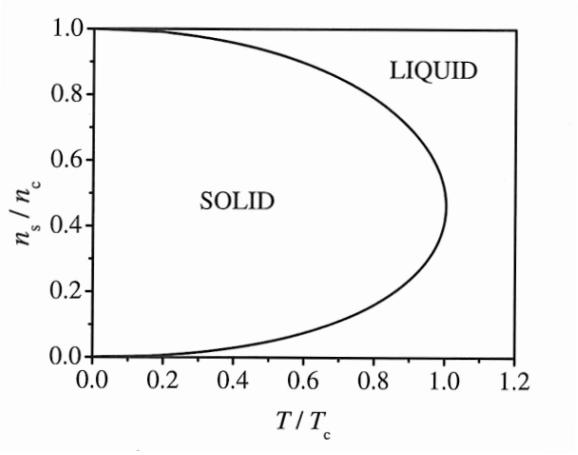

Figure 2.5.: Parametrized phase diagram for two-dimensional electrons on helium. n_c and T_c are the critical density and temperature for melting of the Wigner solid, as calculated in Ref. [105]. Figure taken from Ref. [68], based on [105].

occurs at about $T_c \sim 200$ mK. The measured values are in good agreement with theoretical calculations which are in the range of $\Gamma^{(\mathrm{pl})} = 120 - 130$ [68].

2.2.2 Two-Dimensional Electron Gas and Coulomb Liquid

The physics of the two-dimensional electron gas above liquid helium differs in a number of important ways from the more well-known semiconductor case. Many of the remarkable collective properties of 2DEGs on helium are a direct consequence of the unscreened long-range Coulomb interactions and the atomically smooth, impurity-free surface of the superfluid helium which acts as the host substrate. Here, we briefly contrast the semiconductor and liquid helium cases in terms of practically important properties such as mobility, density and effective mass. Detailed treatments of the scattering mechanisms and electron-electron correlations can be found in Refs. [68], [67] and references therein.

In most conventional semiconductor 2DEGs such as in GaAs, the electrons form a degenerate gas with small effective masses, renormalized g-factors, and strong interactions with excitations of the host lattice, in particular strong piezoelectric coupling to 2D and 3D acoustic phonons. Apart from weak coupling to surface capillary waves, these mechanisms are absent for electrons on helium. This manifests itself in a variety of macroscopic properties:

- **Effective Mass**: The effective mass of electrons on helium is very close to the free electron mass, $m^* \simeq 0.99 \cdot m_e$, while in semiconductors such as GaAs $m^* \simeq 0.067 \cdot m_e$ or Germanium $m^* \simeq 0.56 \cdot m_e$ such that electrons behave like very light quasi particles.

- **Charge**: The effective charge of the quasi particles in semiconductors is reduced by the dielectric constant of the substrate $e^* = e/\sqrt{\varepsilon}$ while for electrons on helium no such screening takes place $e^* = e$.

- **Gyromagnetic Ratio**: The g factor for GaAs is $g \simeq -0.44$ while for electrons on helium $g \simeq 2$ close to the free electron spin g-factor.

- **Mobility**: Electrons on helium have the highest measured mobility of all condensed matter systems, with measured values of up to $\sim 10^{10}$ cm^2/Vs [74, 75]. This is several orders of magnitude larger than in typical semiconductors where $\mu \sim 10^4 - 10^6$ cm^2/Vs [112]. The high mobility is a consequence of the absence of many of the scattering mechanisms present in solids. The electrons are far removed from the surface and at low temperatures where the vapor pressure of liquid helium goes to zero, the only electron scattering mechanism is through capillary surface waves (ripplons). We can distinguish two regimes where electron scattering is dominated by vapor atoms ($T > 1.2$ K) and ripplons ($T < 0.7$ K) [68]. Early mobility measurements where limited to temperatures $T > 0.8$ K and observed a characteristic exponential increase of mobility with decreasing temperature [71] while more recent experiments clearly show the transition to the ripplon-limited regime and the abrupt drop in mobility as the system crystallizes [74, 75, 113, 114].

- **Density**: Typical electron densities on bulk liquid helium are on the order of $10^8 - 10^9$ cm^{-2}, limited by a hydrodynamic instability which is discussed in detail in section 2.3.3. Varying the density in a 2DEG on helium over several orders of magnitude can be achieved in-situ by changing the DC voltages applied to submerged electrodes. Semiconductors show much larger electron densities ($\sim 2 \times 10^{11}$ cm^{-2} in GaAs heterostructures) and generally less variability in density which is in principle limited by the donor concentration. As shown below, the bulk limit for electron density ($n_s \simeq 2.2 \times 10^9$ cm^{-2}) can be significantly increased using micro-channel geometries rather than bulk films.

2.2.3 Wigner Crystallization

The existence of an electron-liquid to solid phase transition in infinite 3D Fermi systems at low densities was first predicted by Wigner in 1934 [115]. A collection of electrons in a

uniform neutralizing charge background at high densities behaves like a gas of weakly interacting Fermions, sometimes referred to as an electron plasma. In the high density limit, the energy of the system can be expanded to second order into an average kinetic energy term plus a term accounting for exchange energy, which gives the entire electrostatic contribution in this limit. The exchange correction is small for high densities and the kinetic energy dominates. Wigner found that the situation should in principle be reversed for low densities where exchange energy dominates kinetic energy, which led him to postulate the existence of an ordered solid phase at low densities. In this limit, the expansion of the ground-state energy of the system acquires higher order terms that include the zero-point motion of electrons about their lattice sites [115,116]. Van Horn later showed that for crystallization to occur in three dimensions, the mean electron spacing must be at least ~ 6.4 times the Bohr radius [70]. This is very difficult to achieve in conventional solid state systems and the Wigner crystal phase in 3D was long considered a physically unattainable state of matter except, possibly, for certain exotic physical systems such as a degenerate ion gas at the core of a white dwarf star [70]. In 1971, Crandall and Williams hypothesized the existence of a Wigner crystal transition for 2D electrons on liquid helium [117] and an analogous transition for semiconductor inversion layers was proposed shortly thereafter [69]. The Wigner crystal phase transition in electrons on helium was first observed by Grimes et al. [111] by taking advantage of the field-dependent coupling of Wigner crystal phonons to ripplon modes [107]. As discussed in more detail in section 2.3.5, electrons in a vertical holding field deform the helium surface, leading to the formation of 'dimples' of depth ~ 0.01 Å. If the electrons are in a correlated lattice structure like a Wigner crystal, the corresponding dimples form a lattice themselves. Thus, an oscillatory motion imposed on the electron crystal is accompanied by the excitation of coherent ripplons, which can be measured in an RF absorption experiment, a method first proposed by Shikin [118]. An alternative way of observing Wigner crystallization in electrons on helium is through its effect on transport properties such as mobility, conductivity and scattering time for transport parallel to the surface [119–122].

The phenomenon of Wigner crystallization is absent in a system of neutral particles. For an ordinary neutral system, the interaction energy of the particles increases with density at a rate higher than their kinetic energy and the particles eventually localize to lattice sites to minimize energy. For low densities, the kinetic energy dominates the interaction potential and the system is in a liquid or gas phase. The opposite is the case for charged particles due to the long-range nature of the Coulomb interaction, which decreases much more slowly

with decreasing density. For low electron densities and temperatures, the interaction energy can become much larger than the kinetic energy and a system of electrons can transition into an ordered crystalline phase to reduce energy. As shown in section 2.2.1, this occurs when the ratio of mean potential to kinetic energy exceeds $\Gamma^{(\mathrm{pl})} \gtrsim 135$. We can carry out an analogous calculation for regular semiconductor 2DEGs by replacing m with the effective mass m^* (for GaAs $m^* \simeq 0.067m$) and the charge by $e/\sqrt{\varepsilon}$ where ε is the dielectric constant of the host substrate. This decreases the Coulomb energy by one to two orders of magnitude and increases the quantum kinetic energy such that the ratio $\overline{K_e}/\overline{V_c}$ is larger by typically two to three orders of magnitude in semiconductors, where electrons do not crystallize into a Wigner solid in the absence of magnetic fields [69]. Electron localization can only be achieved using magnetic fields in which case an analogous magnetically-induced Wigner transition takes place [123].

Wigner Crystal Phonons

In the absence of external magnetic fields, the excitation spectrum of the Wigner solid consists of transverse $\Omega_{t,k}$ and longitudinal phonon modes $\Omega_{l,k}$. In the long-wavelength limit $k \ll 1/r_0$ for excitation wavelengths large compared to the electron lattice spacing, the dispersion relation of longitudinal modes coincides with 2D plasmon modes [103]

$$\Omega_{l,k} = \sqrt{\frac{n_s e^2}{2m_e \varepsilon_0 \varepsilon_{\mathrm{He}}} k} \tag{2.29}$$

which is independent of the lattice structure. The square-root dependence markedly differs from the phonon dispersion in neutral solids where the interactions are more short-range due to screening effects. In the long-wavelength limit, the transverse modes have a sound-like linear dispersion relation which takes the form [124]

$$\Omega_{t,k} = c_t \cdot k \quad , \quad c_t = \sqrt{0.138 \frac{e^2}{m_e r_0}} \tag{2.30}$$

for a triangular lattice (other lattice configurations have been shown to be unstable). Here, c_t is the transverse sound velocity. For short and intermediate wavelengths the phonon spectrum has to be evaluated numerically [124]. Due to the small mass of electrons on helium, magnetic fields can significantly affect the phonon dispersion curves. An external magnetic field can lead to coupling of longitudinal and transverse long wavelength oscillations of the

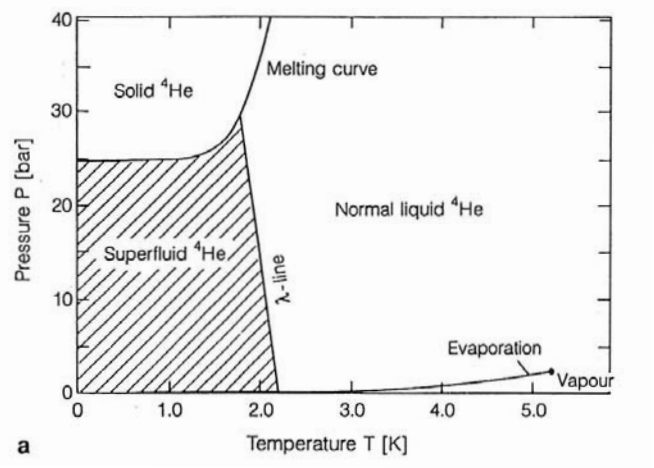

Figure 2.6.: Phase diagram of ^{4}He, showing the lambda transition line that separates normal, superfluid and solid phases of helium. Figure taken from [125].

crystal [110].

2.3 Superfluid Helium and Quantum Liquids

The unique physical properties of normal liquid and superfluid helium allow for the formation of bound surface states and 2DEGs in an experimentally accessible regime. The physics of superfluid helium is of great importance for most of the work done for this PhD project, in particular the superfluid experiments discussed in chapter 5 and the decoherence mechanisms of single-electron quantum dots presented in section 3.6. This section provides a brief review of the physics of superfluid helium. Starting with a discussion of the thermodynamics of ^{4}He in section 2.3.1, transport properties and thin film dynamics are explored in section 2.3.2. Charged helium films and the occurrence of hydrodynamic instabilities at high electron densities are discussed in section 2.3.3. The film dynamics in micro-channel geometries are particularly important for the experiments presented later on and are the focus of section 2.3.4. An introduction to ripplons and other elementary superfluid excitations is given in section 2.3.5. They represent the main decoherence mechanisms for lateral electron motion, which is discussed in much detail in section 3.6. Finally, alternative cryogenic substrates supporting bound surface states such as ^{3}He or solid Ne are briefly discussed in section 2.3.6, together with a summary of the main advantages of ^{4}He.

2.3.1 Thermodynamic Properties

The well-known phase diagram of ^{4}He is shown Fig. 2.6. Helium liquifies under its own vapor pressure below the critical temperature $T_c \simeq 4.21$ K. Below the λ-transition at $T_s \simeq 2.177$ K (under its own vapor pressure), ^{4}He transitions into a quantum liquid, which manifests itself macroscopically in a variety of ways. The fluid state exists down to absolute zero and ^{4}He solidifies only under at least 25 bar of pressure. Unlike all other known liquids, ^{4}He does not become solid under its own vapor pressure, even when cooled to absolute zero. The origin of the peculiar properties of ^{4}He lies in the interplay of weak interatomic binding forces and the large quantum-mechanical zero-point energy as a result of the small mass of helium atoms.

The binding forces between ^{4}He atoms are very weak. Due to the closed electronic s-shell there is no static permanent dipole moment and hence helium atoms interact only via induced dipole interaction, i.e. van-der-Waals forces. Helium has the smallest known atomic polarizability at $\alpha = 0.123$ cm^3/mol, which corresponds to a dielectric constant of $\varepsilon \simeq 1.0572$. Furthermore, due to their small atomic mass m, helium atoms exhibit very large vibrational zero-point energies

$$E_0 = \frac{h^2}{8ma^2} \quad , \quad a = \left(\frac{V_m}{N_0}\right)^{1/3} \tag{2.31}$$

where V_m is the molar volume and $N_0 = 6.022 \times 10^{23}$ atoms/mol is Avogadro's constant. The zero-point energy is large enough to make the solid phase unstable due to the comparatively weak binding forces. Helium-4 therefore melts under its own zero-point energy. Put differently, the zero-point energy is larger than the latent heat of crystallization of helium, making the liquid phase energetically favorable at low temperatures. Below the superfluid transition temperature, bulk helium condenses into a Bose-Einstein gas in which a substantial fraction of the atoms condense into the ground state with a macroscopic occupation.

In the superfluid phase, liquid helium has the highest known thermal conductivity of all substances at $c \sim 85$ kW m^{-1} k^{-1} [126], which is about a factor of 2×10^2 greater than for Cu and a factor of 10^7 for normal state liquid at the same temperatures. This is surprising at first since liquid helium does not have a valence band of free electrons, which are responsible for heat transfer in most other good thermal conductors. The mechanism of heat conduction in superfluid helium is unique and quantum-mechanical in nature. Heat propagates in the

form of waves, often referred to as *second sound*, with a group velocity of $v_g \simeq 20$ m/s at $T = 1.8$ K. Thermal conduction therefore takes place by convection, which is much more efficient than by gradual heat diffusion as in metals or normal liquids. In that sense, one can think of superfluid helium as a sort of 'superconductor of heat'. The high thermal conductivity is responsible for the extremely homogeneous temperature in bulk superfluid helium. As opposed to normal liquids, superfluid vaporizes without boiling as evaporation from liquid to vapor can only take place at the surface.

2.3.2 Transport Properties & Thin Film Dynamics

In its superfluid state, liquid helium can have flow velocities below the critical London velocity v_L, leading to a vanishing viscosity $\nu \to 0$ for flow through fine capillaries or holes. The critical flow velocity corresponds directly to the critical current in superconductors [127]. The vanishing viscosity allows for a persistent superfluid flow, just like persistent currents occurring in superconductors. The critical velocity is typically on the order of $v_L \sim 60$ m/s. In analogy to superconductors, vortices can lead to a breakdown of the superfluid phase even below v_L. The vanishing viscosity has a number of important consequences in narrow-channel geometries such as the coplanar waveguide resonators used in our experiments.

In a container filled partly with normal state liquid helium, the walls are coated with a thin film of helium due to the adsorption of atoms from the vapor phase. Since ^{4}He atoms experience a comparatively strong van-der-Waals interaction with most solid substrates, this so-called *van-der-Waals film* is unusually thick at $t \sim 30$ nm at saturated vapor pressure. In the normal liquid state this film is static and stable due to the finite viscosity. In the superfluid state, the viscosity vanishes $\nu \to 0$ and this film becomes mobile, covering all surfaces and creeping towards regions of higher temperature where the superfluid eventually evaporates. The fact that the van-der-Waals interaction between liquid helium and other substrates is large is related to the low polarizability/small dielectric constant of ^{4}He. The polarizability of liquid helium is greater than that of vacuum but less than that of the container wall substrate, corresponding to a negative Hamaker coefficient [125]. As a result, the interaction between the walls and vacuum across the superfluid film is repulsive and it is energetically favorable to have more superfluid between the walls and vacuum. The liquid tries to put as much of itself as possible near the solid wall to the extent that the van-der-Waals energy can pay for this mass displacement against gravity. Now consider a layer of bulk superfluid

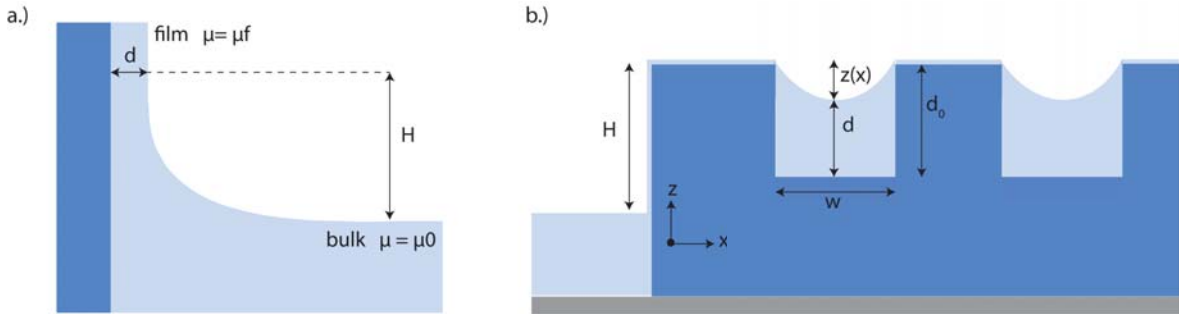

Figure 2.7.: Superfluid thin film formation: (a) Formation of a thin van-der-Waals film of $d \simeq 30$ nm on a substrate wall next to bulk liquid helium. (b) Capillary action filling of a micro channel array of depth d_0 and channel width w next to a low-lying reservoir of bulk liquid helium, where H is the distance between the channel top and the bulk liquid level in the reservoir, which determines the radius of curvature R_c and hence the superfluid level at the channel center $d = d_0 - z(x)$, see discussion in text.

helium next to a wall, as shown schematically in Fig. 2.7 a. The thickness of the coating film at height h above the bulk level can be estimated from the chemical potential of the film μ_f [125]:

$$\mu_f = \mu_0 + \rho g h - \frac{\alpha}{d^n} \tag{2.32}$$

where the last term is the van-der-Waals potential with $n = 3$ for $d \leq 5$ nm and $n = 4$ for $d > 10$ nm, α is the van-der-Waals constant and $\rho = 0.154 \times 10^{-3}$ kg/cm^3 the mass density of liquid helium. In thermal equilibrium, the chemical potential of the atoms on the bulk and film surfaces has to be equal such that we find for the film thickness as a function of the height above the bulk level

$$d = \left(\frac{\alpha}{\rho g h}\right)^{1/n} \tag{2.33}$$

which gives a value of about 30 nm for thick bulk levels $d > 10$ nm.

2.3.3 Charged Helium Films and Hydrodynamic Instability

Many of the early experiments with electrons on helium where carried out on bulk liquid helium films with thicknesses many orders of magnitude larger than the effective Bohr radius $a_0 \sim 8$ nm of the electrons [71, 91, 111]. The liquid helium surfaces were typically charged with electrons using thermionic emission from tungsten filaments, discussed in detail in section 4.1.4. Due to the polarization of the dielectric liquid, the electrons collect as a sheet on the helium surface and form a two-dimensional electron gas or Wigner crystal. As discussed in section 2.2, the liquid-to-crystal phase transition depends strongly on electron density and temperature. While the electron density can be easily varied in-situ through applied DC

fields, the attainable areal densities in bulk helium experiments are limited to $n_s \sim 2 \times 10^9$ cm^{-2} due to the occurrence of a hydrodynamic instability in charged helium films [67, 128]. Following Ref. [129], the total z-directed pressure on a charged helium surface can be written as

$$p(z) = \rho g z + \sigma \left(\frac{\partial^2 z}{\partial x^2} + \frac{\partial^2 z}{\partial y^2} \right) - 4\pi n_s^2 e^2 \nabla z \tag{2.34}$$

where the first term describes hydrostatic pressure due to gravity with $\rho = 0.154 \times 10^{-3}$ kg/cm^3 being the mass density of liquid helium, the second term describing surface tension with $\sigma = 0.378 \times 10^{-3}$ N/m and the third one arising from the mutual repulsion of electrons which acts in a destabilizing way. Taking the Fourier transform of $p(z)$ we have

$$p(k) = \left(\rho g + \sigma k^2 - 4\pi n_s^2 e^2 \right) Z(k) \tag{2.35}$$

where $Z(k)$ is the Fourier transform of the vertical displacement z. The surface is stable as long as the above polynomial in k is positive, which gives a critical electron density of

$$n_c = \left(\frac{\rho g \sigma}{(2\pi e^2)^2} \right)^{1/4} \sim 2.25 \times 10^9 \, \text{cm}^{-2} \tag{2.36}$$

in good agreement with experiment [130]. A number of methods have been developed to avoid the hydrodynamic instability and allow going to higher electron densities, in particular the use of fractionated micro-channel structures [129].

2.3.4 Capillary Action and Micro-Channel Geometries

Microchannel geometries and fractionated surfaces allow overcoming the hydrodynamic instability and reaching electron densities one to two orders of magnitude higher than the limit given in (2.36) [129]. A typical micro channel geometry next to a low lying bulk helium reservoir is shown schematically in Fig. 2.7 b. The helium film does not follow the substrate form but fills the depressions through capillary condensation provided that the distance between the elevations is smaller than the capillary length. The micro-channel structures are therefore filled with superfluid helium from a lower-lying reservoir by capillary action. In the absence of electrons, the radius of curvature of the helium film in a micro-channel is determined by surface tension and gravity

$$R_c(H) = \sigma / \rho g H \tag{2.37}$$

where $\sigma = 0.378 \times 10^{-3}$ N/m is the surface tension of the superfluid helium/vacuum interface, $\rho = 0.154 \times 10^{-3}$ kg/cm^3 and H is the distance between the channel top and bulk liquid surface in the reservoir. In our device geometries, the reservoir is typically on the order of $H \sim 5$ mm deep such that $R_c \sim 50\,\mu$m. If the channel width is much smaller than the radius of curvature $w \ll R_c$, the gap will be filled with helium by capillary action. The profile of the liquid surface across the channel, as shown in Fig. 2.7 b,can be approximated by a semi-circular shape [131]

$$z(x) = R_c \left(1 - \sqrt{1 - \left(\frac{x}{R_c} \right)^2} \right) \sim \frac{x^2}{2R_c} \tag{2.38}$$

where the x-origin is at the l.h.s wall of the channel (i.e. the channel center is at $x = w/2$ in Fig. 2.7 b).The film thickness at the center of a channel of width w and geometric depth d_0 can then be expressed as

$$d = d_0 - z(w/2) = d_0 - \frac{w^2}{8R} = d_0 - \frac{w^2}{8}\frac{\rho g H}{\sigma} \tag{2.39}$$

Thus the helium film thickness can be controlled by the geometry of the channels and the helium level in the reservoir. For a typical device with $w = 10\,\mu$m, $d_0 = 1\,\mu$m one needs a radius of curvature of at least $R_c \simeq 20\ \mu$m to get any significant level in the gap from capillary action effects. As the reservoir fills up $H \to 0$, the channels are completely filled with liquid helium as the radius of curvature diverges $R_c \to \infty$. The helium level in the gaps is self-stabilized by capillary action as long as $R_c \geq w$. The fill dynamics in the capillary action regime will be the subject of experiments presented in chapter 5, where we use a high quality factor coplanar waveguide resonator to observe changes in R_c through shifts in resonance frequency caused by changes in capacitance per unit length.

Charged Micro-Channels

For a charged bulk helium film, the presence of electrons adds another component to the surface pressure which leads to a hydrodynamic instability at a critical electron density of $n_c \simeq 2.2 \times 10^9$ cm^{-2}, as discussed above. However, for micro-channel geometries the instability can be suppressed by fractionating the liquid helium surface and imposing a lower limit for the allowed wave vectors of surface deformations, as suggested in Refs. [129, 132]. If the electron density is above the critical density given in eq. (2.36), $n_s > n_c$, the second

order polynomial $p(k)/Z(k)$ in (2.35) is negative when the wave number k lies between the two real positive roots of the equation. By forbidding surface deformations for such wave vector values, the critical density n_c can be increased. This can be achieved by fractionating the surface, such as in a micro-channel geometry, which imposes a minimum allowed wave vector value $k_m \simeq \pi/w$ where w is the width of the channel. The condition for stability then gives a critical density of

$$n_c = \sqrt{\frac{\sigma\pi\varepsilon_0\varepsilon_{\mathrm{He}}}{we^2}} \tag{2.40}$$

where $\sigma = 0.378 \times 10^{-3}$ N/m is the surface tension. For a channel width of $w = 10\,\mu$m this yields $n_c \approx 2.1 \times 10^{-10}$ cm^{-2} which is about an order of magnitude larger than the bulk limit.

In addition to hydrodynamic instability, the maximum density can be limited by the electronic pressure exerted on the helium film. For a charged helium film, the radius of curvature decreases to

$$R_c = \frac{\sigma}{\rho g H + \frac{n_s^2 e^2}{2\varepsilon_{\mathrm{He}}\varepsilon_0}} \tag{2.41}$$

compared to (2.37). The modified film thickness at the center of the gap then reads

$$d(n_s) = d_0 - \frac{w^2}{8R_c} = d_0 - \frac{w^2}{8\sigma}\left(\rho g H + \frac{n_s^2 e^2}{2\varepsilon_{\mathrm{He}}\varepsilon_0}\right) \tag{2.42}$$

This sets a limit on the maximum electron density through $d(n_c) = 0$ such that

$$n_c = \sqrt{\frac{2\varepsilon_{\mathrm{He}}\varepsilon_0}{e^2}\left(\frac{8\sigma d_0}{w^2} - \rho g H\right)} \tag{2.43}$$

For a channel of width $w = 10\,\mu$m and depth $d = 1\,\mu$m this yields $n_c \approx 1.5 \times 10^{-10}$ cm^{-2} (assuming $H = 0$).

2.3.5 Ripplons and Elementary Surface Excitations

Ripplons are quantized capillary waves propagating on the surface of superfluid helium. They can be thought of as the analog of 2D surface phonons at solid interfaces with a somewhat unusual dispersion relation. Although in principle present in normal-state liquids, ripplons are overdamped due to the large viscosity and hence generally unobservable. In the superfluid state on the other hand, the viscosity goes to zero, allowing long-lived capillary waves to propagate on the surface of the superfluid. Ripplons were first observed directly in neutron scattering experiments [133, 134], but indirect evidence in the long wavelength

regime was already obtained in some of the early electrons on helium experiments [111,113]. In the long wavelength limit ($q \ll 10^8$ cm^{-1}), the ripplon dispersion relation is to a good approximation given by [68]

$$\omega_q^2 = \frac{\alpha}{\rho}\left(q^2 + \kappa^2\right) q \tanh(qd) \tag{2.44}$$

$$\kappa^2 = \frac{\rho}{\alpha}(g + g_d) \quad , \quad g_d = \frac{3\alpha}{\rho d^4} \tag{2.45}$$

where α and ρ are the surface tension and mass density of liquid helium, respectively, d is the helium film thickness and g the gravitational constant. The additional acceleration term g_d is due to van-der-Waals forces. In the thick film limit and for wave vectors $q \gg \kappa$ the dispersion relation simplifies to

$$\omega_q = \sqrt{\frac{\alpha}{\rho}} q^{3/2} \tag{2.46}$$

For electrons on helium, we are primarily interested in this long wavelength ripplon regime since typical thermal electron wave numbers are small compared to atomic scales and single-ripplon scattering requires momentum and energy conservation. Ripplons can be described quantum-mechanically in terms of the surface displacement operator $\xi(\mathbf{r})$, which in second quantization can be expanded in the ripplon creation and annihilation operators [135]

$$\xi(\mathbf{r}) = \frac{1}{\sqrt{A_s}} \sum_{\mathbf{q}} (b_{\mathbf{q}} + b_{-\mathbf{q}}^\dagger) Q_q e^{i\mathbf{q}\cdot\mathbf{r}} \tag{2.47}$$

where A_s is the quantization surface area and the amplitude is given by

$$Q_q = \sqrt{\frac{\hbar q \tanh(qd)}{2\rho\omega_q}} \tag{2.48}$$

Here, $b_{\mathbf{q}}, b_{\mathbf{q}}^\dagger$ are the ripplon creation and annihilation operator, respectively, with the usual commutator $[b_{\mathbf{q}}, b_{\mathbf{q}'}^\dagger] = \delta_{\mathbf{q}\mathbf{q}'}$. The coupling of electrons above the surface to ripplons via the surface displacement operator (2.47) is discussed in detail in section 3.6. As shown later on, this coupling represents one of the major decoherence mechanisms for electron lateral motional qubits. The second important type of quantized excitation are phonons, which can be thought of as propagating density modulations that couple to the floating electrons through a form of piezoelectric interaction [3]. Details on the interaction of electrons and

[3] Note that the dispersion curve for phonons in superfluid helium is strongly non-linear, with a roughly linear dependence for low momenta. Excitations with momenta in the non-linear region are sometimes referred to

elementary superfluid excitations are given in section 3.6.

2.3.6 Alternatives to Superfluid Helium

An obvious question that comes to mind is if there are other cryogenic liquids and substrates, apart from superfluid helium, that can support quantized vertical motional states. Indeed a number of other host substrates have been investigated both experimentally and theoretically [68]. In this section, we briefly discuss alternative cryogenic substrates such as liquid ^{3}He and solid Neon and conclude with a summary of the main advantages of superfluid ^{4}He.

The most thoroughly studied alternative to ^{4}He is the ^{3}He isotope which forms an $I = 1/2$ fermionic liquid below $T_c = 3.2$ K at one atmosphere of pressure and becomes superfluid only at 0.25 mK in the absence of magnetic fields [125]. The electron injection barrier is similar to ^{4}He at $V_0 \simeq 0.9$ eV but ^{3}He provides an even more transparent substrate with a dielectric constant close to unity $\varepsilon_3 \simeq 1.0423$ [68]. This in turn means that the effective nuclear charge $Z = \Lambda e$ for bound electronic surface states is smaller, leading to a larger Bohr radius of $a_0 \simeq 10.2$ nm and weaker binding potentials. For ^{3}He, the ground state energy is on the order of ~ 4.2 K and the average electron position above the surface is $\langle 1|z|1\rangle \simeq 153.3$ Å. The measured transition frequency from ground to first excited state is $\omega_{12}/2\pi \simeq 69.8$ GHz [136], in good agreement with the hydrogen approximation. Surface state electrons above ^{3}He were first observed in Ref. [137], followed by spectroscopic experiments [136] and mobility measurements [75]. A practically important difference between ^{3}He and ^{4}He lies in the much smaller evaporation constant of ^{3}He which corresponds to a significantly higher vapor atom density above the liquid at a given temperature. The mobility of electrons on liquid ^{3}He is therefore limited by vapor atom scattering down to $T \simeq 0.4$ K [75].

Solid Hydrogen and Neon have been investigated as surface state electron substrates as well, in part because of the hydrodynamic instability limit for the electron density on liquid substrates, see section 2.3.3. This kind of instability does not occur for solid substrates, in principle allowing us to go to much higher electron densities. Solid H_2 has been investigated by a number of authors [138–140]. Due to the comparably large dielectric constant of solid H_2, the electrons are much closer to the surface with a mean ground-state distance of only ~ 25 Å and interact strongly with the static surface roughness. Electrons on solid Ne were first

as 'rotons'.

realized in Ref. [141]. The deviation from a hydrogenic spectrum is strongest for solid Ne because of the relatively smaller injection barrier of $V_0 \simeq 0.61$ eV.

While other substrates allow for higher electron densities, superfluid helium has several fundamental advantages for surface state electron experiments, which are summarized below:

- Weak polarizability: The small dielectric constant $\varepsilon_{\mathrm{He}} \simeq 1.0572$ leads to small effective nuclear charges Λe and large Bohr radii a_0 such that electrons are levitated at a macroscopic distance from the surface, several orders of magnitude larger than typical atomic scales.

- Vanishing vapor pressure: Since the vapor pressure of ^{4}He vanishes in the superfluid phase below $T \sim 600$ mK, there are no surface defects or irregularities and hence no scattering of isolated helium atoms. The substrate is perfectly flat and the only scatterers available are quantized excitations of the surface such as ripplons.

- Self-stabilized films: The vanishing viscosity and capillary action allows for the formation of self-stabilized films, reducing the effects of vibrations in experiments with micro channel geometries. For a micro-channel array next to a low-lying bulk superfluid reservoir as shown in Fig. 2.7, the relative bulk level H sets the radius of curvature in the channel R_c. For example, for $H = 5$ mm we have $R_c \approx 53\,\mu$m and the sensitivity of the film thickness d in the channel to changes in reservoir level H are reduced by several orders of magnitude for a channel width of $w = 10\,\mu$m:

$$\frac{\partial R_c}{\partial H}\frac{\partial d}{\partial R_c} = \frac{w}{H} = 10^{-4} \tag{2.49}$$

- Topological defects (vortices) and elementary excitations (ripplons, phonons, rotons) are well understood, making it easier to calculate their effects on electron transport properties and decoherence times.

- No nuclear spin: ^{4}He has zero nuclear spin with a natural isotopic purity of $1 - 2 \times 10^{-7}$ ^{3}He atoms. This is an important property for spin qubit implementations using electrons on helium [76]. Interaction with nuclear spins in the host substrate represents a limiting factor for spin coherence in semiconductor quantum dots.

3 Circuit Quantum Electrodynamics with Electrons on Helium

CAVITY quantum electrodynamics (QED) studies the interaction of matter and light at the quantum level and allows resolving the coherent exchange of energy between the two [31]. In its most general form, a cavity QED system consists of a quantized single mode radiation field, described as a harmonic oscillator, coupled to an anharmonic quantum system such as an atomic electron, described as a spin 1/2 particle. While originally developed in the context of atomic physics [32–34, 142], the cavity QED concept is quite general and in principle independent of the specific physical implementation of the harmonic and anharmonic oscillator components. In particular, it is not restricted to "real" atoms and optical cavities with mirrors. Indeed, cavity QED experiments have now been realized using a variety of physical systems, including Rydberg atoms coupled to optical and microwave cavities [30], superconducting charge, phase and flux qubits coupled to transmission line resonators [43, 143, 144] and three-dimensional cavities [46, 52], quantum dots coupled to photonic crystal cavities as well as superconducting resonators [35–37, 145], nanomechanical oscillators coupled to superconducting circuits [38, 39, 146] as well as early experiments with nitrogen vacancy centers in diamond coupled to photonic crystal and transmission line cavities [40, 41, 66, 147]. The superconducting circuit implementation in the microwave regime, called circuit quantum electrodynamics (cQED) [16, 42, 43], has proven to be a particularly versatile cavity QED architecture, in part because of the large atom-photon coupling strengths available and the ability to engineer many of the relevant properties of the atomic and photonic component of system such as photon lifetimes, transition frequencies and atom-photon coupling strengths. This has allowed for a number of fascinating quantum optics experiments [48, 49, 52, 144, 148–150] and significant progress towards quantum information processing with superconducting circuits in recent years [24, 53–58].

The strong coupling to microwave photons possible in circuit QED architectures has also sparked interest in creating hybrid quantum systems capable of combining the advantages of different implementations of the atomic component. In these proposals, a superconducting transmission line cavity acts as an interface between superconducting circuits and microscopic quantum systems, such as polar molecules and molecular ions [59–61], electron spins [62, 63, 66], or ultracold atoms [151], typically with smaller couplings but much better coherence than superconducting qubits. As shown in chapter 2, the motion of electrons bound to the surface of superfluid helium becomes quantized with a strongly anharmonic energy spectrum. Analogous to semiconductors, they form a two-dimensional electron gas that can be controlled with electrostatic gates. This makes electrons on helium a potentially promising building block for circuit QED and quantum information processing systems.

In this chapter we investigate the coupling of electrons on superfluid helium to superconducting transmission line cavities. We show how quantum dots on liquid helium can be defined via submerged electrostatic gates, in analogy to 2DEGs in semiconductors, and that the lateral quantized motion of such a trapped electron can be engineered to have frequencies in the 1 - 10 GHz range, matching those of typical superconducting cavities. We discuss how both spin and lateral motional degrees of freedom can be coupled to microwave photons in a transmission line resonator via dipole interaction, making it possible to realize strong coupling cavity QED with electrons on helium. We start with a discussion of cavity quantum electrodynamics as a general concept in section 3.1 and introduce the Jaynes-Cummings interaction and some of the basic physics. Superconducting coplanar waveguide cavities and transmission line resonators are discussed in section 3.2. In section 3.3, electrostatic traps and lateral quantized electron motion are presented. Section 3.4 focuses on the coupling of quantum dots on helium to superconducting cavities and section 3.5 discusses spin-motion coupling via gradient magnetic fields and the resulting enhanced spin-cavity coupling. Decoherence mechanisms for both lateral electron motion and spin are presented in section 3.6. Finally, section 3.7 explores trapped many-electron vibrational states and how to couple them to cavities.

3.1 Cavity Quantum Electrodynamics

The most fundamental system for studying the interaction of matter and light is given by a quantum-mechanical two-level system coupled to a simple harmonic oscillator. Although it

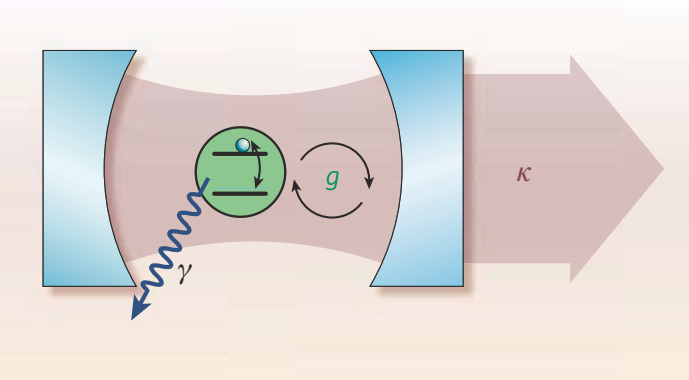

Figure 3.1.: Schematic layout of a cavity QED system: A quantum-mechanical two-level system (green) coupled via dipole interaction to a single-mode radiation field (red) with photon decay rate κ, coupling strength g and two-level decoherence rate γ. In the strong coupling limit $g \gg \kappa, \gamma$, the two-level system can coherently exchange energy with the radiation field at rate g. Figure taken from Ref. [16]

is possible to realize such a pure spin-oscillator system in practice, most cavity QED experiments work with approximations to this idealized case. In particular, atoms, ions or artificial atoms in the form of superconducting circuits have energy spectra consisting of many levels rather than just two. However, provided these spectra have sufficiently strong anharmonicity, we can truncate the Hilbert space of the anharmonic oscillator to its lowest two energy eigenstates and describe the system to a good approximation using relatively simple cavity QED models. This section provides a brief review of cavity QED physics independent of physical implementation. First, atom-radiation field coupling and the Jaynes-Cummings Hamiltonian are explored, followed by a discussion of the resonant and dispersive limits in the strong-coupling regime in sections 3.1.1 and 3.1.2. Note that in this section we use the terms "atom" and "atomic" as generic terms for an anharmonic oscillator, which can be a quantum two-level system such as a spin, the Rydberg levels of an atom or a superconducting charge or phase qubit. Cavity QED is a wide and rich field with connections to quantum optics, quantum information and quantum field theory. We limit ourselves here to the essentials required for a good understanding of the remaining parts of this thesis. For a detailed treatment of cavity QED the interested reader is referred to the excellent account given in Ref. [31] with the broader topics of quantum optics and quantum electrodynamics discussed in depth in Refs. [152] and [153]. Circuit QED with superconducting qubits is presented in detail in Refs. [44, 154, 155].

The atom-cavity field interaction is illustrated in Fig. 3.1. A two-level system of frequency ω_a interacts via dipole interaction with the electromagnetic field in a cavity defined by two

mirrors. The separation of the mirrors determines the frequency of the photons in the cavity field and their rate of escape κ is determined by the reflectivity of the mirrors. As shown below, the interaction energy $\hbar g$ depends on the dipole moment of the two-level system and the mode volume of the radiation field. The Hamiltonian for this model system can be derived from first principles. A general free-space electromagnetic field is described by a vector potential $\mathbf{A}(\mathbf{r}, t)$, as defined by Maxwell's equations [1], and has a continuous mode density. If the field is constrained to a certain physical volume V, the mode density becomes discrete as the quantization of the field supports only specific orthogonal modes whose wave vectors are such that they "fit" within the volume. In second quantization, the vector potential can then be expanded in a discrete set of orthogonal plane-wave modes, written as a linear combination of photon creation and annihilation operators:

$$\mathbf{A}(\mathbf{r}, t) = \sum_k \left(\frac{\hbar}{2\varepsilon_0 \omega_k \mathcal{V}_k} \right)^{1/2} \left[a_k \mathbf{e}_k e^{i(\mathbf{k}\cdot\mathbf{r} - \omega_k t)} + a_k^\dagger \mathbf{e}_k^* e^{-i(\mathbf{k}\cdot\mathbf{r} - \omega_k t)} \right] \tag{3.1}$$

where $a_k, a_k^\dagger$ are the ladder operators for the kth mode with $[a_k, a_j^\dagger] = \delta_{jk}$, ω_k is the frequency of the kth mode as determined by the volume V and $\mathbf{e}_k$ are unit polarization vectors. The mode volume $\mathcal{V}_k$ is given by

$$\mathcal{V}_k = \int_V \left| \mathbf{e}_k \cdot e^{i(\mathbf{k}\cdot\mathbf{r} - \omega_k t)} \right| d^3\mathbf{r} \tag{3.2}$$

For a simple box of length L this gives $\mathcal{V}_k = L^3$ such that in the free space limit $L \to \infty$ the mode density goes to infinity, as expected. The root-mean-square electric field amplitude of the vacuum in the kth mode is then given by [2]

$$\mathcal{E}_{\mathrm{rms}}^{(k)} = \sqrt{\frac{\hbar \omega_k}{2\varepsilon_0 \mathcal{V}_k}} \tag{3.3}$$

which depends on mode frequency and volume. Using the definition of the electromagnetic energy density, each mode of the radiation field can be described as a harmonic oscillator

[1] Recall that in Coulomb gauge

$$\mathbf{B} = \nabla \times \mathbf{A} \quad , \quad \mathbf{E} = -\frac{\partial \mathbf{A}}{\partial t} \quad , \quad \nabla \cdot \mathbf{A} = 0 \quad , \quad \Delta \mathbf{A}(\mathbf{r}, t) = \frac{1}{c^2} \frac{\partial^2 \mathbf{A}(\mathbf{r}, t)}{\partial t}$$

[2] The rms field amplitude can be derived from an integral over the energy density of the field, see e.g. Ref. [31].

such that the total field is governed by the Hamiltonian [152]

$$\mathcal{H} = \sum_k \hbar\omega_k \left(a_k^\dagger a_k + \frac{1}{2} \right) \tag{3.4}$$

where the independence of the mode oscillators is a consequence of the orthogonality of the plane wave modes in the expansion (3.1). The interaction of an atomic system, such as an electron bound in a hydrogen-like atom or an artificial superconducting atom, with a discrete mode field (3.1) is described by the Pauli Hamiltonian (see appendix A) which gives a dipole interaction term

$$\mathcal{H}_I = -\mathbf{d}(\mathbf{r}) \cdot \mathbf{E}(\mathbf{r}, t) \,. \tag{3.5}$$

where $\mathbf{d}(\mathbf{r}) = q \cdot \mathbf{r}$ is the atomic dipole operator and the electric field is given by $\mathbf{E} = -\partial \mathbf{A}/\partial t$. The spontaneous emission and absorption of photons by the atomic system strongly depends on the mode density and distribution. In the extreme case of a free-space field, the atom has a continuum of vacuum field states available for spontaneous emission of radiation. If the field is constrained to a fixed volume V, the mode density becomes a sum of δ-functions and spontaneous emission and radiation behavior is drastically modified. If the transition frequency of the atom matches one of the mode frequencies ω_k, spontaneous emission is greatly enhanced while if there is no matching mode, emission and absorption can be strongly suppressed. The dispersive interaction with off-resonant modes manifests itself as small energy corrections to the atomic levels (Lamb and Stark shift). For the case of a single mode field, spontaneous emission can in fact be suppressed in the off-resonant case $\omega_a \neq \omega_0$, while in the resonant case the interaction manifests itself in the form of Rabi oscillations [3]. The irreversible physical process of spontaneous emission in free space therefore becomes a reversible process (Rabi oscillations) if the field is restricted to a single mode. This is the key idea of cavity QED. It ultimately enables the coherent exchange of energy between matter and light and the controlled entanglement of atoms and photons.

Returning to the simple model shown in Fig. 3.1, the two-level atom can be described by a spin-1/2 Hamiltonian

$$H_a = \frac{\hbar\omega_a}{2}\sigma_z = \frac{\hbar\omega_a}{2}(\sigma^+\sigma^- - \sigma^-\sigma^+) \tag{3.6}$$

[3] Note that in reality any field has an infinite number of modes given by the higher order harmonics of the fundamental mode with frequencies that are integer multiples of ω_k.

where $\sigma^+ = |e\rangle\langle g|$ and $\sigma^x - = |g\rangle\langle e|$ are the atomic ladder operators. Note that the dipole operator has odd parity and can be expressed in terms of $\sigma^\pm$ as

$$\mathbf{d} = d(\mathbf{e}_a\sigma^- + \mathbf{e}_a^*\sigma^+) \tag{3.7}$$

where $d\mathbf{e}_a = q \cdot \langle g|\mathbf{r}|e\rangle$ and d is the dipole matrix element and $\mathbf{e}_a$ a unit vector describing the atomic transition polarization direction. The interaction term (3.5) can be simplified further using the dipole and rotating wave approximations. In the dipole approximation, we take advantage of the fact that the size of the two-level dipole is typically much smaller than the wavelength of the mode, hence allowing us to restrict evaluation of the vector potential to the position of the dipole (at the origin) $\mathbf{A}(\mathbf{r}) \approx \mathbf{A}(0)$. Furthermore, in the rotating wave approximation we can neglect terms that describe the simultaneous excitation ($\sigma^+a^\dagger$) and de-excitation (σ^-a) of both the two-level system and the cavity [4]. Making both of these approximations in (3.5) and combining this with (3.4) and (3.6), we arrive at the well-known Jaynes-Cummings Hamiltonian describing a two-level system coupled to a single-mode radiation field:

$$\mathcal{H}_{\mathrm{JC}} = \mathcal{H}_R + \mathcal{H}_A + \mathcal{H}_I = \hbar\omega_r\left(a^\dagger a + \frac{1}{2}\right) + \frac{\hbar\omega_a}{2}\sigma_z + \hbar g(a^\dagger\sigma^- + \sigma^+ a) \tag{3.8}$$

where the coupling strength g is given by

$$g = \frac{d}{\hbar}\mathcal{E}_{\mathrm{rms}} = \sqrt{\frac{\omega_r}{2\varepsilon_0\hbar\mathcal{V}_r}} \cdot d\,. \tag{3.9}$$

The Hamiltonian (3.8) describes the emission and absorption of cavity photons by the two-level system. A photon bouncing back and forth between the two mirrors can be absorbed by the atom in its ground state (σ^+a term). Similarly, if the atom is excited it can decay back to the ground state by emitting a photon into the cavity ($a^\dagger\sigma^-$ term). The rate of this atom-photon interaction is given by the coupling strength g, which is determined by the size of the dipole matrix element d and the mode volume of the cavity. A smaller mode volume corresponds to a higher energy density and hence larger coupling. Likewise, a larger dipole corresponds to a larger cross-section for photon absorption and hence also larger coupling. Interestingly, there is a fundamental upper bound for the magnitude of the coupling, which limits the coupling strength to about 10 % of the cavity frequency ω_r [44, 156]. This can be

[4] This amounts to neglecting fast-oscillating terms exponential in $\pm 2\omega_r$

seen explicitly by rewritting the dimensionless coupling strength g/ω_r in terms of the fine structure constant and the ratio of mode volume to dipole size. The best one can do is to use a dipole that completely fills the transverse dimension of the cavity.

So far we have ignored any dissipation mechanisms of the atom-cavity system. In practice, the lifetime of photons is limited by the reflectivity of the mirrors. Photons leak out of the cavity at a rate $\kappa = \omega_r/Q$ determined by the quality factor Q of the cavity, which gives an additional dissipation term $\mathcal{H}_\kappa$ in (3.8). In addition, the two-level system can decay into modes other than the cavity mode and relax or dephase via its coupling to the environment at a corresponding rate γ. The atomic decoherence mechanisms are captured by another term $\mathcal{H}_\gamma$ in the Hamiltonian. The exact form of these terms depends on the specific decoherence mechanisms present in a given cavity QED implementation. For the case of quantum dots on helium coupled to transmission line resonators those will be discussed in detail in section 3.6. The dynamics of the system depend strongly on the relative magnitude of the relaxation rates κ and γ with respect to the coupling rate g. If the coupling strength is much larger than both of the relaxation rates $g \gg \gamma, \kappa$, an excitation can oscillate coherently many times between cavity field and atom, implying that a single atom in a cavity is sufficient to sustain a laser-like oscillation on resonance $\omega_a = \omega_r$ [31]. In the off-resonant case $\omega_a \neq \omega_r$, such Rabi oscillations are suppressed by the frequency mismatch and the coupling manifests itself as a dispersive, state-dependent shift of the cavity and atom frequencies. Those two limiting cases are the topics of the following two sections.

3.1.1 Resonant Strong Coupling Limit

The strong coupling regime of cavity QED is obtained when the atom-cavity coupling strength g exceeds the relaxation rates of both system components $g \gg \kappa, \gamma$. In practice, this requires a combination of long coherence times for the atomic degree of freedom, low loss cavities (high Q factors) and large coupling strengths (small mode volumes and/or large dipoles). In the strong coupling regime, the dissipative terms in the Jaynes-Cummings Hamiltonian $\mathcal{H}_\gamma$ and $\mathcal{H}_\kappa$ can be neglected and it becomes possible to diagonalize (3.8) exactly. First, note that the uncoupled product states $|g, n\rangle = |g\rangle \otimes |n\rangle$ and $|e, n+1\rangle = |e\rangle \otimes |n+1\rangle$ are eigenstates of the unperturbed Hamiltonian $\mathcal{H}_A + \mathcal{H}_R$, where $|g, e\rangle$ denotes the two-level eigenstate and $|n\rangle$ the photon number states of the cavity. They form a basis which can be used to represent the eigenstates of the full Hamiltonian $\mathcal{H}_{JC}$, the so-called dressed states which are

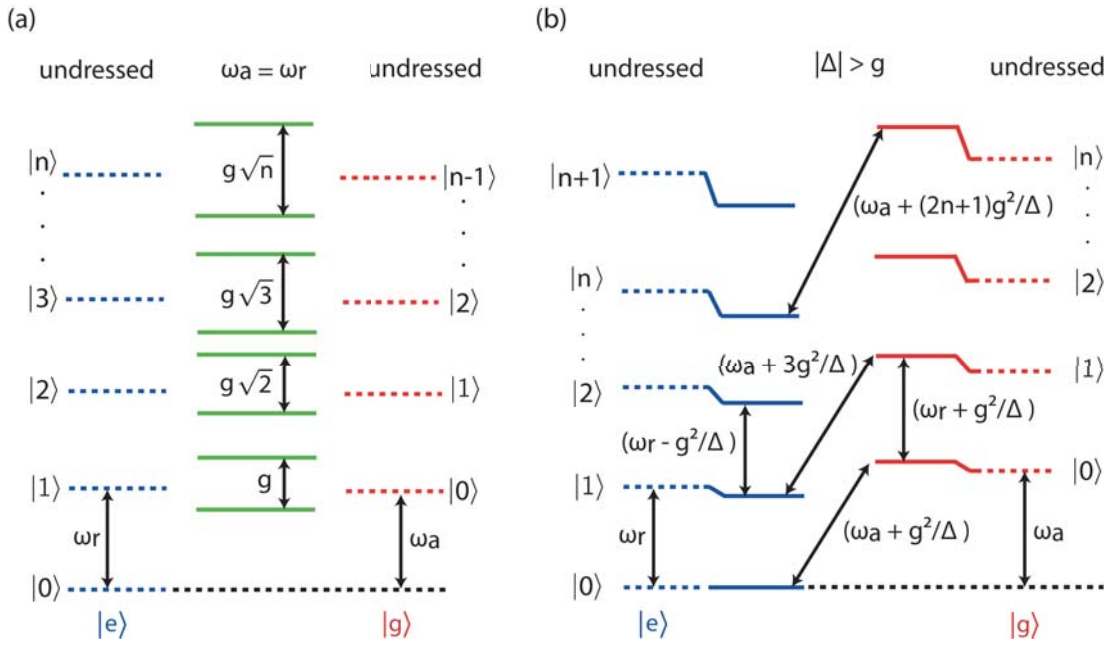

Figure 3.2.: Energy level diagram of the Jaynes-Cummings hamiltonian. The dashed lines are the eigenstates of the uncoupled Hamiltonian, where left is qubit in the ground state and right in the excited state with $|n\rangle$ corresponding to the different photon number states. The solid lines are the energies in the presence of dipole coupling. Both strong dispersive (b) and resonant strong regime (a) are shown with energy level separations and dispersive shifts indicated accordingly. As shown in (a), the spectrum of the hybridized system on resonance is anharmonic with an energy level separation that is a function of the number of excitations in the system.

superpositions of the unperturbed eigenstates:

$$|+,n\rangle = \cos\Theta_n\,|g,n\rangle + \sin\Theta_n\,|e,n+1\rangle \tag{3.10}$$

$$|-,n\rangle = -\sin\Theta_n\,|g,n\rangle + \cos\Theta_n\,|e,n+1\rangle \tag{3.11}$$

with the mixing angle

$$\Theta_n = \frac{1}{2}\arctan\left(\frac{2g\sqrt{n+1}}{\Delta}\right) \tag{3.12}$$

and $\Delta = \omega_a - \omega_r$. The dressed states diagonalize the Jaynes-Cummings Hamiltonian (3.8) exactly and the corresponding eigenenergies are given by

$$E_{\pm,n} = (n+1)\hbar\omega_R \pm \frac{\hbar}{2}\sqrt{4g^2(n+1)+\Delta^2}\,, \tag{3.13}$$

The energy level diagram is shown in Fig. 3.2. One can distinguish between two qualitatively different regimes depending on the detuning Δ between the two-level atom and the cavity field. For $\Delta > g$, atom and cavity interact only dispersively and the weak coupling term can be treated perturbatively using the uncoupled product states $|g\rangle \otimes |n\rangle$ and $|e\rangle \otimes |n+1\rangle$.

This case is shown in Fig. 3.2 b and will be discussed separately in section 3.1.2. For the remainder of this section we will focus on the near resonant case $\Delta \to 0$, shown in Fig. 3.2 a. If the detuning between atom and cavity is small, the two systems can freely and reversibly exchange energy. Excitations in the system hybridize in the sense that they are equal parts atomic excitation and cavity photon. To see this, consider the limit $\Delta \to 0$ where the mixing angle is $\Theta_n = \pi/2$ such that the eigenstates are equally weighted superpositions of the unperturbed states

$$|\pm, n\rangle = \frac{1}{\sqrt{2}} \left(|e, n+1\rangle \pm |g, n\rangle \right). \tag{3.14}$$

The eigenstates of the atom-cavity system are therefore maximally entangled on resonance and all excitations are equally shared between the atom and the photon field. The two systems can then no longer be considered as separate entities. The on-resonance energy level diagram for the dressed states (3.14) is shown in Fig. 3.2 a, together with the unperturbed energy levels. The energy level spectrum is strongly non-linear and the separation between the two dressed states $|\pm, n\rangle$, called the vacuum Rabi splitting, is a function of the number of excitations in the system,

$$\Delta E_n = \hbar g \sqrt{n} \tag{3.15}$$

The coherent and reversible oscillation between atomic excitation and cavity photon can be seen explicitly from the time evolution of the system. Suppose we start in the state $|\psi(0)\rangle = |g, n\rangle$ at time $t = 0$ where an atom in its ground state is inside a cavity with n photons. We can express the initial state in the basis of the dressed states $|\psi(0)\rangle = (1/\sqrt{2})(|+, n\rangle - |-, n\rangle)$. At time t the system is in the state

$$|\psi(t)\rangle = e^{-i\mathcal{H}_{\mathrm{JC}} t/\hbar} |g, n\rangle = \frac{1}{\sqrt{2}} e^{-i(n+1)\omega_R t} \left[e^{-itg\sqrt{n+1}} |+, n\rangle - e^{itg\sqrt{n+1}} |-, n\rangle \right] \tag{3.16}$$

The probability for being in the initial state $|g, n\rangle$ at time t is therefore

$$P_{g,n}(t) = |\langle g, n|\psi(t)\rangle|^2 = \cos^2(g\sqrt{n+1}t) \quad , \quad P_{e,n+1}(t) = 1 - P_{g,n}(t) \tag{3.17}$$

Hence we see that the excitation oscillates between atom and cavity photon at a frequency $\omega_{\mathrm{rabi}} = g\sqrt{n+1}$, the n-photon Rabi frequency. This makes the change from irreversible spontaneous emission in free space to reversible oscillation of energy in a cavity explicit. In free space, an atom initially in the excited state relaxes to the ground state via spontaneous emission of a photon which is then lost irreversibly. In a cavity on the other hand, the photon

is trapped and can be reabsorbed by the atom, then emitted again and so on. Depending on the cavity loss rate κ, the atomic relaxation rate γ and the coupling strength g, this process of absorption and re-emission can happen many millions of times before the photon escapes.

3.1.2 Dispersive Limit

As shown above, the resonant interaction of atom and cavity leads to coherent exchange of energy and the two systems lose their individual character in this limit. A qualitatively different regime is reached when atom and cavity are detuned from each other $\Delta > g$. In this dispersive limit of large detunings, the residual weak interaction manifests itself in the form of frequency shifts and the Jaynes-Cummings Hamiltonian can be treated perturbatively. Making a Schrieffer-Wolff-type transformation

$$U = \exp\left[\frac{g}{\Delta}(a\sigma^+ - a^\dagger\sigma^-)\right] \tag{3.18}$$

of the Hamiltonian (3.8) in combination with the Baker-Campbell-Hausdorff lemma and expanding to second order in the small parameter g/Δ gives the effective Hamiltonian [5]

$$\mathcal{H}_{\text{eff}} = UHU^\dagger \approx \hbar\omega_r\left(a^\dagger a + \frac{1}{2}\right) + \frac{\hbar}{2}\left(\omega_a + 2\chi a^\dagger a + \chi\right)\sigma_z \tag{3.19}$$

where $\chi = g^2/\Delta$ and the interaction term was adiabatically eliminated. We see from the effective Hamiltonian that the atom-cavity interaction reduces to frequency shifts in the dispersive limit. The atom transition frequency ω_a acquires a shift proportional to the cavity field population $n = \langle a^\dagger a\rangle$, the ac Stark shift $\delta_S = 2\chi n$, as well as a virtual photon shift $\delta_L = \chi$ due to its interaction with the vacuum field fluctuations $\langle a^\dagger a\rangle = 0$, the Lamb shift. The presence of both 'real' and virtual photons inside the cavity manifests itself as a renormalization of the energy of the atom in the dispersive limit. Conversely, the dispersive interaction can also be viewed in terms of its effect on the cavity frequency. Regrouping the effective Hamiltonian as

$$\mathcal{H}_{\text{eff}} = \hbar\left(\omega_r + \chi\sigma_z\right)\left(a^\dagger a + \frac{1}{2}\right) + \hbar\frac{\omega_a}{2}\sigma_z\,. \tag{3.20}$$

[5] Note the following commutation relations to arrive at this result:

$$[\sigma^+ a - a^\dagger\sigma^-, a^\dagger, a] = \sigma^+ a + a^\dagger\sigma^- \quad , \quad [\sigma^+ a - a^\dagger\sigma^-, \sigma^\pm] = \pm\sigma_z a \quad , \quad [\sigma^+ a - a^\dagger\sigma^-, \sigma_z] = 2(\sigma^+ a + a^\dagger\sigma^-)$$

we see that the cavity frequency ω_r acquires a state-dependent shift given by $\langle\sigma_z\rangle\,\chi = \pm\chi$. The energy level diagram for the dispersive regime and the corresponding frequency shifts are illustrated in Fig. 3.2 b. The dispersive atom-state-dependent cavity shift forms the basis of quantum non-demolition (QND) measurements in cavity QED systems [31]. In an ideal QND measurement, we can repeatedly measure a quantum-mechanical system without changing its state. In the Heisenberg picture, this requires that the measurement operator A does not change during the time we are measuring, as expressed by the equation of motion

$$\frac{dA}{dt} = \frac{1}{i\hbar}[A, H] = 0 \tag{3.21}$$

In the dispersive regime, all terms in $\mathcal{H}_{\text{eff}}$ commute with the total Hamiltonian and thus the cavity shift $\pm\chi$ can be used to infer the state of the two level system $\langle\sigma_z\rangle = \pm 1$.

3.2 Superconducting Coplanar Waveguide Cavities

In the traditional form of atomic cavity quantum electrodynamics encountered in section 3.1, the harmonic oscillator component is realized in the form of an optical cavity. The photon loss rate κ is determined by the quality factor Q of the cavity, which is in turn set by the reflectivity of the mirrors. In the solid state circuit QED version, superconducting coplanar waveguide resonators represent the electrical circuit analog of the cavities in atomic cavity QED. Typically operated in the microwave frequency range of $\sim$ 1 - 20 GHz, the quality factors of these quasi two-dimensional distributed resonators are determined by coupling impedances such as capacitors and inductors, which represent the analog of mirrors in this implementation. The high achievable quality factors of up to $Q \sim 10^6$ [45] combined with small mode volumes of $10^{-6}\,\lambda^3$ and the ease of device fabrication via conventional lithography techniques make coplanar waveguide resonators well-suited for cavity QED and photon detection experiments, with applications in quantum optics and quantum information processing [16]. The recently developed three-dimensional superconducting microwave cavities represent a natural evolution of this concept [46]. The larger mode volumes of $0.1\,\lambda^3$ make these devices much less sensitive to surface dielectric losses with measured quality factors of up to $Q \sim 5 \times 10^8$ [46, 47] [6]. In addition to superconducting charge and phase qubits, coplanar waveguide resonators are being actively developed for coupling and mea-

[6] The decrease in qubit-cavity coupling strength due to the larger mode volumes is compensated via an increase in dipole moments through larger superconducting qubit electrodes [46].

suring a variety of other quantum systems such as electron spin ensembles in diamond and ruby [65, 157] or ensembles of ultra cold atoms [151]. The coplanar waveguide geometry is particularly well-suited for trapping and detecting electrons on helium. The planar resonator structures realize a micro-channel geometry (section 2.3.4) for confining electrons and supporting self-stabilized films of superfluid helium [64].

This section focuses on superconducting coplanar waveguide cavities and the various ways of implementing and coupling them to the outside world. In section 3.2.1 we start with a general discussion of open- and short-circuited transmission lines and the resulting resonant behavior. Inductively- and capacitively-coupled LCR oscillator circuits are then introduced in section 3.2.2 where we derive expressions for external quality factors for various types of coupling. In section 3.2.3 inductively- and capacitively coupled transmission lines are mapped to lumped element LCR circuits around resonance, showing how both series and parallel resonant structures can be realized using different terminations. Circuit quantization is briefly reviewed in section 3.2.4. For this thesis, we use quasi two-dimensional coplanar waveguide structures as the cavity implementation, which are discussed in the final subsection 3.2.5.

3.2.1 Terminated Transmission Lines

There are many possible ways of realizing a circuit that behaves like a harmonic oscillator, the most simple example being a parallel or series lumped-element LCR circuit. In the microwave regime, we are dealing with wavelengths on the order of $\lambda \sim 100\,\mu m - 1$ m and thus a true lumped element oscillator is somewhat difficult to realize. A transmission line resonator can be regarded as the distributed element version of an LCR oscillator circuit and, as we will see below, there exists a direct mapping between the two. Circuit analysis makes the assumption that the characteristic length scale of the circuit elements is negligibly small compared to the electrical wavelength. This is not the case for transmission lines where the phase and amplitude of the currents and voltages can change significantly over the length of the device.

In the most general sense a transmission line is simply a parallel pair of two conductors, the standard coaxial cable being an everyday example. Transmission lines are characterized by an inductance L_ℓ, capacitance C_ℓ, resistance R_ℓ and conductance G_ℓ per unit length and they can be described as a series of lumped element LCR circuits. Signals on a transmission

line propagate as voltage or current waves with propagation coefficient [158]

$$\gamma = \sqrt{(R_\ell + j\omega L_\ell)(G_\ell + j\omega C_\ell)}\,. \tag{3.22}$$

where the imaginary part $\beta = \mathrm{Im}[\gamma]$ defines the phase velocity $v_{\mathrm{ph}} = \omega/\beta$ and wavelength $\lambda = 2\pi/\beta$ and the real part $\alpha = \mathrm{Re}[\gamma]$ describes signal attenuation. The characteristic impedance of a transmission line is then given by

$$Z_0 = \sqrt{\frac{R_\ell + j\omega L_\ell}{G_\ell + j\omega C_\ell}}\,. \tag{3.23}$$

For the nearly lossless case, such as in a superconducting transmission line, we can make the approximations $\gamma \simeq j\omega\sqrt{L_\ell C_\ell}$, $v_{\mathrm{ph}} \simeq \sqrt{1/L_\ell C_\ell}$ and $Z_0 \simeq \sqrt{L_\ell/C_\ell}$. A piece of transmission line terminated at both ends by a load impedance Z_L can realize a distributed resonant circuit that supports standing waves with a wavelength determined by the length and characteristic impedance of the line. The type of resonance and the resonant wavelength for a given physical length L depends on the load impedance. The input impedance of a transmission line terminated by a load impedance Z_L can be expressed as [158]

$$Z_{\mathrm{in}} = Z_0 \frac{Z_L + Z_0 \mathrm{tanh}\gamma\ell}{Z_0 + Z_L \mathrm{tanh}\gamma\ell} \tag{3.24}$$

where ℓ is the distance from the terminating load impedance. If the load impedance is an open ($Z_L = \infty$) we have

$$Z_{\mathrm{in}}^{\mathrm{open}} = Z_0 \mathrm{coth}\gamma\ell = Z_0 \frac{1 + j\mathrm{tan}\beta\ell\,\mathrm{tanh}\alpha\ell}{\mathrm{tanh}\alpha\ell + j\mathrm{tan}\beta\ell}\,. \tag{3.25}$$

while for a short ($Z_L = 0$)

$$Z_{\mathrm{in}}^{\mathrm{short}} = Z_0 \mathrm{tanh}\gamma\ell = Z_0 \frac{1 - j\mathrm{cot}\beta\ell\,\mathrm{tanh}\alpha\ell}{\mathrm{tanh}\alpha\ell - j\mathrm{cot}\beta\ell}\,. \tag{3.26}$$

For the lossless case these simplify to

$$Z_{\mathrm{in}}^{\mathrm{open}} = -jZ_0\cot(\beta\ell) \quad , \quad Z_{\mathrm{in}}^{\mathrm{short}} = jZ_0\tan(\beta\ell) \tag{3.27}$$

Both expressions are periodic in ℓ, albeit with different periods. For the open-circuited line, we see that whenever the length is a multiple of half a wavelength $\ell = n\lambda/2 = n\pi/\beta$ the

input impedance diverges and a high impedance resonance occurs. Conversely for the short-circuited line, Z_{in} diverges when the length is an integer multiple of a quarter wavelength $\ell = n\lambda/4 = n\pi/2\beta$.

In this PhD project, we use both high impedance terminations (opens or nearly opens in the form of capacitors) as well as low impedance terminations (shorts in the form of inductors to ground). Both types of terminations can be used in practice to realize high Q transmission line resonators. Experiments with electrons on helium require precise control of the DC potentials and the electromagnetic environment on the chip. A transmission line open-circuited on both ends represents a floating electrode at DC and is therefore prone to charging effects. Hence to keep the transmission line electrodes at DC ground potential at all times, a short termination on at least one end is desirable. On the other hand, an open termination in the form of a capacitor can be advantageous to avoid leakage of electrons and ensure confinement to the resonator region. As will be shown in chapters 5 - 7, we take advantage of these possible design choices in various experiments.

3.2.2 Inductively- and Capacitively-Coupled LCR Oscillators

In this section, we briefly review lumped element LCR oscillator circuits and derive expressions for internal and external quality factors of capacitively and inductively coupled oscillators through Norton and Thévenin equivalent representations. In section 3.2.3, the open- and short-circuited transmission lines of the previous section will be mapped to lumped element LCR circuits to arrive at an intuitive understanding of transmission line resonators around resonance.

Consider the parallel LCR circuit shown in Fig. 3.3 a. Neglecting the external load circuitry for the moment (shown in dashed boxes in Fig. 3.3 a), it follows directly from Kirchhoff's rules that the time evolution of the charge in a parallel LCR circuit obeys $q(t) = q_0 \exp(i\omega_0 t - \kappa \cdot t/2 + \phi)$. Thus the charge in this circuit oscillates with frequency $\omega_0 = 1/\sqrt{LC}$ and decays at a rate of $\kappa = 2/RC$, which describes the damping of the oscillation. The corresponding internal quality factor is defined as $Q_{\text{int}} = \omega_0/\kappa$ and describes the number of oscillations per decay time $T_\kappa = 1/\kappa$. The imaginary part of the total impedance of the parallel LCR circuit

$$Z^{(p)}_{\text{LCR}} = \left(\frac{1}{R} + \frac{1}{j\omega L} + j\omega C\right)^{-1} = \left[\frac{1}{R} + j\omega C\left(\frac{\omega^2 - \omega_0^2}{\omega^2}\right)\right]^{-1} \tag{3.28}$$

vanishes on resonance $\omega = \omega_0$. The resonances have a Lorentzian line shape and their half

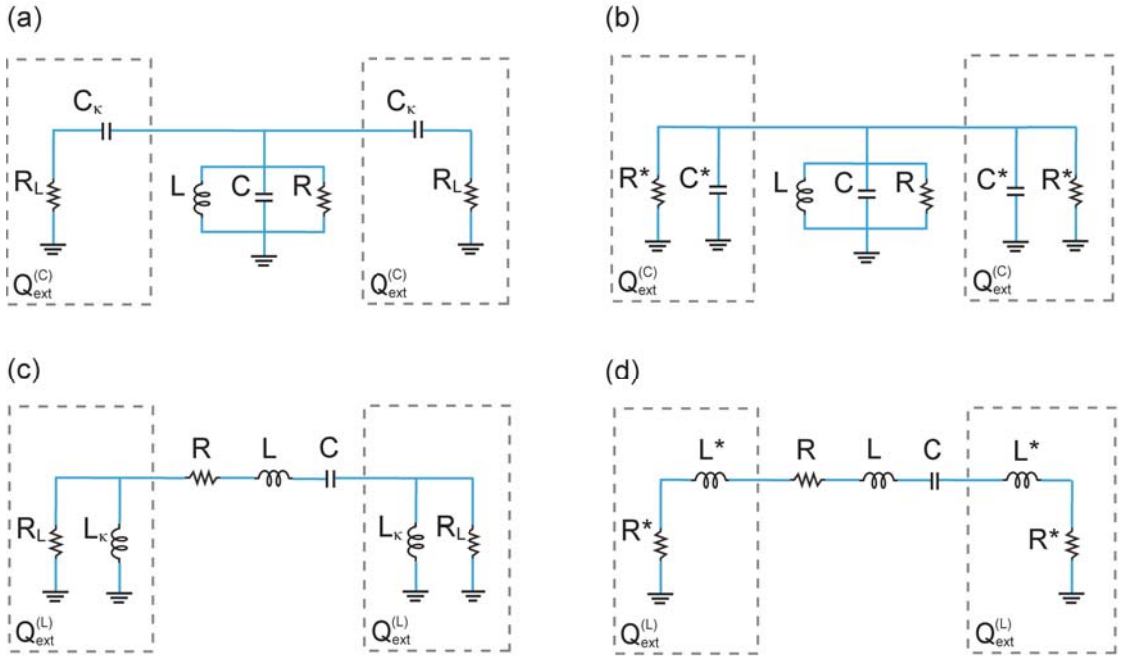

Figure 3.3.: Lumped element LCR oscillator circuits with various load impedances: (a) Parallel LCR oscillator circuit capacitively coupled to a load impedance R_L. (b) Norton equivalent circuit of the loaded parallel LCR circuit in (a). (c) Series LCR oscillator circuit inductively coupled to a load impedance R_L. (d) Thévenin equivalent circuit of the loaded series LCR circuit in (c).

width at half maximum (HWHM) can be expressed by the quality factor $\delta\nu = \nu_0/2Q$. A high Q resonant circuit will thus have sharp, narrow resonances and the charge will oscillate many times before it decays, whereas a low Q circuit has a broad resonance and decays more quickly. Close to resonance, we can write $\omega = \omega_0 + \Delta\omega$ with $\Delta\omega$ small and use the approximation $\omega^2 - \omega_0^2 = (\omega - \omega_0)(\omega + \omega_0) = \Delta\omega(2\omega - \Delta\omega) \sim 2\omega\Delta\omega$ such that

$$Z_{\mathrm{LCR}}^{(p)} \simeq \frac{R}{1 + 2j\Delta\omega RC} = \frac{R}{1 + 2jQ_{\mathrm{int}}^{(p)}\Delta\omega/\omega_0} \tag{3.29}$$

where the internal quality factor is $Q_{\mathrm{int}}^{(p)} = R/\omega_0 L = \omega_0 RC$. This approximate expression will be used in section 3.2.3 to map a capacitively-coupled $\lambda/2$ transmission line resonator to an equivalent lumped LCR circuit.

Next, consider the series LCR circuit shown in Fig. 3.3 c. Again neglecting the load circuitry for the moment, the resonance behavior is very much analogous to the parallel LCR circuit. The series LCR has the same resonance frequency expression $\omega_0 = 1/\sqrt{LC}$ but the inverse internal quality factor expression $Q_{\mathrm{int}}^{(s)} = \omega_0 L/R = 1/\omega_0 RC$, which is a manifestation of the duality of series and parallel oscillator circuits. The input impedance of the series LCR

is

$$Z_{\mathrm{LCR}}^{(s)} = R + j\omega L\left(1 - \frac{1}{\omega^2 LC}\right) = R + j\omega L\left(\frac{\omega^2 - \omega_0^2}{\omega^2}\right) \tag{3.30}$$

Using the same approximate expansion as for the parallel LCR case yields

$$Z_{\mathrm{LCR}}^{(s)} \simeq R + j2L\Delta\omega = R + j\frac{2RQ_{\mathrm{int}}^{(s)}\Delta\omega}{\omega_0} \tag{3.31}$$

The quality factors considered so far represent internal properties of the circuits but in practice the series and parallel LCR oscillators will inevitably have to be coupled to other circuitry. This external load circuitry has the effect of lowering the overall quality factor. Here, we consider two ways of coupling the oscillator circuits to the environment.

Capacitive Coupling

The parallel LCR circuit shown in Fig. 3.3 a is symmetrically coupled to a load impedance at its input/output via two capacitors (see dashed boxes). A capacitor corresponds to an impedance mismatch, which has an effect analogous to a semi-transparent mirror in the optical part of the spectrum. To understand the effect of the capacitive coupling C_κ and load impedance R_L on the overall quality factor we can transform the load circuitry to its Norton equivalent circuit as shown in Fig. 3.3 b. The equivalent resistance and capacitance are

$$R^* = \frac{1 + \omega_0^2 C_\kappa^2 R_L^2}{\omega_0^2 C_\kappa^2 R_L} \quad , \quad C^* = \frac{C_\kappa}{1 + \omega_0^2 C_\kappa^2 R_L^2} \tag{3.32}$$

which shows explicitly how the small capacitor C_κ transforms the load impedance $R_L \rightarrow R^*$. In this representation, the overall, loaded quality factor of the coupled circuit can be worked out in a straight-forward way by noting that the Norton equivalent capacitances and resistances combine in parallel with the internal C and R. For symmetric coupling, R combines in parallel with $R^*/2$ and C in parallel with $2C^*$ such that the loaded quality factor is

$$Q_L^{(p)} = \omega_0^* \frac{C + 2C^*}{1/R + 2/R^*} \tag{3.33}$$

where the resonance frequency shifted by the capacitive loading is

$$\omega_0^* = \frac{1}{\sqrt{L(C + 2C^*)}} \tag{3.34}$$

For small capacitive coupling we can set $\omega_0^* \approx \omega_0$ and $C + 2C^* \approx C$ and separate the loaded quality factor into a parallel combination of an external and internal quality factor:

$$\frac{1}{Q_L^{(p)}} = \frac{1}{Q_{\text{ext}}^{(p)}} + \frac{1}{Q_{\text{int}}^{(p)}} \tag{3.35}$$

with

$$Q_{\text{int}}^{(p)} = \omega_0 RC \quad , \quad Q_{\text{ext}}^{(p)} = \frac{\omega_0 R^* C}{2} = \frac{1}{2Z_0}\left(\frac{1}{\omega_0^2 C_\kappa^2 R_L} + R_L\right) \tag{3.36}$$

where we have used $Z_0 = 1/\omega_0 C$. In the overcoupled regime where $Q_{\text{ext}}^{(p)} \ll Q_{\text{int}}^{(p)} \rightarrow Q_L^{(p)} \approx Q_{\text{ext}}^{(p)}$ we see that the loaded quality factor is primarily determined by the size of the coupling capacitor while in the undercoupled regime $Q_L^{(p)} \approx Q_{\text{int}}^{(p)}$ the internal losses of the circuit limit the overall quality factor.

Inductive Coupling

The same transformation methods as in the capacitively-coupled parallel LCR circuit also apply to the inductively coupled series LCR oscillator shown in Fig. 3.3 c. This time, we transform the load circuitry to its Thévenin equivalent to get a simple expression for the quality factor as a function of coupling inductance. As in the capacitively coupled case, the inductor to ground creates a large impedance mismatch. The Thévenin equivalent circuit is shown in Fig. 3.3 d where the equivalent load resistance and series inductance are

$$R^* = \frac{L_\kappa^2 R_L \omega_0^2}{R_L^2 + L_\kappa^2 \omega_0^2} \quad , \quad L^* = \frac{L_\kappa R_L^2}{R_L^2 + L_\kappa^2 \omega_0^2} \tag{3.37}$$

The overall loaded quality factor of the symmetrically-coupled circuit is then determined by the series combination of the internal and coupling inductances

$$Q_L^{(s)} = \omega_0^* \frac{L + 2L^*}{R + 2R^*} \quad , \quad \omega_0^* = \frac{1}{\sqrt{(L + 2L^*)C)}} \tag{3.38}$$

where the resonance frequency is shifted down by the load inductance. As in the capacitive case, we can approximate $\omega_0^* \approx \omega_0$ and $L + 2L^* \approx L$ for small inductors and factor Q_L into internal and external parts:

$$\frac{1}{Q_L^{(s)}} = \frac{1}{Q_{\text{ext}}^{(s)}} + \frac{1}{Q_{\text{int}}^{(s)}} \tag{3.39}$$

with

$$Q_{\text{int}}^{(s)} = \frac{\omega_0 L}{R} \quad , \quad Q_{\text{ext}}^{(s)} = \frac{\omega_0 L}{2R^*} = \frac{Z_0}{2}\left(\frac{R_L}{\omega_0^2 L_\kappa^2} + \frac{1}{R_L}\right) \tag{3.40}$$

where we have used $Z_0 = \omega_0 \cdot L$.

3.2.3 Inductively- and Capacitively-Coupled Transmission Line Resonators

Close to resonance, the open- and short-circuited transmission lines (TL) discussed in section 3.2.1 can be mapped to the equivalent lumped element LCR oscillators of section 3.2.2. This kind of mapping will provide us with a more intuitive understanding of the behavior of distributed resonators around resonance and will also be useful for quick design calculations. For this thesis, we consider a variety of terminations and couplings to realize both series and parallel LCR oscillators, with the following mappings:

- Open-circuited $L = \lambda/4$ TL $\rightarrow$ Series LCR oscillator
- Short-circuited $L = \lambda/4$ TL $\rightarrow$ Parallel LCR oscillator
- Open-circuited $L = \lambda/2$ TL $\rightarrow$ Parallel LCR oscillator
- Short-circuited $L = \lambda/2$ TL $\rightarrow$ Series LCR oscillator

A fundamental difference between distributed TL resonators and the ideal lumped element oscillators lies in the mode structure. While a distributed resonator supports higher harmonics at integer multiples of the fundamental frequency $\omega_n = n \cdot \omega_0$, a lumped element LCR has only one mode.

Short-Circuited $\lambda/2$ and $\lambda/4$ Line

The input impedance of a transmission line at a distance ℓ from a terminating short ($Z_L = 0$) is given by eq. (3.26). For excitation frequencies close to resonance $\omega_n = n\omega_\lambda + \Delta\omega_n$ with $\Delta\omega_n$ small we can write

$$\beta\ell = \frac{n\omega_\lambda \ell}{v_p} + \frac{\Delta\omega_n \ell}{v_p} \tag{3.41}$$

where the distributed resonance frequency is given by

$$\omega_\lambda = \sqrt{\frac{1}{L_\ell C_\ell}}\frac{\pi}{\ell}\,. \tag{3.42}$$

For a half-wave resonance $\ell = \lambda/2 = \pi v_p/\omega_\lambda$ we thus find

$$\beta\ell = n\pi + \frac{\Delta\omega n\pi}{\omega_n} \tag{3.43}$$

Using the periodicity and small argument property of the tangens in (3.26) we then get

$$\tan\beta\ell = \tan\left(\frac{\Delta\omega_n \pi n}{\omega_\lambda}\right) \approx \frac{\Delta\omega_n \pi n}{\omega_\lambda} \tag{3.44}$$

Finally, for small attenuation $\alpha\ell \ll 1$, we can make the approximation $\tanh\alpha\ell \approx \alpha\ell$ such that the input impedance of a short-circuited $\lambda/2$ transmission line is approximated by

$$Z_{\text{in}}^{(\text{short})} \approx Z_0\left(\alpha\ell + j\frac{\Delta\omega_n n\pi}{\omega_\lambda}\right) \tag{3.45}$$

This maps to the impedance of a series LCR oscillator (3.31) with the following effective lumped element quantities:

$$\omega_n = n\omega_\lambda \quad , \quad R_{\text{eff}} = Z_0\alpha\ell = R_\ell \cdot \ell \quad , \quad L_{\text{eff}} = \frac{Z_0 n\pi}{2\omega_\lambda} = \frac{n}{2}L_\ell \cdot \ell \quad , \quad C_{\text{eff}} = \frac{1}{\omega_n^2 L_{\text{eff}}} \tag{3.46}$$

The internal and external quality factors for a symmetrically terminated $\lambda/2$ transmission line resonator can then be approximated by

$$Q_{\text{int}} \simeq \frac{\omega_n L_{\text{eff}}}{R_{\text{eff}}} = \frac{\beta}{2\alpha} \quad , \quad Q_{\text{ext}} = \frac{n\pi Z_0}{2}\left(\frac{R_L}{\omega_n^2 L_\kappa^2} + \frac{1}{R_L}\right) \tag{3.47}$$

For the overcoupled case $Q_L \approx Q_{\text{ext}}$ the overall quality factor of a short-circuited $\lambda/2$ resonator can therefore be controlled by adjusting the coupling inductor. Fig. 3.4 b shows the external quality factor of an inductively, symmetrically coupled transmission line with a characteristic impedance of $Z_0 = 50\,\Omega$ and a matching load $R_L = 50\,\Omega$ for a resonance frequency of $\omega_0/2\pi = 5$ GHz as a function of coupling inductance.

Using the same approximations as in the $\ell = \lambda/2$ case, we find for the input impedance of a short-circuited $\lambda/4$ transmission line close to resonance

$$Z_{\text{in}}^{(\text{short})} \approx \frac{Z_0}{\alpha\ell + jn\pi\Delta\omega_n/2\omega_\lambda} \tag{3.48}$$

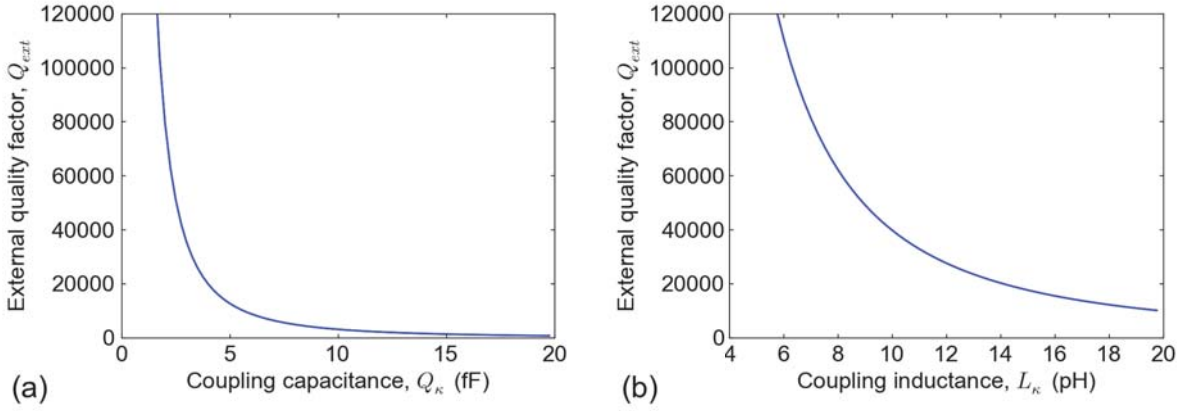

Figure 3.4.: External quality factors of coupled transmission lines at $\omega_0/2\pi = 5$ GHz and $Z_0 = R_L = 50\,\Omega$, using the LCR mapped expressions (3.47) and (3.51) valid close to resonance: (a) Q_{ext} as a function of coupling capacitance, (b) Q_{ext} as a function of coupling inductance.

which maps to the impedance of a parallel LCR oscillator (3.29). The equivalent parallel LCR oscillator for a quarter-wave transmission line is thus given by

$$R_{\text{eff}} = \frac{Z_0}{\alpha\ell} \quad , \quad L_{\text{eff}} = \frac{1}{\omega_n^2 C_{\text{eff}}} \quad , \quad C_{\text{eff}} = \frac{n\pi}{4\omega_n Z_0} \tag{3.49}$$

Open-Circuited $\lambda/2$ and $\lambda/4$ Line

Equivalent lumped element expressions can be derived for transmission lines terminated in an open ($Z_L = \infty$) using an analogous procedure close to resonance and for small attenuation. This shows that the open-circuited $\ell = \lambda/2$ transmission line resonator maps to a parallel LCR oscillator with

$$R_{\text{eff}} = \frac{Z_0}{\alpha\ell} \quad , \quad L_{\text{eff}} = \frac{2}{n\pi}\frac{Z_0}{\omega_n} = \frac{2}{n^2\pi^2} L_\ell \cdot \ell \quad , \quad C_{\text{eff}} = \frac{n\pi}{2\omega_n Z_0} = \frac{1}{2} C_\ell \cdot \ell \tag{3.50}$$

The external quality factor for a symmetrically, capacitively-coupled $\lambda/2$ transmission line can then be approximated as

$$Q_{\text{ext}} = \frac{n\pi}{4Z_0}\left(\frac{1}{\omega_n^2 C_\kappa^2 R_L} + R_L\right) \tag{3.51}$$

which is plotted in Fig. 3.4 a for a $Z_0 = R_L = 50\,\Omega$ transmission line at $\omega_0/2\pi = 5$ GHz as a function of coupling capacitance. Likewise, an open-circuited quarter-wave transmission

line maps to a series LCR oscillator with

$$R_{\text{eff}} = \frac{\pi Z_0 \alpha}{2\beta} \quad , \quad L_{\text{eff}} = \frac{n\pi Z_0}{4\omega_n} \quad , \quad C_{\text{eff}} = \frac{4}{n\pi Z_0 \omega_n} \tag{3.52}$$

3.2.4 Circuit Quantization

As shown in the previous section, a transmission line resonator effectively behaves like a lumped-element parallel or series LCR oscillator close to resonance. Both open- and short-terminated transmission lines can therefore be used to realize harmonic oscillators. What remains to be shown is that such an electrical resonator can behave like a quantum harmonic oscillator and hence realizes the harmonic component in the Jaynes-Cummings Hamiltonian (3.8). In this section, we briefly discuss circuit quantization and show that an LC oscillator can be mapped to a simple quantum harmonic oscillator Hamiltonian.

An electrical circuit can be described quantum-mechanically by the canonical conjugate variables charge q and flux Φ with the commutator $[\Phi, q] = i\hbar$ [159, 160]. The charge plays the role of momentum and Φ corresponds to the position of a mechanical oscillator. For the lossless LC oscillator, charge and flux are related by the voltage across the circuit $V = -L(\partial I/\partial t) = q/C$. The energy of a linear LC oscillator is then governed by the Hamiltonian

$$\mathcal{H}_{\text{LC}} = \frac{q^2}{2C} + \frac{\Phi^2}{2L} \,. \tag{3.53}$$

consisting of electric energy stored in the capacitor and magnetic energy in the inductive part. Comparing this to the Hamiltonian of a mechanical harmonic oscillator $H = p^2/2m + (1/2)m\omega^2 x^2$, we identify the mapping $\omega = 1/\sqrt{LC}$ and $m = C$. Furthermore, we can define the dimensionless creation and annihilation operators of the circuit

$$a = \frac{1}{\sqrt{2\hbar\sqrt{L/C}}}(\Phi + i\sqrt{L/C}q) = \frac{1}{\sqrt{2\hbar Z_0}}(\Phi + iZ_0 q) \tag{3.54}$$

$$a^\dagger = \frac{1}{\sqrt{2\hbar\sqrt{L/C}}}(\Phi - i\sqrt{L/C}q) = \frac{1}{\sqrt{2\hbar Z_0}}(\Phi - iZ_0 q) \tag{3.55}$$

which obey the usual commutation relation $[a, a^\dagger] = 1$. Thus, the Hamiltonian of the LC circuit can be written in the form of a harmonic oscillator Hamiltonian

$$\mathcal{H}_{\text{LC}} = \hbar\omega\left(a^\dagger a + \frac{1}{2}\right) \,. \tag{3.56}$$

	mechanical oscillator	electrical LC oscillator
momentum	$p_x(t)$	$q(t)$
position	$x(t)$	$\Phi(t)$
mass	m	C
frequency	ω	$1/\sqrt{LC}$
commutator	$[x, p_x] = i\hbar$	$[\Phi, q] = i\hbar$

Table 3.1.: Correspondence table of a one-dimensional mechanical oscillator and an electrical LC oscillator circuit.

and the voltage operator V can be introduced as

$$V = \sqrt{\frac{\hbar\omega}{2C}}(a + a^\dagger). \tag{3.57}$$

The voltage operator can be thought of as a quantum voltage generated by the photons inside the resonator. To a good approximation, a lossless TL resonator thus represents a cavity that is described by a harmonic oscillator Hamiltonian of the form (3.56). From a quantum optics point of view, each set of values $\{\Phi, q, L, C\}$ represents a certain mode of the cavity with an average photon number $\langle n\rangle = \langle a^\dagger a\rangle$. The analogy of a one-dimensional mechanical oscillator, such as a massive particle moving in a harmonic potential, and a resonant LC circuit is summarized in the correspondence table Tab. 3.1.

3.2.5 Coplanar Waveguide Geometry

The transmission line resonators discussed in sections 3.2.1 - 3.2.3 have so far been treated conceptually as parallel pairs of conductors with some characteristic impedance, terminated with a near open or short on both ends. In practice, a certain physical implementation has to be chosen. There are many possible geometries for realizing a transmission line resonator and for this thesis we use the coplanar waveguide (CPW) geometry, shown schematically in Fig. 3.5 a and b. A CPW is a quasi two-dimensional structure that can be thought of as a planar version of a coaxial cable. As shown in Fig. 3.5 a, a CPW consists of a thin metallization layer of thickness d patterned on a dielectric substrate of thickness $h \gg d$ and dielectric constant ε_r with a center pin conductor of width $2a$ flanked by quasi-infinite, parallel ground planes on both sides separated by $2b$. Such a structure supports a transverse electromagnetic mode of wave propagation (TEM$_{nm}$) and hence constitutes a transmission line as discussed in the preceding sections. As we will see below, the geometric dimensions, in particular the ratio a/b, in combination with the dielectric substrate properties determine the capacitance

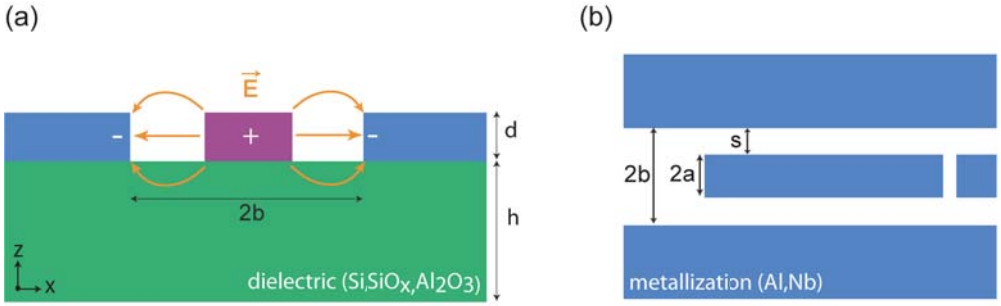

Figure 3.5.: Schematic cross-section and top view of coplanar waveguide geometry: (a) Cross-sectional view with center pin (magenta) and ground planes (blue) on a dielectric substrate (green) of thickness h. Electric field lines are sketched in orange. (b) Top view where $2a$ is the width of the center conductor, $2b$ the spacing between the two ground planes and the thickness of the metallization. The materials used in this thesis are indicated accordingly.

C_ℓ, inductance L_ℓ and resistance R_ℓ per unit length and hence the characteristic impedance of the transmission line. Analytical expressions for C_ℓ, L_ℓ and Z_0 and the effective phase velocity v_{ph} can be derived using a well-known conformal mapping technique [161]. This in turn allows engineering transmission line resonators with resonance frequencies $\omega_0/2\pi \sim 1-10$ GHz and $Z_0 \approx 50\,\Omega$, typically down to the few % precision [45]. The effective dielectric constant of a CPW on a finite thickness substrate is defined as the ratio of the waveguide's total capacitance per unit length and the partial capacitance in the absence of all dielectrics, $\varepsilon_{\mathrm{eff}} = C_\ell/C_{\mathrm{air}}$, which in turn sets the phase velocity $v_{\mathrm{ph}} = c/\sqrt{\varepsilon_{\mathrm{eff}}}$. $\varepsilon_{\mathrm{eff}}$ can be expressed analytically through elliptical integrals [161]

$$\varepsilon_{\mathrm{eff}} = 1 + \left(\frac{\varepsilon_r - 1}{2}\right)\frac{K(k')K(k_1)}{K(k)K(k_1')} \tag{3.58}$$

where $K(\cdot)$ denotes the complete elliptical integral of the first kind and the geometry-dependent quantities are given by

$$k = \frac{a}{b} \quad , \quad k' = \sqrt{1-k^2} \tag{3.59}$$

$$k_1 = \frac{\sinh(\pi a/2h)}{\sinh(\pi b/2h)} \quad , \quad k_1' = \sqrt{1-k_1^2} \quad , \quad \beta = \frac{2\pi\nu}{c}\sqrt{\varepsilon_{\mathrm{eff}}} \tag{3.60}$$

The characteristic impedance of the CPW can be expressed as [161]

$$Z_0 = \sqrt{\frac{L_\ell}{C_\ell}} = \frac{1}{\sqrt{\varepsilon_{\mathrm{eff}}}}\left[\frac{\mu_0}{4\varepsilon_0}\frac{K(k')}{K(k)}\left(\frac{1}{2}\frac{K(k')}{K(k)}\right)\right]^{1/2} \tag{3.61}$$

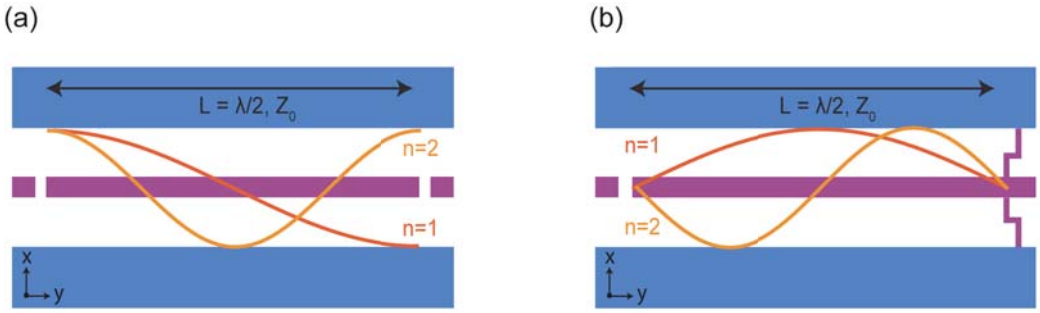

Figure 3.6.: Schematic top view of coplanar waveguide resonators and the voltage distributions of the $n = 1$ (red) and $n = 2$ mode (orange). Center pin (magenta) and ground planes (blue) are shown, not to scale. (a) Symmetrically, capacitively-coupled $\lambda/2$ CPW resonator, (b) Asymmetrically, inductively- and capacitively-coupled resonator.

where we have neglected kinetic inductance contributions which decrease quadratically with temperature, see Ref. [44] for a good discussion. To get a desired value of $Z_0 = 50\,\Omega$ for a sapphire substrate $\varepsilon_r = 9.4$ (c-plane) of thickness $h \approx 500\,\mu$m, we use ratios of $a/b \sim 0.5$ at absolute dimensions of $2a \approx 10\,\mu$m and $2b \approx 19\,\mu$m. Typical capacitance and inductance per unit length values are $C_\ell \approx 100 - 200$ pF and $L_\ell \approx 100 - 200$ nH, respectively. The various inductive and capacitive load impedances and terminations introduced in section 3.2.3 can be realized in quasi lumped form. Capacitors are realized in the form of planar gap or interdigitated finger structures while inductors can be made as narrow wires connecting the center pin electrode to ground. Optical microscope pictures of typical coupling capacitors and inductors fabricated for this thesis are shown in Fig. 3.7. Details on fabrication methods and recipes are provided in chapter 4. Full inductively and capacitively coupled CPW resonators are shown schematically in Fig. 3.6 a and b, together with the voltage distributions for the lowest two modes. The fundamental $n = 1$ mode of the symmetrically, capacitively coupled $\lambda/2$ resonator has a voltage node at the center while the inductively coupled version has an anti-node at that point, a symmetry which will be exploited later on for DC-biased center pin designs, see chapter 7.

The attentive reader may have noticed the close similarity of the CPW geometry and the microchannel structures introduced in section 2.3.4. As demonstrated throughout this thesis, the CPW geometry lends itself naturally to electrons on helium experiments and has been put to a variety of uses, for example to measure ultra-thin films of superfluid helium (chapter 5), as an on-chip helium level monitor (chapter 6) or as a large planar electron trap or reservoir (chapter 7). A novel type of DC-biased center pin resonator, which exploits the symmetry of the voltage distribution and has a higher aspect ratio between center pin and

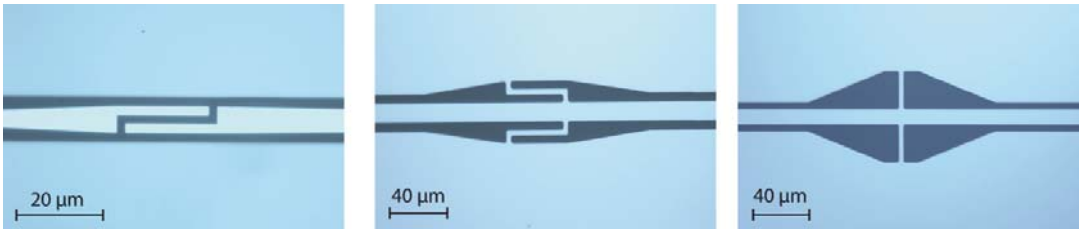

Figure 3.7.: Optical microscope images of coupling capacitors (left) and inductors (center and right) fabricated at Yale using optical lithography techniques. See chapter 4 for details on fabrication.

ground plane thickness, will be presented in section 7.1.1.

3.3 Quantum Dots on Superfluid Helium

In chapter 2 we saw that an isolated electron above a film of superfluid helium is bound to the surface via polarization of the dielectric liquid, leading to quantization of the electron's vertical motion with transition frequencies on the order of a few hundred GHz. At low temperatures, the electron is effectively frozen into its vertical motional ground state while its unconstrained lateral motional states are simple plane waves. As shown in section 2.2, a collection of many electrons above the surface of liquid helium then forms a two-dimensional electron gas or Wigner crystal, depending on temperature and electron density. In analogy to gate-defined quantum dots in semiconductor heterostructures [162–167] this exotic type of two-dimensional electron system can be potentially used to build quantum dots on helium operated in the single-electron regime. This is one of the core ideas of this PhD thesis. Using confinement via electrostatic gates submerged in liquid helium, the electron's motion parallel to the surface can be quantized with a motional energy spectrum that can be engineered by geometry and applied DC voltages. Electrostatic traps holding small numbers of electrons have recently been realized and used to count individual electrons on helium [168] and to observe few electron Wigner molecules using a single-electron transistor [101]. However, so far there have been no observations of coherent single electron motion or intradot quantization for electrons on helium, in large part because of the lack of suitable detection and readout mechanisms. Detection and measurement in conventional semiconductor quantum dots is typically based on gated transport and current measurements using quantum point contacts at low frequencies ~ 100 Hz [162, 169]. This is difficult to achieve with electrons on helium, in part because it is not possible to attach leads directly to the electron gas region. In this thesis, we show how a circuit quantum electrodynamics setup can be used to iso-

late, detect and control quantized single electron motion via dipole coupling to a microwave field.

This section discusses the theory and design of single-electron quantum dots with electrons on helium. Lateral electrostatic traps are first discussed in general in section 3.3.1, together with the basic parabolic trap geometry. In section 3.3.2 we present a quartic anharmonic oscillator model that approximates the parabolic confining potential as a fourth order polynomial. This conceptually simple model captures most of the essential physics of trapped electron states and provides an intuitive picture. In section 3.3.3, we follow up with a discussion of various numerical methods that can be used to diagonalize the quantum dot Hamiltonian for potentials simulated via finite-element techniques. Finally, section 3.3.4 gives a comparison between lateral electron motional states and superconducting transmon qubits, showing that one can be mapped onto the other via quartic anharmonic oscillator modeling.

3.3.1 Lateral Electrostatic Traps

In the absence of any free charges, the electrostatic potential for a general three-dimensional geometry is described by a simple source-free Poisson equation

$$\Delta\Phi(\mathbf{r}) = (\partial_x + \partial_y + \partial_z)\,\Phi(\mathbf{r}) = 0 \tag{3.62}$$

with appropriate boundary conditions for equipotential surfaces $\Phi(\mathbf{r} \in S_j) = V_j$ where S_j denotes a surface at potential V_j . The separability of this equation depends on the symmetry of the confining geometry. The effective trap potential a charged particle experiences is a function of both geometry and applied DC voltages. First, note that it is in fact impossible to trap a charged particle in three dimensions using only electrostatic potentials. This is expressed by Earnshaw's theorem which states that a point charge cannot be maintained in a stable, stationary equilibrium in $\mathbb{R}^3$ in purely electro- or magnetostatic potentials [7]. For this reason, trapping of ions is achieved using quadrupole Penning or Paul traps that use time-dependent RF potentials [170]. For an electron above the surface of liquid helium, however, one dimension of motion is automatically eliminated by the surface binding po-

[7] The proof is a simple consequence of Gauss's law: A DC potential obeys Laplace's equation $\Delta\phi(\mathbf{r}) = 0$ and hence the corresponding electrostatic force $\mathbf{F} = -\nabla\phi$ is divergence-free such that there are no local minima. It is interesting to note that an Earnshaw-type restriction applies not only to Coulomb interactions but in fact to any inverse square law force such as gravitational.

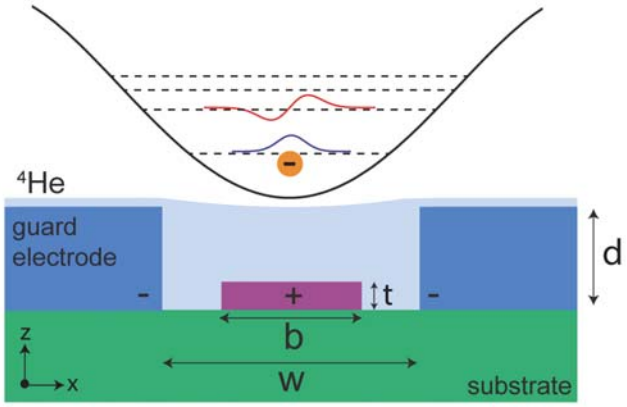

Figure 3.8.: One-dimensional single-electron trap on liquid helium with energy levels and wavefunctions of electron motional states: The electron is bound to the surface of a film of superlfuid ^{4}He of thickness d via image charge attraction. A DC trap electrode of width b (magenta), fabricated on top of a dielectric substrate, is biased positive relative to two guard electrodes (blue), which are typically at ground potential and form a micro channel with a self-stabilized helium film. The configuration generates a confining potential that is to first order harmonic but flattens over the guard electrodes, resulting in a small softening anharmonicity, see discussion in text. The ground (dark blue) and first excited (red) motional wave functions are shown together with the anharmonic energy levels (dashed lines). Note that the extent of the electron zero-point motion x_0 is usually much smaller than the physical size of the trap w.

tential. As we saw in chapter 2, the energy separation between ground and first excited state is $\omega_{12}/2\pi \simeq 120$ GHz or about 5.7 K such that at low enough temperaturs the electron will be frozen into its vertical ground state. We can therefore treat the z motion parametrically and assume a constant vertical position of $z_0 = \langle 1|z|1\rangle \simeq 11$ nm. This approximation obviously breaks down when the vertical field component becomes large enough to Stark ionize the electron, see section 2.1.2. To further reduce the dimensionality of the problem, we assume a sufficiently asymmetric electrode configuration such that motion along the x and y direction effectively decouple. The potential therefore separates $\Phi(\mathbf{r}) = \Phi_x \cdot \Phi_y \cdot \Phi_z$ such that

$$(\partial_x + \partial_z)\,\Phi_x(x)\Phi_z(z) = 0 \quad \rightarrow \quad \Phi(x,z) = V_0 e^{-kz}\cos(kx) \quad , \quad k = \frac{2\pi}{w}n \tag{3.63}$$

where we have assumed periodic boundary conditions along the lateral axis, $\Phi(x=0) = \Phi(x=w)$ and Dirichlet boundary conditions for the vertical motion $\Phi_z(z \rightarrow +\infty) = 0$. The assumption of periodic boundary conditions and the resulting cosine potential are useful to arrive at a simple approximation for typical electrode geometries, as shown below.

The basic one-dimensional electrostatic trap configuration for electrons on helium is shown schematically in Fig. 3.8. The trap consists of a single DC-biased electrode of width b at the center surrounded by two negative or grounded guard electrodes separated by w. The guard electrodes form a micro-channel of width w and depth d that supports a self-stabilized

capillary action film of superfluid helium (see section 2.3.4). The trap is symmetric about the center axis such that the we have the boundary conditions $\Phi(x = 0) = \Phi(x = w)$ and the trap potential is similar to (3.63). However, the trap is not periodic so we expand the cosine to fourth order, which gives

$$V(x) \approx V_t(z_0) - \frac{V_t(z_0)}{2}(kx)^2 + \frac{V_t(z_0)}{24}(kx)^4 \tag{3.64}$$

where we have introduced the effective trap depth

$$V_t(z_0) = V_0 e^{-k(d+z_0)} = V_0 e^{-2\pi(d+z_0)/w} \tag{3.65}$$

where V_0 is the DC voltage applied to the center electrode and $d + z_0 = d + \langle 1|z|1\rangle \simeq d$ is the electron's distance from the bias electrode. For physically reasonable trapping parameters - helium channel depth $d = 500$ nm, trap width $w = 500$ nm and bias voltage $V_0 = 10$ mV, we get a trap depth of $eV_t/h \approx 20$ GHz or about 1 K, deep enough to prevent thermal escape at milli-Kelvin temperatures. The exact potential depends on the specific boundary conditions of the electrode geometry under consideration and can be inferred from numerical simulations, see section 3.3.3.

3.3.2 Quartic Anharmonic Oscillator Model

The parabolic approximation for the trapping potential in eq. (3.64) allows us to analytically estimate the scaling of the system parameters in the electron Hamiltonian with trap geometry and bias voltages. The quantized lateral motional states of a single-electron quantum dot can then be described as anharmonic oscillator states. This approximation is useful to arrive at an intuitive picture of the most important electron-qubit parameters such as energy level anharmonicity α, transition frequency ω_p and the zero-point trap size x_0. As will be shown in section 3.3.3, finite-element simulations of the trap potentials generally agree well with the fourth order polynomial shape. Using the quartic approximation for the trap potential, the motion of a single electron along the trap axis is described by the one-dimensional Hamiltonian

$$\mathcal{H} = \frac{p_x^2}{2m} + \frac{eV_t}{2}(kx)^2 + \frac{eV_t}{4!}(kx)^4 \tag{3.66}$$

where we have subtracted a constant term eV_t that does not change the dynamics of the system. Mapping the first two terms in (3.66) to $\mathcal{H} = p^2/2m + (1/2)m\omega_p^2 x^2$, we can identify

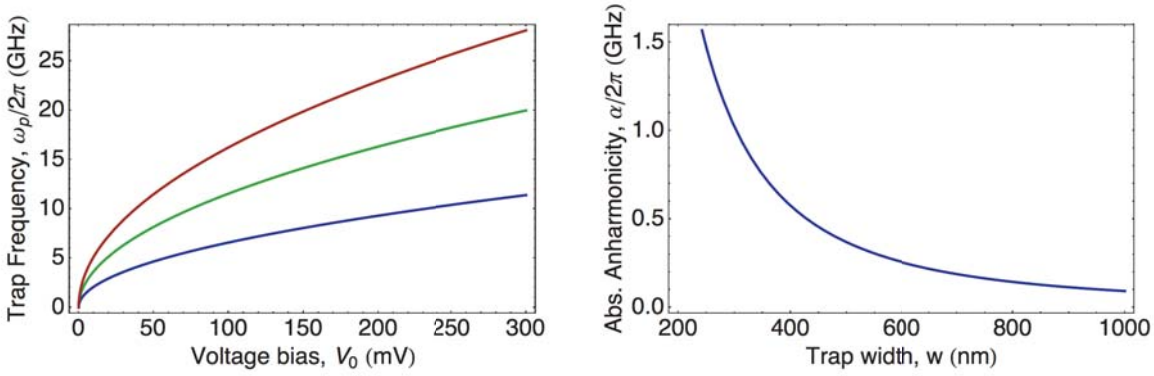

Figure 3.9.: Quartic anharmonic oscillator model: Scaling of system parameters with bias voltage and trap geometry. (a) Trap frequency eq. (3.67) as a function of voltage bias on the center electrode for three different trap dimensions: $w = 400$ nm (blue), $w = 500$ nm (green) and $w = 600$ nm (red), (b) Absolute trap anharmonicity eq. (3.83) as a function of geometric trap width w.

the electron's trap oscillation or plasma frequency

$$\omega_p = \sqrt{\frac{eV_t k^2}{m}} = 2\pi\sqrt{\frac{eV_t}{mw^2}} \tag{3.67}$$

The electron motional frequency can therefore be tuned via the DC voltage V_0 applied to the center electrode, and also depends parametrically on the trap geometry through w and $V_t(z_0)$. Motional tuning curves are shown in Fig. 3.9 a for several typical trap dimensions. Changing the voltage bias by a few tens of mV allows us to tune the motional frequency over a wide band of GHz frequencies. We can write the Hamiltonian explicitly as a quartic anharmonic oscillator

$$\mathcal{H} = \mathcal{H}_0 + \mathcal{H}_Q = \frac{p_x^2}{2m} + \frac{1}{2}m\omega_p^2 x^2 + \frac{1}{4!}m\omega_p^2 k^2 x^4 \tag{3.68}$$

where $\mathcal{H}_Q$ is the fourth order perturbation to the simple harmonic oscillator. The length scale of our system is set by the spatial extension of the lateral motional ground state, the zero-point trap size x_0, which has the usual form

$$x_0 = \sqrt{\frac{\hbar}{m\omega_p}}\,. \tag{3.69}$$

Note that the oscillator is quite large because of the small electron mass. At microwave frequencies $\omega_p/2\pi \simeq 5$ GHz we have $x_0 \simeq 60$ nm. Now introducing the dimensionless variable $\xi = x/x_0$ and scaled energy $\mathcal{E}_n = E_n/\hbar\omega_p$, we arrive at the dimensionless Schrödinger

equation

$$\left[\frac{\partial^2}{\partial\xi^2} - \xi^2 - \frac{1}{12}x_0^2k^2\xi^4\right]\Psi_n(\xi) = -2\mathcal{E}_n\Psi_n(\xi)\,. \tag{3.70}$$

As opposed to the harmonic oscillator case, this equation can not be reduced to a hypergeometric differential equation and hence its solutions cannot be written in simple analytic form using Hermite polynomials. One generally has to resort to brute-force numerical diagonalization (see section 3.3.3) or various approximation methods, for example Rayleigh-Schrödinger perturbation theory (shown below), WKB or path integral methods [171]. Alternatively, one can go back to the original cosine potential (3.63) and work with the resulting Matthieu equation

$$y'' + \left[E - 2h^2\cos(2z)\right]y(z) = 0 \tag{3.71}$$

which has known analytical solutions.

Algebraic Formulation

The Hamiltonian (3.68) can be expressed in algebraic form by introducing the usual ladder operators with the standard commutator for dimensionless conjugate variables $\left[b, b^\dagger\right] = 1$

$$b = \frac{1}{\sqrt{2}}\left[\frac{x}{x_0} + i\frac{x_0}{\hbar}p_x\right] \tag{3.72}$$

$$b^\dagger = \frac{1}{\sqrt{2}}\left[\frac{x}{x_0} - i\frac{x_0}{\hbar}p_x\right] \tag{3.73}$$

such that

$$p = \frac{i}{\sqrt{2}}\frac{\hbar}{x_0}(b^\dagger - b) \quad , \quad x = \frac{1}{\sqrt{2}}x_0(b + b^\dagger) \tag{3.74}$$

The anharmonic oscillator Hamiltonian then takes on the form of a Duffing oscillator

$$\mathcal{H} = \mathcal{H}_0 + \mathcal{H}_I = \hbar\omega_p\left(b^\dagger b + \frac{1}{2}\right) + \frac{1}{4!}\frac{\hbar^2k^2}{4m}\left(b + b^\dagger\right)^4 \tag{3.75}$$

with the perturbation term quartic in the ladder operators. This form lends itself to an easy algebraic treatment in non-degenerate, time-independent perturbation theory, which provides more insight into the scaling of the Hamiltonian with system parameters, in particular the energy level anharmonicity.

Perturbation Theory & Anharmonicity

The unperturbed lateral motional states of the electron are the usual harmonic oscillator number states $|n\rangle$ with $\mathcal{H}_0 |n\rangle = E_n |n\rangle$, $E_n = \hbar\omega_p(n + 1/2)$ which in dimensionless position basis take the standard form

$$\Psi_n(\xi) = \langle\xi|n\rangle = \sqrt{\frac{1}{2^n n!}} \left(\frac{1}{\pi}\right)^{1/4} e^{-\xi^2/2} H_n(\xi) \ . \tag{3.76}$$

where $H_n(\cdot)$ denote the normalized Hermite polynomials of order n

$$\int_{-\infty}^{+\infty} H_n(x) H_{n'}(x) e^{-x^2} dx = \delta_{n,n'}(\sqrt{\pi} 2^n n!) \tag{3.77}$$

The eigenfunctions are characterized by the parity relations

$$\Psi_n(\xi) = (-1)^n \Psi_n(-\xi), \qquad \Pi |n\rangle = (-1)^n |n\rangle \tag{3.78}$$

i.e. they are symmetric and anti-symmetric eigenstates of the parity operator in alternating order with the quantum number n, as expected from the symmetry of the potential. This in turn leads to a general constraint for the matrix elements in the case of parity conserving interactions

$$\langle i|\mathcal{A}|j\rangle = 0 \quad \forall i, j : (-1)^{i+j} = -1 \tag{3.79}$$

where $\mathcal{A}$ is some Hermitian operator satisfying $[\mathcal{A}, \Pi] = 0$ with Π denoting the parity operator. The unperturbed states $|n\rangle$ are non-degenerate and form a complete orthonormal set such that they can be used for elementary Rayleigh-Schrödinger perturbation theory. This gives the corrected eigenenergies to first order

$$E_n \approx E_n^{(0)} + \Delta E_n^{(1)} = \hbar\omega_p \left(n + \frac{1}{2}\right) + \langle n|\mathcal{H}_I|n\rangle \tag{3.80}$$

$$= \hbar\omega_p \left(n + \frac{1}{2}\right) + \frac{3}{4!} \frac{\hbar^2 k^2}{4m} [2n(n+1) + 1] \tag{3.81}$$

Note that only terms of the form $(b^\dagger b)^2$ give non-vanishing diagonal matrix elements due to the parity properties. The leading-order correction to the state $|n\rangle$ is given by

$$|n^{(1)}\rangle = \frac{1}{4!} \frac{\hbar^2 k^2}{4m} \sum_{i \neq n} \frac{\langle i|(b + b^\dagger)^4 |n\rangle}{E_i - E_n} |i\rangle \tag{3.82}$$

which shows that the quartic perturbation causes mixing of the state $|n\rangle$ with the states $|n \pm 2\rangle$ and $|n \pm 4\rangle$. To lowest order, the absolute anharmonicity of the energy levels is then given by

$$\alpha = (E_{12} - E_{01})/\hbar = \frac{\hbar k^2}{8m} = \frac{\hbar \pi^2}{2mw^2} \tag{3.83}$$

where $E_{ij} = E_j - E_i$. Note that α is independent of voltage bias and solely determined by the physical trap size w. This is an important result which shows that, to lowest order, oscillation frequency ω_p and anharmonicity α can be controlled independently. One can tune the motional frequency by adjusting the bias voltage, determine the anharmonicity by the trap size (confinement effects) and trade off sensitivity in bias voltage for sensitivity in trap height (recall $V_t = V_0 \exp(-2\pi d/w)$). The numerical calculations presented in section 3.3.3 show a weak dependence of anharmonicity on voltage bias but largely confirm the intuitive picture given here. The electrons on helium quantum dot geometry shown in Fig. 3.8 is generally expected to give negative anharmonicities $\alpha < 0$ since the trap is small and the potential must flatten at the outer guard electrodes. Fig. 3.9 b shows the lowest order anharmonicity as a function of trap width w. Larger traps lead to more harmonic potentials and hence smaller α. The n to $n+1$ transition frequency can be approximated as

$$\omega_{p,n} \simeq \omega_{p,0} + (n+1)\alpha \tag{3.84}$$

and the Hamiltonian can be written in terms of the anharmonicity

$$\begin{aligned} \mathcal{H} &= \hbar\omega_p \left(b^\dagger b + \frac{1}{2} \right) + \frac{\hbar\alpha}{12} \left(b + b^\dagger \right)^4 \\ &= -\frac{\hbar^2}{2m} \frac{1}{x_0^2} \frac{\partial^2}{\partial \xi^2} + \frac{1}{2} m\omega_p^2 x_0^2 \xi^2 + \frac{1}{3} \hbar\alpha \xi^4 \end{aligned} \tag{3.85}$$

a form which will be useful later on when comparing single electron quantum dots to transmon qubits. Note that since α is the prefactor of the fourth order term, we see immediately that the anharmonicity per length scale x_0 is essentially determined by the fourth order derivative of the trap potential, which provides us with a quick intuitive check of wether or not a given trap potential yields large or small anharmonicity.

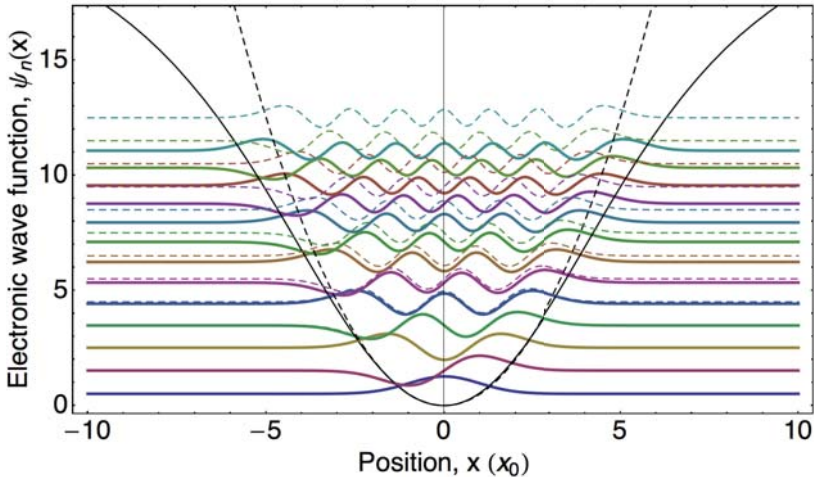

Figure 3.10.: Numerical potentials, wave functions and energy levels obtained from electrostatic finite-element simulations of a three-dimensional trap geometry. Solid lines are quantities obtained by numerical diagonalization of the Hamiltonian containing the simulated potential along one of the principal trap axes. Dashed lines are the corresponding perfect harmonic oscillator quantities obtained from a pure quadratic potential scaled to the same energy. Dimensionless wave functions are offset by their respective energy quantum numbers n and energy levels are shown in units of n. The position coordinate is shown in units of the zero-point motional size x_0.

3.3.3 Numerical Methods and Trap Simulations

Our analysis of quantum dots on helium has so far been based on approximating the anharmonicity of the trap potential by an additional quartic term in the Hamiltonian. Further implicit approximations made so far include the assumption of a perfectly flat helium surface, neglecting curvature effects and the effect of DC voltages on the superfluid film thickness. This section presents some of the numerical techniques used for finding exact wavefunctions and eigenenergies based on finite-element simulations of the trap potential and numerical diagonalization of the quantum dot Hamiltonian. This allows us to obtain more accurate results for the key parameters anharmonicty, trap frequency and trap size and to make more informed design choices.

For a given trap geometry, we simulate the electrostatic potential along the trap axis using finite element methods, essentially brute-force solving Maxwell's equations on a discrete mesh. This can be done using commercially available software packages such as *Ansoft Maxwell3D*. The accuracy of the simulation depends on a number of parameters such as mesh discretization size (triangle side length), mesh refinement per iteration and error threshold. The output of the simulation then serves as input for the generic Hamiltonian $\mathcal{H} = p^2/2m +$

$V(x)$. We start by fitting the potential to the general form

$$V = a(x - x_{\text{off}})^2 + b(x - x_{\text{off}})^4 + c \tag{3.86}$$

where x_{off} and c are general offsets and estimate anharmonicity and trap frequency through

$$a = \frac{1}{2} m\omega_p^2 \quad , \quad b = \frac{\hbar\alpha}{3x_0} \tag{3.87}$$

The bias voltage is set to $V_0 = 1$ V in all simulations such that scaling of ω_p, x_0 and α becomes straightforward. To construct the Hamiltonian matrix we use the unperturbed harmonic oscillator basis

$$\begin{aligned} \mathcal{M} = \{|n\rangle\}_{n=1,\ldots,D} \quad , \quad \langle n'|\mathcal{H}_0|n\rangle = n\delta_{n',n} \quad , \quad \langle n'|n\rangle = \delta_{n',n} \\ \mathcal{H}_0 = \sum_n \mathcal{H}_{n,n} |n\rangle \langle n| \quad , \quad \mathcal{H}_{n,n} = \langle n|\mathcal{H}_0|n\rangle \end{aligned} \tag{3.88}$$

where $\mathcal{M}$ denotes the state space and D the dimensionality of the Hilbert space we take into account. Typically, $D \sim 20 - 30$. The matrix elements for the full Hamiltonian are then calculated via numerical integration

$$\mathcal{H}_{ij} = \langle i|\mathcal{H}|j\rangle = \int \Psi_i^*(x) \left(-\frac{\hbar^2}{2m}\frac{\partial^2}{\partial x^2} + V(x) \right) \Psi_j(x) dx \tag{3.89}$$

where $V(x)$ is an interpolation function obtained from the finite-element simulation and $\Psi_i(x)$ are the harmonic oscillator wavefunctions given in eq. (3.76). For symmetric traps we can take advantage of the parity selection rule

$$\langle i|\mathcal{H}|j\rangle = 0 \quad \forall i, j : (-1)^{i+j} = -1 \tag{3.90}$$

where the potential term satisfies $[V, \Pi] = 0$. To avoid under- or overflow issues, it is advantageous to transform all expressions into dimensionless units first, i.e. scale the potential and position by the size of the motional ground state x_0. The matrix with elements (3.89) can be diagonalized using standard inversion schemes, for example using the `numpy.linalg.eigh` module in *Python* or the eigensystem solver in *Mathematica*. The resulting eigenvectors and eigenvalues give the desired motional wavefunctions and energies for the given bias voltage V_0. Numerically simulated potentials, wavefunctions and energies for a typical trap geometry are shown in Fig. 3.10, together with the equivalent harmonic oscillator quantities

obtained for a purely quadratic potential of the same energy scale. Note the small anharmonicity in the energy levels and the increasing deviation from perfect harmonic behavior higher up the energy ladder as the potential flattens out. To extract the tuning curves for frequency and anharmonicity as functions of voltage bias, we repeat the diagonalization procedure by scaling the simulated potential with the appropriate bias voltage.

3.3.4 Comparison to Transmon Qubits

Pioneered at Yale, the transmission-line shunted plasma oscillation qubit (Transmon) [156, 172] represents a charge-insensitive Josephson junction qubit design that has been successfully used in many circuit QED experiments, both in two-dimensional cQED [53] and with increased coherence times in three-dimensional architectures [46]. The key behind the transmon design is to reduce sensitivity to charge fluctuations by trading in a decrease in energy level anharmonicity. In this section we map the single-electron quantum dot on helium to the corresponding expressions for a transmon qubit. This highlights the conceptual similarity between the two qubit implementations and is particularly useful when considering hybrid approaches that combine both types of qubits in the same architecture. For a good introduction to transmon and Cooper pair box qubits see Ref. [44].

The transmon Hamiltonian can be expanded to fourth order for small phase angles [156]

$$\mathcal{H} = 4E_C(n-n_g)^2 - E_J\cos\phi \approx 4E_C(n-n_g)^2 - E_J + E_J\frac{\phi^2}{2!} - E_J\frac{\phi^4}{4!} \tag{3.91}$$

where E_C and E_J are the charging and Josephson tunneling energies, respectively, n is the number operator describing the number of Cooper pairs transferred between the superconducting islands, n_g is the offset charge and ϕ the gauge-invariant phase difference between the islands. As pointed out in section 3.2.4, the charge and phase operators form a canonically conjugate pair of variables $[n,\phi] = i$. The cosine potential already hints at the similarity with the single-electron quantum dot potential, which was motivated in section 3.3.1 by considering periodic boundary conditions. Writing the expanded Hamiltonian (3.91) in terms of the transmon ladder operators one finds

$$\mathcal{H} = \sqrt{8E_JE_C}\left(b^\dagger b + \frac{1}{2}\right) - \frac{E_C}{12}\left(b+b^\dagger\right)^4 \tag{3.92}$$

Comparing this expression to (3.85), we can identify the mapping between the properties of

	Transmon		Quantum Dot on ^{4}He	
Plasma frequency, $\omega_p/2\pi$	$\frac{1}{h}\sqrt{8E_JE_C}$	1 - 10 GHz	$\sqrt{\frac{eV_t}{mw^2}}$	1-10 GHz
Trap Depth, eV_t/h	E_J/h	3 - 10 GHz	$\frac{eV_0}{h}e^{-2\pi d/w}$	20 GHz
Anharmonicity, $\alpha/2\pi$	E_C/h	300 - 500 MHz	$-h/8m_ew^2$	50 - 100 MHz
Oscillator size ratio	$(E_J/E_C)^{1/4}$	1 - 3	w/x_0	1 μm/30 nm
Energy ratio	E_J/E_C	10 - 100	$\frac{eV_t}{\hbar\alpha}$	1800

Table 3.2.: Mapping between transmon and quantum dot on helium properties, based on comparison of quartic anharmonic oscillator approximations for each. Left-hand column shows expression in quartic approximation and right-hand column typical numerical values for both transmon and quantum dot. Representative transmon values taken from [156, 172].

the motional states in a quantum dot and the transmon, shown in Table 3.2 together with representative numerical values. The two types of anharmonic oscillators can indeed have comparable properties. For typical trap geometries in the μm to sub-μm size range with mV biases, the quantum dot on helium oscillator corresponds to a transmon with large E_J/E_C ratio.

3.4 Circuit QED: Single Electron-Cavity Coupling

One of the core ideas of this PhD project is that a single electron trapped in a quantum dot on helium (section 3.3) can be coupled to a superconducting coplanar waveguide cavity (section 3.2) to realize a cavity quantum electrodynamics system (section 3.1). This section puts all the different parts from the previous sections together and shows how an electron can be coupled to the microwave field in a CPW resonator via dipole interaction. In section 3.5 we will extend this idea and show how the internal spin degree of freedom of an electron in a quantum dot can be coupled indirectly to the cavity through spin-orbit interaction. Section 3.7 will furthermore focus on collective coupling of many electron states to CPW cavities.

A single electron in a parabolic trap such as the one shown in Fig. 3.8 is fundamentally just an oscillating point charge with an associated dipole moment given by $\mathbf{d} = -e \cdot \mathbf{r}$. In section 3.1, it was shown how the Jaynes-Cummings interaction (3.8) in a cavity arises from the dipole interaction of the atomic component with the quantized electromagnetic field in the cavity. Coupling an electron on helium to a coplanar waveguide cavity can then be achieved by aligning the dipole with the cavity field. The challenging part is to find effective ways of integrating the quantum dot into a CPW in such a way that the coupling strength is maximized. This can be achieved by fabricating the electrode configuration directly in the

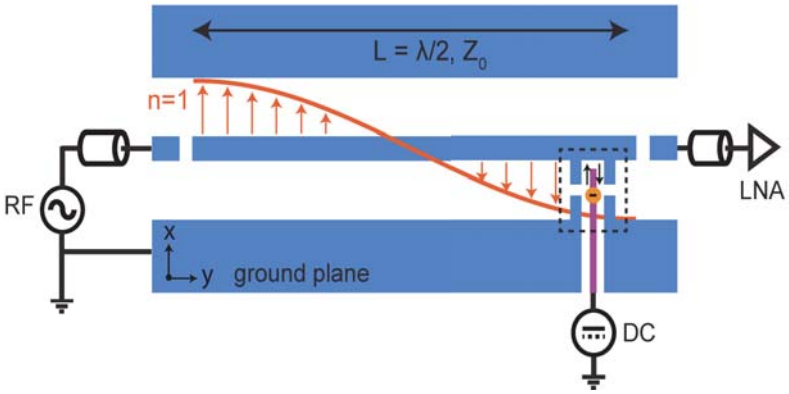

Figure 3.11.: Top view of an electrostatic electron trap integrated into a capacitively-coupled coplanar waveguide resonator. Ground plane and cavity center pin are shown in blue while the DC-biased trap electrode is shown in magenta. The center pin and ground plane configuration forms a split-guard ring around the trap electrode, see dashed box and zoom-in in Fig. 3.12 a. Manipulation and readout are performed via radio frequency voltages applied to the input port of the resonator with the modified signal measured by a cryogenic low-noise amplifier at the output port.

gap of the coplanar waveguide as shown schematically in Fig. 3.11. The principal trap axis is aligned with the cavity field, positioned at or near a maximum of the voltage distribution, i.e. at the ends of the capacitively-coupled resonator in Fig 3.11. As pointed out in section 3.2.1, it is in practice advantageous to use inductive coupling to keep the center pin at DC ground potential and to avoid charging effects. Fig. 3.12 a shows details of the integrated trap design (dashed box region in Fig. 3.11). The cavity center pin and ground plane form a split-guard ring configuration around the positively biased trap electrode. Note the high aspect ratio of this geometry with respect to x and y axes. The motional states of the electron along the two orthogonal trap axes have distinct motional frequencies for a given voltage bias $\omega_x \ll \omega_y$. This mismatch in characteristic frequencies allows us to separate the two-dimensional Hamiltonian for the trapped electron and reduce the problem to one dimension. The theory developed in section 3.3 therefore applies well to this type of trap geometry, see Fig. 3.12 b. The Jaynes-Cummings expression for the coupling strength (3.9) was derived for a two-level system but the result readily generalizes to arbitrary number of levels

$$g_{ij} = \frac{d_{ij}}{\hbar}\mathcal{E}_{\mathrm{rms}} = \sqrt{\frac{\omega_r}{2\varepsilon_0 \hbar \mathcal{V}_R}}\, d_{ij} \tag{3.93}$$

where the dipole matrix element for the transition $|i\rangle \rightarrow |j\rangle$ is given by

$$d_{ij} = \langle i|e \cdot x|j\rangle = e\int_{-\infty}^{+\infty} \Psi_i^*(x) \cdot x \cdot E_{||}(x)\Psi_j(x)dx \tag{3.94}$$

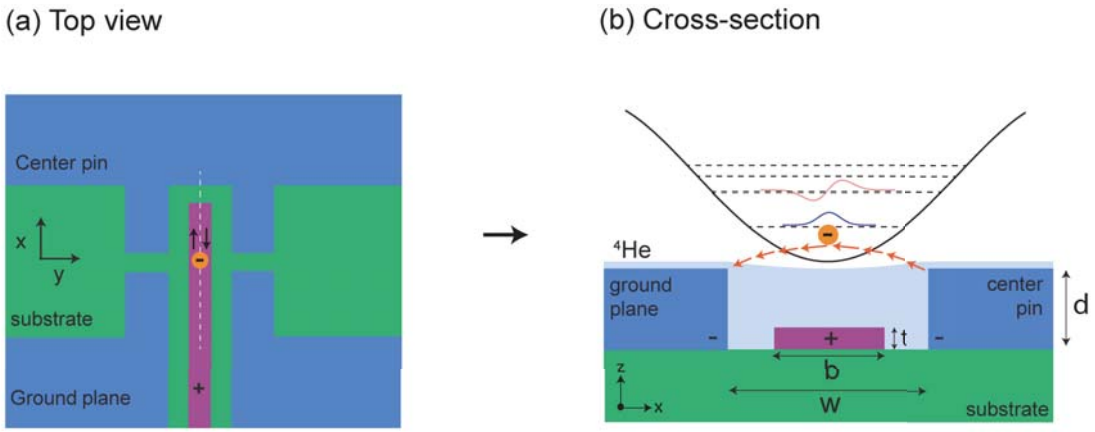

Figure 3.12.: Split-guard ring trap geometry and mapping to a one-dimensional parabolic trap. (a) Top view of split-guard ring configuration formed by the cavity center pin and ground plane (blue) around the trap electrode (magenta), see dashed box region in Fig. 3.11. The trap has a high-aspect ratio such that electron motion along the x and y axes effectively decouples due to the large frequency mismatch $\omega_x \ll \omega_y$. (b) Cross-sectional mapping to a one-dimensional parabolic trap model (along dashed white line in (a)). Cavity electric field lines are shown by red arrows.

where $E_{||}(x)$ is the cavity electric field component along the x axis and $\Psi_i(x)$ are the wave functions of the trapped electron. A simple expression for the coupling between the quartic anharmonic oscillator of section of 3.3.2 and the cavity harmonic oscillator can be derived by writing the dipole operator in terms of ladder operators (see eq. (3.74))

$$d = e \cdot x = e\frac{x_0}{\sqrt{2}}\left(b + b^\dagger\right) \tag{3.95}$$

and using the cavity voltage operator derived in section 3.2.4,

$$V = \sqrt{\frac{\hbar\omega_r}{2C_\ell}}\left(a + a^\dagger\right) \tag{3.96}$$

where C_ℓ is the capacitance per unit length. The dipole interaction term thus reads

$$\mathcal{H}_I = d \cdot E = e\frac{x_0}{\sqrt{2}}\sqrt{\frac{\hbar\omega_r}{2C_\ell}}\frac{1}{w}\left(b + b^\dagger\right)\left(a + a^\dagger\right) = \hbar g(b^\dagger a + b a^\dagger) \tag{3.97}$$

where the coupling strength is defined as

$$\hbar g = \frac{e x_0}{\sqrt{2}}\frac{1}{w}\sqrt{\frac{\hbar\omega_r}{2C_\ell}} = \frac{e x_0}{\sqrt{2}}\mathcal{E}_{\mathrm{rms}} \tag{3.98}$$

and the rotating-wave approximation was used. An alternative way of thinking about the

coupling is as a dielectric effect. The electron's motion within the trap is affected by and induces an electric field in the cavity. In the dispersive regime it acts like a small piece of dielectric that shifts the cavity frequency in a state-dependent way. As pointed in section 3.3, the extent of the ground state wave function in an electron on helium quantum dot is unusually large due to the small electron mass with typical values of $x_0 \sim 30-60$ nm, which leads to large dipole moments of $ex_0/\sqrt{2} \sim 1-2\times10^3$ Debye. In combination with the large zero-point electric field strengths available in conventional CPW resonators $\mathcal{E}_{\rm rms} \sim 0.2\,\mathrm{V/m}$, we find coupling strengths on the order $g/2\pi = 20$ MHz. The discussion of electron decoherence mechanisms in section 3.6 shows that motional state decoherence times are expected to exceed 15 μs. We therefore expect this system to be capable of reaching the strong-coupling cavity QED regime $g \gg \gamma, \kappa$.

3.5 Spin-Motion Coupling

In addition to the motional degree of freedom, a trapped electron on helium carries an internal spin degree of freedom, which represents a potentially highly coherent quantum resource for information storage and processing purposes. Indeed, electrons on helium have some of the longest predicted spin coherence times of any condensed matter system with lifetimes that are expected to exceed seconds [76]. Those remarkable spin properties are a direct consequence of the atomically-smooth and nuclear-spin free helium surface, which has a natural abundance of the spin 1/2 ^{3}He isotope of only $< 10^{-6}$. Unfortunately, the bare coupling of cavity photons to electron spin is many orders of magnitude weaker than for motion. It can, however, be enhanced via controlled spin-motion coupling. In this section we show how the analog of atomic spin-orbit coupling in quantum dots on helium can be used to control and measure the spin degree of freedom via the quantized lateral motion in the dot. Spin decoherence will be discussed in detail in section 3.6.8.

The coupling of the spin degree of freedom to the electromagnetic field in a transmission line resonator is in general very weak compared to the coupling of charge. To see this, consider the magnetic dipole coupling Hamiltonian for a spin in a magnetic field

$$\mathcal{H}_I = -\boldsymbol{\mu}\cdot\mathbf{B} = -\gamma\frac{\hbar}{2}\mathbf{B}\cdot\boldsymbol{\sigma} \tag{3.99}$$

where $\boldsymbol{\mu} = -\gamma\mathbf{s} = \gamma\hbar\boldsymbol{\sigma}/2$ is the magnetic moment of a spin 1/2 particle with the vector of

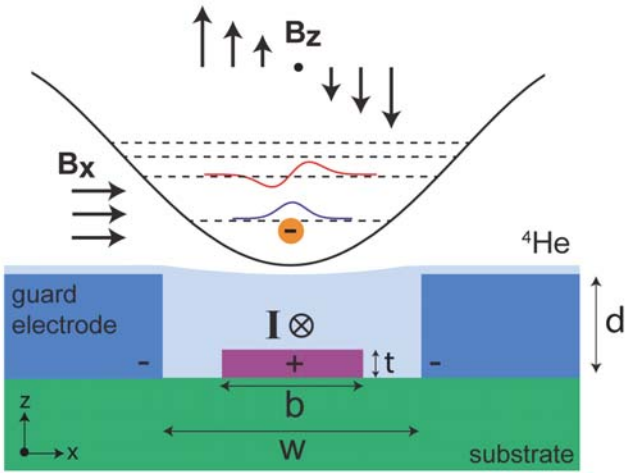

Figure 3.13.: One-dimensional single-electron trap on liquid helium with uniform and gradient magnetic fields. To define a spin quantization axis, a uniform magnetic field B_x in the x direction is applied, which sets the Larmor frequency of the trapped electron. To couple the motional and spin degrees of freedom, a current is passed through the center electrode, creating a z-field gradient within the trap.

Pauli matrices $\boldsymbol{\sigma} = (\sigma_x, \sigma_y, \sigma_z)^{\mathrm{T}}$. For a single electron on helium $\gamma = g_e\mu_B/\hbar$ with $g_e \simeq 2$ and the Bohr magneton $\mu_B = e\hbar/2m_e \simeq 9.3 \times 10^{-24}$ J/T. The interaction Hamiltonian for an electron on helium in a magnetic field along the x direction is then

$$\mathcal{H}_I = \frac{g_e}{2}\mu_B B_x \sigma_x = -\frac{\hbar\omega_L}{2}\sigma_x \tag{3.100}$$

where the Larmor frequency $\omega_L = \gamma B_x = -g_e\mu_B B_x$ was defined, which gives the precession frequency of a spin in an external field. For an electron on helium the Larmor frequency per unit field is approximately $\omega_L/2\pi B_x \approx 2.89$ MHz/G such that circuit QED range frequencies of ~ 6 GHz require fields of about 2 kG. A Jaynes-Cummings type interaction for the spin can be derived in complete analogy to the case describing the electric dipole coupling to a quantized single-mode radiation field that was presented in section 3.1. One finds for the single spin-cavity coupling strength [152]

$$g_s/\hbar = m_0\mathcal{B}_{\mathrm{rms}}/\hbar = m_0\sqrt{\frac{\hbar\mu_0\omega_r}{2\mathcal{V}_r}} \tag{3.101}$$

where m_0 is the matrix element of the transition magnetic dipole moment and the zero-point magnetic field of the cavity $\mathcal{B}_{\mathrm{rms}} = \sqrt{\mu_0\omega_r/2\hbar\mathcal{V}_r}$ was defined. For a single electron, $m_0 = 2\mu_B \sim 1.88 \times 10^{-23}$ J/T and for typical CPW cavities $\mathcal{B}_{\mathrm{rms}} \sim 2$ nT, which gives a single spin coupling strength of $g_s/2\pi \sim 60$ Hz, about a factor of 10^6 smaller than the motional coupling strength! One way of improving on this is to couple an ensemble of N electrons collectively

to the cavity, which enhances the coupling to $g_{\text{eff}} = \sqrt{N} g_s$ for independent electrons. This method has recently been used to couple solid-state spins in diamond and ruby (Al_2O_3:Cr^{3+}) to coplanar waveguide cavities and reach the strong-coupling regime $g_{\text{eff}} \gg \gamma, \kappa$ [65, 157]. Here, we propose to exploit the analog of spin-orbit interaction in quantum dots to enhance the single spin-cavity coupling. This can be achieved using an inhomogeneous gradient magnetic field in the trap region, shown schematically in Fig. 3.13. A spin quantization axis is first established via a uniform magnetic field B_x along the trap axis, which is used to tune the spin transition frequency $\omega_L = -g_e \mu_B B_x$ into resonance with the superconducting cavity. A non-uniform z-field component with a gradient $(\partial_x B_z)$ along the motional trap axis can be generated by passing a current through the center trap electrode in the y direction. Such a gradient field introduces a spin-orbit type interaction, which can be seen by expanding the z-field component to first order

$$B_z(x) \approx B_z\,|_{x=0} + x \frac{\partial B_z}{\partial x}\,|_{x=0} \tag{3.102}$$

such that the spin coupling to the z-field component becomes

$$\begin{aligned} \mathcal{H}_I &= -\boldsymbol{\mu} \cdot \mathbf{B} = -g_e \mu_B \frac{\hbar}{2} \boldsymbol{\sigma} \cdot \mathbf{B} \\ &= -g_e \mu_B s_z B_z\,|_{x=0} - g_e \mu_B s_z \cdot x \cdot \frac{\partial B_z}{\partial x}\,|_{x=0} \end{aligned} \tag{3.103}$$

Hence we get an additional term that couples the spin to the electron motion in the dot,

$$\mathcal{H}_{SI} = -2\mu_B s_z \cdot x \cdot \frac{\partial B_z}{\partial x} \tag{3.104}$$

This interaction is analogous to the spin-orbit interaction of an electron bound to a nucleus, where the electron magnetic spin moment interacts with the magnetic field generated by its motion around the nucleus. The interaction (3.104) in turn leads to an enhanced spin-cavity coupling mediated by lateral electron vibrations with corresponding strength given by

$$g_s = \mu_B x_0 \frac{\partial B_z}{\partial x} \frac{g\sqrt{2}}{\hbar \omega_p (1 - \omega_L^2/\omega_p^2)} \tag{3.105}$$

where ω_p is the motional frequency as derived in section 3.3 and g is the coupling of the electron motion to the cavity from section 3.4. Thus the spin can be coupled indirectly to the cavity electric field through the motion. The above coupling strength can be derived in

an intuitive way using a semi-classical argument in the Heisenberg picture. Modeling the trapped electron in the cavity field as a driven oscillator, $m\partial_t^2 x + \omega_p^2 x = eE$ and looking for solutions of the form $x = x_0 \cos(\omega_L t)$ that describe forced oscillations at the bare Larmor frequency yields

$$x = -\frac{e\,E}{m(\omega_L^2 - \omega_p^2)} \tag{3.106}$$

where E is the cavity electric field operator. Plugging this back into (3.104) gives a spin-mode coupling term $\propto s_z E$ and the coupling strength (3.105). Note that this type of spin-cavity coupling is proportional to the applied current, allowing the coupling strength to be tuned in situ on nanosecond time scales by changing the current passed through the trap electrode. For a 1 mA current 500 nm away from the electron we get a field gradient of $\partial B_z/\partial x \sim 8$ mG/nm. If the spin transition is far detuned from the motion $\omega_L \ll \omega_p$ this gives coupling strengths of $g_s \sim 8$ kHz. However, for moderate detunings $\omega_x - \omega_L \sim 30$ MHz the coupling can be made large $g_s \sim 0.5$ MHz, potentially allowing the single spin-cavity system to reach the strong coupling regime. Note that the current also leads to a second order variation in the x component of $\mathbf{B}$ with an interaction term

$$\mathcal{H}_{SI}^{(2)} = -\mu_B s_x \cdot x^2 \cdot \frac{\partial^2 B_x}{\partial x^2} \tag{3.107}$$

which can potentially be used for side-band based cooling schemes [64]. If the homogeneous field is applied along the y direction, this term allows simultaneously changing spin and motional states by applying an RF drive at the sum and difference frequencies $\omega_\pm = \omega_x \pm \omega_L$. An alternative method for spin-cavity coupling enhancement in semiconductor double quantum dots, based on Raman transitions and electron-spin resonance pulses that simultaneously flip charge and spin, was pointed out in [173].

3.6 Decoherence Mechanisms

The discussion in the preceding sections has shown that electrons on helium can be used to build quantum dots in the single electron regime which can be coupled via dipole interaction to superconducting cavities, realizing a cavity QED system with sizeable coupling strengths for both quantized lateral motion $g \simeq 20$ MHz and spin $g_s \simeq 1$ MHz. Reaching the strong coupling regime of cavity QED $g \gg \gamma, \kappa$, where the electron can coherently exchange energy with the cavity, requires sufficiently long lifetimes of the electron states. Moreover, in the

context of quantum information processing long coherence times are of paramount importance for the implementation of quantum error correction codes and quantum memories [22]. The two major sources of decoherence for electrons on helium are electrical fluctuations in the bias leads and elementary excitations of the superfluid (ripplons and phonons).

In this section we discuss the different possible decoherence channels for electron motional and spin states. In section 3.6.1, we start off with a brief primer on the basic concepts of quantum coherence that will be used throughout this part of the thesis. Radiative decay from the excited motional state via spontaneous emission, which can occur into free space, through the cavity (Purcell effect) and through the trap bias electrode, is discussed in section 3.6.2. Decay through coupling to elementary superfluid excitations, specifically capillary surface waves (ripplons) and bulk phonons, is the subject of section 3.6.3. Dephasing due to ripplon scattering (section 3.6.5) and trap bias fluctuations (section 3.6.4) is discussed afterwards while the effects of classical helium level fluctuations are considered in section 3.6.6. A summary of the different motional decoherence rates is given in section 3.6.7. Finally, decoherence of the spin degree of freedom is discussed in section 3.6.8, which inherits motional decoherence in the presence of the spin-motion coupling presented in section 3.5. We will see that inelastic phonon scattering emerges as the limiting mechanism for electrons on helium motional and spin coherence, giving conservative coherence time estimates of 15 μs for motion and 0.5 ms for spin. To keep things compact, we will focus here on the main results and a discussion of the physical mechanisms. Detailed derivations and calculations can be found in the supplementary materials of Ref. [64].

3.6.1 Decoherence Primer

In the context of quantum information processing, decoherence refers to the fact that a quantum-mechanical two level system or qubit can lose its information content to the environment. There are two qualitatively different forms of decoherence in open quantum systems, *energy relaxation* and *dephasing*. Although they can sometimes have identical sources, they cause changes in different quantum-mechanical properties of a qubit. Here, we follow the Bloch-Redfield approach [174] which describes the decoherence of a two-level system in terms of the two rates Γ_1 (energy relaxation) and Γ_2 (dephasing). We adopt the following general notation: $\Gamma_1^{(\alpha)}$ denotes energy relaxation rates with the superscript indicating the specific decay mechanism while $\Gamma_2^{(\alpha)}$ denotes dephasing rates.

Energy Relaxation

Energy relaxation and heating are processes that lead to incoherent changes of the state of a qubit. The interaction with an environmental noise bath causes the qubit to flip randomly between its two states. The time T_1 is the characteristic time over which a qubit is excited and de-excited by the environment. It is defined as the inverse of the sum of the corresponding excitation and de-excitation rates [175]

$$T_1 = \frac{1}{\Gamma_\uparrow + \Gamma_\downarrow} \,. \tag{3.108}$$

A powerful and universal approach for describing coupling and leakage to the environment is the Kraus or super-operator formalism [22] . In this representation, we can describe the time evolution of a qubit without having to explicitly consider detailed properties of the environment. Everything we need to know is wrapped up in a superoperator that acts on the density operator of the qubit. In this way, the states of the environment itself are traced out and only the perturbed time evolution of the qubit remains such that all we need to consider is the interaction Hamiltonian of qubit and environment. In general, energy relaxation is treated as a perturbation that couples a qubit operator $\boldsymbol{\xi}$ to an environment or noise bath operator $\mathbf{M}$ through $\mathcal{H}_I = \boldsymbol{\xi} \cdot \mathbf{M}$. Here, $\boldsymbol{\xi}$ represents the specific variable of the qubit that is affected. The qubit operator $\boldsymbol{\xi}$ either contains σ_z or $\sigma_\perp = \sigma_x + \sigma_y$ components, depending on the type of decoherence that is caused by a given noise source. Energy relaxation (Γ_1) refers to the decay of the diagonal z component of the qubit density matrix while dephasing (Γ_2) describes the decay of the off-diagonal part [22]. The noise bath on the other hand is characterized by a spectral noise density $S_M(\pm\omega)$ which depends on temperature and frequency.

Dephasing

Dephasing refers to processes that cause a qubit to accumulate a random phase rather than to change its quantum state directly. Although dephasing of overall phases is irrelevant, this form of decoherence more importantly changes the *relative* phase in superposition states. T_ϕ is the characteristic time scale over which the qubit accumulates a random phase shift of π. The phase is determined by the frequency and thus the root of dephasing lies in fluctuations of the qubit transition frequency. The overall decoherence rate generally consists of three

contributions

$$\Gamma_2 = \frac{\Gamma_1}{2} + \Gamma_\phi + \Gamma_\phi^* \tag{3.109}$$

All mechanisms of energy relaxation also lead to dephasing at rate $\Gamma_1/2$ since dephasing describes the decay of the amplitude of a quantum state. This in turn also sets a dissipation-imposed upper limit for the overall decoherence time of $T_2^* = 2T_1$. A qubit that satisfies $T_2^* \simeq 2T_1$ is said to be *homogeneously broadened*. The second term in (3.109) is due to fluctuations that occur during one decay lifetime of the qubit while the third contribution describes fluctuations on longer time scales, which is sometimes referred to as *inhomogeneous broadening*.

3.6.2 Radiative Decay and Spontaneous Emission

A trapped electron in an excited motional state can decay radiatively via spontaneous emission into free space (continuous mode spectrum), into a cavity mode (referred to as the Purcell effect) as well as through the trap bias electrode. The different radiative decay channels are discussed below. Most of the calculations are based on Fermi's golden rule with an appropriate matrix element for the specific process under consideration. As a reminder, Fermi's golden rule[8] gives the transition rate (transition probability per unit time) for a system in an initial state $|\Phi_i\rangle$ going to a final state $|\Phi_f\rangle$ subject to a perturbation $\mathcal{H}_I$ in first order perturbation theory:

$$\Gamma_{i\to f} = \frac{2\pi}{\hbar}\rho(\varepsilon_f)|\langle\Phi_f|\mathcal{H}_I|\Phi_i\rangle|^2 \tag{3.110}$$

where $\rho(\varepsilon_f)$ is the density of final states. For a discrete set of final states, $\rho(\varepsilon_f)$ is simply a series of Dirac delta functions.

Free Space

Radiative energy loss into the electromagnetic continuum of free space represents a very small effect, both because the size of the trapped electron wave function is small and because the electromagnetic environment can be carefully controlled in circuit QED systems. The rate of photon emission via electric-dipole radiation into the vacuum can be estimated using the continuum version of Fermi's golden rule with the dipole interaction $\mathcal{H}_I = \mathbf{d}\cdot\mathbf{E}$ and the density of states of the vacuum electromagnetic field $\rho(\omega) = L^3w^2/\pi^2c^3$ with mode volume

[8] Note that Fermi's golden rule was first derived by Wentzel [176].

$L \sim \lambda$:

$$\Gamma_1^{(v)} = \frac{2}{3}\frac{e^2}{\hbar c}\left(\frac{2\pi x_0}{\lambda}\right)^2 \omega_p \sim \left(\frac{x_0}{\lambda}\right)^2 \tag{3.111}$$

where ω_p is the transition frequency between the ground and first excited motional state and $\lambda = 2\pi c/\omega_p$ is the corresponding wavelength. As shown in section 3.3, we have for a trapped electron on helium at 5 GHz $x_0 \sim 6 \times 10^{-8}$ m and $\lambda \sim 6 \times 10^{-2}$ m such that $\Gamma_1^{(v)}$ is negligibly small. If this were the only decay mechanism, the excited motional state would be expected to last for more than 100s.

Purcell Effect and Decay into Cavity Modes

The electron motional state can also decay via spontaneous emission into one of the cavity modes, which can be strongly enhanced or suppressed depending on the detuning of cavity and electron motion. This kind of enhanced spontaneous emission was first described by Purcell in the context of spin magnetic resonance [177] and has recently been studied in detail in circuit QED systems [178]. The reason for the enhanced decay rate close to resonance lies in the much larger mode density of the cavity field compared to free space. For a simple two-level system coupled to a single mode radiation field in a cavity of frequency ω_r, the spontaneous emission rate for dispersive coupling $g \gg |\omega_p - \omega_r|$ is given by [44]

$$\Gamma_1^{(\mathrm{cav})} = \frac{g^2\kappa}{(\omega_p - \omega_r)^2} \tag{3.112}$$

where $\kappa = \omega_r/Q$ is the cavity decay rate (i.e. the average photon loss rate). Assuming a detuning of $\Delta \sim 500$ MHz, a coupling strength of $g/2\pi \sim 20$ MHz and a quality factor $Q \sim 20000$ this yields $\Gamma_1^{(v)} \sim 1.5 \times 10^4$ s^{-1}. For the case of resonant coupling and a low Q cavity $\kappa \gg g, |\omega_p - \omega_r|$, the decay rate is $\Gamma_1^{(\mathrm{cav})} = g^2/\kappa$, while in the limit of strong coupling $g \gg \kappa$ on resonance $\Gamma_1^{(\mathrm{cav})} = \kappa/2$. As shown in Ref. [178], spontaneous emission rates can be strongly influenced by far off-resonant modes of the cavity. The effect of higher harmonics of the cavity on motional decay rates could be captured in a way analogous to the decay of superconducting qubits into higher modes, e.g. by using a multi-mode Jaynes-Cummings Hamiltonian or possibly by mapping to a semiclassical circuit model [178].

Bias Electrode

In addition to spontaneous emission into cavity modes and the free space continuum, the electron can also decay via its capacitive coupling to the trap bias leads. The corresponding decay rate can be found by considering the effect of Johnson-Nyquist noise of the bias electrode on the electron motion. This decay channel is suppressed by a parity-selection rule for a perfectly symmetric trap, but for slight deviations from symmetry this turns out to be a dominant radiative decay channel and hence we will discuss it in some detail here. The decay rate can be calculated using Fermi's golden rule. As pointed out in section 3.6.1, relaxation can be thought of as a perturbation $\mathcal{H}_I = \boldsymbol{\xi} \cdot \mathbf{M}$ coupling a given electron operator $\boldsymbol{\xi}$ to a bath operator $\mathbf{M}$ where the bath noise is characterized by a spectral noise density $S_M(\mp\omega)$ [175]. In our case, the bias lead represents the bath and voltage noise on the bias leads represents excitations of the bath. The decay rate from excited to ground state due to coupling to such a noise bath can be shown to be [175]

$$\Gamma_{e\to g} = \frac{1}{\hbar^2} |\langle g|\xi|e\rangle|^2 S_M(\mp\omega_a) \tag{3.113}$$

where ω_a is the transition frequency. The corresponding relaxation time is then $T_1 = 1/(\Gamma_{e\to g} + \Gamma_{g\to e})$. From (3.113) we see immediately that a parity-conserving bath coupling operator gives zero decay rate. To get the general decay rate for the bias leads, we need the spectral density of the noise and the correct electron operator $\boldsymbol{\xi}$ through which the trapped electron couples to the bias lead. Assuming a bosonic bath (i.e. 1D blackbody radiation) the voltage noise spectral density is given by the Johnson-Nyquist formula [175]

$$S_{V_e}(\omega) = \frac{2\hbar\omega \mathrm{Re}[Z(\omega)]}{1 - e^{-\hbar\omega/k_B T}} \approx 2\hbar\omega \mathrm{Re}[Z(\omega)] \tag{3.114}$$

where $Z(\omega)$ is the impedance of the bias leads and the last expression is the low temperature approximation for the Bose-Einstein distribution. The electron couples to the bias electrode via dipole coupling $\boldsymbol{\xi} = \mathbf{d} \cdot \mathbf{E} = -exE(x)$ where $E(x) = -\nabla V(x)$ and $V(x)$ is the potential of the electrode. For a perfectly symmetric potential, $E(x)$ is an odd function of x and so is the dipole operator. From section 3.3, we know that the ground and first excited state have different parity such that $\langle g|\boldsymbol{\xi}|e\rangle = 0$ and there would be no decay. However, any displacement from the trap bias null, e.g. due to a slight asymmetry in the potential or other stray or intentional fields, will open up a channel for relaxation. Using $eE_x = m_e\omega_p^2\Delta x =$

$\hbar\omega_p \Delta x/x_0^2$ and expanding the field about small deviations Δx from the trap center we find

$$\Gamma_1^{(\mathrm{el})} = \frac{\mathrm{Re}[Z(\omega_p)]}{\hbar/e^2}\left(\frac{\hbar\omega_p}{eV}\right)^2 \omega_p \tag{3.115}$$

where the approximation $\partial E_x/\partial V = E_x/V$ was made. For a bath impedance of $\mathrm{Re}[Z(\omega_p)] \approx 50\,\Omega$ and assuming a conservative deviation of the size of the electron wave function $\Delta x \approx x_0$ this yields $\Gamma_1^{(\mathrm{el})} \approx 1.6 \times 10^3\ \mathrm{s}^{-1}$. Note that the decay rate can be further reduced by engineering the impedance of the bath $Z(\omega)$ around the electron oscillation frequency using a resonant structure.

3.6.3 Decay via Superfluid Excitations

In addition to radiative decay of the motional states into free space, the cavity modes and the trap electrode, the electron can lose coherence to elementary excitations in the superfluid, that is, capillary surface waves (ripplons) introduced in section 2.3.5 and phonons in the bulk superfluid film. As shown below, decay into phonons represents the dominant decay mechanism, in part because of the higher dimensionality of the available phase space for momentum conservation. The superfluid excitations also cause dephasing of the electron wave function, which will be discussed in section 3.6.5. The coupling of electrons to superfluid excitations is mathematically complex, leading to lengthy and quite non-trivial calculations. To keep things compact, we limit ourselves here to a discussion of the underlying physics and the main results. Coupling of electron motion to superfluid excitations is discussed in mathematical detail in Ref. [79].

One-Ripplon Decay

Coupling to ripplons is in general expected to be small because the electron is levitated a distance $a_B \sim 8$ nm above the surface, which greatly exceeds the amplitude of the capillary surface waves. Decay via single ripplon interaction is exponentially suppressed due to the large mismatch of the size of the electron wave function $\sim x_0$ and the ripplon wavelength at the same energy. The characteristic speed of the electron $x_0 \cdot \omega_p$ is significantly larger than the speed of sound in helium $v_s \approx 2.4 \times 10^2$ m/s and the characteristic group velocity of the ripplons. Since ripplons are slow excitations, it is impossible to conserve momentum in the interaction of an electron with a single ripplon. The momentum mismatch is fundamentally a consequence of confinement effects on the electron. The relevant matrix elements decay

exponentially in the product $q \cdot x_0$ where q is the ripplon wave vector and $x_0 = \sqrt{\hbar/m\omega_p}$ the oscillator length scale, hence suppressing decay via single ripplon emission. The single-ripplon decay rate is determined by the matrix elements $\langle 0,0|\exp(i\mathbf{qr})V_\mathbf{q}|1,0\rangle$ where $V_\mathbf{q}$ is the coupling operator between an electron and a ripplon with wave vector $\mathbf{q} = (q_x, q_y)$ (see Ref. [79]) and $|n_x, n_y\rangle$ denotes the two-dimensional in-plane motional state. Evaluating those matrix elements to find the decay rates yields factors of the form [64]

$$\left|\langle 1,0|e^{i\mathbf{qr}}|0,0\rangle\right|^2 = \frac{1}{2}(q_x x_0)^2 \exp\left[-\frac{1}{2}(q_x^2 x_0^2 + q_y^2 y_0^2)\right] \tag{3.116}$$

which are exponentially small for small products of in-plane localization length and ripplon wavenumber $q_x \cdot x_0$.

Two-Ripplon Decay

Due to the exponential suppression of one-ripplon processes, decay into ripplons is dominated by second-order processes in which two ripplons of nearly opposite momentum simultaneously interact with the trapped electron, each with approximately half the electron energy $\sim \hbar\omega_p$. The corresponding decay rate can be estimated from a Fermi golden rule argument using the ripplon surface displacement operator $\boldsymbol{\xi}_\mathbf{q}(\mathbf{r})$ for a ripplon of wave vector $\mathbf{q}$ introduced in eq. (2.47):

$$\Gamma_1^{(2r)} = \frac{2\pi}{\hbar}\sum_{\mathbf{q}_1,\mathbf{q}_2}\left|\langle 0,0|\boldsymbol{\xi}_{\mathbf{q}_1}\boldsymbol{\xi}_{\mathbf{q}_2}e^{i(\mathbf{q}_1+\mathbf{q}_2)\mathbf{r}}V_{\mathbf{q}_1,\mathbf{q}_2}|1,0\rangle\right|^2 \delta(\hbar\omega - \hbar\omega_{\mathbf{q}_1} - \hbar\omega_{\mathbf{q}_2})(\overline{n}_{\mathbf{q}_1} + \overline{n}_{\mathbf{q}_2} + 1) \tag{3.117}$$

where $|n_x, n_y\rangle$ denote the in-plane motional states with quantum numbers n_x, n_y and $\overline{n}_\mathbf{q} = (e^{\hbar\omega_q/k_BT} - 1)^{-1}$ is the average ripplon population. The delta function describes energy conservation in the scattering process and the matrix element $V_{\mathbf{q}_1,\mathbf{q}_2}$ consists of a kinetic and a polarization term. It is in general dominated by the kinetic term such that [79]

$$V_{\mathbf{q}_1,\mathbf{q}_2} \approx -R\mathbf{q}_1\mathbf{q}_2 = -\langle 1|p_z^2/2m|1\rangle_z\,\mathbf{q}_1\mathbf{q}_2 = -\frac{\hbar^2}{2ma_0^2}\mathbf{q}_1\mathbf{q}_2 \tag{3.118}$$

where $|1\rangle_z$ is the vertical motional ground state. Evaluating the above expression yields for the two-ripplon energy relaxation rate $\Gamma_1^{(2r)} \approx 450\,\mathrm{s}^{-1}$ at frequency $\omega_p/2\pi = 5$ GHz and zero-point motion $x_0 = 4.8$ nm. This rate is quite small which is a direct consequence of the fact that the allowed phase volume for decay is limited by the condition on the total ripplon momentum.

Decay into Bulk Phonons

Bulk phonons in the superfluid represent the dominant contribution to decoherence. The coupling to phonons is in direct analogy to the piezoelectric coupling for quantum dots in semiconductors. An electron above the helium surface polarizes the liquid. Phonons in turn modulate the density of the liquid and thus change the polarization, which in turn affects the effective potential the electron sees. However, since liquid helium is almost transparent, the polarization and hence the piezoelectric coupling is much weaker than in semiconductors. In semiconductors, the typical piezoelectric coupling is $e_{\mathrm{pz}} \sim 10^{14}\ e/\mathrm{cm}^2$ [179] while the analog in superfluid helium is $\sim e(\varepsilon_{\mathrm{He}}-1)/4\pi a_B^2 \sim 10^{10}\ e/\mathrm{cm}^2$, which is much smaller due to the large effective Bohr radius. There are two mechanisms through which the electron can decay via phonon emission. In the first (denoted by $\Gamma_1^{(\mathrm{ph1})}$ below), the coupling is mediated by modulation of the dielectric constant along with the density wave corresponding to the phonon, which changes the effective image potential the electron sees. The second mechanism ($\Gamma_1^{(\mathrm{ph2})}$ below) is a form of direct inelastic phonon scattering, where the electron couples to the surface displacement in analogy to the ripplon case. The phonon-induced surface displacement operator is similar to the one for ripplons [79]. In this case, however, single phonon decay is allowed because the momentum is conserved in two dimensions while the excess energy is dumped into the normal phonon component such that the electron decay launches most of the energy normal to the surface. The phonon dispersion relation in liquid helium is linear

$$\omega_Q = v_s \cdot Q \tag{3.119}$$

where Q is the phonon wave vector and $v_s = 2.4 \times 10^4$ cm/s is the speed of sound in helium. For an electron plasma frequency of $\omega_p/2\pi = 5$ GHz, a resonant phonon has a wave vector component orthogonal to the surface of $Q_z = \omega_p/v_s \approx 1.3 \times 10^6\ \mathrm{cm}^{-1}$ while the in-plane electron wave vector component at that frequency is $k_x = \sqrt{m\omega_p/\hbar} \approx 1.6 \times 10^5\ \mathrm{cm}^{-1}$ such that phonons involved in electron decay (inelastic scattering) propagate almost orthogonal to the surface. The phonon-electron coupling Hamiltonian has a form similar to that for ripplon coupling. Evaluating the corresponding matrix element in Fermi's golden rule gives after lengthy calculation a decay rate of $\Gamma_1^{(\mathrm{ph1})} \sim 2.7 \times 10^4\ \mathrm{s}^{-1}$ for dielectric constant modulation decay, assuming a phonon wave number $Q_z = 1.3 \times 10^8\ \mathrm{m}^{-1}$. In section 3.6.7 we will see that this is the dominant decay channel for electron motion in the 1 - 20 GHz band. Note that in the above estimates we assume a thick bulk film of superfluid helium and no geometric

confinement effects on the phonon spectrum and dispersion relation. As a possible extension, one could consider cases where the phonon wave vectors are restricted by imposing boundary conditions through choice of geometry.

The second contribution to the decay rate arises from the surface displacement caused by propagating phonons, which is very much like the decay due to surface displacements caused by ripplons. A crucial difference, however, is that single-phonon decay is allowed since momentum can be conserved in 2D, as opposed to single-ripplon decay which is exponentially suppressed by momentum conservation in 1D. Evaluation of the matrix elements gives a decay rate of $\Gamma_1^{(\mathrm{ph2})} \sim 1.8 \times 10^3\ \mathrm{s}^{-1}$ at $\omega_p/2\pi = 5$ GHz assuming equal size in-plane zero-point motions $x_0 \sim y_0 \sim 4.8$ nm, which constitutes a conservative estimate for our high-aspect ratio traps.

3.6.4 Dephasing due to Voltage Fluctuations

The depth of the potential and thus the electron motional transition frequencies depend on the trap bias voltage. Low frequency noise on the bias electrode will result in electron phase noise as fluctuations in the trap bias voltage V_0 deform the effective trapping potential on time scales short compared to the experiment time, giving a Γ_ϕ contribution in (3.109). Bias fluctuations can result from slow drifts in the voltage source, thermal Johnson voltage noise or potentially local charge noise in the bias leads. Note that fluctuations that are slow compared to the experiment time can be compensated for and are in general not a limiting factor. In section 3.3, we saw that the transition frequency scales like $\omega_p \propto \sqrt{V_0}$ and small fluctuations in V_0 cause frequency shifts of $\Delta\omega_p/\omega_p = -\Delta V_0/2V_0$. For high-precision voltage sources such as the ones used in our experiments (see chapter 4), long term drifts are typically $\Delta V_0/V_0 \sim 10^{-6}$ per hour, corresponding to $\Delta\omega_p \approx 8 \times 10^3\ \mathrm{s}^{-1}$ or 8 MHz at 5 GHz. Since this drift happens over time scales of hours it can be easily compensated for by measuring the transition frequency and readjusting the voltage if necessary. For thermal Johnson voltage noise the noise spectral density is given by $S_{V_0}(\omega) = 4k_BT\mathrm{Re}[Z(\omega)]$ [9]. The corresponding dephasing rate can then be expressed as [180]

$$\Gamma_\phi^{(\mathrm{el1})} = \left(\frac{\partial\omega_p}{\partial V_0}\right)^2 \frac{S_{V_0}(\omega)}{2} = \frac{\omega_p^2 k_B T \mathrm{Re}[Z(\omega)]}{4V_0^2} \tag{3.120}$$

[9] We denote the mean-squared amplitude of voltage noise at frequency ω per 1 Hz bandwidth by S_V and the root-mean-squared quantity by $\mathcal{S}_V$. The magnitude of the voltage noise, described by the mean-squared value $\langle V^2(t)\rangle$, can be obtained from $S_V(\omega)$ through the Wiener-Kinchin theorem. For a good discussion of current and voltage noise in the context of decoherence, the interested reader is referred to Ref. [175].

Assuming a typical voltage bias of $V_0 \sim 10$ mV, a corresponding motional frequency of $\omega_p/2\pi = 5$ GHz and an environment impedance of $Z = 50\,\Omega$ at 50 mK one finds $\Gamma_\phi^{(\mathrm{el1})} \sim 90$ s^{-1}. Thermal Johnson noise should therefore not be a limiting source of dephasing.

The dominant source of dephasing due to fluctuations in voltage is expected to be local $1/f$ charge noise. This type of noise is commonly observed in devices with floating electrodes or islands (e.g. for Josephson junction-based devices) and is believed to arise from mobile charges in substrates. In the proposed device geometries, there are no such floating electrodes or Josephson junctions, but since the origin of $1/f$ charge noise is not fully understood it may also arise in our devices in some form. The corresponding noise spectrum does not lead to a simple expression for the dephasing rate [180], but a quick back-of-the-envelope calculation shows that $1/f$ charge noise should indeed dominate thermal Johnson noise. The magnitude of charge noise in typical Josephson junctions is on the order of $S_q \sim (10^{-4}\mathrm{e})^2/\mathrm{Hz}$. Assuming a capacitance of $C_{\mathrm{eff}} = 1$ fF, this translates into a voltage noise of $S_V = S_q/C_{\mathrm{eff}}^2 \sim (1.6 \times 10^{-8})^2$ V^2/Hz or about $\mathcal{S}_V \sim 10$ $\mathrm{nV}/\sqrt{\mathrm{Hz}}$ at 1 Hz. On the other hand, for thermal Johnson noise at 50 mK and 50 Ω we have $\mathcal{S}_V \sim 6 \times 10^{-3}$ $\mathrm{nV}/\sqrt{\mathrm{Hz}}$, several orders of magnitude lower. More formally, assuming a $1/f$ noise-spectral density $S_{V_e}^{1/f}(f) = S_{V_e}(1\mathrm{Hz})/f$, the expected diffusion of phase over time t as a result of charge noise can be estimated as [180]

$$\begin{aligned} \langle[\phi(t) - \phi(0)]^2\rangle &\sim \left(\frac{\partial \omega_p}{\partial V_e}\right)^2 S_{V_e}(1\mathrm{Hz}) \ln(0.4/f_m t) t^2 \\ &= \frac{(\omega_p t)^2}{4V_e^2} S_{V_e}(1\mathrm{Hz}) \ln(0.4/f_m t) \end{aligned} \tag{3.121}$$

where f_m^{-1} is the total averaging time, i.e. f_m corresponds to the frequency of the entire measurement, which gives a low-frequency cutoff (the logarithmic term results from an integral over frequency with f_m as the lower bound and $\omega_p/2\pi$ as the upper bound). The dephasing time can then be estimated as the time it takes for $\langle[\phi(t_\pi - \phi(0)]^2\rangle = \pi$ such that the effective dephasing rate due to $1/f$ charge noise is $\Gamma_\phi^{(\mathrm{el2})} = t_\pi^{-1}$. To arrive at an order of magnitude estimate for the dephasing rate we again assume $S_{V_e} = S_q/C_{\mathrm{eff}}$ with a typical charge noise value of $S_q(1\mathrm{Hz}) \approx (10^{-4}\mathrm{e})^2/\sqrt{\mathrm{Hz}}$. For a conservatively low estimate of the capacitance of $C_{\mathrm{eff}} = 1$ fF, this gives a dephasing rate of $\Gamma_\phi^{(\mathrm{el2})} \sim 8 \times 10^3$ s^{-1}. In the device designs and geometries considered for this thesis, the capacitance to ground of the leads is in fact orders of magnitude larger than this value, and hence charge fluctuations that cause changes in the effective potential are not expected to be a dominant dephasing mechanism either way.

3.6.5 Ripplon-Induced Dephasing

In addition to decay, coupling to elementary excitations of the superfluid can lead to fluctuations in the effective potential the electron sees, therefore changing the motional frequency and leading to dephasing. The most important dephasing contribution comes from thermally-excited two-ripplon coupling. Thermal fluctuations in the helium lead to random modulation of the energy difference between motional states, which can be described as quasi-elastic scattering of thermal excitations off an electron. This scattering depends on the electron state and therefore randomizes the phase difference between the wave functions of the states, but without causing any transitions. As discussed in section 2.3.5, ripplons are in general rather soft excitations with a large density of states at low energies such that there are excitations present even for very low temperatures. At $T = 100$ mK, the typical wave number of a thermal ripplon ($\hbar\omega_{q_r} = k_B T$) is $q_T \approx 4.1 \times 10^6$ cm^{-1} and for $T = 50$ mK $q_T \approx 2.5 \times 10^6$ cm^{-1}. The two-ripplon coupling Hamiltonian can be written in the basis of the in-plane motional states $|n_x, n_y\rangle$, where n_i is the motional quantum number for direction i, and in terms of the ripplon ladder operators,

$$\mathcal{H}_I^{(2r)} = \sum_{j=1,2} \sum_{\mathbf{q_1},\mathbf{q_1}} v_j(\mathbf{q_1},\mathbf{q_2}) b^\dagger_{\mathbf{q_1}} b_{\mathbf{q_2}} |j,0\rangle \langle j,0| \tag{3.122}$$

The terms in the sum over the ripplon wave vectors $\mathbf{q_1}, \mathbf{q_2}$ describe scattering of a ripplon with wave vector $\mathbf{q_2}$ into a ripplon with wave vector $\mathbf{q_1}$, the excess momentum being transferred to the electron and no transitions occurring between electron motional states. The matrix elements $v_j(\mathbf{q_1},\mathbf{q_2})$ are given by

$$v_j(\mathbf{q_1},\mathbf{q_2}) = \frac{\hbar}{\rho}\sqrt{\frac{\mathbf{q_1 q_2}}{\omega_{\mathbf{q_1}},\omega_{\mathbf{q_2}}}} V_{\mathbf{q_1},-\mathbf{q_2}} \langle j,0|e^{i(\mathbf{q_1}-\mathbf{q_2})\mathbf{r}}|j,0\rangle \tag{3.123}$$

where $V_{\mathbf{q_1},-\mathbf{q_2}}$ is the matrix element of the interaction Hamiltonian of ripplons and out-of-plane ground state wave functions $|1\rangle_z$. $V_{\mathbf{q_1},-\mathbf{q_2}}$, already encountered in section 3.6.3, consists of a kinematic and a polarization part [79]. The polarization part describes the change of the polarization energy due to changes in surface curvature caused by a ripplon. The kinematic term dominates for $q_T r_B \gg 1$, which is the case for higher temperatures $T \gtrsim 100$ mK. However, for lower temperatures the polarization term can become comparable because the characteristic thermal ripplon wave number q_T decreases rapidly with temperature. The

dephasing rate caused by the interaction (3.122) can be estimated as [64]

$$\Gamma_{\phi}^{(2r)} \approx \frac{\sqrt{2\pi}}{192}\frac{\rho R^2}{\sigma^3 x_0}\left(\frac{k_B T}{\hbar}\right)^3 \tag{3.124}$$

where $R =_z \langle 1|p_z^2/2m|1\rangle_z = \hbar^2/2ma_0^2$ is the vertical kinetic matrix element and ρ and σ are the mass density and surface tension of liquid helium as usual. At $T = 100$ mK this gives $\Gamma_{\phi}^{(2r)} \sim 1.4 \times 10^4$ s^{-1} and at $T = 50$ mK we have $\Gamma_{\phi}^{(2r)} \sim 1.7 \times 10^3$ s^{-1}. Hence, despite the large density of states of thermal ripplon excitations at low temperatures, the dephasing rates remain small because the coupling is weak. As opposed to ripplons, phonons are not a significant source of dephasing at low temperatures since their density of states is much smaller at $T \sim 100$ mK.

3.6.6 Classical Helium Level Fluctuations

So far we have only considered quantum mechanical variations in the height of the superfluid surface (ripplons). Classical fluctuations in the liquid level can also contribute to dephasing since any change in thickness of the helium above the electrostatic gates will change the effective potential seen by the electron and hence the transition frequencies. Such slow fluctuations in the liquid helium level are caused by either fluctuations in temperature or mechanical vibrations of the chip. Because this type of fluctuation is slow, it is unlikely to cause dephasing during the decay lifetime of the electron and should be susceptible to spin-echo techniques. It can, however, lead to slow drifts in the transition frequency, making it necessary to readjust the bias parameters between experiments. In section 3.3 we saw that the trap plasma frequency depends parametrically and exponentially on the helium film thickness d through the effective voltage $V_t(d) = V_0 \exp(-2\pi d/w)$ where w is the geometric trap width. This corresponds to a film thickness sensitivity of $\partial\omega_p/\partial d \approx 10$ MHz/nm. However, the high-aspect ratio trap designs discussed in section 3.3 represent micro-channels (see section 2.3.4) that support the formation of a capillary action-stabilized van-der-Waals film. The channels are filled from a reservoir located well below the chip. The distance of the bulk level in the reservoir from the channel top H sets the radius of curvature of the film in the trap channel $R_c = \sigma/\rho g H$, see section 2.3.4 and the experimental results presented in chapter 5. This drastically reduces the sensitivity of the transition frequency. For $H = 5$ mm we have $R_c \approx 53\,\mu$m and the trap is well filled with sensitivity reduced by $\partial_H \partial R_c \partial_{R_c} d = w/H \approx 10^{-4}$.

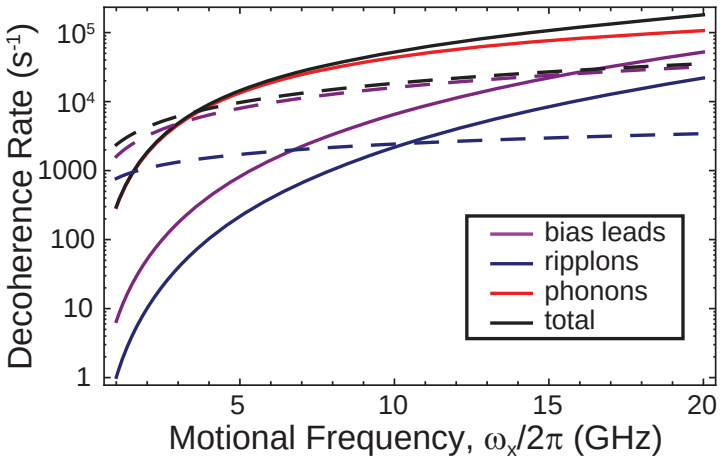

Figure 3.14.: Summary of electron motional decoherence rates as a function of trap frequency at $T = 50$ mK. Solid lines are energy relaxation rates $\Gamma_1/2$ and dashed lines are dephasing rates Γ_ϕ: Decoherence due to voltage and charge fluctuations in the bias leads (magenta), elastic and inelastic ripplon scattering (blue) and phonon scattering (red). Note that single ripplon decay rates and phonon dephasing rates are not shown as their rates are negligibly small $< 1\ \mathrm{s}^{-1}$.

3.6.7 Summary of Motional Decoherence Rates

The decoherence rates due to the mechanisms described in sections 3.6.2 - 3.6.5 are summarized in Fig. 3.14 and plotted as functions of electron motional frequency $\omega_x/2\pi$ at $T = 50$ mK, with dashed lines depicting dephasing rates Γ_ϕ and solid lines energy relaxation rates $\Gamma_1/2$. The decoherence rates generally decrease quite strongly with frequency. The dominant mechanism of energy relaxation over the 1 - 20 GHz band is decay via inelastic phonon scattering, in particular due to coupling mediated by the dielectric modulation that is caused by the phonon density waves, see section 3.6.3. At 5 GHz we estimate $\Gamma_1^{(\mathrm{ph})} \sim 3 \times 10^4\ \mathrm{s}^{-1}$, corresponding to an energy relaxation time of $T_1 = 2/\Gamma_1 \sim 15\,\mu$s. The dominant source of dephasing over the frequency band 1 - 15 GHz are electrical fluctuations in the bias leads (section 3.6.4), specifically due to 1/f charge fluctuations in the leads. Under the conservative assumptions of anomalously small capacitive screening and typical 1/f charge noise spectral densities, we estimate $\Gamma_\phi \sim 8 \times 10^3\ \mathrm{s}^{-1}$ at 5 GHz (see section 3.6.4). For more realistic capacitive screening of charge fluctuations it is possible that the dominant dephasing comes from two-ripplon scattering (section 3.6.5). Note that single ripplon energy relaxation (section 3.6.3) and phonon dephasing rates are $< 1\ \mathrm{s}^{-1}$ and hence not shown in Fig. 3.14. In summary, the overall lifetime of the motional state appears to be limited by phonon emission, coupled via modulation of the dielectric constant.

3.6.8 Spin Decoherence

The spin of a completely free electron has no internal decay mechanisms and would hence live forever. For an isolated electron on liquid helium, the situation gets somewhat close to free-electron case as the physical environment is very clean and well-controlled and the electron interacts only electrostatically with the nuclear spin-free liquid. Many of the dominant spin decoherence mechanisms present in semiconductor heterostructures (GaAs or Si/SiGe substrates), such as spin-orbit interaction, coupling to nuclear spins in the substrate or strong piezo-electric coupling, are either strongly reduced or absent entirely for electrons at the interface of vacuum and superfluid helium. This has lead to exceptionally long predicted spin coherence times in the absence of enhanced spin-orbit interaction, expected to exceed $T_2 > 100$ s [76]. In particular, the motion of two-dimensional electrons in semiconductor heterojunctions comes with an associated effective magnetic field as a result of spin-orbit interaction, which makes it difficult to preserve spin coherence during electron transport [181]. This mechanism is many orders of magnitude weaker for electrons on helium due to their large distance from the liquid surface [76]. Furthermore, ^{4}He has zero nuclear spin and very low atmospheric concentrations of the spin 1/2 ^{3}He isotope $< 10^{-6}$, which can be further isotopically purified to $< 10^{-13}$ if necessary [182]. Spin coherence times due to the presence of such nuclear spins has been calculated to exceed 10^7 s [76].

This all looks very promising at first, however, in the presence of spin-motion coupling (section 3.5), the electron spin inherits all of the motional decoherence mechanisms discussed above with a reduced matrix element, proportional to the gradient term in the interaction Hamiltonian (3.104)

$$\rho_{\mathrm{sm}} \propto \mu_B \frac{\partial B_z}{\partial x} x_0 \frac{1}{\hbar \omega_p} \tag{3.125}$$

At $\omega_p/2\pi = 5$ GHz and a gradient of $\partial B_z/\partial x \sim 8$ mG/nm (corresponding to a current of 1 mA at a distance of 500 nm), this dimensionless reduction factor is $\rho_{\mathrm{sm}} \sim 10^{-4}$. However, the spin-motion coupling can be tuned in situ and hence it is possible to reduce the inherited spin decoherence mechanism by changing the spin motion detuning or turning off the gradient field.

In addition to motion-inherited decoherence, the spin can dephase through fluctuating magnetic fields caused by Johnson current noise in the trap electrodes, which has spectral

noise density

$$S_I = 4kT\Delta\omega/\mathrm{Re}[Z] \tag{3.126}$$

where $\Delta\omega$ is the bandwidth of interest and Z is the environment impedance, typically $\mathrm{Re}[Z] \sim 50\,\Omega$. The field created at the electron position by a current in the bias electrode at distance 500 nm is $B = 4 \times 10^3$ mG/mA, which corresponds to a shift in Larmor frequency of $\Delta\omega_L = 3.5 \times 10^7$ s^{-1}/mA. Assuming a Johnson current noise of 100 pA/$\sqrt{\mathrm{Hz}}$, this gives a dephasing time of $T_{\phi,I} \sim 20$ s. Another possible source of magnetic field noise is 1/f flux noise typically found in experiments with superconducting SQUID loops and Josephson junction devices [183], which has magnitudes of order $S_\phi^{\mathrm{rms}} \sim 10^{-6}\,\Phi_0/\sqrt{\mathrm{Hz}}$, where $\Phi_0 = h/2e$ is the flux quantum. The quantum dot geometry considered in this thesis does not have any Josephson junctions or superconducting loops, so this mechanism may not be present at all, although this is difficult to predict since 1/f flux noise is not well understood in this case. However, conservatively assuming flux noise to be evenly distributed over the trap area at magnitude S_ϕ^{rms} gives a dephasing rate of only $\Gamma_\phi \sim 200$ s^{-1}.

3.7 Trapped Many Electron States

The μm-sized single electron traps discussed in section 3.3 are designed to trap single electrons at typical equilibrium electron separations of $\sim 1\,\mu$m. Extending the dimensions of the confining electrode geometry, a trap can potentially fit multiple electrons along the trap axis. Depending on the confining potential, electrons on helium can then form quasi one-dimensional linear chains analogous to ion chains in quadrupole traps [31, 184]. The phonon modes of such one-dimensional few-ion chains have been investigated in great detail [184–186] and they represent a crucial resource for quantum information processing and quantum optics experiments with trapped ions [13]. In this section, we explore the physics of vibrational states created by confining multiple electrons in a parabolic potential formed by a large DC electrode configuration. In chapter 7 we then show how this type of geometry can be realized using a high-aspect ratio coplanar waveguide resonator capable of trapping electrons directly inside the CPW gap. First, we derive expressions for the modes of $N = 2$ and $N = 3$ electron chains in section 3.7.1 and develop general solutions for arbitrary numbers of electrons closely following methods used for analyzing ion chains [185]. The coupling of electron chain vibrational modes to the quantized electric field in a coplanar waveguide

cavity is studied in section 3.7.2. Finally, section 3.7.3 discusses the effects of helium film curvature and the resulting oscillatory motion as a consequence of the image-charge induced restoring force.

3.7.1 One-Dimensional Electron Chains in Parabolic Traps

Consider the case of $N = 2$ and $N = 3$ electrons confined in a one-dimensional parabolic trap, shown schematically in Fig. 3.15. The trap dimensions are on the order of $w \sim 10\,\mu$m and $d \sim 1\,\mu$m, about a factor of 10 larger in the lateral dimension than the single electron traps of section 3.3, allowing multiple electrons to fit at an equilibrium mean spacing of $r_0 \sim 1\,\mu$m. A natural consequence of increasing the trap size is a decrease in anharmonicity and hence an almost purely quadratic, harmonic oscillator potential, as shown in section 3.3.2. By expanding the Coulomb interaction about the electron equilibrium positions, we first show that the system can be described by several distinct and independent vibrational modes. Using methods analogous to those developed for ion traps [185], we then generalize to N electrons in a parabolic trap and show that the system has N independent modes. In analogy to section 3.3.1, we will again assume an asymmetric geometry and a sufficiently strong binding potential in the vertical direction such that the characteristic frequencies of x, y and z motion are very different, the potential separates and the system can be considered quasi one-dimensional. In the following calculations, we assume the electrons are at a fixed distance of $a_0 \sim 8$ nm above a flat surface of superfluid and we keep the z coordinate fixed. We will relax this restriction in sections 3.7.3 and consider the effects of film curvature and changes in coupling strength as a function of z.

$N = 2$ Electron Case

Two electrons in a parabolic potential, as shown in Fig. 3.15 a, can be described as a pair of harmonic oscillators with the same oscillation frequency but coupled via Coulomb interaction:

$$\mathbf{H} = \frac{1}{2m}\left[p_1^2 + p_1^2\right] + \frac{1}{2}m\omega_0^2\left[x_1^2 + x_2^2\right] + \frac{e^2}{4\pi\epsilon_0|x_1 - x_2|} = \mathbf{H}_{\text{kin}} + \mathbf{V} \tag{3.127}$$

The equilibrium separation of the electrons is determined by the competition of trap oscillation and Coulomb repulsion and is obtained by minimizing the overall potential

$$\left[\frac{\partial \mathbf{V}}{\partial x_k}\right]_{x_k = x_k^{(0)}} = 0 \tag{3.128}$$

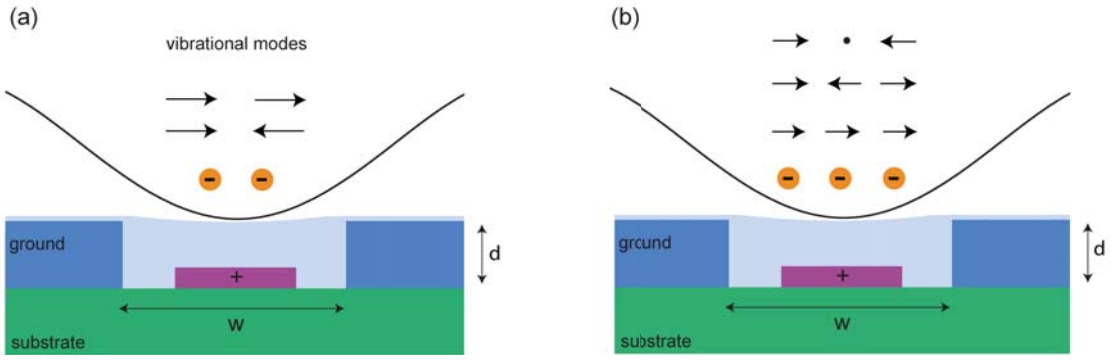

Figure 3.15.: One-dimensional electron vibrational modes in a parabolic trap formed by a DC center electrode (magenta) and grounded guard electrodes (blue). The vibrational modes of the chains are indicated by arrows. (a) Two electrons in a harmonic potential. The dynamics of the electron pair can be described by two distinct, independent vibrational modes, a stretch or breathing mode (bottom) and a center of mass mode (top), see text for details. (b) Three electrons in a harmonic potential, supporting a center of mass mode (bottom), a stretch mode (middle) and a scissor mode (top).

where $x_k^{(0)}$ is the equilibrium position of the kth electron with $k = 1, 2$. Solving this coupled system of equations gives

$$x_1^{(0)} = -x_2^{(0)} = \left(\frac{1}{2}\right)^{2/3} \left(\frac{e^2}{4\pi\epsilon_0 m\omega_0^2}\right)^{1/3} . \tag{3.129}$$

The electron equilibrium separation is therefore

$$x_c = |x_1^{(0)} - x_2^{(0)}| = \left(\frac{e^2}{2\pi\epsilon_0 m\omega_0^2}\right)^{1/3} \tag{3.130}$$

such that the electrons are located at positions $\pm x_c/2$ symmetric about the channel center. For a fundamental trap frequency of $\omega_0/2\pi = 5$ GHz the electrons are then separated by $x_c \approx 1\,\mu$m. Introducing the center-of-mass and relative motion coordinates

$$Z_1 = \frac{x_1 + x_2}{2} \quad , \quad P_1 = p_1 + p_2 \quad , \quad Z_2 = x_1 - x_2 \quad , \quad P_2 = \frac{p_1 - p_2}{2} \tag{3.131}$$

we can write the Hamiltonian as

$$\mathbf{H} = \left[\frac{1}{4m}P_1^2 + \frac{1}{m}P_2^2\right] + 2m\omega_0^2 Z_1^2 - m\omega_0 x_1 x_2 + \frac{e^2}{4\pi\epsilon_0|Z_2|} \tag{3.132}$$

Expanding the Coulomb interaction term in Z_2 for small amplitude oscillations around the equilibrium separation x_c to second order gives

$$\begin{aligned}\frac{e^2}{4\pi\epsilon_0|Z_2|} &\approx \frac{e^2}{4\pi\epsilon_0}\left[\frac{2}{x_c}-\frac{Z_2}{x_c^3}+\frac{1}{x_c^3}(Z_2-x_c)^2\right] \\ &= \left[\frac{e^2}{2\pi\epsilon_0 x_c}-\frac{1}{4}m\omega_0^2x_c^2\right]+\frac{3}{4}m\omega_0^2(Z_2-x_c)^2-\frac{1}{4}m\omega_0^2(x_1-x_2)^2\end{aligned}$$

where we have used (3.130). Dropping the constant first term, which is equal to the rest energy of the two-electron crystal, and introducing the coordinates $Q_1 := Z_1$ and $Q_2 := Z_2 - x_c$, the Hamiltonian can be written as

$$\mathbf{H} = \left[\frac{1}{4m}P_1^2+\frac{1}{m}P_2^2\right]+m\omega_0^2Z_1^2+\frac{3}{4}m\omega_0^2Q_2^2 \tag{3.133}$$

and thus separates into two independent oscillators

$$\mathbf{H} = \mathbf{H}_{\rm cm}+\mathbf{H}_{\rm rel} = \left[\frac{P_1^2}{2m_1}+\frac{1}{2}m_1\omega_1^2Q_1^2\right]+\left[\frac{P_2^2}{2m_2}+\frac{1}{2}m_2\omega_2^2Q_2^2\right] \tag{3.134}$$

with masses $m_1 = 2m$ and $m_2 = m/2$ and frequencies $\omega_1 = \omega_0$ and $\omega_2 = \sqrt{3}\omega_0$, respectively. The oscillatory motion in both modes is indicated by arrows in Fig. 3.15 a.The first part $\mathbf{H}_{\rm cm}$ describes the common mode oscillation at frequency ω_0, which corresponds to both electrons oscillating back and forth as if they were campled together. The second term $\mathbf{H}_{\rm rel}$ is the stretch-mode oscillation at frequency $\sqrt{3}\omega_0$ where the center of mass of the electrons remains fixed but the inter-electron spacing oscillates around the equilibrium distance x_c, which is sometimes referred to as the *breathing* or *stretch mode*. Note that the common mode has zero-point fluctuation $\Delta_1 = \sqrt{\hbar/4m\omega_0}$ while the stretch mode has $\Delta_2 = \sqrt{\hbar/m\omega_0\sqrt{3}}$.
Introducing the ladder operators for the kth mode

$$Q_k = \sqrt{\frac{\hbar}{2m_k\omega_k}}(a_k+a_k^\dagger) \quad , \quad P_k = i\sqrt{\frac{\hbar m_k\omega_k}{2}}(a_k^\dagger-a_k) \tag{3.135}$$

we can write the Hamiltonian in the usual harmonic oscillator form

$$\mathbf{H} = \sum_{k=1}^{2}\hbar\omega_k\left(a_k^\dagger a_k+\frac{1}{2}\right) \tag{3.136}$$

and the wave functions of the two modes in dimensionless form

$$\psi_n^{(k)}(\xi_k) = \sqrt{\frac{1}{2^n n!}} \left(\frac{1}{\pi}\right)^{1/4} e^{-\xi_k^2/2} \mathcal{H}_n(\xi_k) \tag{3.137}$$

where $\xi_k = Q_k/Q_k^{(0)}$, with the oscillator length scale $Q_k^{(0)} = \sqrt{\hbar/m_k\omega_k}$, and $\mathcal{H}_n(\cdot)$ are the Hermite polynomials. At a trap frequency of $\omega_0/2\pi = 5$ GHz, the two oscillators have sizes

$$Q_1^{(0)} = \sqrt{\frac{\hbar}{2m\omega_0}} \approx 43\,\text{nm} \quad , \quad Q_2^{(0)} = \sqrt{\frac{2\hbar}{m\sqrt{3}\omega_0}} \approx 86\,\text{nm} \tag{3.138}$$

compared to 61 nm for a single trapped electron in the same potential and at the same frequency.

$N = 3$ Electron Case

The three electron case can be described in analogy to the $N = 2$ case by defining the collective coordinates

$$Z_1 = \frac{x_1 + x_2 + x_3}{3} \quad , \quad Z_2 = \frac{x_3 - x_1}{2} \quad , \quad Z_3 = \frac{x_1 - 2x_2 + x_3}{6} \tag{3.139}$$

After some algebra, the three-electron Hamiltonian can be written as the sum of three uncoupled harmonic oscillators

$$\mathbf{H} = \sum_{k=1}^{3} \left[\frac{P_k^2}{2m_k} + \frac{1}{2} m_k \omega_k^2 Q_k^2\right] \tag{3.140}$$

The lowest frequency mode $Q_1 = Z_1$ is the center-of-mass mode with the same frequency as in the $N = 2$ electron case $\omega_1 = \omega_0$ but slightly heavier at $m_1 = 3m$. The second mode

$$Q_2 = Z_2 - 5^{1/3} x_c \tag{3.141}$$

also has the same frequency as the stretch mode in the $N = 2$ case, $\omega_2 = \sqrt{3}\omega_0$, but four times the mass $m_2 = 2m$ and different offset by a factor $5^{1/3}$. The third term is the *scissor mode* $Q_3 = Z_3$ with the highest frequency $\omega_3 = \sqrt{29/5}\,\omega_0$ and effective mass $m_3 = 6m$. As shown schematically in Fig. 3.15b, in the scissor mode the two outer electrons oscillate together in one direction with the same amplitude while the center electron oscillates with twice the amplitude in the opposite direction. The sizes of the oscillators at a fundamental

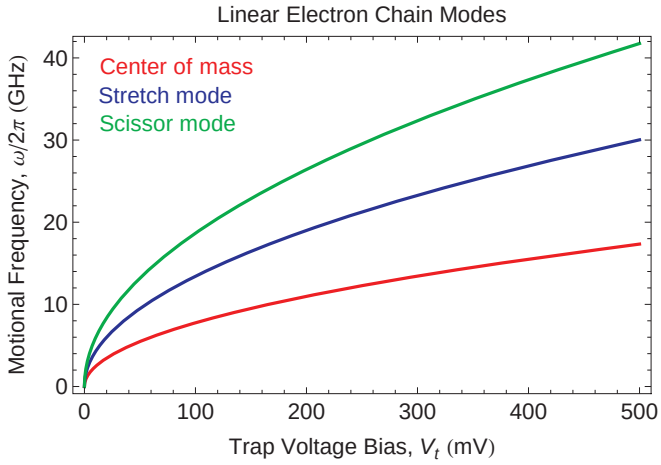

Figure 3.16.: Simulated frequencies for the center-of-mass (red), stretch (blue) and scissor mode (green) in a one-dimensional $N = 3$ electron chain as a function of voltage bias applied to the trap electrode.

trap frequency of $\omega_0/2\pi = 5$ GHz are

$$Q_1^{(0)} = \sqrt{\frac{\hbar}{3m\omega_0}} \approx 32\,\mathrm{nm} \quad , \quad Q_2^{(0)} = \sqrt{\frac{\hbar}{2m\sqrt{3}\omega_0}} \approx 30\,\mathrm{nm}$$
$$Q_3^{(0)} = \sqrt{\frac{\hbar}{6\sqrt{29/5}\omega_0 m}} \approx 15\mathrm{nm} \tag{3.142}$$

As expected, the oscillators become smaller compared to the two electron case due to the increased Coulomb interaction energy. We can simulate the trapping potential for a given geometry using finite-element methods and extract the motional frequencies by fitting the potential to a harmonic or slightly anharmonic oscillator potential (see section 3.3.3 for details on numerical methods used). Simulated frequencies of the three different modes for a $N = 3$ electron chain are shown in Fig. 3.16 as a function of voltage bias for a trap with dimensions $w = 10\,\mu$m $d = 1\,\mu$m and maximum helium level $h = d$. The oscillation frequencies are generally in the range of tens of GHz and could potentially be tuned over a wide band by changing the trap voltage over a few hundred mV. The frequencies scale like the square-root of trap voltage, as expected from the single electron case (section 3.3.2).

Arbitrary Number of Electrons

The $N = 2$ and $N = 3$ electron cases generalize qualitatively to the case of N interacting electrons in a parabolic potential. The lowest mode is always the center of mass mode where the crystal oscillates like a rigid body at the fundamental trap frequency ω_0. The next highest mode is always the stretch mode where the displacement of each electron is proportional to

its distance from the trap center $x = 0$. However, while qualitatively similar to the $N = 2$ and $N = 3$ cases, the normal modes for arbitrary numbers of electrons cannot be solved for analytically anymore and we have to resort to numerical solutions. A general numerical framework for finding the modes of an N electron crystal in a parabolic trap is presented in appendix B, closely following the method used in Ref. [185] for one-dimensional ion chains in Paul traps.

The Hamiltonian for N electrons in a parabolic potential of frequency $\omega_0/2\pi$ coupled via Coulomb interaction is given by

$$\mathcal{H} = \sum_{i=1}^{N} \frac{p_i^2}{2m} + \sum_{i=1}^{N} \frac{1}{2} m\omega_0^2 x_i^2(t) + \frac{1}{2} \sum_{i \neq j=1}^{N} \frac{e^2}{4\pi\varepsilon_0} \frac{1}{|x_i(t) - x_j(t)|} = \mathcal{H}_{\text{kin}} + V \tag{3.143}$$

Using a Lagrangian formalism, this Hamiltonian can be transformed into an uncoupled oscillator form (see appendix B)

$$\mathcal{H} = \sum_{p=1}^{N} \left[\frac{P_p^2}{2m} + \frac{1}{2} m\omega_p^2 Q_p^2 \right] \tag{3.144}$$

where $P_p = m \cdot \dot{Q}_p$ and the normal mode coordinates Q_p can be found algebraically in terms of the individual electron positions x_j, $j = 1, \ldots, N$. For $N = 4$ electrons, one finds that the first two modes ($p = 1, 2$) are the center of mass and stretch modes already encountered in the $N = 3$ case, both with the same frequencies as in that case, $\omega_1 = \omega_0$ and $\omega_2 = \sqrt{3}\omega_0$. The third and fourth mode are different types of scissor modes with higher frequencies. Compared to the $N = 3$ case, the normal mode oscillators generally have different masses and charges. Furthermore. one finds that the equilibrium electron spacing decreases with trap population, as expected. Note, however, that there is a limit to the number of electrons that can be stored in a given confining potential as the transverse vibrational states become unstable. Above a critical number of electrons, the electron crystal will adopt a zig-zag type configuration two dimensions that minimizes overall energy, which has been studied in for ions in the context of structural phase transitions using molecular dynamics simulations [187].

3.7.2 Electron Chain-Cavity Coupling

Just like in the single electron case, the oscillator frequencies of the electron chain modes from section 3.7.1 can be tuned through the voltages applied to the center electrode of the

trap shown in Fig. 3.15. We can simulate the exact potential and solve for the eigenenergies, wave functions and the dipole matrix elements numerically, see section 3.3.3 for details on the method. In analogy to the single electron trap case (section 3.4), the many-electron states couple to the field in a transmission line resonator $\mathbf{E}$ via dipole interaction $\mathcal{H}_g = \mathbf{d}_k \cdot \mathbf{E}$ where $d_k = q_k \mathbf{Q_k}$ is the dipole moment of the k mode with q_k being the effective charge of the mode and $\mathbf{Q_k}$ the coordinates of the mode, see section 3.7.1. The coupling strength of the $|\psi_1^{(k)}\rangle \rightarrow |\psi_2^{(k)}\rangle$ transition of the kth transverse many-electron mode is given by the dipole matrix element

$$\begin{aligned} \hbar g_k &= \langle \psi_2^{(k)} | \mathbf{d}_k \cdot \mathbf{E} | \psi_1^{(k)} \rangle = \langle \psi_2^{(k)} | q_k \cdot \mathbf{Q}_k \cdot \mathbf{E} | \psi_1^{(k)} \rangle \\ &= q_k \int_{-\infty}^{+\infty} \psi_2^{(k)}(Q_k) \cdot Q_k \cdot E_{\parallel}(Q_k) \psi_1^{(k)}(Q_k) dQ_k \end{aligned} \tag{3.145}$$

where $E_{\parallel}(Q_k)$ is the electromagnetic field component along the transverse direction (parallel to the electron chain) and $\psi_j^{(k)}$ are the harmonic oscillator wave functions from section 3.7.1. The coupling between a single electron crystal mode and the cavity field is then described as usual by a Jaynes-Cummings hamiltonian

$$\mathcal{H}_{\mathrm{JC}} = \hbar\omega_r \left(a^\dagger a + \frac{1}{2} \right) + \hbar\omega_k \left(b_k^\dagger b_k + \frac{1}{2} \right) + \hbar g_k \left(a^\dagger b_k + a b_k^\dagger \right) \tag{3.146}$$

where ω_k is the oscillator frequency of the kth mode. The effective mode charge in (3.145) for the $N = 2$ electron case is $q_{1,2} = 2e$ and for the $N = 3$ electron case $q_{1,3} = 3e$ and $q_2 = 2e$. The coupling strength depends on the specific geometry and the magnitude of the electric field component along the principal axis of the electron crystal, which can be obtained from finite-element simulations of the geometry. We will look at this in detail for the specific case of a DC-biased center pin resonator in chapter 7. In this design, the resonator itself forms the many-electron trap and the vibrational modes are centered above the center pin of the coplanar waveguide geometry.

3.7.3 Helium Curvature Effects

In the linear chain calculations of section 3.7.1 we have assumed a flat helium surface and fixed electron position in the z direction of $a_0 \sim 8$ nm above the surface. In a uniform holding field perpendicular to the surface, an electron bound to a curved surface of helium experiences a restoring force that leads to oscillatory motion in addition to any harmonic os-

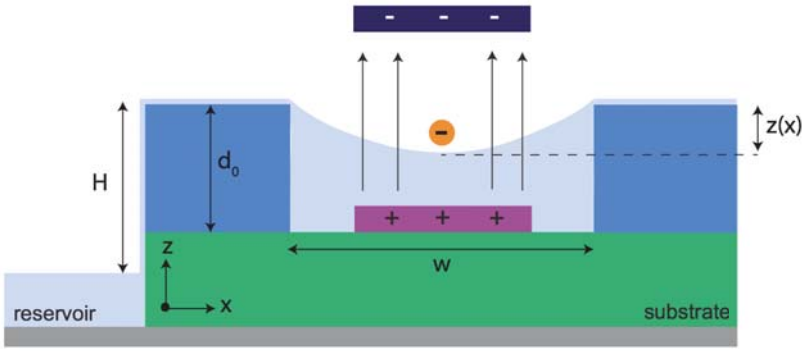

Figure 3.17.: Helium curvature effects for single trapped electron: The helium curvature causes a restoring force that attracts the electron to the channel center, corresponding to an oscillatory motion at a frequency determined by the radius of curvature and the electric field.

cillation due to the parabolic trapping potential. The effective electron motion is determined by a combination of the parabolic trap potential and the restoring force caused by the film curvature.

To understand the origins of the curvature-induced oscillatory motion we start by considering the case of a single electron in a uniform, perpendicular DC holding field, as shown in Fig. 3.17. The lateral one-dimensional motion of a single electron in a micro channel such as the one shown in Fig. 3.17 is governed by [188]

$$\mathbf{H} = \frac{p_x^2}{2m} + V(x,z) = \frac{p_x^2}{2m} + e \cdot E_\perp \cdot z(x) \tag{3.147}$$

where $E_\perp$ is the vertical DC holding field and the z coordinate is a function of the lateral motion along x since the electron is bound to the curved helium film. In other words, the vertical motion of the electron is constrained by the curvature of the helium film. Approximating the profile of the liquid surface across the gap by a semi-circular shape we have (see section 2.3.4)

$$z(x) = R_c \left(1 - \sqrt{1 - \left(\frac{x}{R_c} \right)^2} \right) \sim \frac{x^2}{2R_c} \tag{3.148}$$

where $R_c = \sigma/\rho g H$ is the radius of curvature (Note: $x = 0$ is at the lhs of the gap, $x = w$ at the rhs with $w = 10\,\mu$m being the width of the gap in Fig. 3.17). The total Hamiltonian for motion parallel to the film surface can then be written as

$$\mathbf{H} = \frac{p_y^2}{2m} + \frac{p_x^2}{2m} + \frac{1}{2} m \omega_0^2 x^2 \tag{3.149}$$

where the harmonic trap frequency was introduced

$$\omega_0 = \sqrt{\frac{eE_\perp}{mR_c}} = \sqrt{\frac{eE_\perp \rho g H}{m\sigma}} \tag{3.150}$$

The resulting oscillatory motion in the x direction will be quantized if $\hbar\omega_0 \gg k_B T$. The Hamiltonian is separable in x and y and the corresponding two-dimensional wave functions are

$$\Psi_n(x,y) = \frac{1}{\sqrt{\pi^{1/2}\ell L_x 2^n n!}} e^{ik_y y} e^{-x^2/2\ell^2} \mathcal{H}_n(x/\ell) \tag{3.151}$$

These are plane waves in the longitudinal direction y and harmonic oscillator wave functions in the transverse direction x. Here,

$$\ell = \sqrt{\frac{\hbar}{m\omega_0}} \tag{3.152}$$

is the characteristic length scale of the oscillator, $k_y = 2\pi/L_y$ with L_y being the longitudinal channel size and $\mathcal{H}_n(\cdot)$ the Hermite polynomials. Note that typically $L_y \gg w$ in our device geometries and hence the y motion can be regarded as unconstrained at the relevant energies. The energy spectrum is given by

$$E_{k_y,n} = \frac{\hbar^2 k_y^2}{2m} + \hbar\omega_0 \left(n + \frac{1}{2}\right) \tag{3.153}$$

The confining effects in the x direction are caused by the external holding field $E_\perp$ which leads to a restoring force that moves the electron towards the center of the gap, i.e. the minimum of the curved helium surface. Upon displacement by an amount x, the potential energy increases by

$$V(x) = \frac{eE_\perp}{2R_c} x^2 \tag{3.154}$$

and the motion will be oscillatory at frequency $\omega_0/2\pi$. From (3.150) we see that the transverse motional frequency of a single electron depends on the radius of curvature like $\sim R_c^{-1/2}$. To keep the frequency constant as the radius of curvature increases, we have to increase the holding field proportionally. In the geometry shown in Fig. 3.15, the electric field is not perfectly uniform or orthogonal to the surface but one can expect to get similar effects due to the curvature-restoration force. It is important to note that this oscillatory motion is in addition to any quantized motion that results from the parabolic trap potential. However, the curvature-induced oscillation frequencies are small at curvature radii on the order of the channel width $R_c \sim 10 - 50\,\mu$m unless subject to large electric fields. For a typical curvature

radius of $R_c = 50\,\mu$m a curvature-induced frequency of $\omega_0/2\pi = 5$ GHz would require perpendicular fields of $E_\perp \sim 3 \times 10^3$ V/cm or 300 mV/μm for a single electron.

4 Experimental Setup and Device Fabrication

THE implementation of a circuit QED setup for electrons on helium experiments requires a combination of a wide variety of techniques and methods, including microwave, RF and DC engineering, nano- and micro-fabrication of superconducting devices and low temperature physics and cryogenics. The superconducting circuits that define the cavity and electron traps are fabricated via optical and electron-beam lithography on sapphire substrates. The resulting 2×7 mm chips are mounted in a hermetically-sealed, superfluid leak-tight sample cell at the 15 mK base stage of a dilution refrigerator. Helium is supplied to the cell in a controlled fashion through a capillary tube supply system. Electrons are generated via pulsed thermionic emission from a tungsten filament and the motion and energy of the electrons on the superfluid surface are controlled via submerged DC gate electrodes on the chip. The electron-cavity system is probed in transmission measurements at microwave frequencies and nano-Watt powers. The measurement instrumentation is controlled using custom software written in *Python* and *Labview*. This chapter provides a discussion of the various components of our circuit QED setup and the fabrication methods used. Section 4.1 starts with an overview of the cryogenic measurement setup, with particular focus on the microwave and DC circuitry, the capillary helium supply system, the sample cell and the low-energy electron sources. In section 4.2 we review phase-sensitive detection and homodyne and heterodyne measurements and section 4.3 concludes with a discussion of various nano- and micro-fabrication methods.

4.1 Measurement Setup

This section provides a discussion of the measurement and electron control setup used in our experiments. Starting with an overview of the setup in section 4.1.1, we discuss cryogenics and filtering and the RF, microwave and DC measurement circuitry assembled for this thesis.

Section 4.1.2 focuses on the capillary tube helium supply setup and section 4.1.3 provides details on the hermetic sample cell and other superfluid leak-tight components used at base temperature. Finally, section 4.1.4 discusses the physics and implementation of the low-energy cryogenic electron sources used in our experiments.

4.1.1 Setup Overview

The experiments presented in this thesis were carried out in a pulse-tube cooled dilution refrigerator by *Oxford Instruments* (models *DR 200* and *Triton 200*), capable of reaching base temperatures of $T \simeq 15$ mK at cooling powers of 1 μW. In addition, a pumped continuous flow cryostat by *ICE Oxford* with a base temperature of 1.4 K was used for testing many of the individual components such as the capillary helium supply lines and the filament electron sources. A simplified diagram of the measurement and control setup in its entirety is shown in Fig. 4.1. Annotated images of the lower stages of the cryostat and the room-temperature signal synthesis and DC instrumentation are shown in Fig. 4.2. In this section, we will give an overview of the setup and briefly walk the reader through the different stages, starting at room temperature down to base. Individual setup components are discussed in detail in the following sections. The input/output lines of the setup can be roughly segmented into three parts, indicated by different colors in Fig. 4.1: (1) RF and microwave measurement circuit for cavity transmission measurements (black), (2) Electron generation and DC control circuits (magenta) and (3) Capillary helium supply system (yellow).

Cryogenics and Filtering

The *Oxford DR200* and *Triton 200* pulse-tube cooled dilution refrigerators operate using two separate cycles, a pre-cooling and a dilution cycle, and consist of five different temperature stages, as indicated in Fig. 4.1 by dashed colored boxes with approximate temperatures shown on the l.h.s and cooling powers on the r.h.s. In contrast to conventional cryostats, the precooling of the ^{3}He/^{4}He mixture in a 'dry fridge' is achieved using a pulse-tube cooler (PTC) rather than a liquid ^{4}He bath. The dilution refrigerator does therefore not require the use of any external cryogens, apart from the liquid nitrogen trap outside the refrigerator. The PTC is a two-stage cryo-cooler whose first stage reaches a temperature of ~ 70 K while the second stage reaches about 4 K (see also Fig. 4.1). During pre-cooling, the circulating ^{3}He/^{4}He mixture is first purified in a charcoal trap which is thermally connected to the first

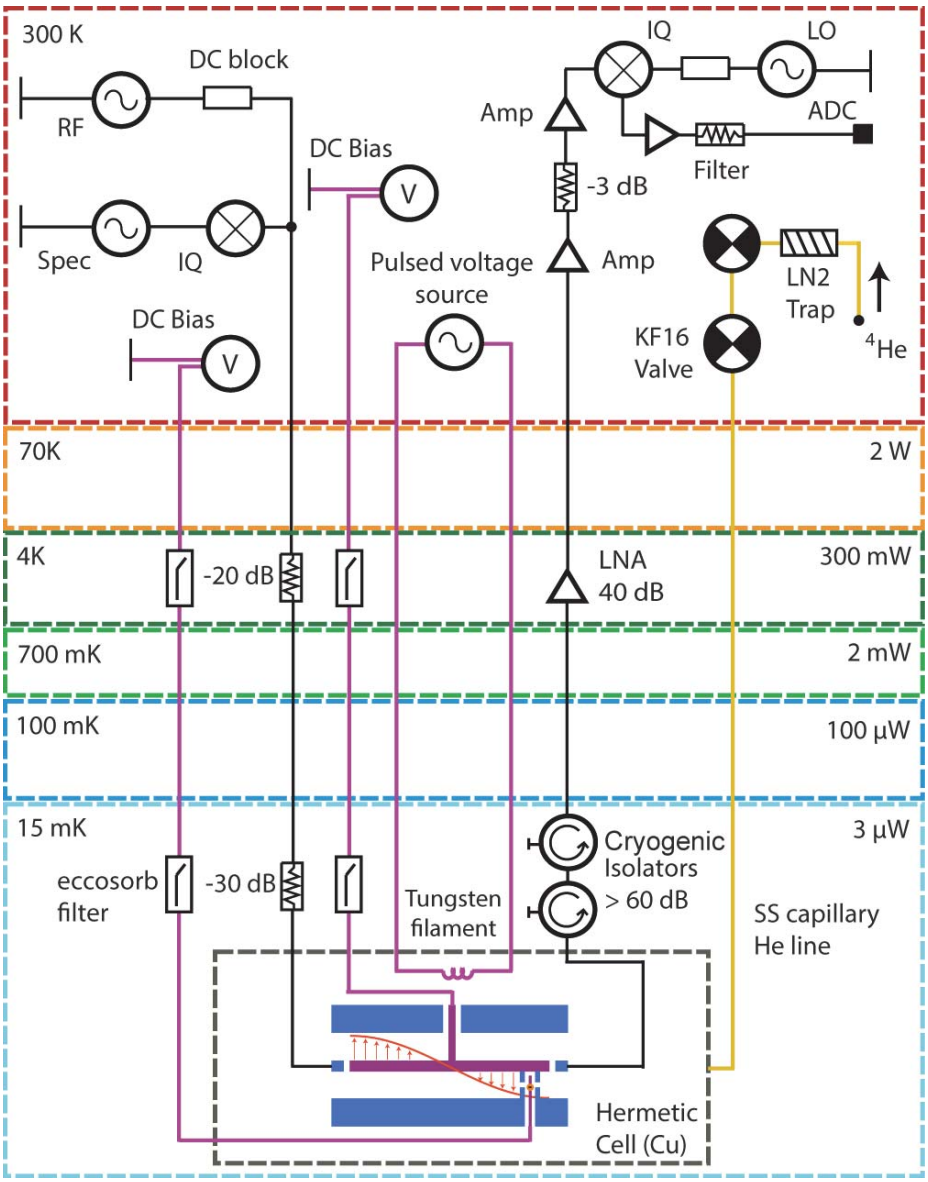

Figure 4.1.: Measurement and control setup for circuit QED experiments with electrons on helium, mounted in a pulse-tube cooled dilution refrigerator. The different temperature stages of the cryostat are indicated by colored boxes, together with approximate temperatures (l.h.s) and cooling powers (r.h.s). DC lines for electron generation, trapping and manipulation are shown in magenta while MW and RF lines for cavity transmission measurements are shown in black. The sample is mounted in a hermetic cell (see section 4.1.3) at base to which ^{4}He is supplied through a capillary tube line (yellow, see section 4.1.2) The MW and RF drives are synthesized at room temperature and transmitted to the sample via coaxial cables after attenuation at 4K and base. The signal transmitted through the cavity is passed through cryogenic isolators before amplification by a low-noise amplifier at 4K. Back at room-temperature, the signal is further amplified and mixed-down to 1 - 10 MHz using an IQ mixer, at which point it is acquired digitally in a data acquisition card. The DC gate signals for electron control are low-pass filtered to 0.5 GHz using eccosorb filters at 4K and base. Electrons are generated thermionically by applying voltage pulses to a tungsten filament (see section 4.1.4).

stage of the PTC and is then pre-cooled by a heat exchanger at the second stage of the PTC to about 4 K. In the condensing phase, milli-Kelvin temperatures are reached by the dilution of liquid ^{3}He into ^{4}He like in a regular cryostat. Fully automated cooldowns to $\sim$ 15 mK are possible in which the switch between pre-cooling and condensing phase is handled automatically by the software. For more details on the design and operation of cryostats and dry dilution refrigerators see Refs. [125, 189, 190].

Probing the interaction of electrons on helium with superconducting cavities down to the few photon level requires signals of extremely low powers which can only be generated, modulated and resolved by careful filtering, amplification and attenuation. The system is driven and measured in transmission at frequencies of 1 - 10 GHz through coaxial cables which are thermally anchored at each stage of the dilution refrigerator. At those frequencies, thermal Johnson noise can be significant down to a few hundred mK. To suppress thermal photons from the higher stages from reaching the sample at base, we use 20 and 30 dB of attenuation on the RF input line at 4 K and base, respectively. In addition, the coaxial cables themselves give some frequency-dependent attenuation, depending on their lengths and material properties. At $\nu \sim 5$ GHz total cable attenuation in our setup is typically about 10 dB for semi-rigid stainless steel cables (UT 85-SS), giving a total attenuation of ~ 60 dB before the RF drive reaches the sample input. Depending on the cavity quality factor, the transmitted power $P \simeq n\hbar\omega_0\kappa$ can be extremely low for small photon numbers n. To measure such small signals, a cryogenic low-noise amplifier (*Low Noise Factory LNC4_8A*) is used on the output line at the 4 K stage, providing about 43 dB of gain at 5 GHz. Two in-series cryogenic isolators (*QuinStar CWJ1019-K414*) are used at base instead of regular attenuators such that thermal photons from the higher temperature stages (S_{12}) are attenuated before reaching the sample output while the small signal from the cavity (S_{21}) is transmitted nearly without loss. The isolators provide about 30 dB of isolation (S_{12}) each in the 4-8 GHz range. To minimize the attenuation of the signal between the cryogenic isolators and the input of the amplifier, we use superconducting Nb coaxial cables on the output line between base and 4K stage, which provide good thermal isolation and small electrical attenuation. At room temperature, two more stages of amplification are used before the signal is mixed down (see below).

The filtering of the DC and low-frequency lines (magenta in Fig 4.1) used for electron generation, trapping and tuning can be achieved using low-pass filters which provide attenuation at RF and microwave frequencies but not at DC. We can get away with this since most

of the thermal noise power is located at RF frequencies and the required bandwidth is much smaller than for the cavity transmission signals. The filament electron source (section 4.1.4) is biased through DC wires (Nb-Ti loom), while the trap and gate electrodes are controlled through coaxial cables, which allows applying additional RF pulses through the gates using a bias tee if needed (not shown in Fig. 4.1). The trap bias lines are filtered by custom-made Eccosorb filters at the 4 K and base stages with 3 dB cutoffs of $\sim$ 600 MHz and $>$ 40 dB attenuation at 5 GHz, see Refs. [155, 191] for details on design and construction of this type of filter. The various filters and attenuators serve the dual purpose of thermally anchoring the coaxial cables to the stages of the cryostat, in particular they thermalize the center pins of the cables.

RF and Microwave Measurement Circuit

At room temperature, the microwave signals are generated and modulated on the input side before entering the cryostat (upper left in Fig. 4.1) and subsequently down-converted and analyzed after amplification on the output side (upper right in Fig. 4.1). This signal synthesis and readout infrastructure is common to many circuit QED experiments and discussed in detail in Refs. [48, 154]. Hence, we limit ourselves to a brief description here, with the digital homodyne and heterodyne signal processing principles reviewed in section 4.2. Microwave signals for cavity transmission measurements are generated by an *Agilent E8257D* analog signal generator with an operating range of 250 kHz to 20 GHz. DC blocks are used at the outputs of all generators to maintain a common experiment ground. On the output side, the signal is down-converted and mixed with the LO signal (offset by 1 - 10 MHz from the original RF signal) after two stages of room temperature amplification. Before sampling in the data acquisition card (ADC), the down-converted 1 - 10 MHz signal is further filtered (DC - 22 MHz low-pass filters by *Mini-Circuits*) and amplified by a DC - 350 MHz pre-amplifier by *Stanford Research Systems*. The down-conversion and demodulation is necessary to acquire the amplitude and phase information of the signal digitally since no commercial acquisition boards exist that can stably acquire at 5 - 10 GHz frequencies. Note that all microwave sources and generators are coherent and phase-locked. A 10 MHz rubidium frequency standard by *Stanford Research Systems* is used as a frequency reference to all RF sources and the data acquisition card.

Electron Generation and DC Control Circuits

To control the DC potentials of the single- and many-electron trap electrodes, high-stability DC sources (*Yokogawa 7651* and *GS200*) are used. As mentioned before, the DC lines are filtered by Eccosorb filters at 4 K and base, low-passing the gate signals to $\sim$ 600 MHz. A pulsed, voltage-biased tungsten filament is used to generate electrons via thermionic emission, which is discussed in detail in section 4.1.4.

4.1.2 Capillary Lines and Helium Supply System

Supplying ^{4}He gas at room temperature to a sample cell at the 15 mK base stage of a cryostat, where it condenses into superfluid form, poses a number of practical challenges. The unique properties of superfluid helium (see section 2.3) such as its vanishing viscosity and the formation of mobile van-der-Waals films make it especially difficult to transport and contain helium across large temperature gradients, in particular when non-permanent interface seals are required. Containing a fixed volume of superfluid in a sample cell at base temperature can be achieved using hermetically-sealed components with conventional indium joints, see section 4.1.3 for details. In this section we briefly discuss the capillary tube setup that is used to supply helium from room temperature to the sample cell.

The helium supply system built for this thesis (shown schematically in yellow in Fig. 4.1 with images in Fig. 4.2) consists of a custom liquid nitrogen (LN2) trap and pumping line at room temperature and a series of stainless steel capillary tubes by *IDEX Stainless Steel Tubing*, mounted at each stage inside the cryostat and connected to the sample cell at base. The supply line is evacuated prior to each cooldown and room temperature helium is first passed through the LN2 trap to remove any residual air and other contaminations prior to entering the cryostat. In a typical experiment, helium is supplied in gas form in small increments of size $V \simeq 0.01$ cm^3 at 1 atm pressure, which is defined by the dead volume between two in series KF16 valves mounted at the top of the cryostat (upper right in Fig. 4.1). The stages of the dilution refrigerator span four orders of magnitude in temperature (20 mK - 300 K) with cooling powers ranging from 3 μW to several hundred mW. All coaxial lines and microwave components must be properly heat sunk at each stage and care must be taken to keep the thermal load below the cooling powers of the individual stages as indicated in Fig. 4.1. As discussed in section 2.3, superfluid helium forms a saturated van-der-Waals of about 30 nm thickness coating all surfaces, including the inner walls of the sample cell and

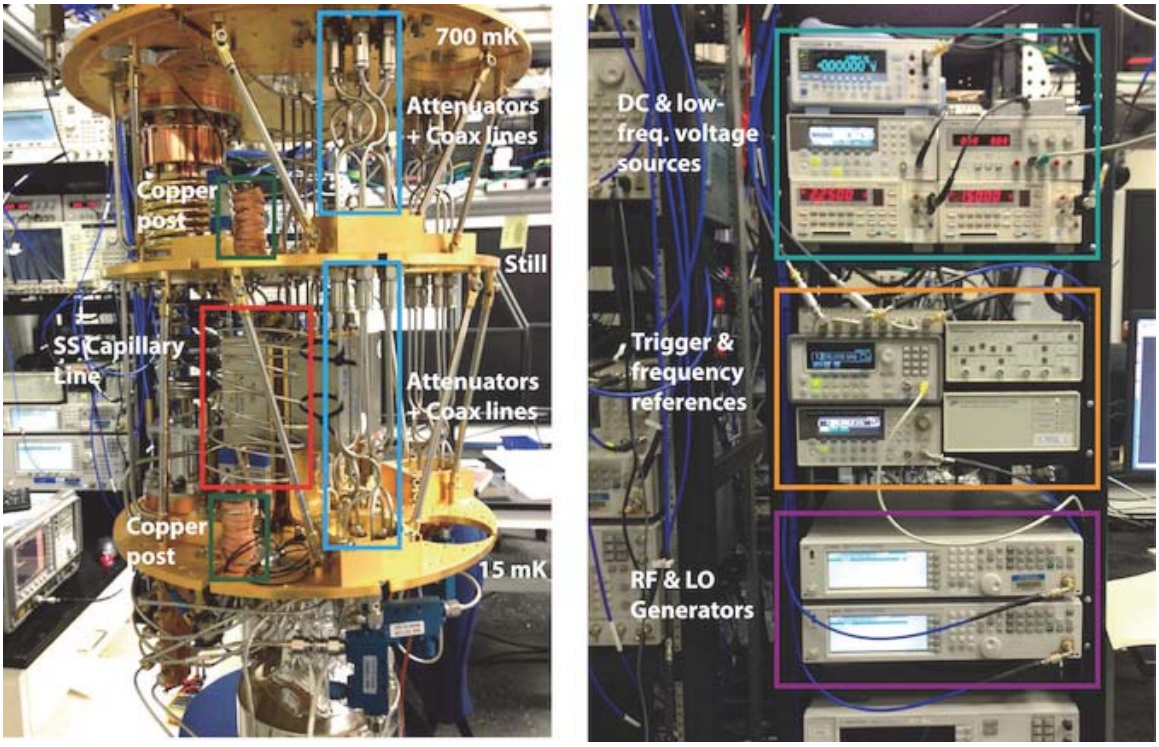

Figure 4.2.: Annotated images of the cryogenic setup and control instrumentation at room temperature: (a) Lowest three stages of the dilution refrigerator (700 mK, Still and 15 mK base from top to bottom), showing the stainless steel capillary line mounted on copper posts and the RF coaxial lines including attenuators. (b) Measurement and control instrumentation at room temperature, showing the DC and low-frequency voltage sources used for electron gate control and filament excitation (top), the Rubidium 10 MHz frequency reference, AWG for card triggering and the room-temperature amplifier (center) and the RF and LO generators (bottom).

the capillary tube. Due to the vanishing viscosity this film is mobile and creeps towards regions of higher temperature where it eventually transitions into gas form. In the case of a capillary tube connected to a large sample volume at base temperature, this means that the inside of the tube will be covered with superfluid, potentially creating a thermal short between different stages of the cryostat. This is especially problematic due to the exceptionally high thermal conductivity of liquid helium, see section 2.3.1. In addition, low-frequency mechanical vibrations due to the pulse tube and turbo pump mounted at the top of the cryostat can propagate along the semi-rigid capillary and lead to further heating. To minimize the overall heat load, the capillary is hard-soldered [1] into spiral grooves on copper posts mounted at each stage, which serve both to thermalize the capillary and to stabilize it mechanically. Annotated pictures of the capillary tubes, copper posts and the coaxial lines in the cryostat are shown in Fig. 4.2 a. As can be seen, significant excess length of capillary tube (20 - 50 cm) is left between successive stages to account for thermal expansion and to

[1] We use silver solder (75% Ag, 25% Cu), silver brazing paste (*No. 601BA411*) and boron modified flux by *Superior Flux & Mfg. Co.* and Nicrobraz white stop-off mixture, soldered at about 1200° F with a torch.

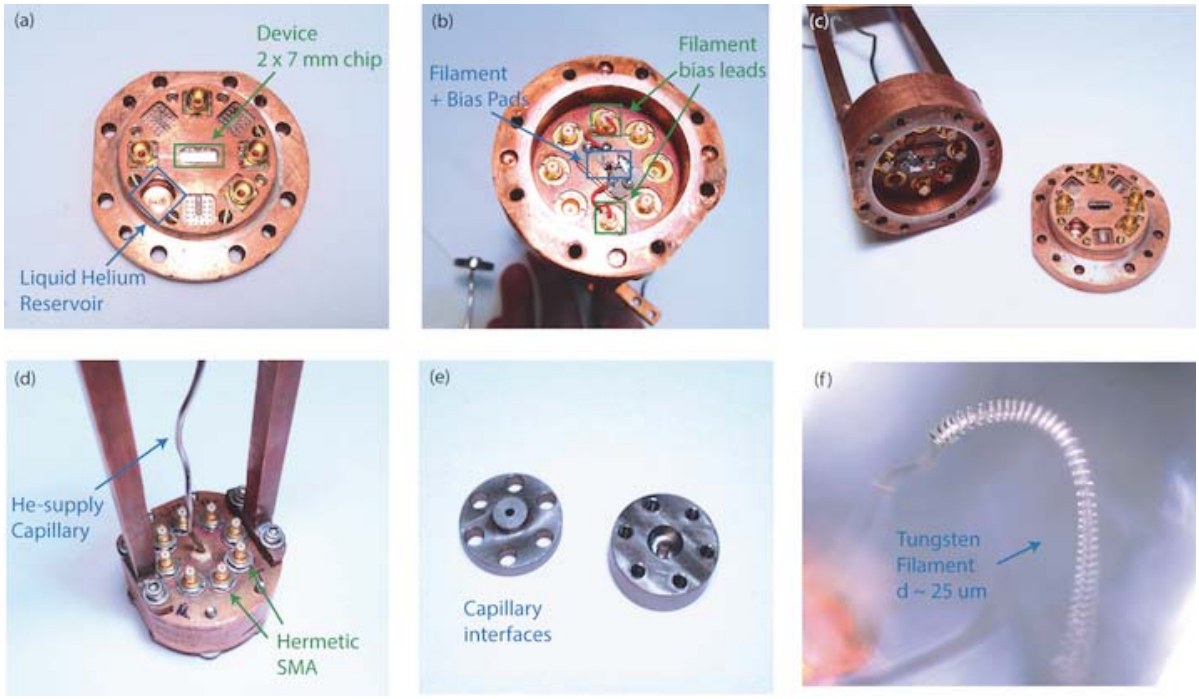

Figure 4.3.: Annotated images of the hermetic sample cell, capillary lines and interfaces and tungsten filament electron source: (a) Bottom part of the cell, showing the cylindrical helium reservoir of radius $r = 3.175$ mm and depth $H = 5$ mm and the 2×7 mm superconducting chip on a PC board with a Copper shim on top, (b) Top half of the cell, showing the tungsten filament mounted on a PC board with the bias pads connected to SMP bullets, (c) Top and bottom half before sealing, (d) Top view of indium-sealed cell, showing hermetic SMA connectors and the ^{4}He supply capillary hard-soldered into the cell, (e) Capillary tube interfaces, (f) Optical microscope picture of a tungsten filament electron source with $d \sim 25\,\mu m$ diameter.

further mitigate the temperature gradient across stages. Different sections of capillary tube are connected using custom stainless steel interfaces, shown in Fig. 4.3 e. The inner diameter of the capillary tube should be kept small to reduce heat load, but at the same time large enough to avoid clogging of the line due to residual air or helium accumulations in the line. The optimal diameter of 0.04 inch (1.016 mm) was found by trial and error (no excessive heat load on the stages and no plugs observed). Smaller diameters (< 0.76 mm) were found to result in frequent plugs. In the final configuration, the dilution refrigerator is capable of maintaining base temperatures of 15 - 20 mK with a completely helium-filled sample cell and capillary tube. No superfluid leaks were found in the capillary supply system in over 30 consecutive cooldowns. Film burners have been found not to be necessary but could be useful in the future to increase the capillary diameter and decrease the length of the line.

4.1.3 Hermetically-Sealed Sample Cells

Containing a fixed volume of superfluid helium in a sample cell at base temperature poses a number of experimental challenges, some of which were already pointed out in section 4.1.2. Due to its vanishing viscosity, helium in the superfluid phase can flow through narrow constrictions with zero flow resistance, penetrating even nm-size pores [192, 193]. A well-established method of making cryogenic seals between interfaces is to use indium metal O-rings [194, 195]. Indium is a soft metal at room temperature and when compressed between two solid surfaces fills any gaps between them, creating a reliable gas and liquid seal that retains its integrity down to mK temperatures. We have designed and constructed a sample cell made of copper that consists of two parts which can be mated together with an indium seal. Pictures of a sample cell are shown in Figs. 4.3 a (bottom part), b (top part) and c. The cell design is inspired by the "octobox" introduced in [155]. The superfluid seal between top and bottom is made by squashing a 0.762 mm (30 mil.) diameter indium wire ring with overlapping ends between the two surfaces. The surfaces are pressed against each other by evenly and progressively tightening stainless steel screws. The helium-supply capillary is hard-soldered into a small hole at the top of the sample holder, see Fig. 4.3 d, using the same procedure as in section 4.1.2. The sample cell also contains eight hermetic SMA connectors (*GPO Male FD to GPO Male FD Thread-in* Hermetic Feed-thru by *Corning Gilbert*, DC -18 GHz) for DC, microwave and RF signal input and output, see Fig. 4.3 d. The connector feedthroughs each have their own indium seal, which remains unbroken once the connectors have been mounted. Note that the connectors are nominally only specified to be vacuum-tight (down to 77 K), but we generally have found them to be superfluid leak-tight down to 10 mK. This leaves only a single indium joint which has to be remade when exchanging samples between experiments. Our hermetic setup has proven to be extremely reliable and robust with no detectable superfluid leaks in well over 30 cooldowns.

4.1.4 Low-Energy Cryogenic Electron Sources

There is a wide variety of methods for generating large numbers of free electrons, including photoemission from Zinc and other metals [196], Fowler-Nordheim emission from a sharp conducting tip [197], corona discharges [198], nuclear beta decay via ionization of helium atoms and thermionic emission from filaments [199–201]. However, not all techniques are suitable for operation in cryogenic environments where any excess heating needs to be min-

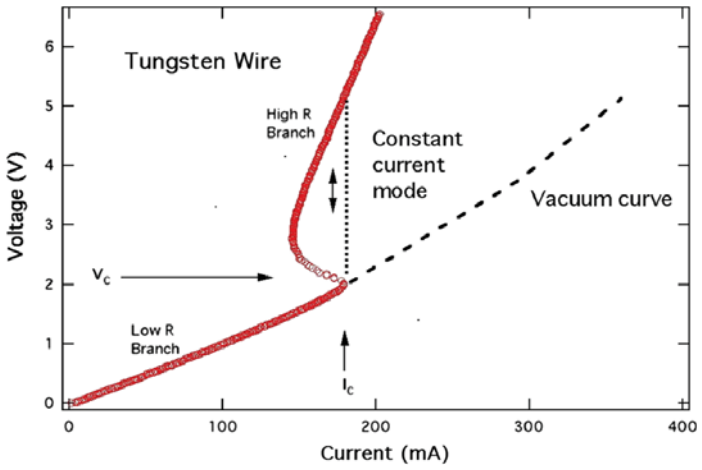

Figure 4.4.: Experimental IV curve of a thoriated tungsten filament with diameter $12.5\ \mu$m operated in the vapor phase of helium at $T \sim 1.3$ K, taken from Ref. [201]. The dashed curve indicates the IV curve for a filament operated in vacuum, where the slope is the resistance R of the filament. The data points shown in red represent measurements in constant voltage operation mode, with the corresponding constant current mode indicated by the dotted line. The low and high resistance branches and the negative resistance region are clearly visible, with critical current and voltage indicated by I_c and V_c, respectively.

imized due to limits in cooling power. For experiments with electrons on helium, another important practical constraint comes from the relatively low electron injection barrier of 1 eV for superfluid helium. In order to form bound surface states, electrons have to reach the helium surface with a kinetic energy lower than the injection barrier needed to penetrate the superfluid.

For the experiments presented in this thesis we use a low-energy electron source in which free electrons are generated by thermionic emission from a voltage-pulsed tungsten filament. Tungsten filaments have been used as reliable and robust sources in electrons on helium experiments for decades, although the physics behind them was not well understood until recently [201, 202]. Remarkably, a tungsten filament covered by a superfluid helium film (or immersed in vapor phase helium) can be operated at temperatures of several thousand Kelvin, emitting electrons by thermionic emission in a cryogenic environment that nevertheless remains at temperatures $T < 1$ K. The reason for this behavior lies in a complex combination of electrical properties of the filament and heat transport mechanisms in superfluid helium [201], which is briefly discussed in the following. Applying a voltage across a tungsten filament leads to Ohmic heating and heat dissipation via blackbody radiation. As the voltage is increased, the center of the filament eventually becomes glowing hot at temperatures of $T \simeq 1500 - 2500$ K and starts emitting electrons following a Richardson

law [201, 202]

$$J = \frac{4\pi m e k_B^2}{h}(1 - R_s)T^2 e^{-\phi/k_B T} \tag{4.1}$$

where $J = I/A$ is the current density emitted from the surface area A, ϕ is the work function of the material, R_s the electron reflection coefficient of the emitting surface and k_B and h are Boltzman's and Planck's constants, respectively. Tungsten is most commonly used because of its relatively low work function of $\phi = 4.53$ eV and high melting temperature of $T_m = 3695$ K. Other materials such as thoriated or cesiated tungsten have been used by experimenters as well because of their lower work functions (2.7 and 1.0 eV, respectively), although they generally also have lower melting temperatures and are more difficult to handle [202]. A filament covered by a film of superfluid helium or operated in the vapor phase of liquid helium has simple ohmic IV characteristics below a certain critical voltage V_c, similar to a filament in a conventional vacuum tube. However, above V_c the IV curve becomes strongly non-linear and branches out into a high resistance curve. Once the filament bias reaches V_c in constant voltage mode, the current falls back to a lower value (i.e. a negative resistance region) and the filament starts emitting electrons [201]. Electron emission increases with increasing voltage above V_c as the wire glows hotter, similar to electron emission from a filament in a vacuum tube. The value of V_c ultimately depends on the material, length and diameter of the wire.

The behavior of filaments immersed in bulk or thin-film superfluid helium is in stark contrast to filaments operated in vacuum, which show no negative resistance branches. While electron emission takes place both in vacuum tubes and for filaments immersed in liquid helium, the difference lies in the extremely efficient heat transport mechanisms for the immersed helium case. An example of a measured IV curve of a filament in vapor phase helium taken from Ref. [201] is shown in Fig. 4.4. Biased below V_c, the filament is on a low resistance branch of operation, where it is cool and no measurable electron emission takes places. In this state, heat is removed from the filament in a highly efficient way since it is in direct contact with superfluid helium, which has the highest known thermal conductivity of all substances. The ohmic behavior below V_c is similar to that of a filament in vacuum. Above V_c, the behavior changes abruptly as the filament switches to a high resistance branch of operation where the distributed resistance of the wire is high and it emits electrons at a temperature of several thousand K. The occurrence of low and high resistance branches was explained by Silvera and Tempere in terms of a first-order phase transition as a consequence

Peak-to-peak Amplitude, V_f	3.0 - 4.2 V
Frequency, ν_f	110 - 120 kHz
Pulse Duration, τ	20 - 40 ms
Pulse Delay, Δt	0.25 - 1 s
DC offset, V_{off}	- 0.1 to - 0.5 V
Number of pulses, N_{p}	5 - 20

Table 4.1.: Typical tungsten filament biasing parameters for thermionic electron emission. The filament is operated in pulsed mode where short voltages pulses of duration τ are applied to the filament using an *Agilent AWG 33259A* arbitrary waveform generator. The pulse duration is set by the number of burst cycles and the frequency and the peak-to-peak amplitude is adjusted according to the critical voltage of the filament, see discussion in text.

of changes in the mode of heat transport in superfluid helium [201]. For filaments immersed in superfluid helium, it was shown that a stable vapor sheath of radius $\sim 100\,\mu$m forms around the filament above V_c to insulate it from the superfluid [199, 200]. The vapor sheath has a much lower thermal conductivity than the superfluid and the filament temperature jumps to a higher value once the liquid can no longer carry the heat and starts to evaporate.

Images of tungsten filament electron sources used in our experiments are shown in Fig. 4.3 b and f. Our filaments have diameters of $d \sim 25\,\mu$m, typical room temperature resistances of $R \approx 15 - 20\,\Omega$ and critical voltages for electron emission of $V_c \approx 3.0 - 4.2$ V. The ends of the filament source are soldered to two copper pads on a PC board, fabricated by wet etching. Contact resistances from the leads have been found to be negligible in this configuration. As can be seen in Fig 4.3 b, the pads are connected to the coaxial bias lines via SMP bullets, with the PC board mounted on the top wall of the sample cell approximately 4.5 mm above the chip. In order to minimize heat load during electron emission, the filament is operated in pulsed voltage mode, with a small negative DC offset with respect to the trap electrodes on the chip. We use a pulsed arbitrary waveform generator (*Agilent AWG 33250A*) and bias the filament with sine voltage waves of frequency $\nu_f = 100 - 120$ kHz and peak-to-peak amplitudes of $V_f \sim 3.5 - 4.5$ V, depending on the critical voltage of the filament. The generator is triggered at ~ 2200 burst cycles, which at $\nu_f = 110$ kHz corresponds to voltage pulses of $\tau = 20$ ms duration. For electron emission, we typically pulse the filament multiple times with delays of $\Delta t \sim 0.5$ s between pulses to temporarily increase the vapor pressure in the sample cell, which helps to decrease the electron kinetic energy after emission. A $C = 1.68\,\mu$F capacitor serves as a bias tee, allowing us to apply additional DC offsets to the filament and the pads through the same lines. A summary of typical filament parameter ranges is given in Tab. 4.1. Here, the pulse amplitude V_f is primarily set by the critical voltage of the filament, while the pulse duration and number of pulses influence the amount of heating in the cell.

The electron energy can be controlled both by changing the DC offset V_{off} between filament and on-chip electrodes as well as by changing the pulse delay Δt. Shorter delays lead to higher temporary increases in vapor pressure and hence lower electron kinetic energy. As discussed in more detail in the context of density measurements in chapter 6, we have found surface electron densities to depend somewhat on all of these parameters. The optimal set of parameters for a desired surface density varies from filament to filament because of small differences in resistance and length. In addition, the density also depends on the superfluid film thickness. Fortunately, the parameter range was found to be quite wide and installing a new filament typically requires only a short characterization sequence. We find that electrons can be loaded into the chip region successfully at the 15 mK base temperature of the cryostat, implying that the electron kinetic energy is sufficiently reduced before they reach the helium surface after emission from the filament. Additional pre-heating of the sample cell to $T \sim 1$ K prior to electron emission is typically reported to be necessary to temporarily increase the vapor pressure and cool the emitted electrons by collision with helium atoms, see e.g. [101]. Filament pulsing and electron emission lead to small temporary increases in base temperature of 40 - 80 mK, but the system usually cools back to 15 mK within a few minutes.

4.2 RF, Microwave and Audio-Frequency Signal Processing

In this thesis electrons on helium have been measured and detected both at audio (10 - 100 kHz) and microwave frequencies (4 - 8 GHz). The Sommer-Tanner electron detection and density measurements presented in chapter 6 were carried out at audio frequencies and are based on detecting small currents of a few pA induced on submerged electrodes. The circuit QED detection presented in chapter 7 on the other hand is based on the coupling of collective excitations of the electron system to the quantized electromagnetic field in a cavity. Even though the underlying physical coupling mechanisms to the readout devices are quite different in the two experiments, the measurements in both are based on the same principle of phase-sensitive detection. This section provides a brief review of lock-in amplification and homo- and heterodyne detection principles.

4.2.1 Phase-Sensitive Detection and Lock-in Amplification

Lock-in amplifiers are designed to detect and measure small AC current and voltage signals, down to a few nA or nV, even in the presence of noise sources many orders of magnitude larger than the signal. The underlying technique is known as phase-sensitive detection in which the component of the signal at a specific reference frequency and phase is singled out. Noise signals at frequencies other than the reference frequency are rejected and do not affect the measurement. Phase-sensitive detection allows measuring the signal of interest with an extremely small bandwidth, much smaller than the best band pass filters can achieve. The currents induced by capacitive coupling of a two-dimensional electron system on helium to submerged planar electrodes (chapter 6) are extremely small (pA or less) for our trapping geometries and thus require a lockin-type measurement.

To perform a lock-in measurement, a frequency reference is required. Typically, the experiment is excited at a fixed frequency from an oscillator or function generator and the lock-in amplifier then detects the response from the experiment at the reference frequency by mixing the experiment signal with the reference signal. For the Sommer-Tanner experiments of chapter 6, a *SR830 DSP* lock-in amplifier by *Stanford Research Systems* was used where the excitation signal is provided by an internal oscillator (50 mHz to 100 kHz) and an internal lock-in reference gives the reference signal for mixing. The RF and microwave measurement setup of section 4.1 can be thought of as a lock-in amplifier "on steroids" operated at microwave frequencies.

Let the experiment excitation signal be a sine wave of the form $V_S \sin(\omega_S t + \theta_S)$ and the corresponding reference signal be $V_R \sin(\omega_R t + \theta_R)$. The lock-in amplifier amplifies the experiment signal and multiplies it by the reference using a phase-sensitive detector (PSD). The output of the PSD is simply the product of the two sine waves

$$V_{\mathrm{PSD}} = V_S \cdot V_R \cdot \sin(\omega_S t + \theta_S) \sin(\omega_R t + \theta_R) \tag{4.2}$$

which can also be written as

$$V_{\mathrm{PSD}} = \frac{1}{2} V_S V_R \left\{ \cos\left([\omega_S - \omega_R]t + \theta_S - \theta_R\right) - \cos\left([\omega_S + \omega_R]t + \theta_S + \theta_R\right) \right\} \tag{4.3}$$

The PSD output therefore consists of two AC signals, one at the difference and the other at the sum frequency of the signal and reference. If the output signal is passed through a

low-pass filter, the AC components of the signal are removed and in general nothing will be left. However, if the signal and reference frequencies are equal $\omega_S = \omega_R$, called *homodyne detection*, we have

$$V_{\mathrm{PSD}} = \frac{1}{2} V_S V_R \cos(\theta_S - \theta_R) - \frac{1}{2} V_S V_R \cos(2\omega_S t + \theta_S + \theta_R) \tag{4.4}$$

If this is passed through a low-pass filter with cutoff $< 2\omega_S$, the AC component is removed and we end up with a pure DC signal proportional to the experiment signal amplitude V_S,

$$V_{\mathrm{PSD}} = \frac{1}{2} V_S V_R \cos(\theta_S - \theta_R)\,. \tag{4.5}$$

The combination of a PSD and a low-pass filter thus only detects signals whose frequencies are very close to the reference frequency $\omega_S \approx \omega_R$. Noise at frequencies far away from the reference are attenuated by the low-pass. On the other hand, noise at frequencies close to the reference will result in low frequency AC outputs from the PSD whose attenuation depends on the bandwidth and roll-off of the low-pass filter. For the lock-in principle to work, the reference must be phase-locked to the excitation signal since otherwise the phase difference $\theta = \theta_S - \theta_R = f(t)$ is subject to drifts and will be a function of time. Lock-in amplifiers therefore use a phase-locked loop (PLL) which locks the internal reference oscillator to an external or internal excitation source (a signal generator) with a fixed phase shift θ. Since the PLL actively tracks the excitation signal, phase drifts do not affect the measurement. Most commercial lock-in amplifiers have a built-in signal generator that is always phase-locked to the internal reference oscillator.

The output of the PSD-low pass filter combination (4.5) can be controlled by adjusting the phase difference θ between signal and reference. If $\theta_S = \theta_R$, we have $V_{\mathrm{PSD}} = (1/2)V_S V_R$. Conversely, if $\theta = \pi/2$ the output will be zero. In order to be able to measure the 90° phase-shifted signal as well, lock-ins usually have a second PSD-low-pass filter combination in parallel to the first PSD. This parallel PSD mixes the signal with the reference oscillator signal shifted by 90°, i.e. $V_R \sin(\omega_R t + \theta_R + \pi/2)$. The filtered output of the second PSD is then

$$V^{(2)}_{\mathrm{PSD}} = \frac{1}{2} V_S V_R \sin(\theta_S - \theta_R) \sim V_S \sin\theta\,. \tag{4.6}$$

Hence, in combination with the output of the first PSD, we get two output signals, one proportional to $\cos\theta$ and the other one to $\sin\theta$. These two outputs are called the *quadratures*

of the signal

$$I = V_S \cos\theta \quad , \quad Q = V_S \sin\theta \tag{4.7}$$

where I is the in-phase and Q the out-of-phase component. The magnitude and phase of the signal can then be obtained from

$$R = \sqrt{I^2 + Q^2} = V_S \quad , \quad \theta = \arctan(Q/I) \tag{4.8}$$

as desired. In the audio-frequency electron measurements presented in chapter 6, the electron induced currents are almost purely capacitive in nature and hence most of the signal lives in the out-of-phase component.

4.2.2 Heterodyne and Homodyne Detection

The measurement setup used in most Yale circuit QED experiments, including the ones presented in this thesis, is based on the phase sensitive detection technique discussed in the previous section. In a typical transmission measurement, the signal from the RF generator (upper left in Fig. 4.1) is used to drive the cavity at frequency ω_{RF}. The returning signal is then mixed in an IQ mixer with the 0° and 90° phase-shifted local reference oscillator (LO) signals at frequency ω_{LO}. The IQ mixer thus produces two output signals, the products of the experiment signal $A_t \sin(\omega_{\mathrm{RF}} t + \phi_t)$ with the LO signal and the $\pi/2$ phase-shifted LO signal at ω_{LO}. Like in section 4.2.1, the two output signals are low-passed such that we get the two quadratures

$$I_t = A_t \cos(\omega_{\mathrm{IF}} t + \phi_t) \quad , \quad Q_t = (A_t + \epsilon_a) \sin(\omega_{\mathrm{IF}} t + \phi_t + \epsilon_\phi) \tag{4.9}$$

where $\omega_{\mathrm{IF}} = \omega_{\mathrm{RF}} - \omega_{\mathrm{LO}}$ and ϵ_A and ϵ_ϕ account for small imbalances between the 0° and the 90° phase-shifted arms of the mixer. Like in a regular lock-in amplifier, there are in general two types of measurements, *homodyne* ($\omega_{\mathrm{IF}} = 0$) and *heterodyne detection* ($\omega_{\mathrm{IF}} \neq 0$). In either case, the signal of interest is down-converted by means of the IQ mixer, which makes it easier to sample and process. Homodyne detection produces pure DC signals (two quadratures of the form (4.7)) as the final output from which the phase and amplitude of the signal can be extracted digitally via (4.8). The down-conversion to DC is done by the hardware in that case and averaging and conversion to phase and amplitude can be done digitally directly from that signal. Unfortunately, DC signals are much more prone to $1/f$ noise and slow drifts.

In a heterodyne measurement, RF and LO frequencies are typically offset by 1 - 10 MHz to get an intermediate signal at frequency ω_{IF} at the output of the mixer. For non-zero ω_{IF}, the conversion to DC can be achieved digitally rather than in hardware. We sometimes refer to this as *digital homodyne* [44]. The amplitude A_t and phase ϕ_t of the signal can be extracted using either one or both of the two quadratures in (4.9) for $\omega_{\mathrm{IF}} \neq 0$. In the first method, referred to as *single-channel digital homodyne*, we keep only one of the quadratures and mix it down digitally. Low-passing is achieved via integration of the signal over one period of the IF frequency $T = 2\pi/\omega_{\mathrm{IF}}$, which yields the averages of both amplitude $\overline{A_t}$ and phase $\overline{\phi_t}$. This method has the advantage of being insensitive to imbalances and offsets between the two arms of the IQ mixer since only one branch is used, but it has the downside that the bandwidth is reduced to the IF frequency ω_{IF} [44]. In order to take the full bandwidth of the IQ mixer, both branches need to be used, which is referred to as *dual-channel digital homodyne*. In this method, one can extract the full amplitude and phase information from a single IQ point rather than a whole IF period. The disadvantage is that we are now sensitive to imbalances in the arms of the mixer. In this thesis, both single- and dual-channel digital homodyne have been used for the cavity measurements presented in chapters 5, 6 and 7.

4.3 Nano- and Microfabrication of Superconducting Devices

One of the key advantages of circuit quantum electrodynamics lies in the ability to engineer many of the system parameters (transition frequencies, coupling strengths, quality factors) using well-established nano- and micro-fabrication techniques similar to those used in today's classical silicon-based processors. In this thesis, we use a variety of advanced fabrication techniques for superconducting resonators and electron traps. The fabrication of devices for electrons on helium experiments is very much analogous to those used in conventional circuit QED experiments [44, 45, 203]. There are, however, a number of additional challenges such as the need for thicker metallization layers (800 nm - 1 μm vs. 150 - 200 nm), which set the micro-channel geometry, the requirement of insulating overlaps and long, narrow constrictions to guarantee electron confinement and the need for multi-layer processes to achieve different metallization film thicknesses for high aspect ratio traps. This section provides an overview of the nano- and micro-fabrication methods used to address these

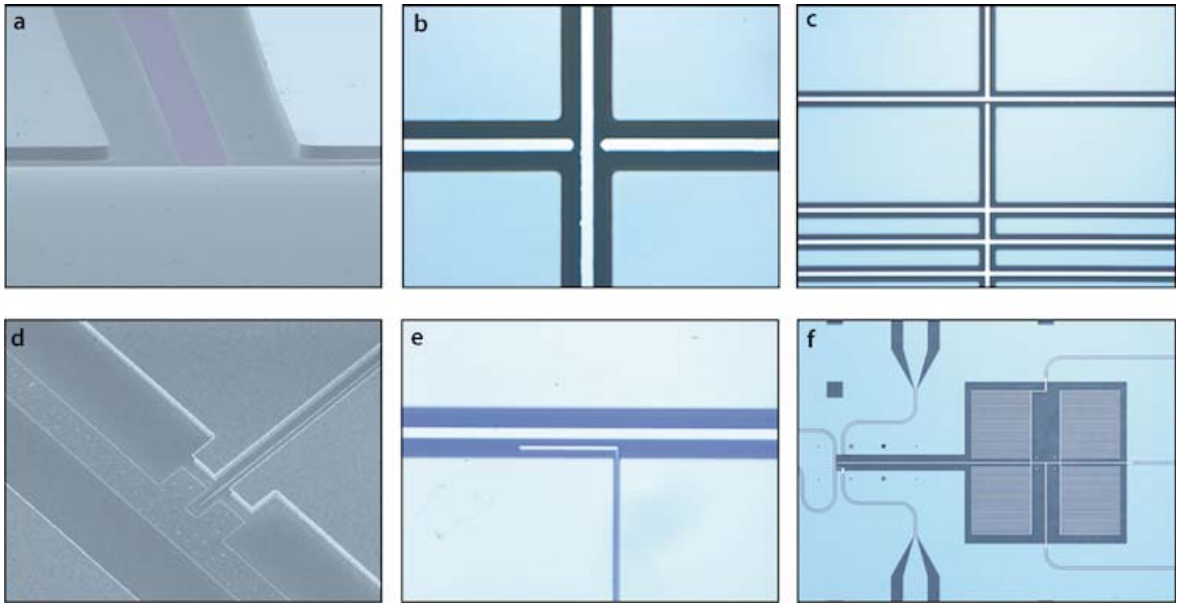

Figure 4.5.: Optical and electron scanning microscopy images of superconducting devices fabricated by two-layer optical lithography (a - c) and two-layer electron beam lithography (d - f). (a) DC-biased center pin waveguide with Nb ground planes of 700 nm thickness and a 40 nm thick Al center pin (false-colored in magenta), (b) Constriction gate for electron confinement, (c) Large micro-channel electron reservoir, (d) Single-electron quantum dot formed by a 40 nm Al center pin, 800 nm Nb ground planes and a 40 nm Al gate electrode, (e) Few-electron trap electrode fabricated next to a center pin, (f) Large-scale Sommer-Tanner micro-channel geometry, serving as a reservoir for a single-electron trap. See text for details on fabrication recipes.

challenges.

Dielectric Substrate

The dielectric substrate used for all devices presented in this thesis was sapphire. Silicon and thermally oxidized silicon have also been used for test devices. Sapphire has an anisotropic dielectric constant that depends on the direction of the cut with respect to the principal axes of the crystal. Sapphire has a hexagonal lattice structure and the principal planes are c-plane (cut parallel to the bottom of the hexagon), $a-b$ plane (cut length-wise) and r-plane (cut diagonally). Most of the wafers used for our experiments are c-plane sapphire of thickness 500 μm with a dielectric constant of $\varepsilon_{\mathrm{sub}} = 9.4$. Sapphire cut along the a-b plane has a slightly higher dielectric constant of $\varepsilon_{\mathrm{sub}} = 11.5$. The r-plane dielectric constant is in between those two values but is difficult to determine exactly.

Coplanar Waveguide Resonators

The inductively- and capacitively coupled coplanar waveguide resonators used in our experiments are fabricated using hard-contact optical lithography on sputter-deposited Nb films.

A Nb film of thickness $d = 200 - 1000$ nm is first deposited on a 2" dielectric substrate wafer in a sputter deposition system (by DC magnetron sputtering in *CMS 18* and *Super System 3* machines by *Lesker*). A layer of photoresist (*S1813* or *S1818* by *Shipley*) is then spun at 4000 rpm for 90s and baked at $110 - 120°$ for 120s on a hot-plate, which gives a resist thickness of $\sim 1.3\,\mu$m. The UV-sensitive resist system is then exposed through a hard-contact chrome lithography mask in an *EVG 620* mask aligner machine, which defines the coplanar waveguide structures and coupling capacitors and inductors. The exposed resist regions are then removed in a developer solution (*MF-319* for typically 70s) and subsequently etched away in a reactive ion etcher (Ar/SF_6 plasma in an *Oxford Plasmalab 80* machine). Resolutions and minimum feature sizes of 1 - 2 μm on up to 800 nm thick Nb can be achieved with this process. More details on optical lithography of CPW structures can be found in Ref. [44]. Optical microscopy images of coupling inductors and capacitors fabricated by this process are shown in Fig. 3.7.

DC-biased center pin resonators, in which electrons can be trapped directly inside the coplanar waveguide gap (see chapter 7), require two metallization layers of different thicknesses. In this type of device, the resonator ground planes of thickness $d_g \sim 500 - 1000$ nm form a micro-channel geometry (section 2.3.4) that supports a self-stabilized capillary action film of thickness $\sim d_g$. The center pin of thickness $d_{\mathrm{cp}} \sim 20 - 50$ nm acts as a submerged gate electrode. High aspect ratios $d_g/d_{\mathrm{cp}} \gtrsim 20$ are desirable to reduce metallic image charge effects and improve many electron transport properties. More details on the physics of this particular trap design can be found in section 3.7, while chapters 5 and 7 present two experiments with DC-biased center pin resonators. To fabricate such devices, we have developed two processes, a two-layer all-optical lithography process and a two-step electron beam lithography process with better alignment properties and higher resolution. In both processes, the ground planes consist of 500 - 1000 nm of sputter-deposited Nb while the center pin is made of ebeam evaporated Al of thickness 20 - 50 nm.

Two-Layer Optical Lithography

For the two-layer all-optical lithography process we use two chrome hard-contact lithography masks, the first one defining the ground planes and the second one the center pin and other thin submerged electrodes. The first layer (Nb ground planes) is fabricated by reactive ion etching using the same recipe as for the single-layer resonator devices (see above). The second layer (Al electrodes) is fabricated using a lift-off process and ebeam evaporation

of Al. For this step we use a bi-layer photo-resist system consisting of a sacrificial bottom layer (*LOR5A* by *Microchem* spun at 4000 rpm for 60s and baked at 195° C for 15 min.) and a primary layer (*S1808* by *Shipley* spun at 4000 rpm for 60s and baked at 115° C for 60s). The bi-layer resist system creates a natural undercut profile after UV exposure and development, which was found to be critical for the lift-off step as it leads to a discontinuous Al film. Following exposure and development, sublimated Al is deposited in a *Plassys MEB550s* ebeam evaporation system. Alignment between the two fabrication steps is achieved in the *EVG 620* mask aligner. We use a set of orthogonal alignment markers that allow for 0.5 - 1 μm alignment precision between the two layers, which is sufficient for resonator structures, albeit not for single or few-electron quantum dots. Whole 2" wafers are processed at once, which are then diced into individual chips using a *ProVectus ADT* dicing saw. Optical microscopy and scanning-electron microscopy (SEM) images of devices fabricated by the two-layer photolithography process are shown in Fig. 4.5 a - c.

Two-Layer Electron Beam Lithography

To achieve better alignment precision and higher feature resolutions, an alternative all-ebeam process was developed for the fabrication of DC-biased center pin resonators and devices with electron traps. This process allows for an alignment precision of $\sim$ 10 nm and minimum feature sizes of $\sim$ 20 nm across a 2" wafer, which is particularly crucial for devices with sub-μm-size single- and many-electron traps. In analogy to the devices fabricated by optical lithography (see above), the ground planes defining the micro-channels are made of sputter-deposited Nb while the submerged gate electrodes consist of electron-beam evaporated Al. The resist patterns, however, are written using electron-sensitive resist systems rather than UV-sensitive resist. To define the ground plane micro-channels, we use a single-layer polymer resist of thickness $\sim$ 900 nm (*Microchem PMMA A7 (950)* spun at 1200 rpm for 150s and baked at 175° C for 20 min.). Prior to e-beam exposure, a $\sim$ 20 nm gold layer is sputtered on top of the resist to avoid charging effects due to the insulating sapphire substrate, see Ref. [155] for more details on e-beam fabrication on insulating substrates. The gold layer is removed after exposure but prior to development using a gold etch solution ($\sim$ 30 s and rinsed in DI water). After development in an MIBK:IPA solution (for $\sim$ 50 s), the exposed regions are etched away in the reactive ion etcher. Similar to the resist system used for the second layer in the optical lithography above, we use a bi-layer resist system for the second lift-off layer consisting of a sacrificial co-polymer bottom layer of thickness

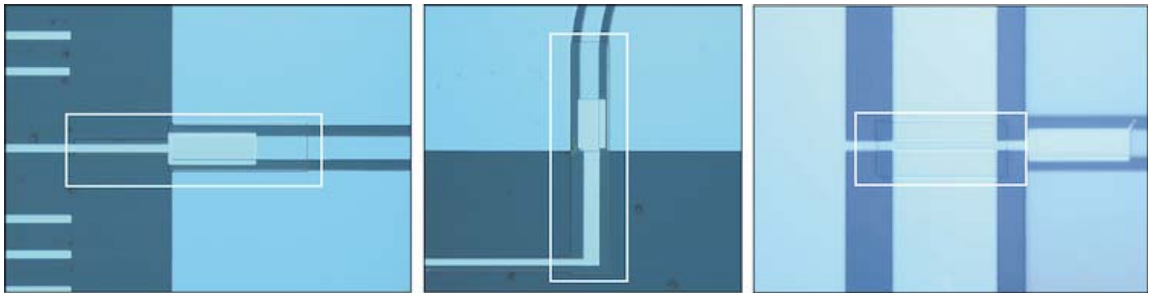

Figure 4.6.: Optical microscope images of silicon-oxide based insulating overlaps between gate electrodes. The silicon-oxide patterns are defined using ebeam lithography and deposited by sublimation sputtering. Thicknesses of $\sim 100 - 150$ nm are typically used, depending on the thickness of the bottom electrode.

~ 800 nm (*Microchem EL13 MAA* spun at 2500 rpm for 90s and baked at 175° for 1 min.) and a primary polymer resist layer of thickness ~ 500 nm (*Microchem PMMA A7 (950)* spun at 2500 rpm for 90s and baked at 175° for 20 min). The resist thicknesses used in this thesis are unusually thick due to the much thicker ground plane metallizations necessary for deeper micro-channel structures. The increased resist thickness was required to create a uniform resist film and to allow using the same plasma etch process as in the optical lithography process. RIE etch rates of ~ 87 nm/min for single- and ~ 95 nm/min for bi-layer ebeam resists have been measured for standard etch parameters using a stepper, both of which are below typical Nb etch rates of ~ 130 nm/min. Following e-beam exposure and development, the Al gate electrodes are deposited by ebeam evaporation in analogy to the optical lithography process above. The ebeam patterns for this thesis were written using two different systems, a modified scanning electron microscope (*FEI XL30*) and an electron beam pattern generator (*Vistec EBPG-5000*) capable of writing entire 2" wafers in one session with an alignment precision down to ~ 10 nm. Optical and SEM images of devices fabricated by two-layer electron beam lithography are shown in Fig. 4.5 d - f.

Insulating Layers and Electrode Overlaps

Confining electrons on helium to well-defined regions on the chip requires guard ring structures which are at negative potential with respect to the trapping electrodes. Guard rings have been realized for this thesis in two different forms: (1) Overlapping electrodes separated by deposited insulating layers, (2) Narrow constrictions that realize effective potential barriers. For the Sommer-Tanner electron detection and density measurement devices (chapter 6), we use guard ring electrodes that overlap the trapping electrodes with dielectric layers in between, while for the cavity electron detection experiments a simple constriction

gate was used. While the overlapping guard electrodes have the advantage of being continuous, the need for an additional dielectric layer inevitably introduces another fabrication step that further complicates the device. In addition, many dielectrics have poor microwave and RF frequency loss characteristics that can severely impact the quantum coherence properties of superconducting devices and trapped electron states. A variety of dielectric layers and methods of fabrication have been explored in this thesis, including enhanced aluminum oxide growth through plasma oxidation in a reactive ion-etcher (*Oxford Plasmalab 80*) and a barrel asher (*MES HF-6*) as well as through heating and UV light exposure at room temperature. Unfortunately, such natively grown aluminum oxides have turned out to be quite fragile and unreliable, leading to frequent shorts even at modest relative voltages between overlapping electrodes. As an alternative, we have used deposition of sublimated silicon-oxide (SiO_x) in a high-vacuum sputtering system (*Super System 3* by *Lesker*). Such deposited insulating layers can be made to have thicknesses of several hundred nm, making them robust and capable of withstanding voltages of $\gtrsim 10$ V. Optical images of deposited SiO_x layers of 150 nm thickness and several μm^2 area are shown in Fig. 4.6.

5 Superfluid Helium on Coplanar Waveguide Cavities

A key step towards circuit QED experiments with electrons on helium is to understand the effects superfluid helium on the resonance frequencies and quality factors of transmission line cavities. As we will show in this chapter, the resonance frequency is highly sensitive to the thickness of superfluid films on the chip surface, making it possible to use CPW resonators as high-precision meters of superfluid helium levels. In analogy to parallel-plate capacitor-based level meters, the method presented here is based on small changes in the capacitance per unit length C_ℓ and the characteristic impedance Z_0 of the waveguide. The high sensitivity of the resonance frequency to changes in C_ℓ, in combination with the exceptional frequency resolution of high-Q resonators (line widths of $\delta\nu \simeq 5$ kHz at $\nu_0 = 5$ GHz are possible), allows measuring superfluid films as thin as ~ 30 nm.

This chapter presents a number of experiments aimed at understanding the resonance behavior of coplanar waveguide cavities covered by superfluid helium films ranging from 30 nm to 20 μm in thickness. Section 5.1 starts with a discussion of the underlying physics of the helium-induced shifts (section 5.1.1) and describes ways of numerically calculating them in the thick (section 5.1.2) and thin-film limits (section 5.1.3). Section 5.2 presents an experiment in which the helium fill dynamics and the different regimes of superfluid film formation are resolved. Finally, section 5.3 shows how a voltage-biased center pin can be used to tune the helium level in a waveguide gap in-situ. The experiments discussed in this chapter represent a first proof of principle, providing us with a basic understanding of superfluid films required for the electron trapping experiments in chapter 6 and 7. There is much room to push this technique further to higher levels of precision, potentially paving the way for more advanced superfluid helium experiments such as detection of ripplons and classical vibrations with superconducting resonators.

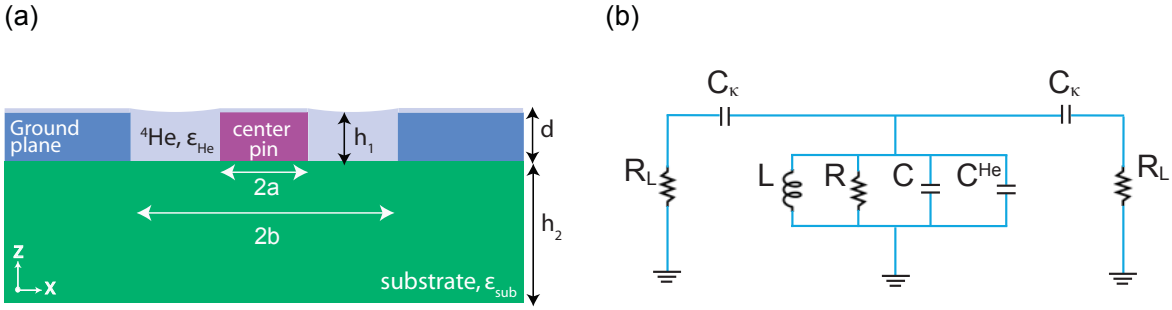

Figure 5.1.: Superfluid helium filling the gaps of a coplanar waveguide structure by capillary action: (a) Schematic cross-section of a waveguide on a substrate of thickness h_2 and a superfluid level h_1 in the gaps. (b) Equivalent lumped element LCR circuit for a capacitively coupled CPW resonator, showing the additional capacitances C^{He} and C_κ^{He} in parallel due to the presence of the superfluid film, see discussion in text.

5.1 Superconducting Resonators as Helium-Level Meters

This section presents the underlying theory for the experiments discussed in sections 5.2 and 5.3. Following a derivation of general frequency shift expressions, various methods for estimating the shifts analytically in the thick-film limit (section 5.1.2) and numerically by finite-element simulation in the thin-film limit (section 5.1.3) are presented.

5.1.1 Helium-Induced Frequency Shifts

A film of superfluid helium covering a coplanar waveguide resonator acts like an additional layer of dielectric that results in observable shifts in resonance frequency. The coplanar waveguide structure represents a micro channel geometry as discussed in section 2.3.4 and can therefore be filled with liquid helium by capillary action, provided the radius of curvature exceeds the gap width $R_c \gtrsim w$ where $w = (b - a)$. The situation is shown schematically in Fig. 5.1 a. The presence of the dielectric liquid ($\varepsilon_{\mathrm{He}} \simeq 1.057$) increases the energy density $\mathcal{E}$ in the gaps and therefore the effective capacitance per unit length C_ℓ of the resonator. The effect of the superfluid can be modeled as an additional capacitance per unit length in parallel $C_\ell^* = C_\ell + C_\ell^{\mathrm{He}}(h_1)$, where h_1 is the thickness of the superfluid film in the gaps with $C_\ell^{\mathrm{He}}(0) = 0$. For $R_c \gg w$ the thickness h_1 is to a good approximation uniform, but C_ℓ^{He} depends in general on the curvature profile in the gap. Using the parallel LCR oscillator mapping of section 3.2.3 for a capacitively coupled resonator, this corresponds to a shift in

resonance frequency that depends on the amount of superfluid in the gaps:

$$\omega_0(h_1) = \sqrt{\frac{1}{L_\ell(C_\ell + C_\ell^{\mathrm{He}}(h_1))}} \cdot \frac{\pi}{\ell} \approx \sqrt{\frac{1}{L(C + C_{\mathrm{He}}(h_1))}} \tag{5.1}$$

where L and C are the mapped quantities from eq. (3.50) and $C_{\mathrm{He}}(h_1) = (1/2)C_\ell^{\mathrm{He}}(h_1)\ell$. The mapped LCR circuit is shown in Fig. 5.1 b. For an interdigitated or gap coupling capacitor such as the ones discussed in section 3.2.5, the coupling capacitor structures will be filled with superfluid as well, which leads to an additional coupling capacitance C_κ^{He} in parallel. The resulting effect on ω_0 and the external quality factor is small since $C_\kappa^{\mathrm{He}} << C$ and will be neglected for the moment. The characteristic impedance of the resonator in the presence of superfluid helium is given by

$$Z_0 = \sqrt{\frac{L_\ell}{(C_\ell + C_\ell^{\mathrm{He}}(h_1))}} \tag{5.2}$$

From eq. (5.1) we find for the helium-induced shift in resonance frequency

$$\Delta\omega(h_1) = \omega_0 - \omega_0(h_1) = \omega_0 \left(1 - \sqrt{\frac{1}{1 + C_\ell^{\mathrm{He}}(h_1)/C_\ell}}\right) \tag{5.3}$$

which shows that the frequency shifts down in the presence of superfluid, as expected. As shown in section 2.3.4, the gap level h_1 depends on the radius of curvature and the absolute level of superfluid in a reservoir below the chip. In the following two sections we will discuss different ways of calculating the magnitude of the helium-induced capacitance $C_\ell^{\mathrm{He}}(h_1)$ and the frequency shifts $\Delta\omega(h_1)$. Since most of the electromagnetic field is concentrated in the gap region the sensitivity of the resonance frequency to small changes in the helium level h_1 can be substantial. At moderate quality factors of $Q \sim 2.5 - 5 \times 10^4$ we have line widths of $\delta\nu_0 \simeq 50 - 100$ kHz at $\nu_0 = 5$ GHz , making it in principle possible to resolve relative shifts as small as a fraction of a percent $\delta\nu_0/\nu_0 \simeq 10^{-5}$ %. This method of helium level measurement is similar to the capacitance measurements in conventional electrons on helium experiments [101, 204, 205]. However, here we take advantage of the high quality factors possible in superconducting resonant structures to significantly increase the achievable resolution of such measurements. As shown in section 5.2 this allows resolving the reservoir fill dynamics on a superconducting chip, detecting level changes down to a few nm.

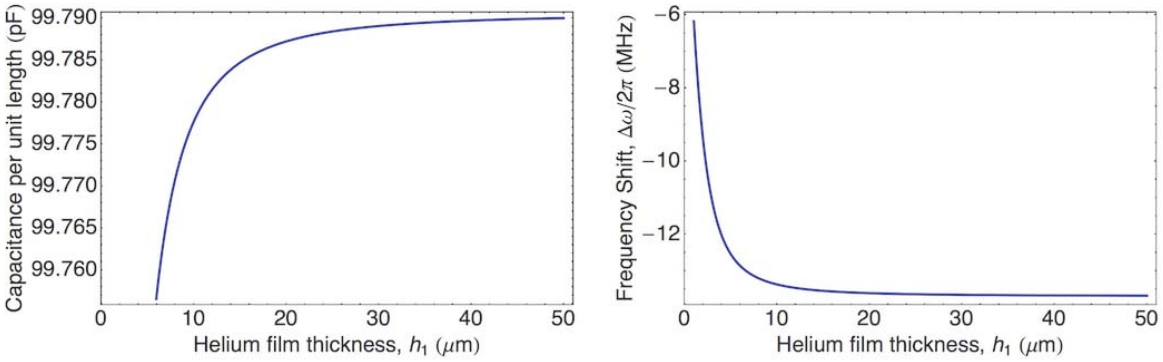

Figure 5.2.: Conformal mapping calculations of liquid helium effects in the thick-film limit. (a) Capacitance per unit length of a waveguide with $a = 1\,\mu$m, $b = 4\,\mu$m on a c-plane sapphire substrate $\varepsilon_{\mathrm{sub}} = 9.4$ as a function of helium film thickness h_1. (b) Calculated frequency shift for a $\omega_0/2\pi = 5$ GHz resonator obtained via eq. (5.3).

5.1.2 Analytic Approximations: Thick-Film Limit

In the limit of thick films of superfluid $h_1 \gg d$ where the film thickness exceeds the depth of the waveguide microchannels, we can model the helium-waveguide system as a CPW structure sandwiched between two different dielectrics of height h_1, h_2 and dielectric constant $\varepsilon_1 = \varepsilon_{\mathrm{sub}}$ and $\varepsilon_2 = \varepsilon_{\mathrm{He}}$ (see Fig 5.1 a). In the limit of vanishing metallization thickness $d \ll h_1, h_2$, we have via conformal mapping for the capacitance per unit length due to the dielectric substrate [161] (see also section 3.2.5)

$$C_{\mathrm{sub}} = 2\varepsilon_0(\varepsilon_{\mathrm{sub}} - 1)\frac{K(k_2)}{K(k_2')} \tag{5.4}$$

where $K(\cdot)$ denotes the complete elliptical integral of the first kind and the geometry-dependent quantities are given by

$$k_2 = \frac{\sinh\left(\frac{\pi a}{2h_2}\right)}{\sinh\left(\frac{\pi b}{2h_2}\right)} \quad , \quad k_2' = \sqrt{1 - k_2^2} \tag{5.5}$$

with a, b, h_2 as shown in Fig. 5.1 a. Analogously, the capacitance due to the liquid helium film is given by

$$C_{\mathrm{He}} = 2\varepsilon_0(\varepsilon_{\mathrm{He}} - 1)\frac{K(k_1)}{K(k_1')} \tag{5.6}$$

with

$$k_1 = \frac{\sinh\left(\frac{\pi a}{2h_1}\right)}{\sinh\left(\frac{\pi b}{2h_1}\right)} \quad , \quad k_1' = \sqrt{1 - k_1^2} \tag{5.7}$$

where h_1 is the helium film thickness. Finally, the vacuum capacitance is written as

$$C_{\mathrm{vac}} = 4\varepsilon_0 \frac{K(k_0)}{K(k_0')} \quad , \quad k_0 = \frac{a}{b} \quad , \quad k_0' = \sqrt{1-k_0^2} \tag{5.8}$$

The total capacitance to ground per unit length is the parallel combination of the different contributions $C_T = C_{\mathrm{He}} + C_{\mathrm{sub}} + C_{\mathrm{vac}}$. The frequency shifts in the thick-film regime can then be calculated using eq. (5.3) with $C_\ell^{\mathrm{He}} = C_{\mathrm{He}}$ and $C_\ell = C_{\mathrm{sub}} + C_{\mathrm{vac}}$. The total capacitance per unit length in the presence of helium and the corresponding resonance frequency shifts for a 5 GHz resonator on a sapphire substrate $\varepsilon_{\mathrm{sub}} = 9.4$ of thickness $h_2 = 500\,\mu$m are shown in Fig. 5.2 as functions of film thickness h_1. The shifts are on the order of $\Delta\omega/\omega_0 \simeq 0.1 - 0.3\,\%$, well within the frequency resolution of typical resonators with line widths of $\delta\nu_0 \sim 100$ kHz at GHz frequencies. The shift saturates as h_1 increases since the capacitance per unit length becomes insensitive to the level. This is as expected since most of the electromagnetic field is concentrated in the CPW plane and the gap region.

5.1.3 Numerical Simulations: Thin-Film Limit

For thin films of superfluid $h_1 \lesssim d$ on the order of the metallization thickness, the profile of the waveguide structure becomes important and the analytic expressions of section 5.1.2 are no longer applicable. In that case, we can use numerical simulations of the energy density in the waveguide structure to calculate the change in effective capacitance and the shifts in resonance frequency as functions of helium level. The method presented here assumes a flat helium surface with uniform h_1 in the gaps. Dependence on curvature and film profile are discussed in section 5.2 below. The total capacitance per unit length of a coplanar waveguide can be approximated by

$$C_{\mathrm{T}} = \frac{2}{V_{\mathrm{rms}}^2} \int_A \mathcal{E}(\mathbf{r}) dA = \frac{2E_A}{V_{\mathrm{rms}}^2} \tag{5.9}$$

where V_{rms} is the rms voltage between center pin and ground plane, A is the cross-sectional area of the waveguide, E_A the total energy and $\mathcal{E}(\mathbf{r})$ the energy density in the plane with $\mathbf{r} = (x, z)^T$. The total energy density can be divided into the energy density in the dielectric substrate, in the vacuum and in the dielectric superfluid:

$$E = \int_{\mathrm{substrate}} \mathcal{E}(\mathbf{r}) dA + \int_{\mathrm{vacuum}} \mathcal{E}(\mathbf{r}) dA + \int_{\mathrm{helium}} \mathcal{E}(\mathbf{r}) dA = E_{\mathrm{sub}} + E_{\mathrm{vac}} + E_{\mathrm{He}} \tag{5.10}$$

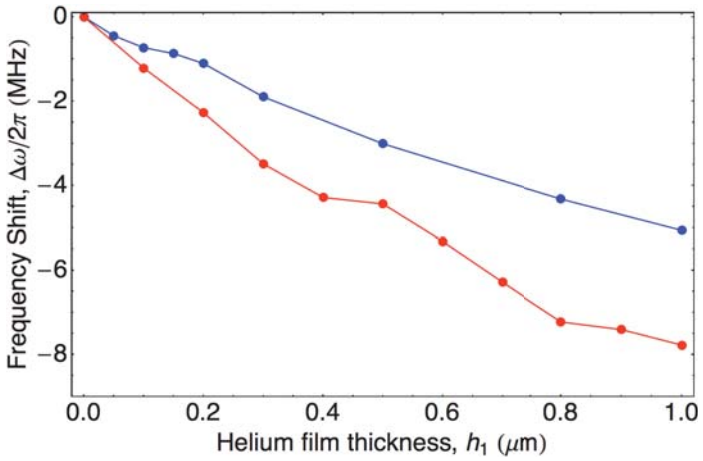

Figure 5.3.: Helium-induced frequency shifts in the thin film limit, obtained by finite-element simulation using the method outlined in section 5.1.3. Results for two different CPW geometries are shown, a conventional $Z_0 = 50\,\Omega$ CPW with metallization thickness $d = 200$ nm, $a = 5\,\mu$m, $b = 9.5\,\mu$m and $\omega_0/2\pi = 5$ GHz (blue), and a high-aspect ratio CPW (red) with different ground plane ($d = 800$ nm) and center pin ($d = 40$ nm) metallization thicknesses and $Z_0 = 80\,\Omega$. The high-aspect ratio design (with a DC-biased center pin) was used in the experiments of sections 5.2 and 5.3.

such that we can split the total capacitance up into different contributions $C_\mathrm{T} = C_\mathrm{vac} + C_\mathrm{sub} + C_\mathrm{He}$. The energies can be calculated from the in-plane electric field and displacement vectors $\mathbf{E} = (E_x, E_y, 0)$ and $\mathbf{D} = (D_x, D_y, 0)$:

$$E_A = \frac{1}{2}\int_A \mathbf{E}\cdot\mathbf{D}\,dA = \frac{1}{2}\int_A (E_x D_x + E_y D_y)\,dA \tag{5.11}$$

We can determine the total energy of each of the different regions using finite-element simulations in *Ansoft Maxwell 2D*. Mapping out the frequency shifts as a function of superfluid level in the gaps can then be achieved with the following procedure:

1. Determine the total energies in substrate and vacuum E_sub and E_vac by FE simulation of the geometry in the absence of any helium. The FE simulation gives the field vectors $\mathbf{E} = (E_x, E_y, 0)$ and $\mathbf{D} = (D_x, D_y, 0)$ at every point of the simulated mesh. The total energy in the waveguide cross-section can then be calculated using eq. (5.11) by integrating over the entire simulated region [1]. This fixes C_ℓ in equation (5.3).

2. Set a helium level in the gap h_1, simulate the electric field and displacement vectors, calculate the total energy per unit length E and the total capacitance per unit length C_T via (5.9) and get the change in capacitance per unit length due to the superfluid via $\Delta C_\mathrm{He} = C_T - C_\ell$ where C_ℓ was determined in step 1. Use eq. (5.3) to find the frequency

[1] Note that in *Maxwell 2D* the integral over the dot product can be calculated directly after completion of the simulation using the *Field Calculator* tool.

shift for a given bare frequency $\omega_0/2\pi$.

3. Repeat 2. for desired set of helium levels h_j. Calculate frequency shift for each level.

Care must be taken to avoid mesh regeneration between successive simulation runs as the position and number of mesh nodes influences the energy density. That is, when changing the film thickness h_1 the field and displacement vectors have to be evaluated at the same points in the plane. The results of such frequency shift simulations for two different waveguide geometries are shown in Fig. 5.3. A conventional 50 Ω CPW with metallization thickness $d = 200$ nm, $a = 5\,\mu$m, $b = 9.5\,\mu$m and $\omega_0/2\pi = 5$ GHz (blue) as well as a high-aspect ratio CPW with different ground plane ($d = 800$ nm) and center pin ($d = 40$ nm) metallization thicknesses (red) are shown. The frequency shifts are roughly linear in superfluid level h_1 in the thin-film regime for both structures. The high-aspect ratio CPW geometry, which was used in the experiments of sections 5.2 and 5.3, is more sensitive to the helium level, which makes sense since the energy density is more strongly concentrated in the gap for this design. Taking the derivative of the interpolation function yields a theoretical sensitivity of $\partial\Delta\nu/\partial h_1 \sim 4$ kHz/nm for the conventional geometry and $\partial\Delta\nu/\partial h_1 \sim 8$ kHz/nm for the high-aspect ratio design.

5.2 Fill Dynamics and Level-Meter Measurements

In the previous sections we saw that the resonance frequency of a coplanar waveguide cavity is highly sensitive to the level of superfluid in the resonator gaps, both in the limit of thin (section 5.1.3) and thick films (section 5.1.2) . In this section we demonstrate how such helium-induced frequency shifts can be used to accurately measure the film thickness. Following a discussion of reservoir fill dynamics and the dependence of the film profile on radius of curvature, we present measurements in which the different filling regimes can be distinguished by resolving film thicknesses ranging from 30 nm to 20 μm. The ability to accurately monitor and adjust the superfluid level is a key ingredient for experiments in the single- and many-electron regimes. We will make use of this technique in both low frequency lock-in measurements (chapter 6) and GHz detection of electrons trapped in a resonator (chapter 7).

In section 2.3.4 we saw how the gaps in a micro-channel structure or fractionated surface can be filled by capillary action provided the radius of curvature $R_c \gg w$ exceeds the

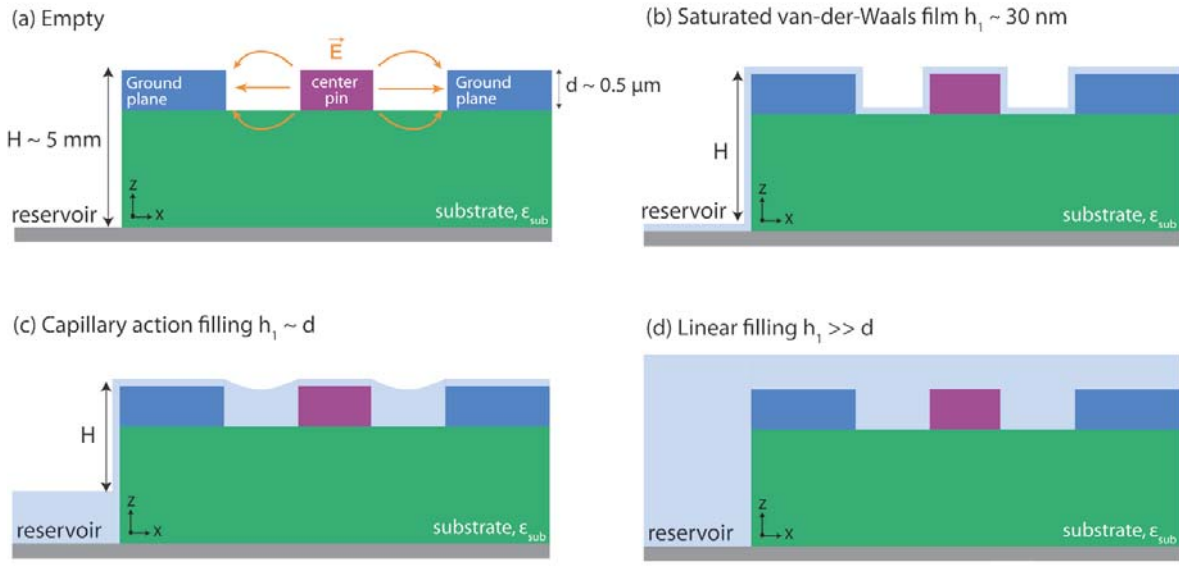

Figure 5.4.: Illustration of superfluid helium reservoir filling regimes. The gaps of a coplanar waveguide resonator structure are filled with superfluid helium from a low-lying reservoir by capillary action. (a) Empty reservoir and gaps with the electric field lines indicated in orange. (b) Low levels of superfluid in the reservoir lead to a thin, continuous van-der-Waals film of 30 nm thickness coating the surface of the waveguide due to the zero viscosity in the superfluid phase. (c) At higher levels (smaller H), the radius of curvature starts to exceed the gap width and the gaps are filled by capillary action. Further decreasing H increases R_c and the film thickness at the center of the gap. (d) Once the reservoir is completely filled, we enter the thick film regime where the helium level on the chip increases linearly. The capacitance per unit length becomes insensitive to film thickness in this regime.

distance between elevations on the surface. The radius of curvature $R_c(H) = \sigma/\rho g H$ is determined by the distance H between the channel top and the bulk superfluid surface in a liquid helium reservoir positioned below the device. The film profile in the gaps has a semi-circular shape given by eq. (2.38) and the film thickness at the gap center is linear in H, see eq. (2.39). In our high-aspect ratio CPW implementation, the coplanar waveguide gaps form a micro-channel geometry of width $w_{\mathrm{G}} = 8 - 10\,\mu$m and depth $500 - 1000$ nm with a $w_{\mathrm{CP}} = 2 - 5\,\mu$m wide center pin electrode, similar to the channel geometries typically used in electrons on helium experiments [129, 206, 207]. The superfluid reservoir is realized as a cylindrical container of height $H = 5$ mm and radius $r = 3.175$ mm (1/4 inch drill), drilled into the bottom plate of the hermetically-sealed sample holder, see Fig. 4.3. The 2×7 mm chips are positioned $\sim$ 5.5 mm above the bottom of the cylindrical reservoir, mounted on a PC board in a hermetically-sealed copper box at 20 mK. Depending on the bulk superfluid level in the reservoir, we can distinguish between several different filling regimes which correspond to different curvature radii and film profiles on the chip. Increasing the reservoir level in small increments and monitoring the cavity resonance frequency will allow us to

transition from thin van-der-Waals films to capillary action profiles to flat bulk films. The four main filling regimes are illustrated in Fig. 5.4 and briefly discussed below:

- **(0) Empty Reservoir** (Fig. 5.4 a): Without superfluid helium, the field in the waveguide gaps is just the unperturbed electromagnetic field and the resonator is at its unshifted resonance frequency $\omega_0/2\pi$.

- **(I) Saturated van-der-Waals Film** (Fig. 5.4 b): At low levels of helium in the reservoir (large H), a thin, continuous van-der-Waals film of about ~ 30 nm thickness forms as the superfluid evenly coats all surfaces of the chip due to the vanishing viscosity, see section 2.3 for details. As a consequence, the frequency of the resonator will shift by a small amount $\Delta\omega(h \simeq 30\,\mathrm{nm})$ according to (5.3), see also the numerical results in Fig. 5.3. In this regime, the level in the reservoir is too low for the radius of curvature to exceed the gap width and hence the waveguide gaps are not filled by capillary action.

- **(II) Capillary Action/Surface Tension** (Fig. 5.4 c): As the reservoir level increases (decreasing H), the radius of curvature R_c increases to a point where surface tension overcomes gravity and the gaps are filled with a self-stabilized capillary action film (section 2.3.4). In this regime, we expect the resonance frequency to shift by a few MHz initially but to remain stable and mostly unchanged as more helium is added to the cell. The shift $\Delta\omega(h_1)$ remains roughly constant even though the reservoir level changes since the gaps are already fully filled once $R_c \gg w$. Further decreasing H only increases the radius of curvature, which changes the meniscus of the film profile in the gaps by a small amount but does not significantly change the film thickness h_1 anymore. Electrons on helium experiments are typically operated in this regime because the film is thick and self-stabilized and the profile is flat up to some small curvature (finite R_c).

- **(III) Linear Filling** (Fig. 5.4 d): Once the reservoir is completely filled, adding more helium to the cell just linearly increases the helium film thickness above the resonator. In this regime, the film is no longer self-stabilized by capillary action and we expect the level of helium to fluctuate as a consequence of vibrations in the setup. The fluctuating helium level $h = h_0 + \delta h$ translates into a fluctuating capacitance per unit length of the waveguide and hence we expect the resonance frequency to fluctuate about $\Delta\omega(h_0)$. The time scales of such classical level oscillations (e.g. due to vibrations from the turbopumps or pulse tubes connected to the dilution refrigerator) are typically in the low

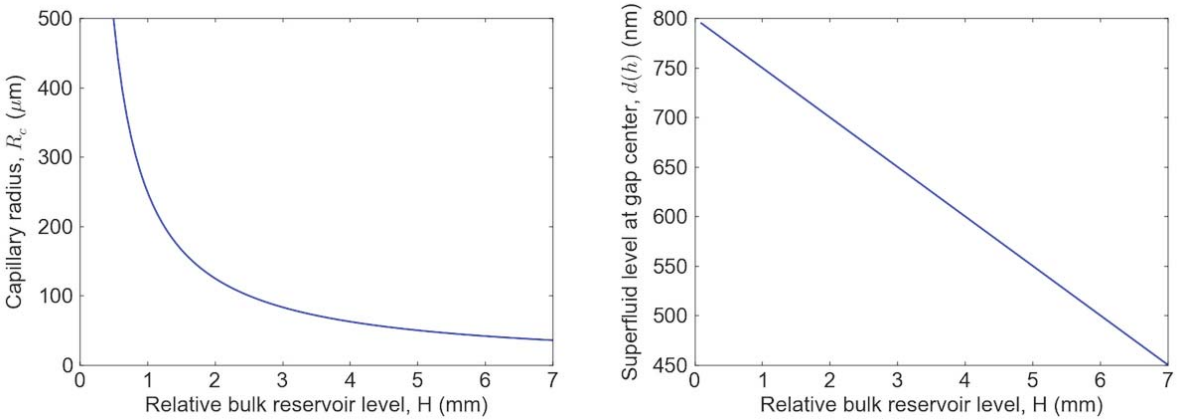

Figure 5.5.: (a) Capillary radius of curvature R_c as a function of reservoir helium level relative to the chip surface. R_c diverges as the reservoir fills up. (b) Superfluid film thickness at the center of the waveguide gap as a function of relative reservoir level for a gap of depth $d = 800$ nm, calculated using expression (2.39). The film thickness is linear in H in this approximation.

frequency regime on the order of a few Hz. Since the amplitudes of such level fluctuations is presumably small compared to the absolute helium level, we expect them to be noticeable primarily at low levels of helium in the linear filling regime. As we go to thicker films $h \gg d$, the frequency shift will saturate at some point $\Delta\omega_{\max}(h)$ since the capacitance per unit length becomes insensitive to the helium level, as expected from the models discussed in section 5.1.

Device and Reservoir Geometry

To observe the fill dynamics and resolve the different regimes experimentally, we measure the resonance frequency of a capacitively-coupled coplanar waveguide resonator in transmission and increase the amount of superfluid helium in the sample cell in small increments. Helium is supplied to the cell mounted at 20 mK via the hermetically-sealed capillary line setup discussed in section 4.1.2. The data presented in this section was taken using a DC-biased center pin resonator. Helium filling experiments have also been performed with a variety of other resonator designs, including inductively-coupled $\lambda/2$ and $\lambda/4$ resonators (see the low-frequency density experiments in chapter 6) and regular capacitively-coupled resonators. The DC-biased center pin device consists of 1000 nm of sputtered Nb on a c-plane Sapphire substrate, which defines the ground plane, and 100 nm of deposited Al defining the center pin. The ground planes form a single gap of depth $d = 1000$ nm and width $w = 8\,\mu$m. The capillary radius of curvature and the film thickness at the center of the gap are shown in Fig. 5.5 for the device and reservoir geometry used in this experiment. A DC bias lead is

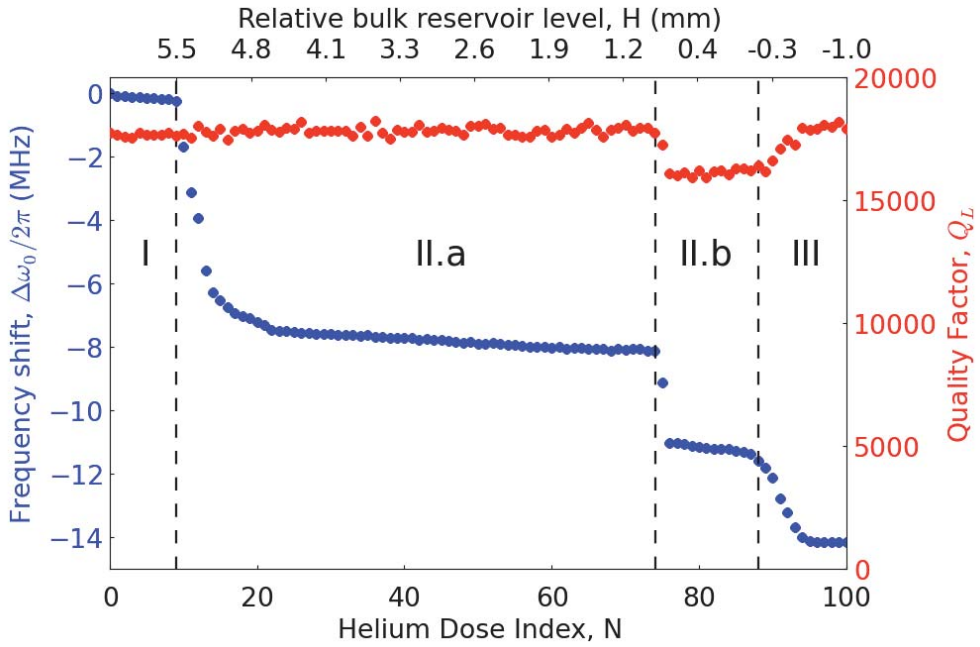

Figure 5.6.: Superfluid helium level-meter experiment: Resonance frequency shift $\Delta\omega_0/2\pi$ (blue) and loaded quality factor Q_L (red) measured as functions of the number of helium doses supplied to the sample cell, which translates to the relative bulk reservoir levels shown on the top axis. Here, the levels H have been estimated by determining the dose index at which the reservoir is completely filled ($H \sim 0$ at $N = 86$). Four different regimes can be clearly distinguished, indicated by dashed lines and numbers: (I) Van-der-Waals film ($N = 1 - 9$), (II.a) capillary action filling of the gaps ($N = 10 - 75$), (II.b) capillary action film suspended from the shim ($N = 76 - 86$) and (III) linear filling ($N > 87$), see text for details. Data for this specific device taken from measurements performed at the University of Chicago.

connected directly to the center pin of the resonator at a voltage anti-node of the fundamental mode such that loss of microwave photons through the bias port is effectively suppressed by symmetry. This design allows applying a tunable DC voltage offset to the center pin, in addition to microwave and RF voltages at the input port, while maintaining high quality factors. The DC-biased resonator design and its use in many-electron experiments is discussed in more detail in chapter 7. For the remainder of this section the center pin is held at DC ground potential. We will take advantage of the biasing capabilities in section 5.3 to tune the helium level and film meniscus in-situ.

Resolving the Filling Regimes

The device is characterized by a bare resonance frequency of $\omega_0/2\pi = 4.792$ GHz and a loaded quality factor of $Q_L \simeq 17760$ at $P_{\text{in}} = -45$ dBm (output power of the RF generator), measured using the setup described in section 4.1. We increase the amount of superfluid helium in the sample cell in small increments of $\Delta V \sim 0.01$ cm^3 liquid volume and fill up

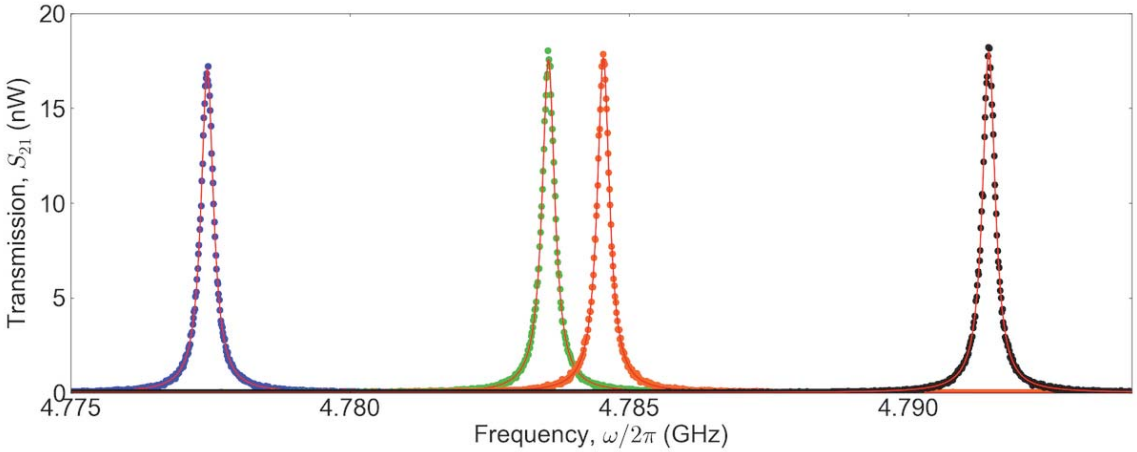

Figure 5.7.: Raw transmission spectra S_{21} and Lorentzian fits in different filling regimes, measured at different positions in Fig. 5.6: (I) Van-der-Waals thin film regime (black, $N = 5$ increments in Fig. 5.6), (II.a) first (red, $N = 40$) and (II.b) second capillary action film (green, $N = 82$) and (III) linear filling regime (blue, $N = 95$).

the reservoir (i.e. decrease H). The resonance frequency and quality factor of the cavity are monitored in transmission during the filling. The results of such a helium filling experiment are presented in Fig. 5.6, which shows frequency shift $\Delta\omega/2\pi$ and quality factor Q_L as functions of the number of increments and the estimated reservoir level H, the distance between the bulk superfluid level and the chip surface. Sample transmission spectra and Lorentzian fits for different helium levels are shown in Fig. 5.7, at the helium levels indicated by dashed lines in Fig. 5.6. Each datapoint in Fig. 5.6 corresponds to adding one dose of helium.

We can clearly distinguish four different regimes in the frequency shift data of Fig. 5.6. Starting from the left at $N = 0$, the first few increments lead to small frequency shifts of -100 to -200 kHz, corresponding to the van-der-Waals thin-film regime shown in Fig. 5.4 b. The frequency is largely constant here as the film thickness quickly saturates at $h_1 \sim 30$ nm. The observed shift of $\Delta\omega/2\pi \simeq -150$ kHz is consistent with the thin-film numerical simulations of section 5.1.3. As more helium is added, the level in the reservoir increases and the radius of curvature R_c becomes on the order of the gap width w, which manifests itself in a rapid increase in frequency shift from $\Delta\omega/2\pi \simeq -200$ kHz to -7.4 MHz as the gap starts filling up by capillary action. Using the finite-element simulations of section 5.1.3, a shift of $\Delta\omega/2\pi \simeq -7.4$ MHz maps to an estimated film thickness in the waveguide gap of $h_1 \sim 900$ nm, indicating that the gap has been filled almost completely [2]. Further increasing the amount of helium in the cell, we enter a regime where the frequency stays roughly constant, increasing over a small range $\Delta\omega/2\pi \simeq -7.4$ to -8.1 MHz over the following 50 doses

[2] Note that curvature effects are ignored in the finite element simulations.

($N = 20 - 70$ in Fig. 5.6). This region corresponds to the capillary action regime (Fig. 5.4 c) where the gap is filled with a self-stabilized film of helium. The observed shifts in this regime are in good agreement with the numerical simulations carried out for this device geometry, see Fig. 5.3. The small increases in frequency shift in this "flat" regime are due to further increases in capillary radius $R_c = \sigma/\rho g H$ and decreases in curvature of the helium surface in the gap. Once $R_c \gg w$, the gap is essentially filled and further changes in R_c have only a small effect on the film thickness in the gap. Based on the thin-film simulations of section 5.1.3, the small increase in frequency shift in the flat capillary regime of ~ 0.7 MHz corresponds to a change in film thickness of $\Delta h_1 \sim 180$ nm. As the reservoir level increases and $H \to 0$, the radius of curvature becomes on the order of the chip dimensions and eventually starts to diverge. We attribute the abrupt jump in frequency after $N = 74$ doses to the formation of a thick self-stabilized film which spans the entire chip and is supported by the shim covering the sample (the shim can be seen in Fig. 4.3 a). The reservoir is not completely filled at this point but the radius of curvature $R_c \gtrsim 2$ mm is large enough to support a curved film across the entire chip, leading to a second capillary action regime of relatively constant frequency shifts $\Delta\omega/2\pi \simeq -11.04$ to -11.23 MHz ($N = 75 - 85$ in Fig. 5.6). As the radius of curvature diverges, the stability of the film decreases and the superfluid film on the chip becomes sensitive to mechanical vibrations and classical fluctuations in the reservoir level. This manifests itself in a perceived drop in quality factor Q_L in the second capillary regime, which remains otherwise constant in the van-der-Waals and first capillary action regimes. Once the reservoir has been completely filled ($H = 0$), the helium level on the chip simply increases linearly with each dose, leading to a corresponding increase in frequency shift from $\Delta\omega/2\pi \simeq -11.4$ to -14 MHz over the next 7 doses. The frequency shift eventually saturates at -14.145 MHz as the capacitance per unit length of the resonator becomes insensitive to the level, in agreement with the thick-film calculations of section 5.1.2 which show frequency shift saturation at ~ -14 MHz above $h_1 \gtrsim 20\,\mu$m. Raw transmission spectra recorded in the four different regimes are shown in Fig. 5.7. The transmission peaks are separated by many line widths across the different regimes and can be easily resolved.

Estimating Film Thickness Sensitivities

One can to map frequency shifts directly to superfluid film thicknesses and estimate the sensitivity of the resonance frequency to changes in film thickness $\partial f_0/\partial h$ in the different filling regimes. In the van-der-Waals regime, we have a final film thickness of $h_1 \sim 30$ nm

with a measured frequency shift of $\Delta\omega_0/2\pi = -190$ kHz, giving a sensitivity of $\partial f_0/\partial h \sim 6.4$ kHz/nm. In the subsequent capillary filling regime we observe a sharp increase in frequency shift from -190 kHz to -7.4 MHz ($N = 10 - 22$ in Fig. 5.6), which maps to an increase in film thickness in the gap to $h_1 \sim 900$ nm based on the finite-element simulations. In the subsequent 'flat' capillary regime ($N = 22 - 70$ in Fig. 5.6) we find a further increase in frequency shift to a final value of $\Delta\omega_0/2\pi \sim -8.1$ MHz. Assuming the gap is completely filled at this point ($h_1 = 1\,\mu$m), this equates to a total change in thickness in the capillary regime of $\Delta h_1 \sim 970$ nm and a sensitivity of $\partial f_0/\partial h \sim 8$ kHz/nm.

Film Stability and Reservoir Level Fluctuations

As shown in section 2.3, the sensitivity to fluctuations in the bulk reservoir level can be reduced by several orders of magnitude in a micro-channel filled by capillary action:

$$\frac{\partial R_c}{\partial H}\frac{\partial d}{\partial R_c} = \frac{w}{H} \sim 2.6 \times 10^{-3} \tag{5.12}$$

for a channel width of $w = 8\,\mu$m and $H = 3$ mm. We can place an estimated upper bound on the size of level fluctuations in the micro-channel and reservoir region using the measured quality factors. As can be seen from Fig. 5.6, no noticeable decrease in quality factor is observed in the capillary action regime (II.a), which implies that fluctuations in resonance frequency are limited to at maximum one linewidth $\delta\omega_0/2\pi \lesssim \kappa/2\pi$ or

$$\frac{\delta\omega_0}{\omega_0} \lesssim \frac{1}{Q} \approx 0.5 \times 10^{-4} \quad , \quad \delta\omega_0/2\pi \lesssim 240\,\text{kHz} \tag{5.13}$$

for the measured device. Assuming a sensitivity to changes in the gap film thickness of 8 kHz/nm this implies maximum fluctuations of about $\delta h_1 \sim 30$ nm, which translates into bulk reservoir fluctuations on the order of $10 - 20\,\mu$m using (5.12). This simple estimate is, however, likely excessively conservative. Using single-shot measurements of the cavity in transmission (with a network analyzer) and extracting $\omega_0/2\pi$ from each measurement, we estimate the root-mean square frequency fluctuations at a fixed gap level of $h_1 \sim 900$ nm in the capillary action regime at $\delta\omega_0^{(\text{rms})}/2\pi \approx 16.6$ kHz based on over 16000 consecutive measurements. This in turn implies rms level fluctuations in the gap of only $\delta h_1^{(\text{rms})} \approx 2.6$ nm.

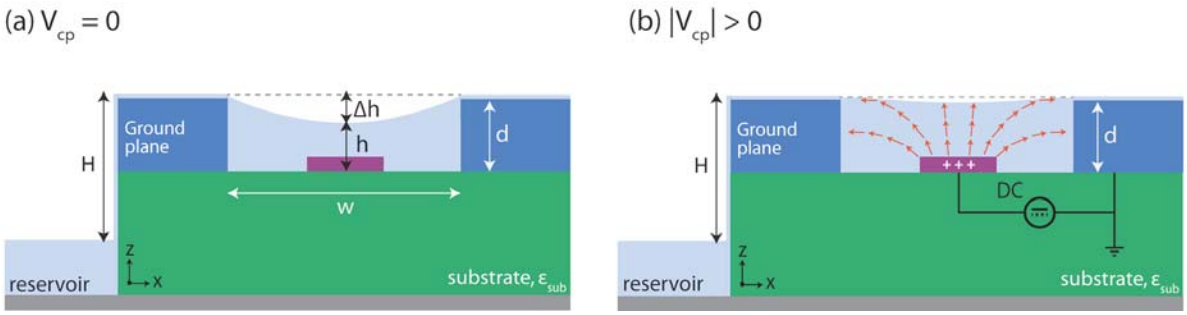

Figure 5.8.: Illustration of helium level tuning in a DC-biased CPW resonator. (a) Curved capillary helium film of thickness h at the gap center at zero center pin bias $V_{\mathrm{cp}} = 0$. The meniscus is determined by the radius of curvature R_c, which is set by the relative bulk reservoir level H. (b) Capillary film for non-zero DC bias $|V_{\mathrm{cp}}| > 0$. The curvature decreases as more superfluid is drawn into the high-field region in the gap, leading to an increase in level h and corresponding frequency shift $\Delta\omega/2\pi$. DC electric field lines are sketched in orange.

5.3 Helium-Level Tuning

In this section, we demonstrate how the superfluid level in the resonator gaps can be tuned in-situ by an applied DC voltage, using a high-aspect ratio resonator with a DC-biased center pin. This type of device was already introduced in the previous section and will be discussed in more detail in chapter 7 in the context of electron trapping experiments. In this section, the response of the superfluid to applied voltages is measured using frequency shifts of the resonator, as discussed in section 5.2. We first derive a simple electromechanical model for the frequency shift as a function of voltage bias in section 5.3.1. Measurements of helium level tuning curves are presented in section 5.3.2.

5.3.1 Electromechanical Force on Helium Film Surface

In the absence of any applied voltages, the equilibrium radius of curvature $R_c = \sigma/\rho g H$ and the helium film profile in a micro-channel geometry are determined by surface tension and gravity. As shown in section 2.3.4, the thickness of a self-stabilized superfluid film in a micro-channel gap can be expressed in terms of the channel geometry and reservoir level by assuming a semi-circular surface profile

$$h = d - z(w/2) = d - \frac{\sigma}{\rho g H}\left(1 - \sqrt{1 - \left(\frac{\rho g H w}{2\sigma}\right)^2}\right) \approx d - \frac{w^2}{8}\frac{\rho g H}{\sigma} \tag{5.14}$$

where h is the film thickness at the center of the gap, d the height and w width of the gap and H the liquid level in the reservoir, see the illustration in Fig. 5.8a. The force per unit length

on the film surface at the gap center due to surface tension is approximately given by

$$\mathcal{F}_{\rm st} \simeq \frac{\sigma w}{R_c} = \frac{8\sigma}{w}\Delta h \quad , \quad \Delta h = d - h \tag{5.15}$$

which is determined by the ratio of channel width to capillary radius. In a DC-biased resonator such as the one used in section 5.2, the center pin can be biased with a DC voltage $V_{\rm cp}$ in addition to any electromagnetic fields at RF and microwave frequencies. The situation is shown schematically in Fig. 5.8 b for $|V_{\rm cp}| > 0$. An applied DC voltage in the gap leads to an additional electromechanical force on the superfluid film, analogous to a piece of dielectric pulled into the high field region in a parallel plate capacitor. We expect an increase in DC voltage to lead to an increase in film thickness in the gap as the superfluid experiences a larger effective field in the gaps, resulting in a pressure to raise the helium level. The exact electric field vectors can be obtained numerically by finite-element simulations. As a first crude approximation we can take the field to be that of a parallel plate capacitor $E = V_{\rm cp}/w$ such that the energy difference between an empty gap and one filled with helium of thickness Δz is approximated by

$$\Delta\Phi_{\rm em} = -\frac{1}{2}(\varepsilon_{\rm He} - \varepsilon_0)E^2 w \Delta z \ell \tag{5.16}$$

where ℓ is the length of the resonator. The corresponding electromechanical force per unit length on the film surface is thus given by

$$\mathcal{F}_{\rm em} = -(1/\ell)(\partial\Phi_{\rm em}/\partial z) \approx -(1/\ell)(\Delta\Phi_{\rm em}/\Delta z) = \frac{1}{2}(\varepsilon_{\rm He} - \varepsilon_0)\frac{V_{\rm cp}^2}{w} \tag{5.17}$$

The equilibrium film thickness at the center of the gap is found by equating surface tension and electromechanical force per unit length $\mathcal{F}_{\rm st} = \mathcal{F}_{\rm em}$:

$$\Delta h = d - h = \frac{V_{\rm cp}^2}{16\sigma}(\varepsilon_{\rm He} - \varepsilon_0) \tag{5.18}$$

where h is the film thickness at zero voltage bias. This translates into a voltage-dependent frequency shift of the resonator. Let $f(h)$ be the resonance frequency of the coplanar waveguide cavity for a given fixed level of helium h at the gap center at zero bias. Applying a DC voltage to the center pin increases the amount of superfluid in the gap such that to lowest

order

$$f(h) \approx f(d) + \frac{\partial f}{\partial h}\Delta h = f(d) + \left(\frac{\partial f}{\partial h}\right)\frac{V_{\mathrm{cp}}^2}{16\sigma}(\varepsilon_{\mathrm{He}} - \varepsilon_0) \tag{5.19}$$

and the frequency therefore shifts according to

$$f(h) - f(d) \approx \left(\frac{\partial f}{\partial h}\right)\frac{V_{\mathrm{cp}}^2}{16\sigma}(\varepsilon_{\mathrm{He}} - \varepsilon_0) \tag{5.20}$$

Here $\partial f/\partial h$ is the sensitivity of the frequency with respect to the helium level. In section 5.2, we found for the sensitivity $\partial f/\partial h \approx 5 - 10$ kHz/nm in the capillary action regime. As shown in the next section, this simple electro-mechanical model is in fairly good agreement with experiment for the given sensitivities.

5.3.2 Level Tuning in a DC-biased Center Pin Resonator

We can study the electromechanical effects on the helium surface and modulate the helium film thickness in the gap using the DC-biased center pin resonator design introduced in the fill dynamics measurements of section 5.2. The center pin of width $w = 2\,\mu$m and thickness $t = 40$ nm is connected to a *Yokogawa 7651* DC voltage supply via standard coaxial cables and eccosorb filters, see section 4.1 for details on the cryogenic circuitry. The lead electrode connects to the center pin of the resonator at a voltage node of the resonator such that coupling to the outside world and energy loss are minimized and high quality factors can be achieved. More details on this device design are presented in chapter 7. The ground planes have a thickness of $d \sim 800$ nm, realizing a micro channel of the type shown in Fig. 5.8 with an aspect ratio of about 20. We start at a fixed helium level in the gap in the capillary action regime (see Fig. 5.4 c and Fig. 5.6 in the range of $N = 20 - 70$ dose increments) by adding $N = 40$ doses of superfluid to the sample cell, which corresponds to a helium level of $\sim 0.7 - 0.8\,\mu$m at the center of the gap at zero voltage bias. We then monitor the cavity resonance in transmission while sweeping the center pin voltage from $V_{\mathrm{cp}} = +12$ to -12 V in 50 mV increments. The measured resonance frequency and loaded quality factor are shown in Fig. 5.9 as functions of V_{cp}. The simple electromechanical model expression (5.19) is plotted as a solid black line in Fig. 5.9 using a typical sensitivity of $\partial f/\partial h \sim 2$ kHz/nm for the capillary regime, which gives good agreement with measured frequency shifts. As expected, the frequency response is quadratic in applied voltage while the quality factor shows no dependence on V_{cp}. Maximum frequency shifts of $\Delta\omega_0/2\pi = 468$ kHz at $V_{\mathrm{cp}} = \pm 12$ V are

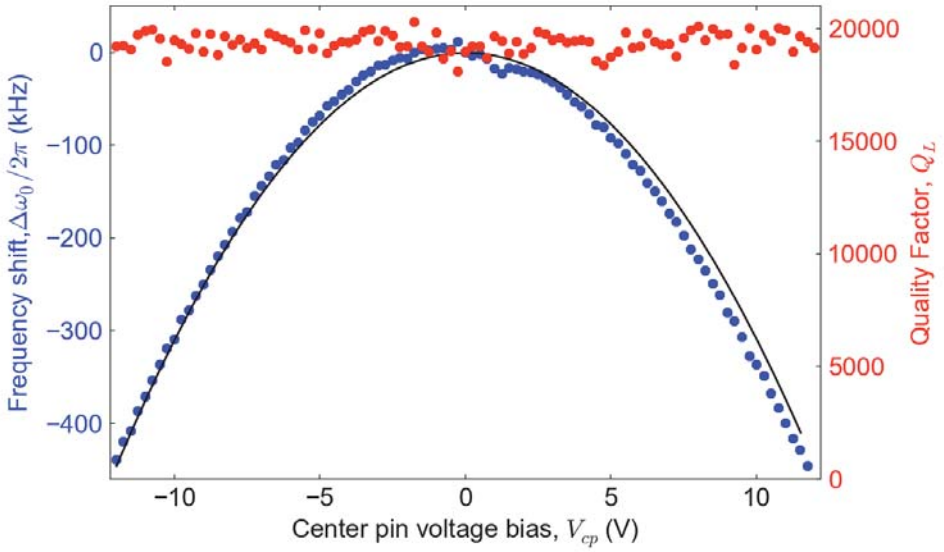

Figure 5.9.: Helium level tuning experiment in the capillary action regime: Frequency shift $\Delta\omega_0/2\pi$ (blue) and loaded quality factor Q_L (red) as functions of the DC bias V_{cp} applied to the resonator center pin. The simple electromechanical model (5.20) is shown as a black solid line for an estimated sensitivity of $\partial f/\partial h \sim 2\,\mathrm{kHz/nm}$. The voltage dependence is parabolic and roughly symmetric about $V_{\mathrm{cp}} = 0$, as expected. For this device, we observe an offset of $\Delta V_{\mathrm{cp}} \simeq 800$ mV. Data for this device taken at Yale University.

observed for this device. Using the thin film simulations of section 5.1.3, the frequency shift between zero bias and $\pm$12V corresponds to a change in film thickness of $\Delta h \simeq 120$ nm at the center of the gap. While the frequency shifts generally agree with the simple quadratic model, we observe a noticeable asymmetry with respect to zero voltage bias. Under ideal conditions the superfluid response is expected to be independent of the sign of the bias. Only the magnitude of V_{cp} should matter. Offset voltages are discussed in more detail below.

The superfluid response to a DC bias on the center pin is expected to depend on the absolute level of liquid in the gaps at zero bias. The frequency response is most sensitive to applied voltages in the thin-film van-der-Waals regime where we can go from thin films $h \sim 30$ nm to completely filled gaps $h \sim 800$ nm by applying a sufficiently large voltage. On the other hand, in the capillary action regime the gap is largely filled already and the applied voltage will lead only to small frequency shifts such as the ones shown above. Finally in the linear filling regime we expect there to be no response to applied voltages as the waveguide is already covered with a thick film of several μm at $V_{\mathrm{cp}} = 0$ and the frequency is insensitive to the small level variations caused by the non-zero bias.

5.3.3 Voltage Offsets

Positive and negative offsets from $V_{\mathrm{cp}} = 0$ are commonly observed during voltage sweeps in our DC-biased center pin devices. Those offsets are noticeable both in helium level tuning sweeps and experiments with trapped electron ensembles (see chapter 7). For example, from the data in Fig. 5.9, we extract an offset of $\Delta V_{\mathrm{cp}} \simeq -800$ mV from zero bias. While the observed voltage offset stays constant once the sample has reached base temperature, it varies from run to run between warmups of the cryostat and from device to device. Analysis of different devices and runs shows that the voltage offsets are typically on the order of $\Delta V_{\mathrm{cp}} \simeq -0.5$ to +0.5 V and appear random in magnitude from run to run but constant over the duration of each experiment.

There are a variety of possible mechanisms that could be responsible for the observed offsets. Random offset charges and stray or patch potentials on electrode surfaces are commonly observed in μm-scale particle traps, for example in microchip ion traps [208, 209]. Stray and patch offsets largely result from non-uniform surface potentials due to the adsorption of oxides and surface contamination of the electrodes, as well as from the random crystallographic orientations present on real metal surfaces [210]. Another possible cause are thermoelectric voltages on the coaxial cables connecting the chip at 15 mK and the room temperature DC sources, which are the result of thermal differences between dissimilar metals. A temperature gradient across a metal interface leads to the diffusion of charge carriers from the high to the low temperature side, which in turn leads to a corresponding voltage (Peltier-Seebeck effect).

The origins of the observed offsets are not well understood at this point and will require further experimental investigation in the future, possibly by varying device geometries. While it is in principle possible to compensate for those offsets once they have been measured, they are likely non-uniform along the length of the resonator if caused by patch potentials or offset charges on the chip. In that case, the offset, measured for example in a helium level tuning experiment, represents an average across the resonator length. Non-uniform potentials near trap electrodes can lead to local deformations of the effective potential seen by electrons on the helium surface, which are difficult to compensate for and will require careful measurement of the electron motional energy spectra. This can be particularly problematic for trap loading schemes which rely on simulated electrostatic potentials, a point which we will come back to in chapter 8.

6 On-Chip Detection of a Two-Dimensional Electron Gas on Helium

An important prerequisite for circuit QED experiments with electrons on helium consists of demonstrating that electrons can be generated and trapped on a superconducting chip at sufficiently high densities and milli-Kelvin temperatures. While experiments with electrons on helium have been carried out routinely for some time, the implementation of the circuit QED architecture proposed in this thesis presents several new challenges due to the much smaller confining geometries (sub-μm size quantum dots, few-electron traps) and ultra-low temperature environment at $T \sim 10$ mK. Historically, electrons on helium experiments have used geometries several hundred μm to mm in size, making it easier to trap electrons even at low densities, and have mostly been carried out in the range of 0.5 - 1.2 K where scattering off of vapor atoms provides a natural cooling mechanism that decreases electron kinetic energy after emission.

The first transport measurements of electrons on helium as well as many subsequent experiments were performed using an electrode configuration known as the Sommer-Tanner architecture [67,71], which represents a robust and effective way of detecting and measuring two-dimensional electron states on liquid helium. The Sommer-Tanner setup can be thought of as the analog of a field-effect transistor (FET) for electrons on heliums. The motion and transport of electrons between different regions is controlled by applied gate voltages. Transport properties such as mobility, relaxation times and effective mass are measured via the AC response of the electron gas at kHz frequencies. In this chapter, we discuss the implementation and measurement of such an electrons on helium FET with an integrated cavity helium-level meter fabricated on the same chip. This serves as an important first experiment that demonstrates the ability to achieve high electron densities at mK temperatures and allows us to test many of the components of our on-chip setup using a well-established

detection scheme. In section 6.1, we start by discussing the underlying theory and basic idea behind the Sommer-Tanner method and show how it can be used for transport measurements of electrons on helium. In section 6.2, we characterize our on-chip implementation of the Sommer-Tanner configuration and discuss the measurement setup. Several experimental results including electron density measurements are presented in sections 6.3 and 6.4.

6.1 Sommer-Tanner Method

The Sommer-Tanner detection method has been a mainstay of electrons on helium experiments since the early 1970s. Originally developed by W. Sommer and D. Tanner for the first electron mobility measurements [71], it has since been used in a wide variety of electrons on helium experiments, including density-dependent mobility measurements [74], observation of dynamical ordering in confined Wigner crystals [206] and point-contact transport measurements [207, 211]. The Sommer-Tanner configuration has also been successfully adapted for electrode-less conductance measurements in thin film semiconductors [212]. The technique is based on the phase-sensitive detection of a two-dimensional electron gas excited at low frequencies and capacitively coupled to a transmission line-like configuration. Electrons on helium have to be detected capacitively since it is not possible to attach leads directly to the electron gas, as opposed to transport measurements in semiconductors and metals. In this section we focus on the physics behind the Sommer-Tanner method and various ways of analyzing the signals. The geometry and basic measurement principle are discussed in section 6.1.1. Section 6.1.2 presents an equivalent lumped element circuit model valid at low excitation frequencies and section 6.1.3 maps the combination of electron-gas and measurement circuit to a transmission line model.

6.1.1 Geometry and Measurement Principle

The basic Sommer-Tanner configuration is shown schematically in Fig. 6.1. It consists of a two-dimensional array of three planar electrodes (*drive*, *gate* and *sense*) of width w submerged under a film of liquid helium of thickness d_{He} and separated by gaps of width $d_e \ll d_{\mathrm{He}} < w$. The superfluid surface above the electrodes is charged with electrons via thermionic emission from a tungsten filament mounted a distance $d_{\mathrm{fil}} \gg d_{\mathrm{He}}$ above the helium surface, see section 4.1.4 for details on cryogenic electron sources. As discussed in

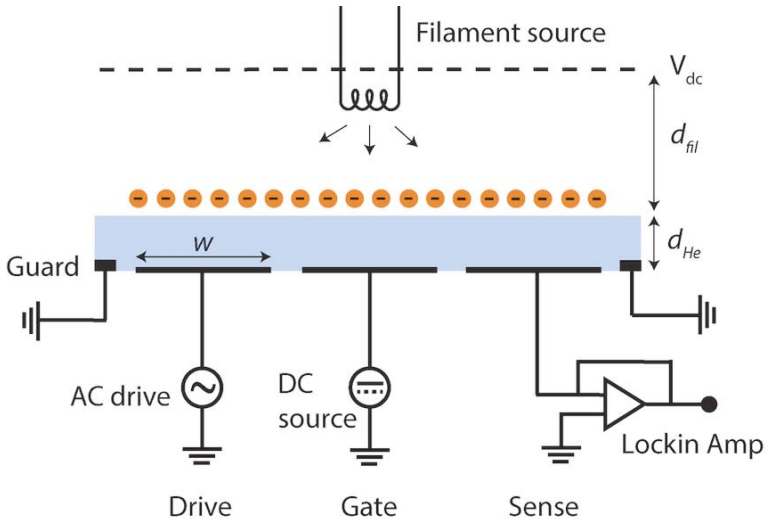

Figure 6.1.: Sommer-Tanner four-electrode configuration: A planar array of electrodes (drive, gate, sense) each of width w submerged under a film of superfluid helium of thickness d_{He}. The superfluid surface is charged via thermionic emission from a filament or other cryogenic electron source mounted a distance $d_{\mathrm{fil}} \gg d_{\mathrm{He}}$ above the surface. The electron gas is excited via an AC voltage applied to the drive electrode which induces a current on the sense electrode that is measured by a lockin amplifier, see text for details. Drive, gate and sense electrode are surrounded by a guard electrode at ground potential that confines the 2DEG to a region of size $A \sim 3w \times \ell$ where ℓ is the length of the configuration.

chapter 2, the electrons collect on the surface as a two-dimensional sheet in the form of a 2DEG or Wigner crystal (illustrated by orange dots in Fig. 6.1), depending on temperature and electron density. The drive-gate-sense configuration is surrounded by a guard ring electrode biased at ground or negative potential relative to the other electrodes. It serves the purpose of confining the electron gas to a well-defined region of size $A \approx 3w \times \ell$, where ℓ is the length of the configuration, and protect it from possible electrostatic sinks in other parts of the sample cell. The drive electrode is connected to an AC oscillator and typically excited at audio frequencies $f \sim 100$ kHz and a few Volts amplitude. The central gate electrode is connected to a tunable DC voltage source (i.e. it is at AC ground potential) and has the dual purpose of reducing the direct geometric cross-capacitance between drive and sense electrode as well as providing a way of modulating the electron density at the center of the electrode array. The sense electrode (far right in Fig. 6.1) is connected to the input of a lock-in amplifier. Both drive and sense electrode usually have an additional DC voltage superimposed with the AC excitation voltages to create a vertical holding field for the electrons, although this is not strictly necessary provided the guard ring is at a sufficiently negative relative voltage. Drive and lock-in amplifier are phase-locked for phase-sensitive current measurements. The basic measurement principle is as follows: An AC voltage at

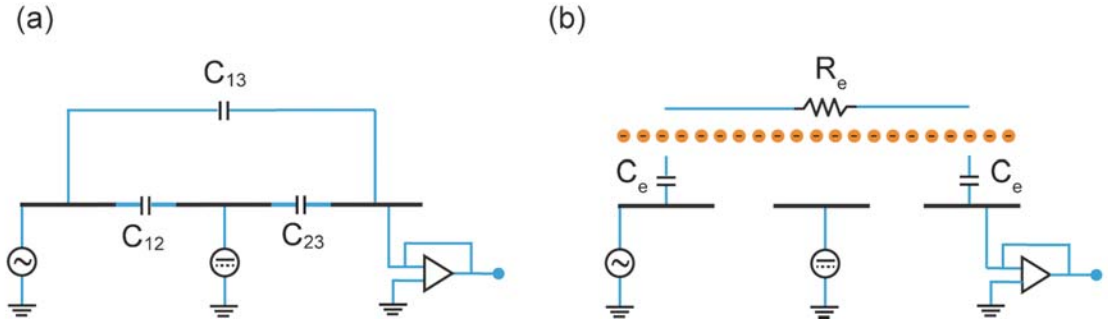

Figure 6.2.: Equivalent lumped element circuit model for the Sommer-Tanner configuration: (a) Cross-capacitance network in the absence of electrons where $C_{13} \ll C_{12}, C_{23}$. (b) Two-dimensional electron gas capacitively-coupled to drive and sense electrode modeled as a series combination of equivalent capacitors and resistors at low excitation frequencies. The capacitance is purely geometric and the resistor models the finite mobility of the gas, see discussion in text.

frequency $f_d = \omega_d/2\pi \sim 10 - 100$ kHz applied to the drive electrode couples capacitively to the charge on the helium surface and leads to a redistribution of the electrons floating on the helium film, corresponding to a local charge density modulation above the drive electrode at frequency f_d. This leads to a charge accumulation above the sense electrode and alters the density in that region after a time delay τ that is determined by the effective mass of the electrons and their finite relaxation time due to scattering off of helium vapor atoms or elementary superfluid excitations such as ripplons. The modulation in charge density above the sense electrode induces a current in the electrode. The relative phase of input and output signals depends on the energy dissipation in the surface layer. The effective mass can be determined from the in-phase component of the signal and the mobility from the out-of-phase component, see below for details. Depending on the DC voltage applied to the gate electrode, the propagation of the density modulations can be controlled. For sufficiently negative voltages, we expect the propagation to be suppressed as the region above the gate is depleted and the induced current on the sense electrode goes to zero. We can express the surface electron gas properties effective mass m^*, mobility μ, conductivity σ and electron density n_e in terms of the measured reactance, admittance and geometric capacitance by mapping the Sommer-Tanner configuration to a transmission line (section 6.1.3) or a lumped element circuit (section 6.1.2).

6.1.2 Lumped Element Circuit Model

The Sommer-Tanner geometry of Fig. 6.1 can be analyzed in terms of an equivalent lumped element circuit model, shown in Fig. 6.2, in the limit of low drive frequencies. The validity of

this approximation depends on the ratio of the two-dimensional skin depth δ_e of the electron gas and the physical length of the electrodes $\delta_e \ll \ell$, which is equivalent to $\omega \ll \sigma/C_A$ as shown below. First, consider the equivalent circuit in the absence of electrons as shown in 6.2 a. The electrodes are close $d_e \ll w$ but planar and hence the direct coupling capacitances C_{12} and C_{23} are small. For example, finite element simulations for an electrode thickness of 150 nm and length $\ell = 1$ mm give $C_{12} = C_{13} \sim 0.15$ pF. The center gate electrode is an AC ground and shields sense from drive electrode, minimizing the geometric cross capacitance C_{13} between the two. This is important as the capacitive coupling between drive and sense mediated by the electron gas is expected to be small. Next, consider the case of a 2DEG floating on top of a helium film above the submerged electrodes, shown in Fig. 6.2 b. Within a simple Drude model approach where the 2DEG is a metal of conductivity $\sigma = n_e \cdot e \cdot \mu = 1/\rho$ with μ being the electron mobility and n_e electron density, the electron gas coupled to drive and sense electrode is modeled as a resistor in series with two capacitors

$$R_e = \ell \cdot R_\ell \quad , \quad R_\ell = \frac{1}{n_e e \mu w} \qquad C_e = \ell \cdot C_\ell \quad , \quad C_\ell = \frac{\varepsilon_0 \varepsilon_{\mathrm{He}} w}{d_{\mathrm{He}}} \tag{6.1}$$

where $\varepsilon_{\mathrm{He}} = 1.057$, w is the width and ℓ the length of the electrodes (see Fig. 6.1) and R_ℓ, C_ℓ are per unit length quantities. The inductance of the 2DEG is purely kinetic:

$$\frac{1}{2} L_\ell I^2 = \frac{1}{2} L_\ell (n_e e v w)^2 = \frac{m^* v^2}{2} \quad \rightarrow \quad L_\ell = \frac{m^*}{n_s e^2 w} \tag{6.2}$$

where m^* is the effective mass of the electrons. At low frequencies, the kinetic inductance contribution can be neglected and the total admittance of the circuit in Fig. 6.2 b is

$$Y = \left(R_e + \frac{1}{j\omega C} \right)^{-1} = \frac{R_e + j\frac{1}{\omega C}}{R_e^2 + 1/\omega^2 C^2} \tag{6.3}$$

where $C = C_e/2$. To get a better idea of the frequency range in which kinetic inductance contributions can be neglected, consider the AC conductivity of an electron gas [104]

$$\sigma(\omega) = \frac{\sigma_0}{1 - j\omega\tau} = \frac{n_e e^2 \tau / m^*}{1 - j\omega\tau} = \frac{n_e e^2 \tau}{m^*(1 + \omega^2\tau^2)} + j \frac{n_e e^2 \omega \tau^2}{m^*(1 + \omega^2 \tau^2)} \tag{6.4}$$

where τ is the scattering time. The imaginary part describes kinetic inductance contributions while the real part describes resistive contributions. For metals we have $\tau \sim 10^{-15}$ s^{-1} [104] such that the inductance term can be neglected even for high excitation frequencies

up to $\omega/2\pi \lesssim 100$ GHz. However, electrons on helium have much longer relaxation times $\tau \simeq \mu m/e \sim 10^{-10}$ s^{-1}, especially at low temperatures where vapor atom scattering is suppressed exponentially. We see that kinetic inductance contributions should still be small for frequencies $\omega/2\pi \lesssim 10$ MHz which is the case for the experiments presented in this chapter where we typically have frequencies $\omega_d/2\pi \sim 10 - 100$ kHz. Measurements at higher frequencies allow estimating the effective mass of the 2DEG electrons via (6.2).

In the limit of a perfect conductor $\rho = 0$, the mediated coupling between drive and sense electrode is purely capacitive and the current induced on the sense electrode is at a $\Delta\phi = \pi/2$ phase angle relative to the excitation voltage on the drive electrode. For finite conductivity, the relative phase contains information on σ and hence the electron mobility. For small angles we have

$$\Delta\phi = \arctan\left[\frac{\mathrm{Re}(Y)}{\mathrm{Im}(Y)}\right] \approx \frac{\mathrm{Re}(Y)}{\mathrm{Im}(Y)} = R\omega C = \frac{\omega C\ell}{n_e e\mu w} \tag{6.5}$$

Now the electron density can be controlled through the DC voltage difference V_{dc} between the filament electrode and the submerged electrodes (see Fig. 6.1) and is to a good approximation given by [213]

$$n_e \simeq \frac{CV_{\mathrm{dc}}}{e\ell w} = \frac{V_{\mathrm{dc}}\varepsilon_0\varepsilon_{\mathrm{He}}}{e \cdot d_{\mathrm{He}}} \tag{6.6}$$

This follows from the fact that saturation is reached once the charge accumulated on the surface has reduced the field between filament electrode and surface to zero, in which case the entire potential difference V_{dc} appears only between the surface and the submerged electrodes [213]. Eq. (6.6) then follows by making a parallel plate capacitor approximation. Using this in combination with (6.5) shows that the mobility can estimated from the measured phase difference between the drive and sense signals

$$\mu \approx \frac{\ell^2\omega}{V_{\mathrm{dc}}\Delta\phi} \tag{6.7}$$

which is the expression originally used by Sommer and Tanner [71]. The lumped element approximation is valid provided the skin depth of the electron gas is much less than the physical length of the electrodes, $\delta_e \ll \ell$. Following Ref. [214], it is instructive to derive an expression for the 2D skin depth for electrons on helium in this setup and show explicitly why $\delta_e \ll \ell$ is satisfied at the typical excitation frequencies used in our experiments. Let $C_A = \varepsilon_{\mathrm{He}}\varepsilon_0/d_{\mathrm{He}}$ be the capacitance per unit area between drive electrode and the electron gas. An AC voltage applied to the drive electrode $V_d = V_0 e^{j\omega t}$ couples capacitively to the

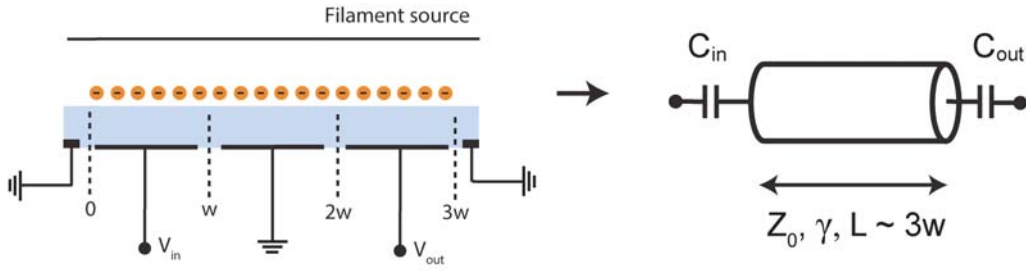

Figure 6.3.: Transmission line mapping of the Sommer-Tanner geometry: The submerged electrode array and the top filament electrode form a capacitively-coupled transmission line in combination with the surface electron layer, with a characteristic impedance Z_0 and propagation coefficient γ that depend on the transport properties of the electron gas.

2DEG and leads to a redistribution of the electron potential of the form $V_e = v(x,y) \cdot e^{j\omega t}$. Let $\mathbf{J}_e = (J_x, J_y)$ be the in-plane current density. Conservation of current then implies

$$\frac{\partial J_x}{\partial x} + \frac{\partial J_y}{\partial y} = -j\omega C_A (V_e - V_d) \tag{6.8}$$

such that writing the current density in terms of the in-plane electric field $\mathbf{J}_e = \sigma \cdot \mathbf{E} = -\sigma \nabla V_e$ gives

$$\frac{\partial^2 V_e}{\partial x^2} + \frac{\partial^2 V_e}{\partial y^2} = -\frac{j\omega C_A (V_e - V_d)}{\sigma} \tag{6.9}$$

For a one-dimensional voltage wave propagating along the x-axis in the 2DEG $V_e = A_0 \cdot e^{j\omega t} e^{-jk_e x}$ we thus get for the dispersion relation at zero drive $V_d = 0$

$$k_e^2 = -\frac{j\omega C_A}{\sigma} \quad \rightarrow \quad k_e = \frac{1-j}{\delta_e} \quad \text{where} \quad \delta_e = \sqrt{\frac{2\sigma}{\omega C_A}} \tag{6.10}$$

which defines the 2D skin depth via the dispersion relation for a damped voltage wave. Analogous to 3D conductors , δ_e can be regarded as the length scale over which an AC density fluctuation will propagate. If $\delta_e \gg \ell$ the phase of the density modulations does not change significantly over the length of the electrodes ℓ and hence a lumped element model can be used. This condition is equivalent to low frequencies $\omega C_A \rho \ll 1$.

6.1.3 Transmission Line Mapping

The lumped element circuit analysis in the preceding section was limited to low excitation frequencies. As shown in Ref. [215], an expression for the complex admittance of the Sommer-Tanner cell, and hence the current induced on the sense electrode, can be derived

for arbitrary frequencies by mapping the geometry to a capacitive transmission line whose characteristic impedance depends on electron density and mobility. The mapping is illustrated in Fig. 6.3. Using the per unit length quantities defined in section 6.1.2, the transmission line has characteristic impedance (see section 3.2.1)

$$Z_0 = \sqrt{\frac{R_\ell + j\omega L_\ell}{j\omega C_\ell}} \tag{6.11}$$

and propagation coefficient

$$\gamma = \sqrt{j\omega R_\ell C_\ell - \omega^2 L_\ell C_\ell} \tag{6.12}$$

For a one-dimensional transmission line of length x, the input voltage and current are related to the output quantities by a scattering matrix [158]

$$\begin{pmatrix} V_{\text{in}} \\ I_{\text{in}} \end{pmatrix} = \begin{pmatrix} \cosh(\gamma x) & Z_0 \sinh(\gamma x) \\ \frac{1}{Z_0}\sinh(\gamma x) & \cosh(\gamma x) \end{pmatrix} \begin{pmatrix} V_{\text{out}} \\ I_{\text{out}} \end{pmatrix} \tag{6.13}$$

Neglecting the small kinetic inductance, the output current measured at the sense electrode can be expressed in terms of the voltage applied to the drive electrode and the skin depth and wave vector introduced in eq. (6.10). One finds after some algebra for the complex normalized current [214, 215]

$$I^* = \frac{I}{I_0} = (1+j)\frac{3}{2}\frac{\delta_e}{w}\frac{\sinh^2(jk_0 w)}{\sinh(j3k_0 w)} \tag{6.14}$$

with current amplitude

$$I_0 = \omega C_A \frac{\ell w}{3} V_0 \tag{6.15}$$

where V_0 is the amplitude and ω the frequency of the drive voltage, ℓ and w are the length and width of the electrodes and the skin depth δ_e and wave vector k_0 are given in eq. (6.10). Since the geometry and helium level are known or can be determined to high accuracy, the measured in-phase component (Re$[I^*]$) and the 90° phase-shifted component (Im$[I^*]$) can be fitted to eq. (6.14) as functions of excitation frequency to determine the density and mobility of the electron gas. Alternatively, one can vary the helium film thickness d_{He} and hence the capacitance per unit area C_A at fixed frequency. This method has been used for high-precision conductance measurements in semiconductors [212].

6.2 Device & Measurement Setup

For this thesis, we have realized an on-chip Sommer-Tanner setup consisting of a four-electrode configuration and an integrated high-Q coplanar waveguide resonator fabricated on the same 2×7 mm chip. Optical microscope pictures of the device and a simplified diagram of the measurement setup are shown in Fig. 6.4. The inductively-coupled resonator on the l.h.s of the chip is used as a liquid helium level meter (see chapter 5) while the four electrodes on the r.h.s of the chip realize a standard Sommer-Tanner configuration consisting of drive, gate and sense electrodes surrounded by a guard ring. The main components of the on-chip and measurement setup are discussed below. Details on the RF and microwave circuitry, filtering and phase-sensitive detection can be found in chapter 4. All experiments were performed at 20 mK in the pulse-tube cooled dilution refrigerator setup discussed in section 4.1.

6.2.1 Inductively-Coupled Cavity Helium Meter

To monitor the helium film thickness on the chip and adjust it such that $d_{\mathrm{He}} \gg d_e$, where d_e is the separation between the Sommer-Tanner electrodes, we use a symmetrically, inductively-coupled $\lambda/2$ coplanar waveguide resonator (section 3.2), see l.h.s of the chip shown in Fig. 6.4. The resonator is characterized by nominal shunt inductances of $L_\kappa = 6.91$ pH and a bare resonance frequency and loaded quality factor of $\omega_0/2\pi = 5.5752$ GHz and $Q_L = 5993$, respectively. The resonator is measured in transmission using the phase-sensitive microwave measurement setup discussed in section 4.2. The bare cavity transmission in the absence of superfluid helium at input power of $P_{\mathrm{in}} = -45$ dBm is shown in Fig. 6.5 a. The high-sensitivity helium level detection method is described in detail in chapter 5. Helium filling curves measured in this experiment are shown in Fig. 6.5 b , see discussion below.

6.2.2 Sommer-Tanner Configuration

In this section we discuss our implementation of the Sommer-Tanner setup for electron detection and density measurements, starting with the on-chip configuration and then walking the reader through the measurement setup, progressing from room temperature down to the base stage of the cryostat, as shown in Fig. 6.4. The device was fabricated using a four-step procedure consisting of an optical lithography step defining the resonator structures and the

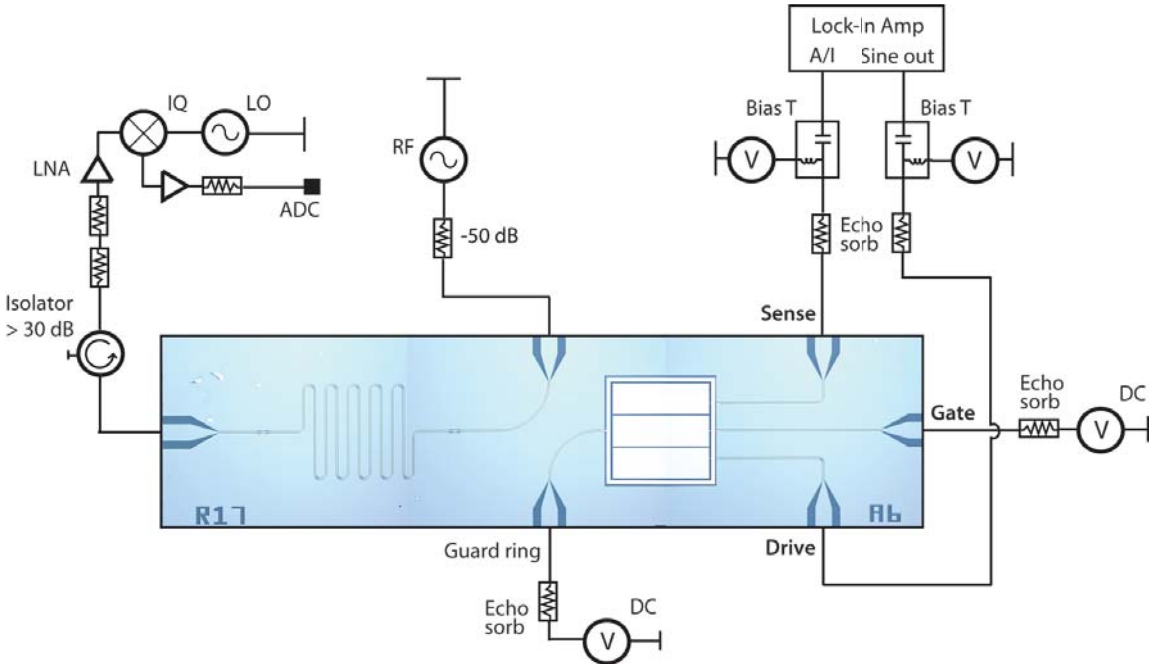

Figure 6.4.: On-chip Sommer-Tanner electron measurement setup with integrated cavity helium-level meter: The optical microscope image of the 2×7 mm Nb/Al on sapphire chip shows the inductively-coupled $\lambda/2$ resonator (meandering structure on the l.h.s) and the Sommer-Tanner four electrode configuration (r.h.s of the chip) consisting of drive, sense, gate and guard ring electrode. The simplified measurement setup and wiring are shown as well. The drive electrode is connected to the internal oscillator of a lockin amplifier which excites the electron gas with a voltage sine wave of amplitude $V_0 \sim 10 - 200$ mV and frequency $f_0 \sim 10 - 100$ kHz. The sense electrode is connected to the current input of the lockin amplifier for phase-locked measurements of the electron gas-induced current. All four electrodes are in addition connected to DC sources at room temperature and filtered inside the cryostat with echo-sorb filters. The resonator is measured in transmission using the standard phase-sensitive RF-LO setup discussed in section 4.2.

bias leads, followed by two e-beam lithography steps and an intermediate silicon-oxide deposition step, see section 4.3 for fabrication recipes. The resonator structures and bias leads are made of 200 nm thick etched Niobium sputtered on a sapphire substrate while the drive, sense and gate electrodes are made of 150 nm thick deposited Aluminum. To guarantee good confinement of the electron gas to a square region of size $\sim 1 \times 1$ mm the guard ring has a thickness of 500 nm deposited separately after a second e-beam lithography step. The guard electrode overlaps the drive, sense and gate leads, which are insulated from the guard by 150 nm of deposited SiO_x. The electrodes each have width $w = 0.284$ mm and length $\ell = 0.86$ mm and are separated by gaps of size $d_e = 4\,\mu$m. Finite-element simulations yield geometric capacitances between adjacent plates of $C_{12} = C_{23} = 0.12$ pF and negligible C_{13} (see Fig. 6.2 a).

For phase-sensitive current and voltage measurements we use a *SR830 DSP* lock-in amplifier by *Stanford Research Systems*, see section 4.2.1 for an introduction to low-frequency phase-locked detection. In order to apply additional DC bias voltages to the drive and

sense electrodes we use two custom made bias tees at room temperature with low cutoff frequencies. The bias tees consist of a $C = 10\,\mu$F capacitor and a $R = 500$ kΩ resistor, large enough to look like an RF short at the typical excitation frequencies $\omega/2\pi \sim 100$ kHz. The DC ports of the bias tees are connected to high-stability *Yokogawa 7561* programmable DC sources and the RF inputs are connected to the input and output of the lock-in amplifier. To perform measurements of small currents induced by the electron gas, the drive is connected to the sine output of the *SR830* lock-in amplifier and excited at voltage amplitudes of $V_0 = 10 - 200$ mV and frequencies $\omega_d/2\pi = 10 - 100$ kHz. The sense electrode is connected to the low-impedance current input of the amplifier. We opted to use the internal oscillator of the lock-in for signal generation in these measurements as it is intrinsically phase-locked with the input reference. The current input has a small input impedance $Z_{\text{in}} = 1$ kΩ and a current gain of $10^6 - 10^8$ V/A and allows measuring full-scale currents down to 2 fA. For high source impedances and small currents it is advantageous to use a low input impedance as it reduces amplitude and phase errors due to the cable capacitance-source impedance time constant. The cable capacitance in this setup ($C_c \sim 50$ pF per ft.) is typically much larger than the capacitance of the electron gas ($C_e \sim 1$ pF for a source impedance of $Z_s \sim 1.6$ MΩ at 100 kHz). Inside the cryostat, each coaxial line for the Sommer-Tanner setup is filtered by eccosorb filters, mounted at the 4K and 20mK base stage of the cryostat, respectively.

6.3 Field-Effect Transistor on Superfluid Helium

The Sommer-Tanner geometry essentially represents the analog of a field-effect transistor (FET) for electrons on helium. In addition to suppressing direct cross-capacitive coupling between drive and sense electrode, the center electrode can be used as a gate electrode to create a depletion region. Below a certain relative threshold voltage $V_g^{(\text{th})}$, electron transport and propagation of density modulations between drive and sense electrode will be suppressed and the current induced on the sense electrode will be switched off. In a first set of experiments, we use this FET effect to detect the presence of electrons in a phase-sensitive lock-in measurement.

We start by filling the sample holder at 20 mK with superfluid helium through the capillary setup presented in section 4.1.2. This is done in a controlled way by monitoring the frequency shift of the CPW resonator on the l.h.s of the chip in transmission, exactly as in the experiments described in chapter 5. Conformal mapping calculations (section 5.1) show

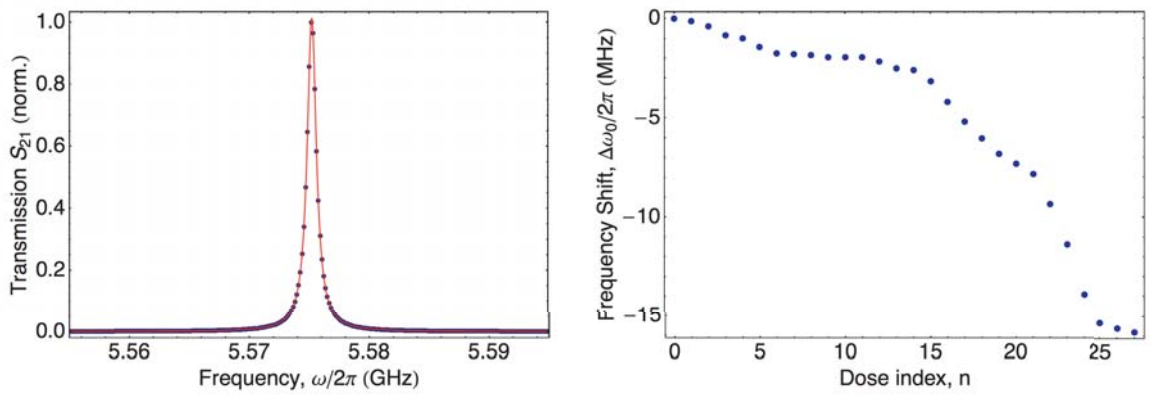

Figure 6.5.: Cavity helium-level measurements: (a) Normalized bare cavity transmission in the absence of superfluid helium at $P_{\rm in} = -45$ dBm input power. Datapoints are in blue and the red line is a fit to a Lorentzian, which yields a resonance frequency of $\omega_0/2\pi = 5.5752$ GHz and a loaded quality factor $Q_L = 5993$. (b) Superfluid helium filling curve, showing measured shift of the cavity resonance frequency as a function of the number of liquid helium doses supplied to the sample cell. A dose corresponds to ~ 0.016 cm^3 of liquid helium, see chapter 5 for details on the level-meter method.

that a frequency shift of $\Delta\omega_0/2\pi \simeq -15.5$ MHz corresponds to a helium film thickness of about 20 μm above the chip for this type of resonator. The device has to be operated in a regime where the film thickness exceeds the gap between the drive, sense and gate electrodes $d_{\rm He} \gg d_e$ to avoid image charge pinning effects. For thin films $d_{\rm He} < d_e$, the electrons are bound to their image charges in the metal and unable to cross the inter-electrode gap such that transport across different electrodes would be largely suppressed. At the same time, however, $d_{\rm He}$ should be kept to a necessary minimum to maximize the capacitive coupling between the 2DEG and the drive and signal electrodes. The helium level-meter fill curve for this experiment is shown in 6.5 b. We reach a frequency shift of $\Delta\omega_0/2\pi = -15.7$ MHz after 27 doses, indicating a sufficiently thick layer of superfluid above the chip. Free electrons are generated using thermionic emission from a pulsed tungsten filament (see section 4.1.4). Biasing the drive, gate and sense electrodes at $V_d = V_g = V_s = +2$ V and the guard ring at $V_{gr} = -0.5$ V, the helium surface is charged to saturation using the following filament pulse parameters: offset bias $V_{\rm off} = -1V$, pulse duration $\tau = 40$ ms, pulse delay $\delta\tau = 1$s, frequency $f = 113$ kHz and number of pulses $N_{\rm p} = 10$. It should be pointed out that electrons were successfully loaded at $T = 20$ mK without the need to temporarily increase the base temperature of the cryostat to $T \gtrsim 0.5$ K. In most experiments with electrons on helium, free electrons are typically first generated at higher temperatures of 0.5 - 1.2 K where scattering off of vapor atoms provides a natural cooling mechanism that decreases electron kinetic energy after emission. This did not appear to be necessary in our setup, presum-

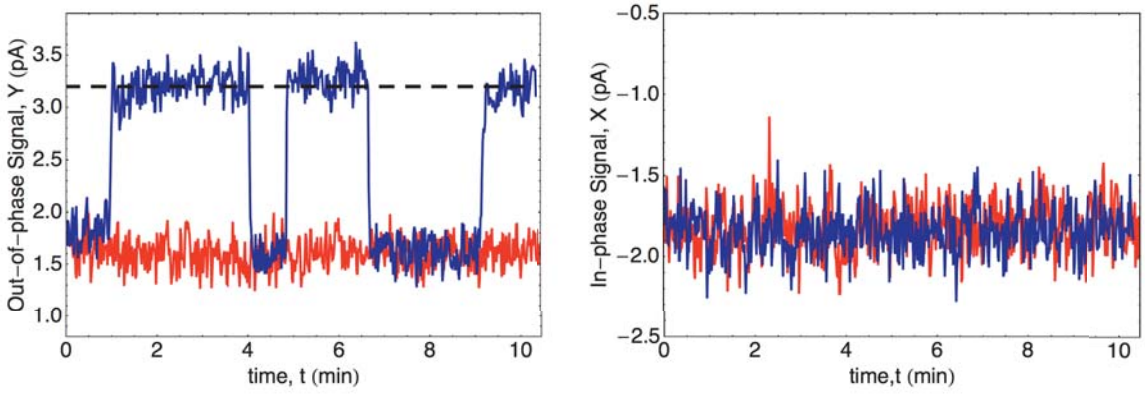

Figure 6.6.: Field-effect transistor with electrons on helium: (a) 90° phase-shifted current Y as a function of time in the presence (blue) and absence (red, control experiment) of electrons. Low currents coincide with negative gate voltages (depletion of center region), high currents with positive gate voltages (electron transport between drive and sense electrode, indicated by dashed line). See text for discussion. (b) Measured in-phase current in the presence (blue) and absence (red) of electrons, same gate biasing sequence as in (a). The small in- and out-of-phase currents in the absence of electrons can be attributed to the residual geometric cross-capacitance between the drive and sense electrode.

ably because the temporary heating effects from the filament pulses generate enough vapor atoms to slow down the electrons. After electrons have been loaded into the 1×1 mm region above the Sommer-Tanner electrodes, we monitor the in-phase (X) and 90° phase-shifted lock-in signals (Y) between drive and sense electrode as a function of time. An AC voltage of frequency $\omega_d/2\pi = 100$ kHz and amplitude $V_d = +10$ mV is applied to the drive electrode, which couples to the electron gas capacitively as explained in section 6.1. The resulting density modulation of the gas at frequency $\omega_d/2\pi$ then propagates to the signal electrode after a time delay determined by the electron relaxation time and effective mass, where it induces a current. We detect the presence of electrons in an FET-style measurement by modulating the gate voltage bias. At negative gate voltages, we expect the induced current measured on the sense electrode to disappear as the region between drive and sense electrode is depleted and electron transport is suppressed. At positive gate voltages, we expect to measure increased current signals. Most of the signal is expected to be in the out-of-phase component as the effect is predominantly capacitive due to the high electron mobility (small resistance) and the low excitation frequencies (small kinetic inductance). The sequence of switching between negative and positive gate voltages is expected to be fully reversible as the guard ring should prevent dissipation of electrons from the Sommer-Tanner region. The results of such a gate-based switching experiment are shown in Fig. 6.6, which shows in- and out-of-phase lock-in signals as functions of time for both charged (blue) and uncharged surfaces (red, control experiments). Starting at $t = 0$ the gate voltage is first held at $V_g = -2$ V, negative

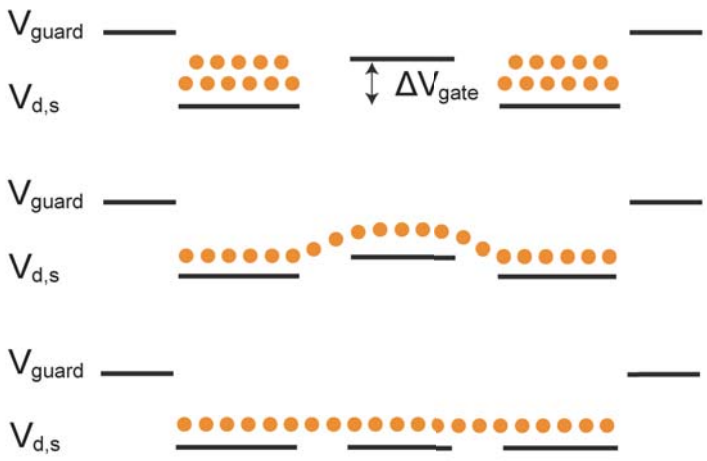

Figure 6.7.: Illustration of FET effect based electron density measurements: Electrons initially distribute uniformly across drive, gate and sense electrode for $V_d = V_g = V_s$ (bottom). As the gate voltage is swept towards negative voltages electrons start to redistribute (middle), eventually leading to complete depletion of the gate region and a redistribution of the electrons above drive and sense electrode (top). The threshold voltage ΔV_{gate} at which the induced current disappears is proportional to the areal electron density n_e.

relative to drive and sense $V_d = V_s = +2$ V. Electron transport is suppressed and we measure small in- and out-of-phase currents due to the residual geometric capacitance between the electrodes (blue data points in Fig. 6.6). We then switch the gate voltage to $V_g = +2V$ and observe an abrupt increase in out-of-phase current. After holding the gate at $V_g = +2V$ for a few minutes where the current stays constant, we adjust the bias back to $V_g = -2V$ and observe that the current switches back to the original level at $t = 4$ min. This sequence is then repeated a number of times, with the same behavior being observed each time. While the electron induced currents are clearly visible in the 90° phase-shifted signal, the in-phase component remains unchanged, which indicates the almost purely capacitive behavior of the electron gas at the given excitation frequencies. In the control experiments, shown in red in Fig. 6.6, we conduct the same sequence of gate biases in the absence of electrons under the same conditions and observe no current switching behavior, which demonstrates that the measured currents are indeed due to electron density modulations. The 2DEG appears to be highly stable with no noticeable decrease in measured induced current even after several hours of operation. This simple implementation of a FET on liquid helium has recently been extended to one-dimensional conduction channels in a device analogous to metal-oxide-semiconductor FETs [216].

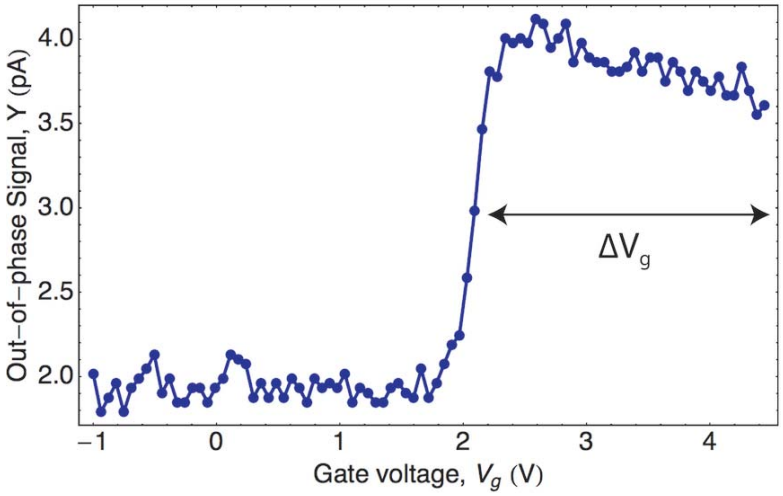

Figure 6.8.: Out-of-phase lock-in current signal as a function of gate voltage V_g. Starting from the r.h.s at $V_g = +4.5$ V, the gate electrode is initially biased at the same voltage as drive and sense electrode ($V_d = V_s = +4.5$ V) and subsequently swept towards negative voltages. The induced current vanishes once the cutoff voltage difference ΔV_g is reached, at which point the gate region is depleted and propagation of density modulations between drive and sense electrode is suppressed. ΔV_g is proportional to the electron density, see discussion in text.

6.4 Density Measurements

The field-effect transistor effect presented in section 6.3 can be used to determine the density of the electron system. The basic idea of this density measurement scheme is illustrated in Fig. 6.7. Starting with all three electrodes at the same positive DC bias $V_d = V_s = V_g$ and a negative guard ring relative to that (bottom in Fig. 6.7), the electrons are initially evenly distributed across the three electrodes with a uniform density n_e except, possibly, at the edges of the region. Decreasing V_g relative to $V_{d,s}$ and sweeping towards negative voltages, the electrons will start to redistribute above the outer drive and sense electrodes as the center region is depleted. At a certain threshold voltage difference $\Delta V_g = V_g - V_{d,s}$, we expect the center region to be depleted entirely and transport to be suppressed. We can express this threshold voltage in terms of the areal electron density n_e using a simple capacitor approximation. The negative relative voltage ΔV_g required to remove all electrons from the center region is

$$\Delta V_g \cdot C_g = n_e \cdot e \quad \rightarrow \quad n_e \approx \frac{\varepsilon_{\mathrm{He}} \varepsilon_0 \Delta V_g}{e \cdot d_{\mathrm{He}}} \tag{6.16}$$

where $C_g = \varepsilon_{\mathrm{He}} \varepsilon_0 / e d_{\mathrm{He}}$ is the capacitance per unit area between electron gas and the gate electrode. Hence, the electron density can be estimated by sweeping the gate voltage relative to drive and sense bias until the electron induced current on the sense electrode vanishes.

The results of such a density measurement are shown in Fig. 6.8. Electrons are initially loaded with all three electrodes at the same positive voltage $V_{d,g,s} = +4.5$ V and the guard negative at $V_{\text{guard}} = -0.5$ V. The gate voltage is then swept from $V_g = +4.5$ V to -1 V while V_d and V_s are held at constant bias. The 90° phase-shifted lock-in signal for the current induced on the sense electrode is measured as a function of gate voltage V_g during the sweep. We observe an abrupt drop in current signal at $V_g \simeq +1.72$ V, corresponding to a negative voltage $\Delta V_g = -2.78$ V relative to drive and sense electrode. This pinch-off in current can be attributed to the depletion of the gate region and a suppression of electron transport between drive and sense electrode. Using eq. (6.16), the measured threshold voltage difference corresponds to an estimated areal electron density of $n_e \sim 8.1 \times 10^8$ cm^{-2} where we have assumed a liquid helium thickness of $d_{\text{He}} \simeq 20\,\mu$m as measured independently in section 6.3. This first result is in good agreement with previously reported densities for electrons on helium generated by thermionic tungsten filament emission [74, 213, 217]. Note the initial *increase* in signal magnitude before the cutoff point as the gate voltage is decreased from $V_g = 4.5$ V to ~ 2.5 V. We attribute this effect to the field dependence of the electron mobility μ, whose absolute value has been shown to be a decreasing function of holding electric fields $E_\perp$ [113, 114].

Controlling Density with Loading Voltage

In section 6.1.2 it was shown that the areal electron density should scale linearly with the voltage difference $V_{\text{dc}} = V_f - V_{d,g,s}$ between filament and the drive, sense and gate electrodes on the chip,

$$n_e \simeq \frac{V_{\text{dc}} \varepsilon_0 \varepsilon_{\text{He}}}{e \cdot d_{\text{He}}}\,. \tag{6.17}$$

To test this relation, we load electrons onto the chip at different values of V_{dc} and perform a gate voltage-based density measurement at each step. The results of such an experiment are presented in Fig. 6.9, where the different colors correspond to different loading voltages V_{dc} and each trace represents one density measurement sweep. For each trace, we first bias all three on-chip electrodes at a given voltage $V_{\text{dc}}^{(i)}$ relative to the tungsten filament and load electrons by pulsing the filament. The gate electrode is then swept form $V_{\text{dc}}^{(i)}$ to -1 V while drive and sense are held constant at the initial loading voltage $V_d = V_s = V_{\text{dc}}^{(i)}$. The out-of-phase current signal is measured and the threshold voltage ΔV_g is recorded for each sweep, which allows inferring the density via eq. (6.16). For the purposes of density determination,

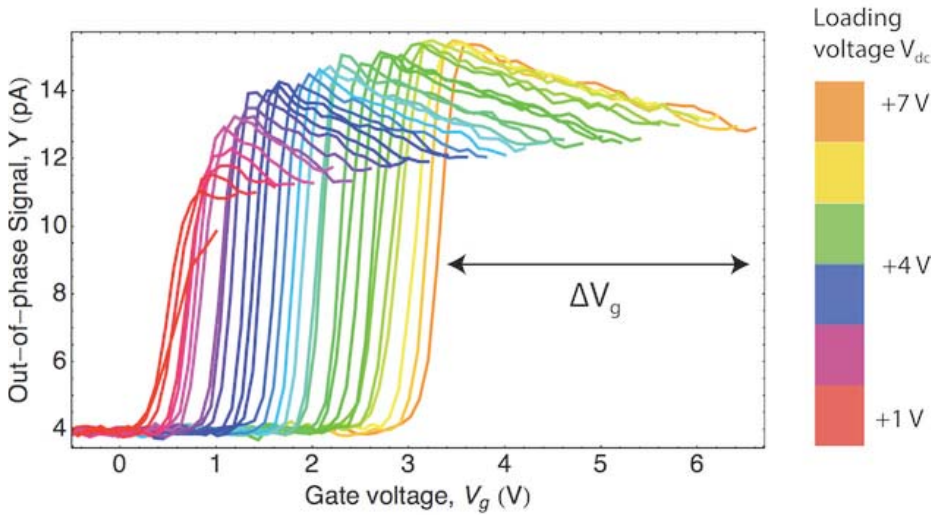

Figure 6.9.: Electron density measurements for different loading voltages: Out-of-phase current signal as a function of gate bias V_g where the different colors correspond to different loading voltages ranging from $V_{\mathrm{dc}} = +1$ to $+7$ V. Each trace represents one density measurement sweep, analogous to the one shown in Fig. 6.8.

the threshold voltage ΔV_g is defined as the point where the out-of-phase current drops to within $20\,\%$ of the current noise floor. The extracted areal electron densities from this experiment are shown in Fig. 6.10 a as a function of loading voltage V_{dc}. The range of obtained densities is $n_e = 10^8 - 10^9$ cm^{-2}, again in good agreement with those typically found for tungsten filament electron sources [68]. The density shows a linear dependence on loading voltage, as expected from the simple parallel-plate capacitor approximation (6.17).

Loading Individual Regions

As a final electron density experiment we show that individual electrodes can be selectively loaded with a density that scales with area. This is achieved by biasing one or more electrodes at a negative voltage during the loading process. To charge only one third of the total area, we initially apply negative voltages to the gate and sense electrode $V_{g,s} = -1$V while the drive electrode is positively biased at a given loading voltage $V_d = V_{\mathrm{dc}}$. Pulsing the tungsten filament, only the area above the drive electrode will be charged initially in this case. We then adjust the bias on the gate and sense electrode to match that of the drive $V_{g,s} = V_d$ such that the electrons will redistribute across all three electrodes. A gate voltage-based density measurement is then performed as outlined above. The same procedure is used to charge two electrodes initially (drive and gate), loading two thirds of the total area. We expect the electron density after redistribution to scale with the size of the area that was initially loaded. The results of such a selective loading experiment are shown in Fig. 6.10 b, which shows that

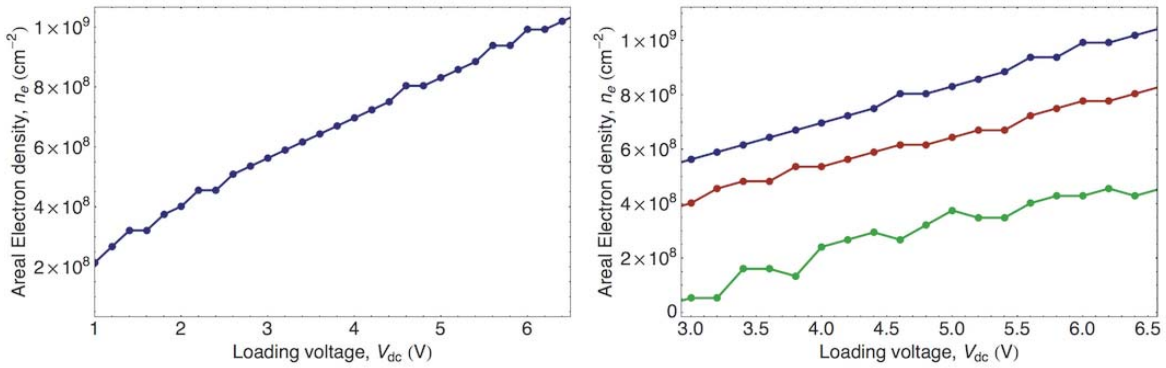

Figure 6.10.: Measured areal electron densities as a function loading voltage V_{dc} applied to the submerged electrodes. Densities are extracted from gate threshold voltage measurements ΔV_g as discussed in the text, see also eq. (6.16). (a) Densities after loading all three electrodes, showing a linear scaling with loading voltage in agreement with eq. (6.17). (b) Fractional loading of one third of the total trap region (green), two thirds (red) and the entire region (blue).

the electron density n_e is linear for all three cases (loading one, two and three electrodes) and does indeed scale with the area that was initially charged. The measured density curves roughly overlap when rescaled by the fractional area that was loaded initially. The results of this experiment show that the electron density in our setup can be varied over an order of magnitude $\sim 10^8 - 10^9$ cm^{-2} by adjusting the gate voltages and hence the electric holding field seen by the electrons after emission. In addition, the filament loading parameters pulse duration τ, pulse delay Δt and number of pulses N_p (see Tab. 4.1) also influence the electron density and provide further variability in the range of available electron densities.

7 Trapping Electrons in a Superconducting Resonator

THE experiments of chapter 6 have demonstrated the trapping and detection of electrons on helium on a superconducting chip at milli-Kelvin temperatures. In those low-frequency measurements we took advantage of the capacitive coupling of surface electrons to submerged electrodes and the differential voltage they induce as result of their motion driven at a few hundred kHz, a technique originally developed by Sommer and Tanner [71]. While this device also contained an integrated coplanar waveguide cavity for measuring the superfluid level on the chip, the electron trapping region was far from the cavity mode volume and no interaction with the cavity field was observed. This chapter presents experiments in which an ensemble of electrons is trapped directly in the gap of a superconducting coplanar waveguide cavity. There are a number of ways an electron ensemble trapped in a waveguide gap can potentially couple to the cavity field, including dipole interaction of collective in-plane motional excitations (transverse and longitudinal modes) and vertical Rydberg states. This allows detecting electrons on helium in cavity transmission measurements where their presence manifests itself through shifts in resonance frequency and increases in linewidth of the fundamental mode of the cavity. Section 7.1.1 starts with a discussion of the DC-biased center pin resonator design and the devices used in our experiments. Potential coupling mechanisms of the electron ensemble in such a resonator are discussed in section 7.1.2, together with numerical simulations of coupling strengths and positional configurations in the resonator. In section 7.2 we present experiments detecting electrons on helium in a CPW cavity through voltage-dependent shifts in frequency of up to 10 cavity linewidths with a decrease in quality factor of $\sim$ 30 %. Electron loss and dissipation at low trapping voltages are investigated in section 7.3 using stability and voltage hysteresis measurements.

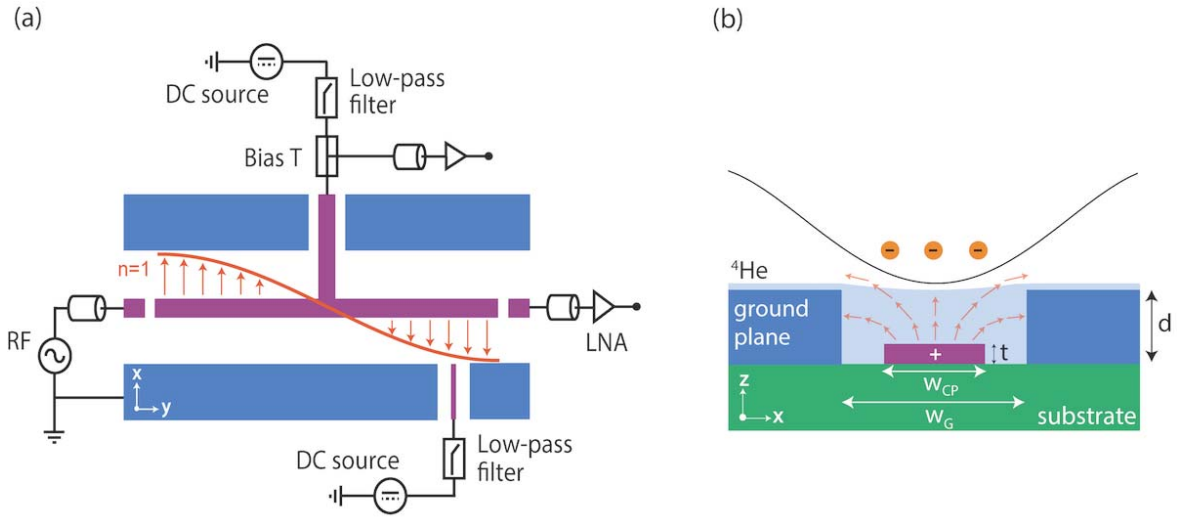

Figure 7.1.: Schematic layout and measurement setup for a capacitively-coupled, DC-biased center pin resonator. (a) Top view of the resonator, showing the voltage distribution of the fundamental mode (red) and the simplified measurement and control circuit. The center pin (magenta) is directly attached to a bias lead at a voltage node of the fundamental mode, minimizing loss of microwave photons through the bias port. A bias tee is used for transmission measurements through the DC port. (b) Cross-sectional view of the waveguide gap in a DC-biased resonator. The ground planes (blue) form a micro-channel of height $d \sim 1\,\mu$m and width $w_G \sim 10\,\mu$m filled with superfluid by capillary action. The submerged, voltage-biased center pin (magenta) of width $w_{CP} \sim 2\,\mu$m and thickness $t \sim 40\,\mu$m creates a parabolic trapping potential for electrons above the surface. RF electric field lines are indicated by arrows.

7.1 Device and Simulations

7.1.1 DC-biased Center Pin Resonators

Experiments with electrons on helium require precise control of the DC potentials and the electromagnetic environment on the chip. This was the original motivation behind the development of inductively-coupled transmission line resonators (section 3.2), where the center pin electrode of the CPW is at DC ground potential at all times. A natural extension of this idea is to directly attach a voltage bias line to the center pin which allows tuning the DC potential on the electrode to desired values. To realize such a device we take advantage of the symmetry of the voltage distribution in a capacitively-coupled transmission line resonator at microwave frequencies. Such a DC-biased coplanar waveguide cavity was already introduced in the helium level-tuning experiments in chapter 5. In this section we discuss this type of device design in some more detail and show how it can be used as a large planar electron trap capable of confining a significant number of electrons ($\sim 10^4 - 10^6$) in the gap region of a CPW.

The schematic layout of a DC-biased center pin resonator and the basic measurement and

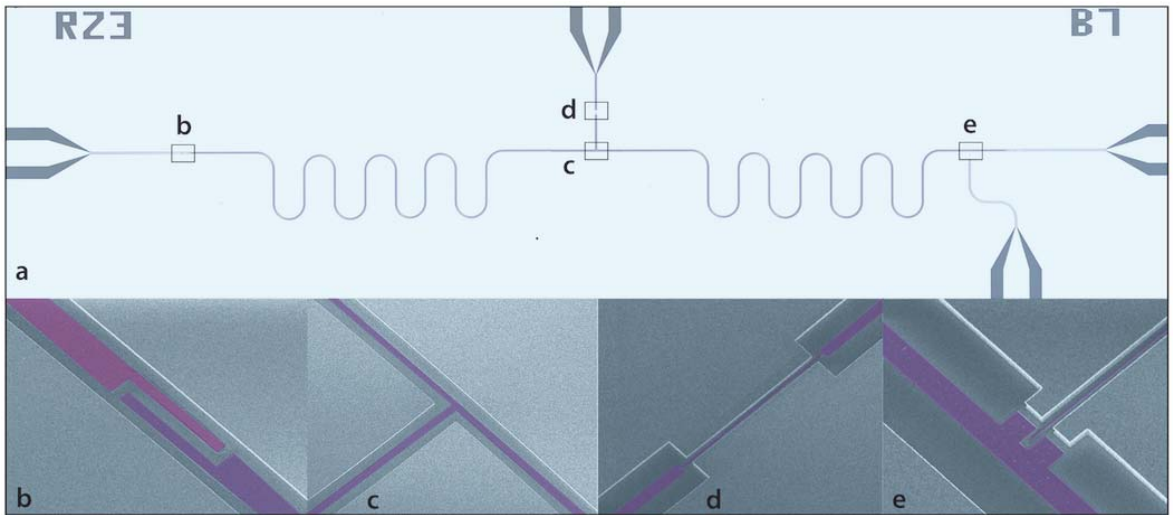

Figure 7.2.: Optical and SEM images of a DC-biased center pin resonator device. (a) Full top view of the 2×7 mm four-port device, (b) interdigitated gap capacitor (gap width of $2\,\mu$m) for coupling on the input side, (c) DC bias port connection to center pin, (d) constriction of width $1\,\mu$m and length $30\,\mu$m on the bias port input, (e) μm-size single electron trap with separate gate electrode. The DC-biased center pin of thickness $t = 40$ nm and width $w_{\mathrm{CP}} = 2\,\mu$m is shown false-colored in magenta for clarity. The ground planes of thickness $d = 800$ nm define a micro-channel geometry of width $w_{\mathrm{G}} = 10\,\mu$m that can be filled with superfluid helium by capillary action from a reservoir below the chip. The gap capacitors and bias port constriction act as implicit guard rings suppressing dissipation of electrons out of the resonator mode volume. The device was fabricated on a sapphire substrate using a two-layer electron beam lithography process (see section 4.3), with the ground plane consisting of sputtered Nb and the center pin and trap electrodes defined by deposition of Al in a lift-off process.

control circuit are shown in Fig. 7.1 a. Optical and SEM images of one of the devices used in our experiments are presented in Fig. 7.2. As shown in Fig. 7.1 a and Fig. 7.2 c, a DC bias electrode is directly connected to the center pin of a symmetrically, capacitively-coupled $\lambda/2$ resonator at a voltage node of the fundamental mode. The center pin is biased by a *Yokogawa GS200* high-stability DC voltage source through a low-pass filter. In addition, an RF line with a cryogenic low-noise amplifier for microwave leakage measurements is connected to the DC port through a bias tee. The cavity is measured in transmission using heterodyne and homodyne detection with the standard circuit QED setup presented in chapter 4. This device design allows applying a tunable DC voltage offset to the center pin, in addition to microwave and RF voltages at the input port, while maintaining high quality factors of the mode used for electron detection. As discussed in more detail below, loss of microwave photons through the bias port is effectively suppressed by symmetry. The transverse cross-section of the waveguide gap is shown schematically in Fig. 7.1 b. The design is characterized by a high aspect ratio of ground plane to center pin metal thickness of $t : d = 1 : 20$ with $d = 800$ nm and $t = 40$ nm. The resonator gap forms a micro-channel geometry of width $w_{\mathrm{G}} = 8 - 10\,\mu$m with a $w_{\mathrm{CP}} = 2\,\mu$m wide bias electrode. This design is similar to the channel

Device ID	Frequency, $\omega_0/2\pi$	Q_L	w_{G}	w_{CP}	d	t
B13	6.11231 GHz	20800	10 μm	2 μm	800 nm	40 nm
I5	6.08241 GHz	20010	10 μm	2 μm	800 nm	40 nm
L3	4.791583 GHz	17750	8 μm	2 μm	1000 nm	100 nm

Table 7.1.: Overview of devices used in many-electron trapping experiments, showing measured resonance frequency $\omega_0/2\pi$ and loaded quality factor Q_L as well as the geometric parameters gap width w_{G}, center pin width w_{CP}, ground plane thickness d and center pin thickness t. Resonance frequencies and quality factors are bare values measured in the absence of any superfluid helium or electrons. Devices B13 and I5 have been measured at Yale and device L3 has been measured at the University of Chicago (Schuster Lab), using nominally identical cryogenic setups for transmission measurements, electron generation and DC control.

geometries typically used in electrons on helium experiments [129, 206, 207] and supports a self-stabilized capillary action film of superfluid helium, as discussed in sections 2.3.4 and 5.2. While the resonator gap is filled by capillary action, the ground plane is covered by a thin saturated van-der-Waals film of thickness ~ 30 nm. Electrons above the ground plane drain away through the van-der-Waals film while electrons in the gap are bound vertically to the helium surface by their induced image charges in the liquid with a hydrogen-like spectrum $E_n = -R/n^2$ (see section 2.1) . In the transverse direction (along the x-axis in Fig. 7.1), a DC voltage applied to the submerged center pin creates a parabolic trapping potential which confines the electrons in the x-direction to the gap region of the CPW. At the typical equilibrium electron separations of $x_c \sim 0.1 - 1\,\mu$m at saturated densities, the resonator gap therefore forms a few-electron trap in the transverse direction similar to the ones discussed in section 3.7.1. Motion along the lateral direction (y-axis) is essentially unconstrained for typical transmission line resonator lengths of $L \simeq 9000 - 10000\,\mu$m. The interdigitated gap capacitors of the resonator with a spacing of $2\,\mu$m (Fig. 7.2 b) act as implicit guard rings at the input and output of the resonator while dissipation of electrons through the center pin bias port is suppressed by a narrow constriction of width $1\,\mu$m and length $50\,\mu$m (see Fig. 7.2 d). No explicit DC biases are applied to the input/output leads of the cavity in this set of experiments, which could be achieved using additional bias tees should electron loss over the gap capacitors turn out to be problematic. In addition to the large electron trap formed by the center pin, the devices also contain smaller sub-μm-size electron traps positioned near the voltage maxima of the fundamental mode for future single-electron experiments (Fig. 7.2 e). The single-electron traps were set to ground potential throughout the experiments discussed in the rest of this chapter [1].

[1] Numerous attempts have been made at loading a variety of single-electron trap designs over the course of this PhD project, but no signatures of single-electron-cavity coupling have been observed so far. See discussion in chapter 8.

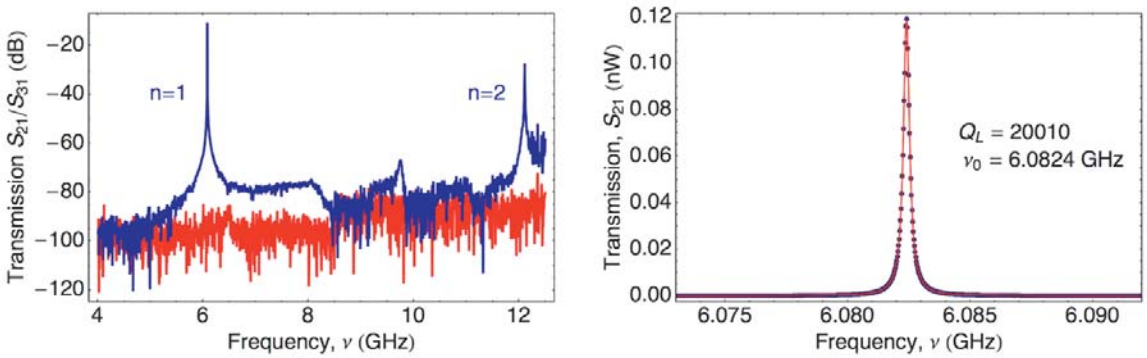

Figure 7.3.: Transmission spectra and behavior around resonance for a DC-biased center pin resonator (device I5): (a) Comparison of transmission through the cavity (S_{21}, blue) and from cavity input through DC bias port (S_{31}, red) over 4 - 12 GHz range, (b) Cavity transmission S_{21} on resonance with Lorentzian fit (red), giving a loaded quality factor of $Q_L = 20010$ and resonance frequency $\nu_0 = 6.0824$ GHz. Loss of photons through the bias port is suppressed by symmetry of the voltage distribution of the fundamental mode such that high quality factors can be maintained.

The resonator structures have been fabricated on a sapphire substrate using the two-layer electron beam lithography technique described in section 4.3. The resulting 2×7 mm chips are positioned 5.5 mm above the bottom of a cylindrical superfluid reservoir of radius $r = 3.175$ mm, mounted in a hermetically sealed copper cell at 15 mK (see Fig. 4.3 and section 4.1.3). As shown in the helium level experiments in chapter 5, the distance H between the bulk surface level in the reservoir and the chip surface sets the radius of curvature of the superfluid film in the gaps. For the experiments presented here, we use coplanar waveguide geometries with center pin widths of $w_{\mathrm{CP}} = 2 - 4\,\mu m$ and gap widths of $w_{\mathrm{G}} = 8 - 10\,\mu m$, corresponding to characteristic impedances in the range of $60 - 80\,\Omega$, slightly higher than usual for circuit QED experiments. The devices are over-coupled by design ($Q_{\mathrm{int}} \gg Q_{\mathrm{ext}}$) with measured loaded quality factors of $Q_{\mathrm{L}} = 1.5 - 2.5 \times 10^4$ and resonance frequencies $\omega_0/2\pi = 4.5 - 6.5$ GHz. The datasets presented in this chapter were taken using three different devices (labelled I5, B13, L3), all with the same constriction-gate based, center pin-biased design but slight variation in trap and cavity parameters. An overview of the device parameters and geometries is given in Tab. 7.1. Devices B13 and I5 have been measured at Yale and device L3 has been measured at the University of Chicago (Schuster Lab), using nominally identical cryogenic setups for transmission measurements, electron generation and DC control.

Bias Port Leakage at Microwave Frequencies

Leakage of microwave photons through the DC bias port is suppressed by symmetry of the voltage distribution of the fundamental mode. The extent to which high quality factors can be maintained depends on the geometric symmetry of the device and the precision to which it can be fabricated in practice. Finite-element simulations of whole 2×7 mm chips with intentional asymmetries (carried out using *Sonnet*) show that leakage through the bias port remains small for asymmetries as large as ~ 0.06 % (bias lead offset from center relative to total resonator length) such that high quality factors can be maintained even for several μm asymmetry on a $L = 10000\,\mu$m resonator. This is well within the alignment precision of the two-layer electron beam lithography process discussed in section 4.3, which can achieve alignment between layers of $\sim$ 20 nm. In addition to electrical symmetry, care must be taken to also ensure geometric symmetry of the chip itself as spurious modes on the chip can influence the quality factors. We can measure microwave leakage through the bias port using an additional bias tee as shown in Fig. 7.1 a. A comparison of transmission spectra over a 4 - 12 GHz range through the cavity (S_{21}) and the bias port (S_{31}) is shown in Fig. 7.3 for device I5. As can be seen, the fundamental mode transmission is not reduced in any significant way by the presence of the bias port and quality factors of $Q_L \simeq 2\times10^5$, reasonably close to design values of 2.5×10^5, can be achieved. As expected, transmission of the first harmonic mode ($n = 2$) is reduced as the voltage distribution of that mode has an anti-node at the center of the resonator. The ~ 20 % deviation from the designed Q values can most likely be attributed to the broken geometric symmetry of this chip design. As can be seen in Fig. 7.2 a, the single electron trap and the attached bias line slightly break the symmetry of the device, leading to small differences in the effective input impedances seen from the center looking into the r.h.s and the l.h.s of the resonator. Simulations of the on-chip current density profile using *Sonnet* can help understand this effect in more detail. The cavity linewidths possible with our simple implementation of a DC center pin bias proved sufficient for the experiments presented in this chapter. More careful engineering of the microwave environment and the geometric symmetry of the chip will likely allow this design to achieve higher quality factors.

7.1.2 Many-Electron Cavity Coupling Mechanisms

At saturated bulk film electron densities of $n_s \simeq 2 \times 10^9$ cm^{-2}, a DC-biased center pin resonator with total gap area $A \sim 10\,\mu\text{m}\times10000\,\mu$m can trap on the order of 10^6 electrons

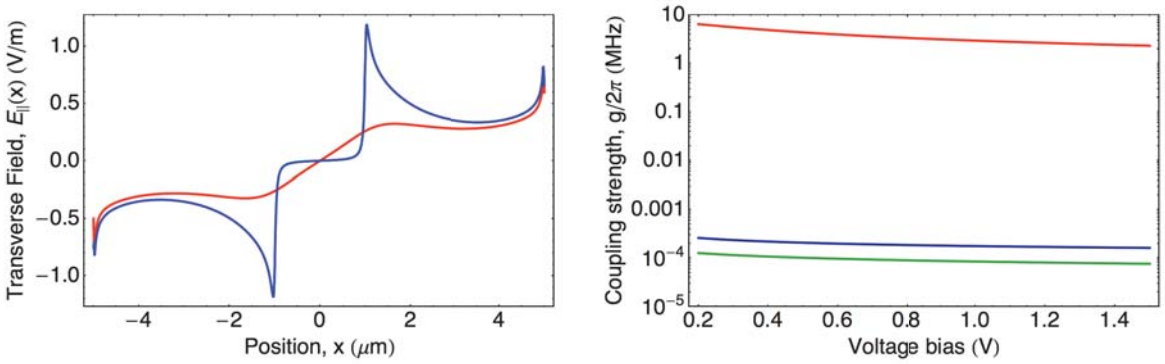

Figure 7.4.: (a) Finite-element simulation of transverse electric field component along the resonator cross-section for a DC-biased resonator (red) with aspect ratio 1/20 (ground plane to center pin thickness) and a regular coplanar waveguide resonator (blue) with aspect ratio 1, assuming a typical rms voltage between center pin and ground plane of 2 μV. A resonator geometry with center pin and channel widths 2 μm and 10 μm was used for the simulations. (b) Numerically calculated coupling strengths as a function of center pin voltage bias for the center-of-mass (blue), scissor (green) and stretch mode (red) of an $N = 3$ electron linear chain (see section 3.7.1), using the same device geometry as in (a).

[2]. At low temperatures and high densities, the trapped electrons form a Wigner crystal or Coulomb liquid as discussed in section 2.2. There are a variety of ways the electron system can potentially couple to the cavity and impact its resonance frequency and quality factor. In this section we explore some of these mechanisms and estimate the corresponding coupling strengths, with particular focus on the dipole interaction of collective electron excitations and the electromagnetic field in the cavity.

Both collective in-plane motion, along the transverse and longitudinal resonator axis, and vertical motion orthogonal to the resonator plane can couple to the cavity via dipole interaction. This type of coupling is similar to the Jaynes-Cummings interaction of lateral motion in single-electron quantum dots discussed in section 3.4 and would manifest itself in dispersive shifts in cavity frequency off resonance. In addition, there are a number of classical ways the presence of electrons can potentially impact the cavity frequency such as electrostatic pressure on the helium surface. Which type of coupling is realized will in general depend on the configuration and density of the electron ensemble as well as its orientation with respect to the electromagnetic field in the cavity. In particular, the spectrum of any in-plane modes of the ensemble is a function of geometry and the ordering of electrons in the trap.

[2] As shown in section 2.3.4, the critical electron density can be significantly increased in micro-channel geometries, by up to 1 - 2 orders of magnitude compared to the bulk film case.

Electromagnetic Field Orientation

We can simulate the electromagnetic field for the DC-biased resonator cross-section using finite-element simulations (*Ansoft Maxwell 2D*). Fig. 7.4 a shows a comparison of the simulated transverse field components of a DC-biased resonator with an aspect ratio of $t : d = 1 : 20$ (red) and a regular transmission line resonator with an aspect ratio of $t : d = 1 : 1$ (blue), where t and d are the thickness of the center pin and ground plane, respectively, see Fig. 7.1. The transverse field components are shown at position $z = 10\,\text{nm}$ above a flat helium surface flush with the ground plane, which is the approximate position of electrons in their vertical ground states for a completely filled micro-channel. A typical rms voltage of $V_{\text{rms}} = 2\,\mu\text{V}$ was assumed. At the center of the resonator gap ($x = 0$), the field vector is parallel to the z direction and the transverse component is zero. The magnitude of the transverse field component is maximized around the edges of the ground plane and center pin. Compared to the regular resonator geometry (shown in blue in Fig. 7.4 a), the DC-biased resonator has a larger transverse field component around the center of the trap ($\pm 1\,\mu\text{m}$), which could be favorable for dipole coupling of transverse collective modes localized in the region about the center, as shown below.

Electron Configuration and Molecular Dynamics Simulations

In section 2.2 we saw how an electron ensemble on liquid helium assumes an ordered state at low temperatures and high densities in the absence of external fields. In this regime, the electrons become localized in the lattice sites of a Wigner crystal. In the presence of external holding potentials, the configuration of electrons in the ensemble is in general determined by the combination of the confining electric fields, the repulsive electron-electron Coulomb interactions and the attractive interactions with image charges in the superfluid and surrounding metal electrodes. Determining the positions of surface electrons in such a trap represents a complex many-body problem that has to be tackled numerically, even for the simple one-dimensional case with $N > 3$ electrons (see section 3.7.1). To simulate the equilibrium electron configuration in two dimensions and obtain information on the ordering of the ensemble in the parabolic trapping potential we can use molecular dynamics simulations. Molecular dynamics (MD) represents a class of deterministic, iterative algorithms that can be used to find solutions to many-body problems [218]. Particles at positions $\mathbf{r}_i(t)$ are displaced in small increments $\mathbf{r}_i(t + \Delta t) = \mathbf{r}_i(t) + \delta\mathbf{r}_i$ subject to an acceleration

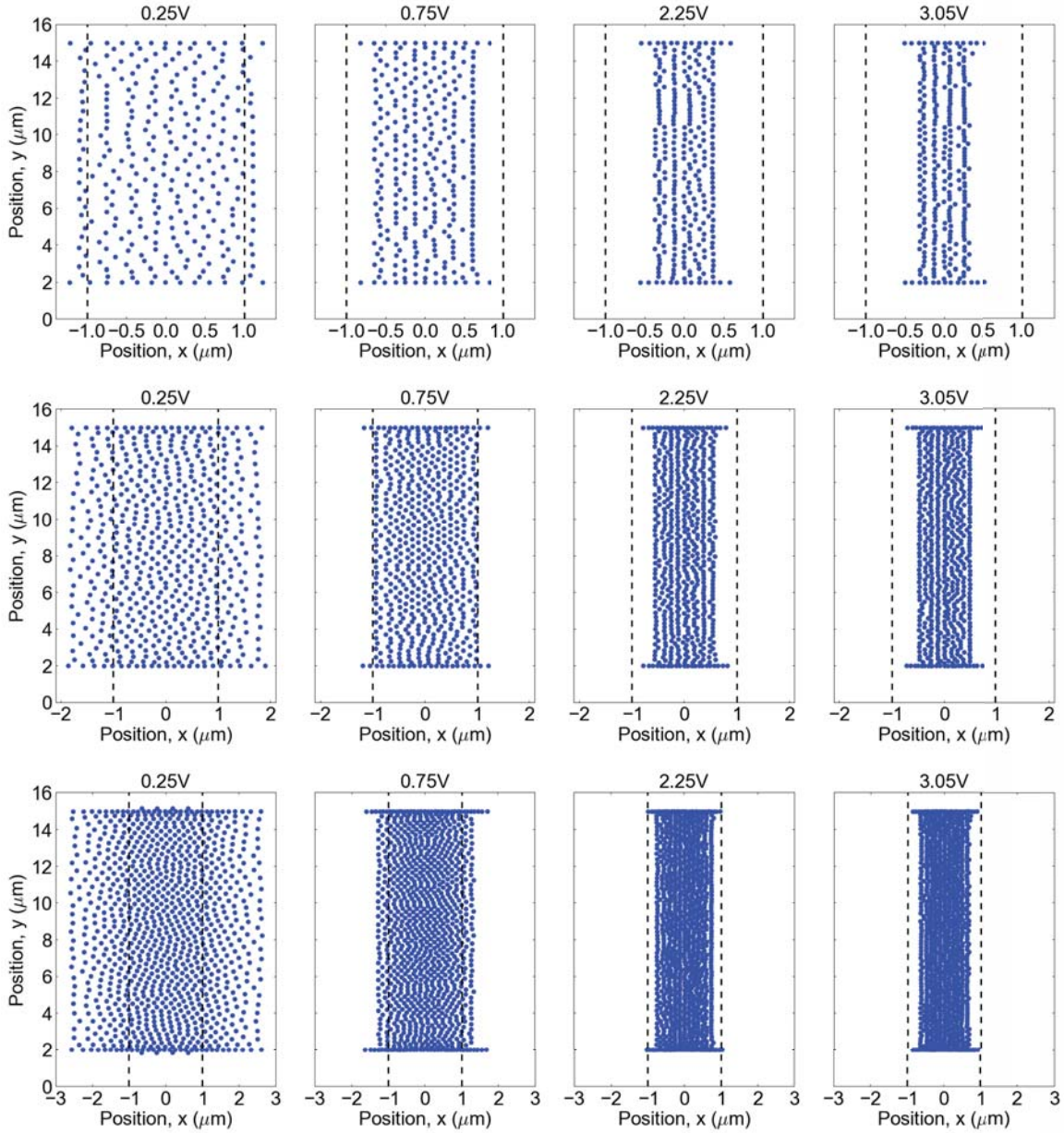

Figure 7.5.: Molecular dynamics simulations of electron configurations in a short section of a DC-biased center pin resonator of length $L = 15$ mm, gap width $w_{\mathrm{G}} = 8\,\mu$m and center pin width $w_{\mathrm{CP}} = 2\,\mu$m for four different trap voltages (columns) and electron densities: $n_e = 2.6 \times 10^8$ cm^{-2} (top row, $N_e = 288$ electrons total), $n_e = 5.1 \times 10^8$ cm^{-2} (center row, $N_e = 576$) and $n_e = 8.6 \times 10^8$ cm^{-2} (bottom row, $N_e = 960$). The region above the center pin between $+1\,\mu$m and $-1\,\mu$m is indicated by dashed lines. The simulations take into account electron-electron interactions as well as image-charge effects in both liquid helium and the metal electrodes. Simulation data courtesy of G. Yang, Schuster Lab, University of Chicago.

$\mathbf{a}_i = (-1/m_i)\nabla V(\mathbf{r} = \mathbf{r}_i)$, where $\delta\mathbf{r}_i$ is calculated using a chosen integrator based on the equations of motions in a force field with potential $V(\mathbf{r})$. More details on MD simulations for electrons on helium in micro-channel geometries can be found in [219]. The results of such simulations for different electron densities and voltage biases are shown in Fig. 7.5 for a short section of a DC-biased center pin resonator of length $L = 15\,\mu$m, gap width $w_G = 8\,\mu$m and center pin width $w_{\mathrm{CP}} = 2\,\mu$m. Electrons are seeded initially at uniform random positions in the trap at the start of each simulations.

As can be seen in Fig. 7.5, at low trap voltages V_{cp} the electrons are spread out over the waveguide gap with some weak ordering present. As V_{cp} increases, the confining potential compresses the electron ensemble and ordering effects start to emerge more clearly. For both low and high densities, the electrons form longitudinal linear chains at high trap voltages and are localized in a small region around the center of the trap, directly above the center pin of the resonator (indicated by dashed lines in Fig. 7.5). In combination with the finite-element electric field simulations, the MD simulations indicate that as the trap voltage decreases a significant number of electrons are localized in a region where the electric field has a large in-plane, transverse component while at high trap voltages they tend to be concentrated in a region where the RF electric field is mostly oriented in the vertical direction orthogonal to the surface. Note that the ordering of electrons at the top and bottom of the simulated region, visible as horizontal linear chains at $y = 15\,\mu$m and $y = 2\,\mu$m, is a consequence of edge effects in the simulations as a result of the finite extent of the region.

Transverse Mode Coupling

The coupling of the cavity field to collective vibrational modes in one-dimensional many-electron traps was investigated in section 3.7.2. Following section 3.7.1, the motional excitations in a parabolic trap, such as along the transverse resonator direction, can be modeled as linear N electron chains. There it was shown that an N electron chain has N independent modes. For $N = 2$ we found a center-of-mass and a 'stretch' mode with different effective mass and oscillation frequencies while for $N = 3$ we obtained an additional 'scissor' mode. For general N, the lowest mode is always the CM mode where the crystal oscillates like a rigid body at the fundamental trap frequency while the next highest mode is always the stretch mode where the displacement of each electron is proportional to its distance from the trap center. Since the wave functions of the many-electron modes are concentrated about the center of the CPW gap where the transverse field component is close to zero (see Fig. 7.4 a),

we expect this type of dipole coupling to be small. However, at typical saturated electron densities there are potentially many such electron chains in parallel along the longitudinal direction. The coupling could therefore be enhanced by a factor proportional to the overall number of electrons N_e. In addition, at high densities a significant portion of electrons can be located in the gap region away from the center pin where the transverse field component is larger. Whether or not such modes are realized in our geometry depends on the specific electron configuration which is a function of density and center pin voltage, as indicated by the MD simulations shown above. Observing the transverse mode-cavity coupling in transmission measurements will also depend on the relative detuning between cavity and vibrational mode. For large detunings, the electron modes would cause a dispersive shift in cavity frequency and any changes in quality factor would depend on coupling strength and the linewidths of the cavity and the modes.

Using the simulated transverse electric field (Fig. 7.4 a) and the transverse mode wave functions (section 3.7.1), we can estimate the coupling strength of the different modes via numerical integration of (3.145). Care must be taken here to use the correct coordinate system for both the simulated field and the wave functions. The collective mode coordinates Q_k for the stretch modes derived in section 3.7.1 contain additional offset terms that must be taken into account. To estimate the coupling strength of a single one-dimensional transverse mode, we first simulate the DC potential along the transverse axis for a given voltage bias and obtain the fundamental trap frequency for $V_{\mathrm{cp}} = 1$ V by fitting to a harmonic oscillator potential, similar to the method used for single-electron quantum dots in section 3.3.3. Using the vibrational mode wavefunctions derived in section 3.7.1, the coupling strength $\hbar g_k$ is then obtained by evaluating the matrix elements (3.145) numerically using the simulated transverse electric field. The coupling strength is a function of trap voltage bias since the size of the vibrational wavefunctions (and hence the size of the dipole moment) changes with voltage. Large voltages lead to tight confinement around the trap center, decreasing the equilibrium electron spacing, as also evidenced by the molecular dynamics simulations. Lowering the voltage bias decreases the vibrational mode frequency and increases the size of the wave functions. Numerically calculated coupling strengths for the $N = 3$ electron case are shown in Fig. 7.4 b as functions of center pin voltage bias. As expected coupling is small, with the center-of-mass and scissor mode coupling three to four orders of magnitude smaller than for the stretch mode. The stretch mode couples more strongly since the corresponding vibrational oscillator is offset from the trap center by an amount proportional to the equilib-

rium electron separation (see section 3.7.1), slightly shifting the dipole into regions with a higher transverse electric field component.

To estimate the collective coupling for N_k transverse modes in parallel along the longitudinal resonator direction, we can treat the modes as independent single-mode harmonic oscillators in a first approximation (sometimes referred to as the *Tavis-Cummings Model* [220,221]). In the dispersive limit of large detunings $\Delta_k = \omega_k - \omega_R$ where ω_k is the frequency of the kth mode, this gives a dispersive shift in cavity resonance frequency of

$$\delta\omega_R = \omega_R \pm \frac{g_{\text{eff}}^2}{\Delta_k} \quad , \quad g_{\text{eff}} = \sqrt{N_k} g_k \tag{7.1}$$

where g_{eff} is the effective, collective coupling strength, g_k the coupling strength of a single kth order transverse mode and N_k the number of modes. Here, the mode frequencies ω_k can be tuned through the center pin voltage. The quality factor of the cavity in this simple single-mode harmonic oscillator model can be written as

$$Q = \frac{\Delta_k^2 + \gamma_k^{*2}}{2g_{\text{eff}}^2 \gamma_k^* + \kappa(\Delta_k^2 + \gamma_k^{*2})} \tag{7.2}$$

where $\kappa/2\pi = \omega_R/2\pi Q$ is the cavity decay rate and $\gamma_k^*/2\pi$ is the effective line width of the kth collective transverse mode. This expression is a good approximation in the limit of γ_k^*, κ or Δ_k large compared to g_{eff}. Note that both Δ_k and g_{eff} are functions of center pin voltage here. The above expressions will be used in section 7.2 for fitting to experimentally observed frequency shifts and quality factors.

The coupling of vertical Rydberg states (section 2.1) can be treated in a similar manner as for the in-plane motional excitations. The transition frequencies between the ground and first excited vertical states ω_{10} can be Stark-tuned through the center pin voltage as discussed in section 2.1.2 and the coupling strength depends on the magnitude of the vertical component of the electric field. Qualitatively, the coupling strength of those transitions is expected to be larger than for the transverse modes as the electrons are localized above the center pin where the RF electric field vector is mostly parallel to their vertical motional axis, leading to larger dipole coupling matrix elements. However, with transition frequencies of > 100 GHz, the detuning $\Delta = \omega_{10} - \omega_R$ will be on the order of hundreds of GHz and the corresponding dispersive cavity shifts $\delta\omega_R$ are expected to be small for a single electron. As for the transverse modes, the collective coupling can be enhanced by a factor of $\sqrt{N_e}$ in an independent

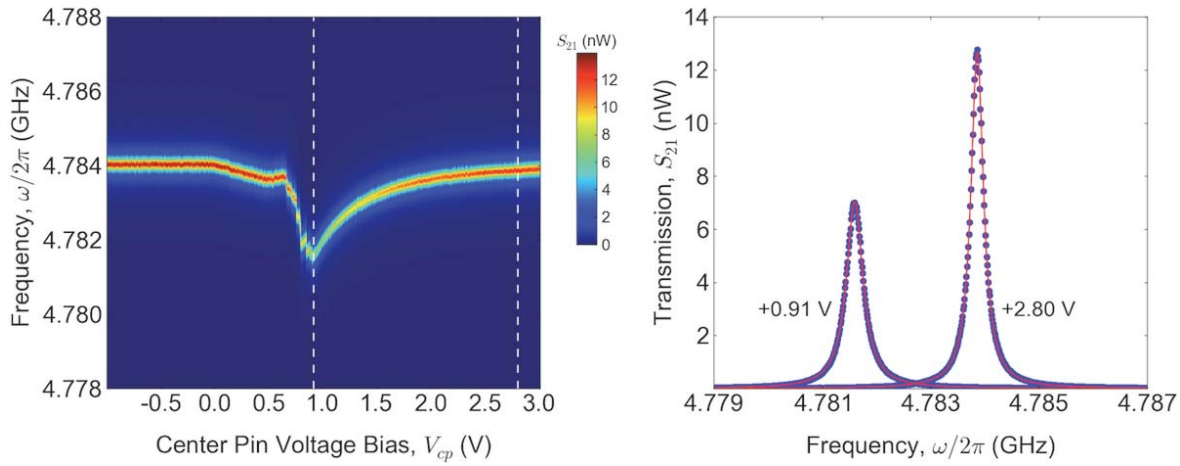

Figure 7.6.: Detection of trapped electrons on helium in a cavity transmission measurement (device L3): (a) Measured cavity transmission as a function of center pin voltage bias $V_{\rm cp}$ plotted versus probe frequency $\omega/2\pi$, (b) Measured cavity transmission as a function of probe frequency $\omega/2\pi$ at two different center pin biases $V_{\rm cp} = +0.91$V and $V_{\rm cp} = +2.80$ V, indicated by dashed vertical lines in (a). Fits to Lorentzian line shapes are shown as solid red lines. Electrons are initially loaded into the gap of the coplanar waveguide cavity by thermionic emission, where they are bound vertically to the surface of a capillary action film of superfluid helium and confined laterally by the parabolic holding potential created by a $V_{\rm cp} = +3$ V bias on the center pin. The center pin bias is swept from $+3$ to -1 V in $\Delta V_{\rm cp} = 4$ mV steps and a full cavity transmission trace is taken at each step.

oscillator model.

7.2 Electron-Induced Frequency and Q Shifts

In this section we present experiments demonstrating how electrons on helium can be trapped in the gap region of a DC-biased center pin resonator. Their presence manifests itself in the form of trap voltage-dependent shifts in cavity resonance frequency of up to ~ 10 linewidths and quality factor reductions of up to ~ 30 %, corresponding to an increase in cavity loss of $\Delta\kappa/2\pi = 125$ kHz. Tuning the center pin voltage changes the effective electron holding potential, which affects all of the coupling mechanisms discussed above in a voltage-dependent way and therefore represents an effective way of detecting electrons.

The data presented in this section was taken from devices L3 and B13 (see Tab. 7.1). Device L3 has a bare resonance frequency of $\omega_0/2\pi = 4.791583$ GHz, loaded quality factor $Q_L = 17750$ and corresponding linewidth $\kappa/2\pi = \omega_0/2\pi Q = 270$ kHz in the absence of any superfluid or electrons, while for device B13 $\omega_0/2\pi = 6.11231$ GHz and $\kappa/2\pi = 294$ kHz. The devices are characterized by slightly different channel geometries as indicated in Tab. 7.1. We start by filling the superfluid helium reservoir below the chip to $H \simeq 2.6$ mm, where H is the distance between the bulk surface in the reservoir and the top of the micro-channel on the

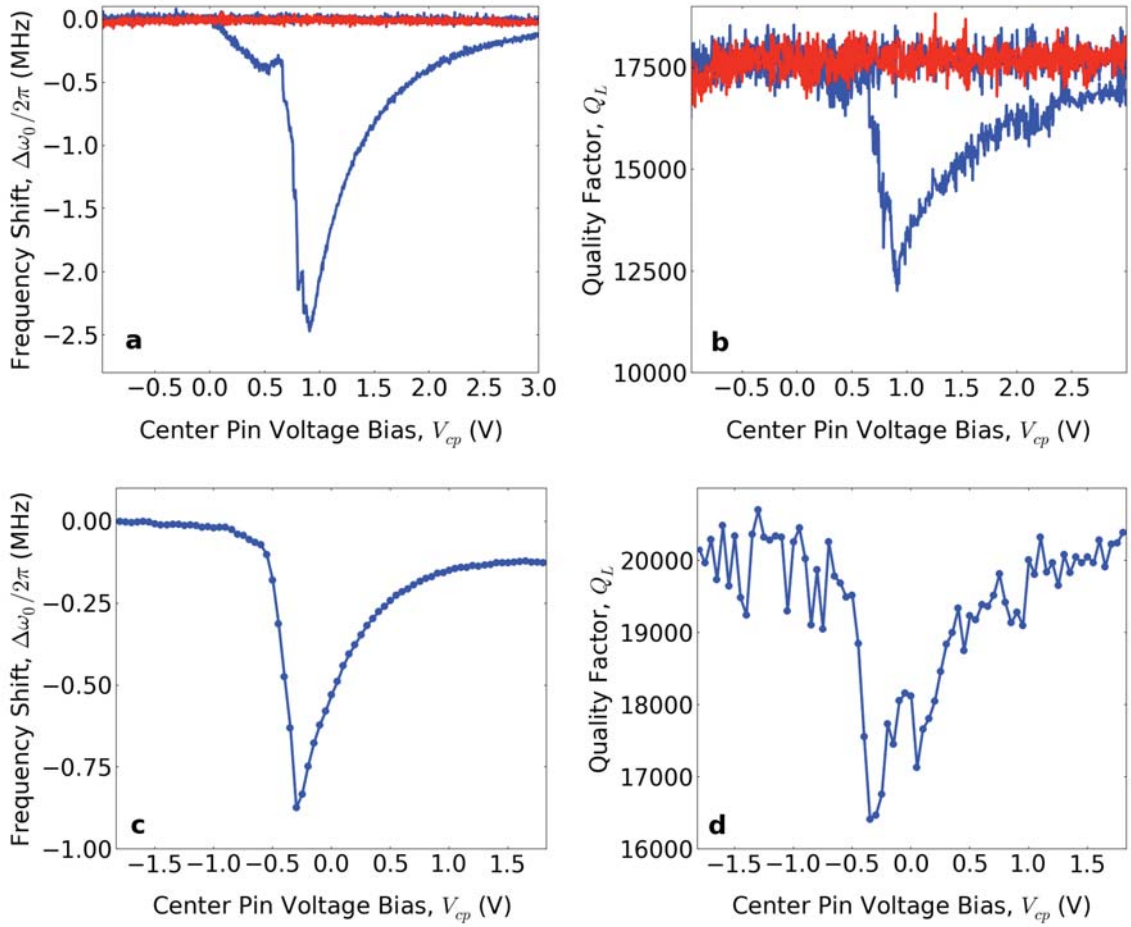

Figure 7.7.: Electron induced shifts in resonance frequency $\Delta\omega_0/2\pi$ and loaded quality factor Q_L for devices L3 (a, b) and B13 (c, d): (a) Measured frequency shift $\Delta\omega_0/2\pi$ as a function of center pin voltage bias $V_{\rm cp}$ in the presence (blue) and absence (red) of electrons in the resonator mode volume. (b) Measured loaded quality factor Q_L as a function of center pin bias $V_{\rm cp}$. (c) and (d) Measured frequency shifts and quality factors for device B13. For device L3, electrons are loaded into the gap of the coplanar waveguide cavity at an initial bias of $V_{\rm cp} = +3$ V which is then swept to -1 V in 4 mV steps (solid blue lines). The sweep direction is subsequently reversed $-1 \rightarrow +3$ V (solid blue lines at top) and no frequency or quality factor shifts are observed, indicating that the resonator mode volume has been depleted of all electrons at negative voltages. Control measurements without electrons in the waveguide gap are shown in red. For device B13, electrons are loaded at an initial bias of $V_{\rm cp} = +1.8$ V and the bias is swept in 50 mV steps.

chip. This corresponds to a radius of curvature of $R_c = \sigma/\rho g H \simeq 96\,\mu$m such that the CPW gap is filled by capillary action in a self-stabilized way. The superfluid level in the gap was determined using the level-meter detection method discussed in chapter 5. For the given level of helium we observe a frequency shift of $\Delta\omega_0/2\pi = -7.56$ MHz in device L3 such that the cavity resonance is located at $\omega_0/2\pi = 4.784021$ GHz in the absence of electrons. This establishes a film of known thickness in the gap that is relatively insensitive to fluctuations in the reservoir (see section 5.2). The level is kept fixed for the remainder of the experiment. Electrons are generated via pulsed thermionic emission from a tungsten filament, mounted about 4.5 mm above the device in vacuum covered by a 30 nm van-der-Waals film of liquid helium, see section 4.1.4 for details. As shown in chapter 6, the saturated electron density can be estimated by $n_s \simeq \varepsilon_{\mathrm{He}}\varepsilon_0 V_{\mathrm{cp}}/eh$ where $h \simeq 1\,\mu$m is the helium film thickness and V_{cp} the center pin voltage bias when pulsing the filament. This corresponds to areal densities of $n_s \sim 1{-}5\times10^9$ cm^{-2} for our device geometry, depending on V_{cp}. The presence of electrons is detected by measuring the cavity resonance in transmission while tuning the electron holding potential through the center pin voltage V_{cp}. The results of such electron cavity-detection experiments are shown in Figs. 7.6 and 7.7. Electrons are first loaded into the resonator gap at an initial center pin bias of $V_{\mathrm{cp}} = +3$ V. We subsequently sweep the DC bias in $\Delta V_{\mathrm{cp}} = 4$ mV steps from +3 to -1 V and take a full transmission trace at each step, going from right to left in Fig. 7.6 a. As can be seen in Fig. 7.6, the presence of the trapped electron ensemble leads to a voltage-dependent shift of the cavity resonance towards lower frequencies before reverting back to its original frequency at negative voltages. The resonance shifts by up to ~ 10 cavity linewidths in frequency while transmitted amplitude is reduced by a factor of 2 (Fig. 7.6 b).

The extracted frequency shift and quality factor are shown in Fig. 7.7 a and b as functions of center pin bias for device L3. The electron-induced frequency shift reaches a maximum of $\Delta\omega_0/2\pi = -2.47$ MHz at $V_{\mathrm{cp}}^{(\mathrm{max})} = +0.91$ V with an overall reduction in quality factor of 5300 or about 30%, which corresponds to an additional cavity loss of $\Delta\kappa_{\mathrm{max}}/2\pi = 125$ kHz. Below $V_{\mathrm{cp}}^{(\mathrm{max})}$, both frequency and quality factor revert to their uncharged values and the signal disappears completely at negative voltages. The reduction in signal below $V_{\mathrm{cp}}^{(\mathrm{max})}$ can be attributed to the dissipation of electrons out of the trapping region, which is investigated in more detail in section 7.3 below. Subsequently reversing the sweep direction and going back to positive voltages $V_{\mathrm{cp}} = -1 \rightarrow +3$ V (left to right in Fig. 7.7, top blue traces), the cavity resonance stays constant with no frequency or quality factor shifts, indicating

the gap region has been depleted of all electrons at negative voltages. Control experiments with uncharged superfluid films under the same conditions, shown in red in Figs. 7.7 a and b, show no voltage-dependent frequency or quality factor shifts. Note that the small voltage-dependent changes in helium level observed in the level tuning experiments of section 5.3 lead to frequency shifts that are an order of magnitude smaller than the observed electron-induced shifts and hence are not visible on the scale of Fig. 7.7. In summary, the data provides strong evidence that the observed shifts are indeed caused by the presence of electrons in the cavity mode volume. The electron-induced frequency and quality factor shifts have been reproduced in independent experiments using three different devices (see Tab. 7.1). Maximum shifts generally vary between 1 - 3 MHz with $V_{\mathrm{cp}}^{(\mathrm{max})} = -0.5$ to 1.0 V depending on helium level, device geometry and electron density. Measured frequency shifts and quality factors for device B13 are shown in Fig. 7.7 c and d, which has been loaded with electrons at an initial center pin bias of $V_{\mathrm{cp}} = +1.8$ V and a helium-induced shift of $\Delta\omega_0/2\pi = -6.914$ MHz indicating to a self-stabilized capillary action film. The maximum electron-induced frequency shift for this device was $\Delta\omega_0/2\pi \simeq -0.9$ MHz with an increase in cavity linewidth of $\Delta\kappa_{\mathrm{max}}/2\pi = 78$ kHz or about 27 % at $V_{\mathrm{cp}}^{(\mathrm{max})} = -0.3$ V. While observed frequency and Q shifts are qualitatively similar and consistent across devices, we find large differences in the values of the maximum shift bias voltages $V_{\mathrm{cp}}^{(\mathrm{max})}$, both between devices as well as between cooldowns of the same device. This is likely a consequence of the same random voltage offsets already observed in the helium level tuning experiments of section 5.3, see the discussion in section 5.3.3. As pointed out earlier, the origin and nature of these voltage offsets is not yet well-understood.

While the observed shifts have been shown to be consistent with the presence of a trapped electron ensemble in the waveguide gap, the coupling mechanisms are not fully understood quantitatively at this point and will likely require further investigation. As a first attempt, we can fit the independent oscillator model for the dipole coupling of transverse vibrational modes of the ensemble as discussed in section 7.1.2. In the limit of large detunings, the coupling of transverse modes leads to dispersive cavity frequency shifts of the form (7.1) and impacts the quality factor according to (7.2). The transverse mode frequencies are tuned by the applied center pin voltage with a dependence $\sim V^{1/2}$, see section 3.7.1. The dispersive cavity shift increases with decreasing detuning (decreasing voltage bias) as the transverse modes are tuned closer to resonance with the cavity. In addition, lower trapping voltages lead to a higher electron density in regions of larger transverse field away from the center

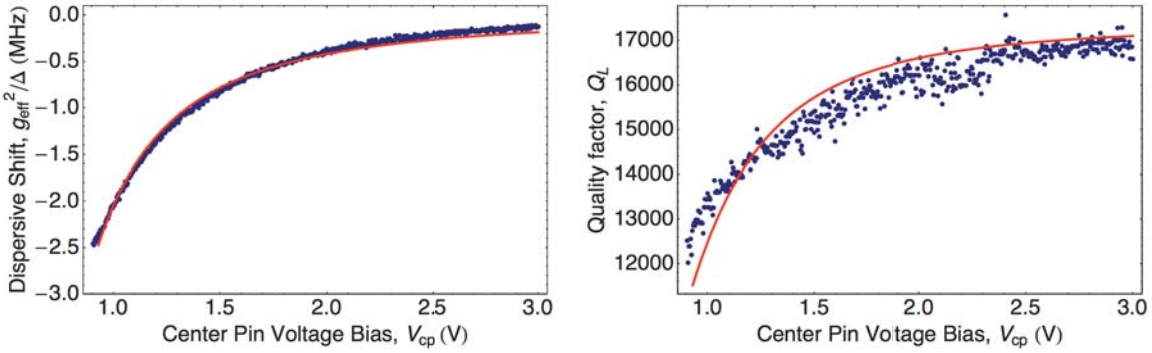

Figure 7.8.: Fits of $N = 3$ electron transverse mode dispersive shifts to measured frequency and quality factor shifts based on an independent oscillator model (see section 7.1.2): (a) Fit of eq. (7.1) to measured frequency shift with fit parameters electron number $N_e = 9050$ and voltage offset $V_{\text{off}} = -0.31$ V, (b) Fit of eq. (7.2) to measured quality factor with fit parameter $\gamma_k^*/2\pi = 885$ MHz using the electron number extracted from the frequency shift fit in (a).

pin. Using the wave functions and transverse field components obtained from numerical simulations as outlined in section 7.1.2, we can fit eqs. (7.1) and (7.2) for a given mode index k to the measured frequency and Q shifts above $V_{\text{cp}}^{(\max)}$ and estimate the electron density in the resonator and the line width γ_k^*. Note that this simple model assumes a uniform coupling strength along the longitudinal resonator axis. Fig. 7.8 shows fits of eqs. (7.1) and (7.2) for the $N = 3$ electron transverse stretch mode to the data of device L3. We obtain a total number of electrons of $N_e = 9050$ from the dispersive shift fit, which corresponds to an electron density of $n_e \sim 10^7$ cm^{-2}. A voltage offset of $V_{\text{off}} = -0.31$ V was used to obtain the fits. The quality factor fit yields a line width for the $N = 3$ electron transverse mode of $\gamma_k^*/2\pi = 885$ MHz. The coupling strengths of the center-of-mass and scissor modes are generally too small and do not fit the data well for any meaningful values of electron density and linewidth. While the transverse mode model fits the data reasonably well, the obtained electron densities are one to two orders of magnitude lower than expected. The molecular dynamics simulations of section 7.1.2 suggest that the true in-plane mode structure is likely more complicated than that of a simple linear chain in the transverse direction since the configuration of the electrons in the ensemble is a strong function of density and voltage bias. Spectroscopic measurements with an additional RF tone have not shown any direct resonant excitation of collective in-plane or vertical modes in the frequency range 4 - 12 GHz.

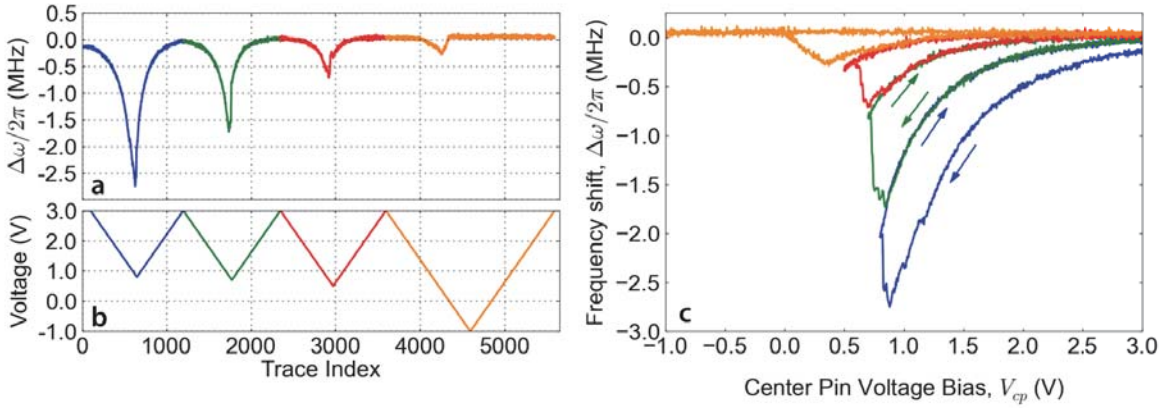

Figure 7.9.: Electron loss and voltage hysteresis measurements (device L3): (a) Measured frequency shift $\Delta\omega/2\pi$ as a function of time (proxied by trace index), (b) Triangular voltage sweep sequence as a function of trace index, (c) Measured frequency shifts as a function of center pin voltage bias V_{cp}, showing the same data as in (a) with sweep directions indicated by arrows. Starting at a positive trapping voltage $V_{\mathrm{cp}}^{(\mathrm{start})} = +3$ V the voltage bias is swept to a positive endpoint $V_{\mathrm{cp}}^{(\mathrm{start})} \rightarrow V_{\mathrm{cp}}^{(\mathrm{end})}$ and the sweep direction is subsequently reversed $V_{\mathrm{cp}}^{(\mathrm{end})} \rightarrow V_{\mathrm{cp}}^{(\mathrm{start})}$. This cycle is repeated for different endpoints $V_{\mathrm{cp}}^{(\mathrm{end})} = +0.8, 0.7, 0.5$ and -1 V, giving the triangular sequence shown in (b). Each color corresponds to one cycle $V_{\mathrm{cp}}^{(\mathrm{start})} \rightarrow V_{\mathrm{cp}}^{(\mathrm{end})} \rightarrow V_{\mathrm{cp}}^{(\mathrm{start})}$.

7.3 Loss and Hysteresis Measurements

To further investigate the origin of the electron-induced shifts in frequency and linewidth and the gradual reduction in signal at voltages below $V_{\mathrm{cp}}^{(\mathrm{max})}$, a series of hysteresis experiments has been carried out. In those measurements we start at a large positive trapping voltage ($V_{\mathrm{cp}} \sim +3$ V), sweep the voltage bias to a positive endpoint $V_{\mathrm{cp}}^{(\mathrm{start})} \rightarrow V_{\mathrm{cp}}^{(\mathrm{end})} < V_{\mathrm{cp}}^{(\mathrm{max})}$ and subsequently reverse the sweep direction $V_{\mathrm{cp}}^{(\mathrm{end})} \rightarrow V_{\mathrm{cp}}^{(\mathrm{start})}$. The resonance frequency shift $\Delta\omega_0/2\pi$ is monitored during such a sweep and the sweeps are repeated for successively lower endpoints. The purpose of such an experiment is to determine the threshold voltages at which electrons start to leave the resonator mode volume and whether or not electron dissipation happens in a gradual or abrupt fashion. A triangular voltage sweep sequence for a typical hysteresis experiment is shown in Fig. 7.9 b as a function of time (proxied by trace index) for $V_{\mathrm{cp}}^{(\mathrm{start})} = +3$ V and $V_{\mathrm{cp}}^{(\mathrm{end})} = +0.8, 0.7, 0.5$ and -1 V. The frequency shift measured during such a sequence is shown in Fig. 7.9 a as a function of time and in Fig. 7.9 c as a function of voltage V_{cp}, where each color corresponds to one cycle $V_{\mathrm{cp}}^{(\mathrm{start})} \rightarrow V_{\mathrm{cp}}^{(\mathrm{end})} \rightarrow V_{\mathrm{cp}}^{(\mathrm{start})}$. In each cycle, we observe a sharp reduction in frequency shift near the endpoint (Fig. 7.9 c), which we attribute to the loss of electrons from the resonator mode volume below $V_{\mathrm{cp}}^{(\mathrm{max})}$. At low trapping voltages, the holding potential is shallow enough such that it becomes energetically favorable for some electrons to leave the trap region. The resulting reduction in

electron density leads to a redistribution of the remaining electrons in the resonator mode volume with an increased equilibrium spacing, which manifests itself in a reduction in frequency shift below $V_{\mathrm{cp}}^{(\mathrm{max})}$. The most likely electron dissipation paths are through the $2\,\mu$m gap capacitors at the input/output of the resonator and the constriction gate at the bias port, which represent relatively low potential barriers. The signal exhibits hysteretic behavior with respect to voltage bias. As can be seen in Fig. 7.9 c, where the sweep directions are indicated by arrows, each subsequent downward sweep $V_{\mathrm{cp}}^{(\mathrm{start})} \rightarrow V_{\mathrm{cp}}^{(\mathrm{end})}$ exactly retraces the previous upward curve, which indicates that the number of electrons remains constant above $V_{\mathrm{cp}}^{(\mathrm{max})}$ as no reduction in signal is observed between sweeps. The final sweep to $V_{\mathrm{cp}}^{(\mathrm{end})} = -1$ V depletes the resonator mode volume of all electrons as evidenced by the vanishing frequency shift on the reverse sweep. The gradual reduction in frequency shift $\Delta\omega_0/2\pi$, which can be assumed to be proportional to surface electron density n_e, shows that it is possible to decrease the number of electrons in the resonator in a controllable fashion by tuning the trap voltage to positive values below $V_{\mathrm{cp}}^{(\mathrm{max})}$. We will take advantage of this in the lifetime measurements below. However, a more detailed understanding of the coupling mechanisms and the exact relation between frequency shift $\Delta\omega_0/2\pi$, electron density n_s and trap voltage V_{cp} is required to quantitatively exploit this effect.

Ensemble Stability Measurements

In a final experiment, we investigate the stability and dissipation of the electron ensemble in the resonator trap over longer time-scales at low trapping voltages. To this end, we conduct a simple experiment in which the trap is biased at a constant voltage close to the maximum shift voltage $V_{\mathrm{cp}}^{(\mathrm{max})}$ and the cavity is monitored in transmission over the course of several hours. The results of such a stability measurement for device L3 are shown in Fig. 7.10 together with a diagram of the experiment protocol. Electrons are first loaded into the resonator mode volume at $+3$ V by thermionic emission from the filament. The electron density is subsequently decreased by briefly reducing the bias to $V_{\mathrm{cp}} = +0.8$ V and swept back to $+3$ V, taking advantage of the controlled unloading demonstrated qualitatively in the hysteresis experiments above. We then bias the center pin at $V_{\mathrm{cp}} = +1.25$ V where the electron-induced signal is significant at a measured frequency shift of $\Delta\omega_0/2\pi = -1.45$ MHz. The trapping voltage is then held constant and the cavity is measured in transmission for 5.5 hours. At the end of this period, we deplete the resonator mode volume of electrons by applying a large negative bias of $V_{\mathrm{cp}} = -1$ V to the center pin such that the resonance frequency of the cavity

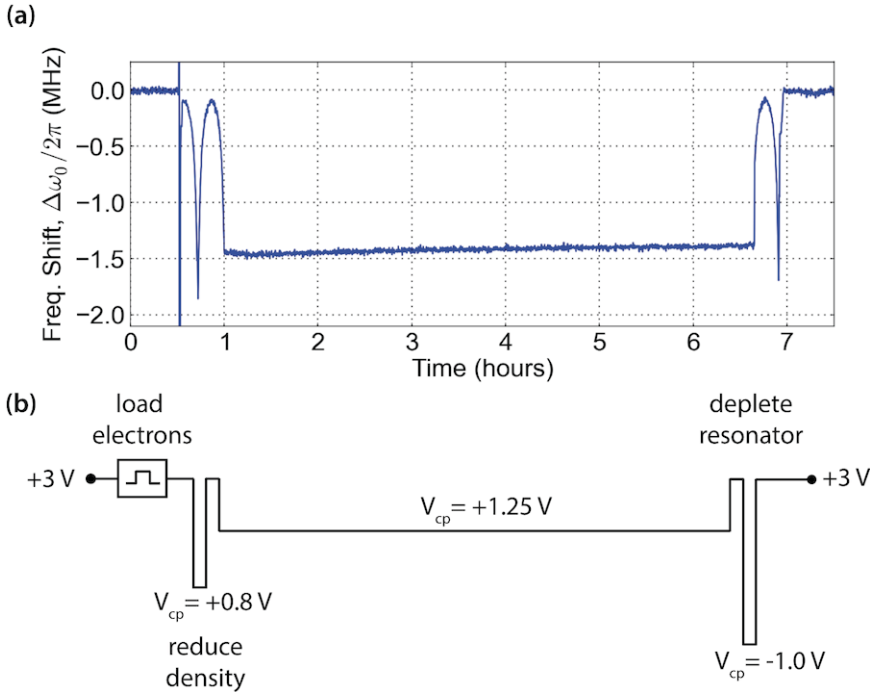

Figure 7.10.: Electron lifetime measurement over long time-scales: (a) Measured frequency shift as a function of time, (b) Diagram of experiment protocol illustrating the sequence of center pin biases. Electrons are initially loaded into the waveguide gap at $V_{\mathrm{cp}} = +3$ V and the electron density is subsequently reduced by biasing the center pin at $V_{\mathrm{cp}} = +0.8$ V, below the maximum shift voltage $V_{\mathrm{cp}}^{(\mathrm{max})} = +0.91$ V, which lowers the electron holding potential to the point where it becomes energetically favorable for some electrons to leave the waveguide gap region. The bias is then kept constant at $V_{\mathrm{cp}} = +1.25$ V over the course of 5.5 hours. The gap region is depleted of electrons at the end of this period by applying a negative voltage $V_{\mathrm{cp}} = -1$ V to the center pin.

returns to its original unshifted value.

8 Conclusion & Outlook

THE concepts and experiments discussed in this thesis represent the first major step towards circuit QED experiments with electrons on helium, laying the foundation for a variety of future quantum optics experiments using the lateral motional and spin degrees of freedom of trapped electrons. While the results presented in this thesis are encouraging and many of the technical hurdles towards 'eonHe cQED' have been cleared, they represent only a first proof principle with many more exciting experiments to come. This chapter provides some reflections on extending the work presented in this thesis and highlights some of the obstacles that have to be overcome towards cavity QED in the single-electron regime and the implementation of a true hybrid circuit QED system.

Reaching the Single-Electron Regime

The ultimate goal is to construct quantum dots with electrons on helium operated in the single-electron regime, where the lateral quantized motion couples to the electromagnetic field in a CPW cavity via dipole interaction. The theoretical basis for such single- and few-electron quantum dots was discussed in detail in chapter 3. Such integrated sub-μm size electrostatic traps have also been fabricated in practice in a variety of designs during this PhD project, some of which are shown in Figs. 4.5 and 7.2 e. However, despite many attempts at coupling single-electron dots to cavities no signatures of strong-coupling cavity QED ($g \gg \kappa, \gamma$) have been observed so far, which would manifest itself either in the form of cavity frequency shifts in the dispersive regime of large detunings ($\Delta \gg g$) or as avoided crossings near resonance ($\Delta \sim 0$), see section 3.1. There are a number of areas that likely require improvements in design, fabrication and theoretical understanding:

- **Efficient Trap Loading**: Our early attempts focused on loading the traps directly with thermionically emitted electrons from the filament. Those attempts were unsuccessful,

in part because the effective electrostatic field of the trap seen by the emitted electrons is too small to attract them to the trapping region (the filament is mounted a distance $d \sim 4.5$ mm above the chip and the trap biased at $V_t \sim 1$ V is only about 1 μm^2 in size). A more promising approach is to load the trap from a larger on-chip reservoir, possibly taking advantage of the CCD clocking techniques developed at Princeton [102,217,222]. The key idea here is to first load electrons into a large area of size 100 - 1000 μm^2 by applying a positive bias to a set of submerged electrodes, giving on the order of $N_e \sim 2 \times 10^3 - 10^4$ electrons at saturated density $n_e \sim 2 \times 10^9$ cm^{-2}, and then shuttle electrons individually into the dot along a gate-defined path. The reservoir ideally provides some way of detecting the presence of electrons and measuring their density, for example using the Sommer-Tanner method discussed in chapter 6. This has the advantage of providing an additional, more well-understood electron detection method in addition to that based on cavity QED effects alone. Several attempts at a reservoir-based loading scheme have been made during this PhD project, including a design in which the reservoir is realized in the form of a large micro-channel based Sommer-Tanner geometry, similar to the ones used in Refs. [206, 207]. A section of one such device is shown in Fig. 4.5. Unfortunately, those types of devices introduce significant complexity into the fabrication process and were challenging to realize in practice at the time. More advanced electron beam lithography equipment with better resolution and alignment, such as the one used for the final batch of devices made for this PhD project, might make these designs easier to implement. Furthermore, care must be taken in designing these more complicated structures to maintain the microwave "hygiene" of the chip and avoid parasitic modes. Our second generation of reservoir-based devices lead to the design of the DC-biased transmission line resonators which have been successfully used in the superfluid helium and electron ensemble experiments of chapters 5 and 7. In this design, the gap of the CPW cavity itself can act as an electron reservoir and the presence of electrons can be detected through frequency and quality factor shifts before attempting to load the single-electron trap.

- **Motional Frequency and Trap Design:** The design-specific simulations in section 3.3.3 have shown that it should be possible to tune the motional frequencies of trapped electrons over a wide range of GHz frequencies, in particular into resonance with a cavity at ~ 5 GHz. However, electrode surface impurities, inhomogeneities and roughness,

stray or patch potentials and image charge effects can lead to deviations and offsets in the trap potential that are not captured by the simulations. For example, such effects are commonly observed in micro-fabricated planar ion traps, where large offsets potentials are often present, leading to additional micro-motion of trapped ions as they are offset from the trap potential minimum [208, 209]. Here, the offsets largely result from charge build-up during ion loading and stray laser light, in addition to patch potentials caused by different crystal planes at the surface of electrodes, which can produce surface potential variations on the order of ~ 100 mV [208]. The extent to which some of these effects are present in our geometry and devices remains to be determined. While the effect of additional image charges in the metal electrodes and the substrate can be taken into account in simulations (see Appendix C), irregularities from stray and patch potentials are difficult to predict and will have to be investigated experimentally. Some indications of electrostatic offsets in DC-biased resonators have been observed in the experiments of chapters 5 and 7.

Many-Electron Coupling Mechanisms

The many-electron trapping experiments of chapter 7, originally designed as a stepping stone for single-electron experiments, have revealed a rich set of phenomena caused by the interaction of collective excitations of electron ensembles with the cavity field. While we have successfully demonstrated that electrons can be detected in cavity transmission measurements through frequency shifts and increases in cavity loss, the origin of those effects is not fully understood at this point. Some of the possible causes have been explored in sections 7.1.2 and 7.2 but a more quantitative understanding of the underlying coupling mechanisms will likely require further experimental and theoretical investigation. A crucial part of solving this puzzle appears to require a more precise knowledge of the surface electron density in our micro-channel geometries. The molecular dynamics simulations in section 7.1.2 indicate that the electron configuration in the resonator trap is highly sensitive to electron density, which would in turn determine the mode structure of any in-plane motional excitations. Direct spectroscopic measurements of collective excitations, such as plasmons or Wigner crystal phonons, could reveal a great deal about the nature of the observed frequency shifts and the ensemble-cavity interactions. Such measurements, performed by sweeping an additional RF tone above the cavity, have been attempted during the experiments of chapter 7, but so far no direct excitation of collective modes has been observed in the accessible

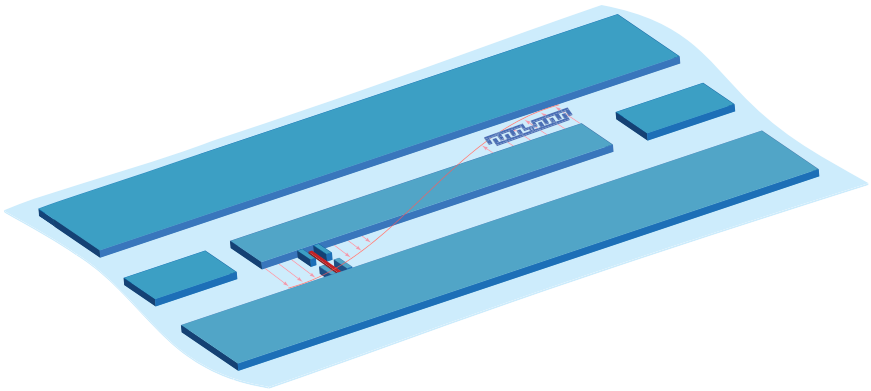

Figure 8.1.: Schematic layout of a hybrid circuit QED architecture. A superconducting coplanar waveguide cavity covered with superfluid helium acts as a mesoscopic electrical interface between a transmon qubit (interdigitated structure at top) and a single-electron quantum dot on helium (bottom, trap electrode shown in red). The cavity functions as a quantum bus allowing for the coherent exchange of microwave photons between the two qubit implementations. Both can be made to couple strongly to the cavity by placing them at opposite ends of the resonator at voltage anti-nodes of the fundamental mode.

frequency range. A better understanding of electron ensemble coupling mechanisms could pave the way for a number of interesting applications such as spin-ensemble based quantum memories with electrons on helium or studying quantum optics phenomena with many emitters.

Coupling to Superconducting Qubits

Circuit QED with Josephson junction-based qubits, such as transmon or phase qubits, has been widely successful over the last decade . The promise of a true hybrid circuit QED architecture capable of interfacing single-electron quantum dots and superconducting qubits was the main motivation behind this PhD project. Conceptually, the on-chip realization of such a system is simple, as shown schematically in Fig. 8.1. A supercondcuting coplanar waveguide cavity covered with superfluid helium acts as a mesoscopic electrical interface between a superconducting qubit and a single-electron quantum dot on helium. The cavity functions as a quantum bus, allowing for the coherent exchange of microwave photons between the two systems. The fabrication of such devices will likely pose a number of practical challenges but there appear to be no fundamental barriers to the implementation once the single-electron regime has been reached with quantum dots on helium.

Some Final Thoughts

Electrons on helium represents an intriguing and exotic system where many phenomena, in particular in the single-electron regime, remain to be observed. While I had some background in circuit QED, I personally had never heard of electrons on helium before coming to Yale but the last five years have convinced me that it is a system well-worth studying, with many exciting applications to come in the future. I hope to have conveyed this excitement to the reader. Much of what has been presented in this thesis is theoretical and experimental groundwork, leaving the many more advanced, and certainly no less challenging, experiments to my collaborators and others who may choose to work on this system in the future. Building an electrons on helium experiment from scratch and integrating it with a circuit QED setup has been a challenging, at times exhausting but ultimately rewarding experience that has taught me a great deal about what matters in research, science and engineering.

Appendix

A Electron-Field Interactions

The dynamics of a charged particle of spin $\vec{\sigma}$ and charge q in a classical electromagnetic field is described by the non-relativistic Pauli-Hamiltonian in Coulomb gauge ($\partial_\mu A^\mu = 0$) [94]

$$\mathbf{H} = \frac{1}{2m}\left(\vec{\sigma}\left[\vec{p} + q\vec{A}\right]\right)^2 + q\Phi \tag{A.1}$$

where $\vec{A}(\vec{r})$ is the vector potential and $V(\vec{r}) = q\Phi(\vec{r})$ the electrostatic potential. As usual, the minimal substitution $i\hbar\partial^\mu \to i\hbar\partial^\mu - qA^\mu$, i.e. $\vec{p} = -i\hbar\vec{\nabla} \to \vec{p} - \frac{e}{c}\vec{A}$ and $E = i\hbar\partial_t \to E - \frac{e}{c}\Phi$, guarantees gauge invariance. Using Maxwell's equations and the usual commutators, the Hamiltonian reads

$$\mathbf{H} = \frac{p^2}{2m} - \frac{q}{m}\vec{A}\cdot\vec{p} + \frac{q^2}{2m}\vec{A}^2 + q\Phi - \frac{q\hbar}{2m}\vec{\sigma}\cdot\vec{B} \tag{A.2}$$

or in CGS units for an electron ($q = -e$)

$$\mathbf{H} = \frac{p^2}{2m} + \frac{e}{mc}\vec{A}\cdot\vec{p} + \frac{e^2}{2mc^2}\vec{A}^2 - e\Phi + \mu_s\vec{\sigma}\cdot\vec{B} \tag{A.3}$$

This Hamiltonian is used repeatedly and implicitly throughout this thesis to describe the different aspects of electrons on helium spin and motional qubits. The electron interacts with the electrostatic field via its dipole moment d (for a homogenous field we have $\Phi = -Ez$ so that $H = ezE = d_z E$). Furthermore, its spin degree of freedom couples to the magnetic field components via its magnetic spin moment $\mu_s = e\hbar/2mc$ in the paramagnetic term $\mu_s\vec{\sigma}\vec{B}$. The diagmagnetic term proportional to $\vec{A}^2$ does not couple to the electronic degrees of freedom and is thus dynamically irrelevant and usually neglected. The interaction term $\vec{A}\vec{p}$ couples the electron angular momentum to the magnetic field. To see this explicitly, we can use

Maxwell's equations in Coulomb gauge

$$\vec{A} = \frac{1}{2}\vec{B} \times \vec{r}, \qquad \vec{\nabla} \cdot \vec{A} = 0 \quad \rightarrow \quad \left[\vec{p}, \vec{A}\right] = 0 \tag{A.4}$$

which yields

$$\vec{A}\vec{p} + \vec{p}\vec{A} = \vec{B}(\vec{r} \times \vec{p}) = \vec{B}\vec{\ell} \tag{A.5}$$

where $\vec{\ell}$ is the angular momentum of the electron. Finally, the Hamiltonian for an electron in a general electromagnetic field is written as

$$\begin{aligned} \mathbf{H} &= \frac{p^2}{2m} + \frac{e^2}{2mc^2}\vec{A}^2 - e\Phi + \frac{e}{2m}\left[\vec{\ell} + \hbar\vec{\sigma}\right]\vec{B} \\ &= \frac{\vec{\mathrm{p}}^2}{2m} + \frac{e^2}{2mc^2}\vec{A}^2 - e\Phi + (\vec{\mu_s} + \vec{\mu_\ell})\vec{B} \end{aligned} \tag{A.6}$$

with the orbital and spin moments

$$\vec{\mu}_\ell = \frac{e}{2m}\vec{\ell}, \qquad \vec{\mu}_s = \frac{e}{m}\vec{s}\,. \tag{A.7}$$

In the absence of any magnetic fields and neglecting the diamagnetic term, the electron-field interaction greatly simplifies and the Hamiltonian collapses to the standard form

$$\mathbf{H} = \frac{\vec{\mathrm{p}}^2}{2m} + V(\vec{r})\,. \tag{A.8}$$

B One-Dimensional N Electron Chains

Here, we discuss a general framework for finding the modes of an N electron crystal in a parabolic trap closely following the method used in Ref. [185] for one-dimensional ion chains in linear Paul traps. The framework presented here allows us to extend the $N = 2$ and $N = 3$ electron cases of section 3.7 to arbitrary number of electrons. We start by determining the electron equilibrium positions by minimizing the potential, in analogy to the $N = 2$ and $N = 3$ electron cases. The general normal modes of the electron crystal are then found by making the usual harmonic approximation and expanding the Coulomb potential in the Lagrangian about the equilibrium positions to second order. General expressions for the normal modes are then obtained by solving the eigenvalue problem given by the Euler-Lagrange equations.

The Hamiltonian for N electrons in a parabolic potential of frequency $\omega_0/2\pi$ coupled via Coulomb interaction is given by

$$\mathcal{H} = \sum_{i=1}^{N} \frac{p_i^2}{2m} + \sum_{i=1}^{N} \frac{1}{2} m\omega_0^2 x_i^2(t) + \frac{1}{2} \sum_{i\neq j=1}^{N} \frac{e^2}{4\pi\varepsilon_0} \frac{1}{|x_i(t) - x_j(t)|} = \mathcal{H}_{\text{kin}} + V \tag{B.1}$$

Just like in the $N = 2$ case, the equilibrium position $x_k^{(0)}$ of the kth electron is determined by

$$\left[\frac{\partial \mathbf{V}}{\partial x_k}\right]_{x_k = x_k^{(0)}} = 0 \tag{B.2}$$

We describe the motion of the kth electron as a small displacement $q_k(t)$ from its equilibrium position $x_k(t) \approx x_k^{(0)} + q_k(t)$. Eq. (B.2) is a coupled set of N non-linear equations. Defining the length scale

$$\ell = \left(\frac{e^2}{4\pi\varepsilon_0 m\omega_0^2}\right)^{1/3} \quad , \quad \ell \approx 0.64\,\mu\text{m} \quad \text{at} \quad \omega_0/2\pi = 5\,\text{GHz} \tag{B.3}$$

and introducing the dimensionless equilibrium positions $u_k = x_k^{(0)}/\ell$, we can evaluate the derivatives and write the coupled set of equations as

$$u_k - \sum_{j=1}^{k-1} \frac{1}{(u_k - u_j)^2} + \sum_{j=k+1}^{N} \frac{1}{(u_k - u_j)^2} = 0 \tag{B.4}$$

This set of equations can be solved analytically for $N = 2$ and $N = 3$, which gives the results derived above. For $N \geq 4$ we have to resort to numerical methods to find the equilibrium position of the kth electron. The values for $N = 4$ and $N = 5$ are [185]

$$\begin{aligned}
N = 4: &\quad u_1 = -1.4368, \quad u_2 = -0.4544, \quad u_3 = 0.4544, \quad u_4 = 1.4368 \\
N = 5: &\quad u_1 = -1.7429, \quad u_2 = -0.8221, \quad u_3 = 0, \quad u_4 = 0.8221 \\
&\quad u_5 = 1.7429
\end{aligned}$$

The smallest separation always occurs between the electrons at the center with the minimum electron separation given by the numerically estimated power law [185, 223]

$$\Delta x_{\min}(N) = \left(\frac{e^2}{4\pi\varepsilon_0 m\omega_0^2}\right)^{1/3} \frac{2.018}{N^{0.56}} \tag{B.5}$$

In analogy to the $N = 2$ and $N = 3$ cases, the Coulomb potential in (B.1) can be expanded about the equilibrium position $x_k^{(0)}$ of each electron to second order in the displacement $q_k(t)$. The truncated Lagrangian in harmonic approximation is then

$$\mathcal{L} = \frac{1}{2}\sum_{i=1}^{N} m\left(\dot{q_i}\right)^2 - \frac{1}{2}\sum_{i,j=1}^{N} q_i q_j \left(\frac{\partial^2 V}{\partial x_i \partial x_j}\right)_0 \tag{B.6}$$

with $\dot{q_i} = \partial q_i/\partial t$ and where we have dropped a constant term equal to the rest energy of the crystal, which does not affect the dynamics of the system. Evaluating the second order partial differentials, we can rewrite the Lagrangian algebraically in the usual form (see e.g. [224])

$$\mathcal{L} = \frac{1}{2}\sum_{i,j=1}^{N} M_{ij}\dot{q_i}\dot{q_j} - \frac{1}{2}\sum_{i,j=1}^{N} A_{ij} q_i q_j \tag{B.7}$$

where $\mathbf{M} = m \cdot \mathbf{1}$ is an N-dimensional diagonal matrix and $\mathbf{A}$ is a real symmetric, positive

semi-definite matrix whose elements are given by

$$A_{ij} = m\omega_0^2 \times \begin{cases} 1 + 2\sum_{p=1}^{N} \frac{1}{|u_j - u_p|^3} & , \quad i = j \\ -\frac{2}{|u_i - u_j|^3} & , \quad i \neq j \end{cases}$$

The Euler-Lagrange equations can then be written in matrix form

$$\ddot{\mathbf{q}} + \left(\mathbf{M}^{-1}\mathbf{A}\right)\mathbf{q} = 0 \tag{B.8}$$

where $\mathbf{q} \equiv |q\rangle = (q_1(t), q_2(t), \ldots, q_N(t))^T$. Hence we see that eq. (B.8) has harmonic oscillator solutions with frequencies that are determined by the eigenvalue problem

$$\mathbf{A}\,|a^{(p)}\rangle = m\omega_0^2\lambda_p\,|a^{(p)}\rangle \tag{B.9}$$

where $|a^{(p)}\rangle$ is the eigenvector with eigenvalue $m\omega_0^2\lambda_p$ and $p = 1, \ldots, N$. Since $\mathbf{A}$ is Hermitian, the eigenvalues are guaranteed to be non-negative real numbers and the eigenvectors form an orthonormal system

$$\langle a^{(n)}|a^{(p)}\rangle = \delta_{np} \quad , \quad \sum_{p=1}^{N} |a^{(p)}\rangle\,\langle a^{(p)}| = \mathbf{1} \tag{B.10}$$

The normal modes of the system are given by projections of the displacement vector onto the eigenvectors

$$Q_p(t) = \langle a^{(p)}|q\rangle = \sum_{j=1}^{N} a_j^{(p)} q_j(t) \tag{B.11}$$

The Lagrangian can therefore be expressed as

$$\mathcal{L} = \frac{m}{2}\sum_{p=1}^{N}\left(\dot{Q_p}^2 - \omega_p^2 Q_p^2\right) . \tag{B.12}$$

The frequency of the pth mode is determined by the corresponding eigenvalue $\omega_p = \sqrt{\lambda_p}\omega_0$. Using $P_p = m \cdot \dot{Q_p}$ we get the final Hamiltonian

$$\mathcal{H} = \sum_{p=1}^{N}\left[\frac{P_p^2}{2m} + \frac{1}{2}m\omega_p^2 Q_p^2\right] \tag{B.13}$$

which consists of p uncoupled harmonic oscillators. The lowest two eigenvectors $|a^{(1)}\rangle$ and

$|a^{(2)}\rangle$, and hence the lowest frequency normal modes, can be found analytically from (B.9) while higher eigenvectors have to be found numerically. The $N = 2$ and $N = 3$ modes derived explicitly above can be recovered from the general formalism. Solving the eigenvalue problem analytically for $N = 2$ we get

$$|a^{(1)}\rangle = \frac{1}{\sqrt{2}} \begin{pmatrix} 1 \\ 1 \end{pmatrix} \quad , \quad |a^{(2)}\rangle = \frac{1}{\sqrt{2}} \begin{pmatrix} -1 \\ 1 \end{pmatrix} \tag{B.14}$$

with eigenvalues $\lambda_1 = 1$ and $\lambda_2 = 3$. Thus the center of mass and stretch modes have frequencies $\omega_1 = \omega_0$ and $\omega_2 = \sqrt{3}\omega_0$, in agreement with the results obtained above. Furthermore, using the equilibrium positions of the two electrons given in eq. (3.129) and translating back from the displaced frame $q_k(t) = x_k(t) - x_k^{(0)}$, the normal modes are given by

$$Q_1(t) = \frac{1}{\sqrt{2}} \left(x_1(t) + x_2(t)\right) \quad , \quad Q_2(t) = \frac{1}{\sqrt{2}} \left(x_1(t) - x_2(t) - 4^{2/3}\ell\right) \tag{B.15}$$

and the resulting Hamiltonian agrees with (3.134), as expected. Likewise, for $N = 3$ we get the modes

$$\begin{gathered} Q_1(t) = \frac{1}{\sqrt{3}} \left(x_1(t) + x_2(t) + x_3(t)\right) \quad , \quad Q_2(t) = \frac{1}{\sqrt{2}} \left(x_3(t) - x_1(t) - 10^{1/3}\ell\right) \\ Q_3(t) = \frac{1}{\sqrt{6}} \left(x_1(t) - 2x_2(t) + x_3(t)\right) \end{gathered} \tag{B.16}$$

in agreement with the result derived directly above. For values $N \geq 4$, the eigenvalue problem (B.9) has to be solved numerically (e.g. using QR decomposition or numerical inversion). For $N = 4$ the eigenvalues and eigenvectors are [185]

$$\lambda_1 = 1 \quad , \quad \lambda_2 = 3 \quad , \quad \lambda_3 = 5.81 \quad , \quad \lambda_4 = 9.308$$

$$|a^{(1)}\rangle = \begin{pmatrix} \alpha \\ \alpha \\ \alpha \\ \alpha \end{pmatrix} , |a^{(2)}\rangle = \begin{pmatrix} -\beta \\ -\gamma \\ \gamma \\ \beta \end{pmatrix} , |a^{(3)}\rangle = \begin{pmatrix} \alpha \\ -\alpha \\ -\alpha \\ \alpha \end{pmatrix} , |a^{(4)}\rangle = \begin{pmatrix} -\gamma \\ \beta \\ -\beta \\ \gamma \end{pmatrix}$$

where $\alpha = 1/2$, $\beta = 0.6742$ and $\gamma = 0.2132$. The first two modes are the center of mass and stretch modes already encountered in the $N = 3$ case, both with the same frequencies as in that case, $\omega_1 = \omega_0$ and $\omega_2 = \sqrt{3}\omega_0$. The third and fourth mode are different types of scissor

modes with higher frequencies. Compared to the $N = 3$ case, the normal mode oscillators generally have different masses and charges. The normal mode coordinates in terms of the individual electron positions are

$$\begin{aligned} Q_1 &= \alpha(x_1 + x_2 + x_3 + x_4) \quad , \quad Q_2 = \beta(x_4 - x_1) + \gamma(x_3 - x_2) + \delta_2 \\ Q_3 &= \alpha(x_1 - x_2 + x_4 - x_3) \quad , \quad Q_4 = \gamma(x_4 - x_1) + \beta(x_2 - x_3) + \delta_4 \end{aligned}$$

where the constant offsets for the two stretch modes are

$$\delta_2 = 2\left(\beta x_1^{(0)} + \gamma x_2^{(0)}\right) \quad , \quad \delta_4 = 2\left(\gamma x_1^{(0)} - \beta x_2^{(0)}\right) \tag{B.17}$$

At $\omega_0/2\pi = 5$ GHz we have $\delta_2 \approx -1.36\,\mu$m and $\delta_4 \approx 0.04$ nm and the equilibrium positions

$$x_1^{(0)} = -x_4^{(0)} = -0.91\,\mu\text{m} \quad , \quad x_2^{(0)} = -x_3^{(0)} = -0.29\,\mu\text{m}\,. \tag{B.18}$$

Compared to the $N = 2$ and $N = 3$ electron case, we see that the equilibrium electron spacing decreases with trap population. Note, however, that there is a limit to the number of electrons that can be stored in a given confining potential as the transverse vibrational states become unstable. Above a critical number of electrons, the electron crystal will adopt a zig-zag type configuration in two dimensions that minimizes overall energy, which has been studied in for ions in the context of structural phase transitions using molecular dynamics simulations [187].

C Image Charge Effects

In addition to any image charges induced in the superfluid film, the presence of electrons also leads to image charges in the surrounding metal electrodes. Depending on device geometry, those metallic images are typically orders of magnitude farther away from the electron than the corresponding charges in the helium. However, because of the unit dielectric constant . We can calculate the change in effective potential due to the presence of images in the metal by considering the Poisson equation with appropriate boundary conditions. The field due to a single electron at position $\mathbf{r}_e = (x_e, y_e, z_e)$ in the vicinity of a grounded metallic surface S is governed by

$$\Delta\Phi(\mathbf{r}) = -\frac{q}{\epsilon_0\epsilon_r}\delta(\mathbf{r}-\mathbf{r}_e) \quad , \quad \Phi(\mathbf{r}\in S) = 0 \tag{C.1}$$

We can reformulate the problem by writing the total potential as a combination of the single electron potential and an image charge potential

$$\Phi(\mathbf{r}) = \Phi_{\mathrm{im}}(\mathbf{r}) + \frac{q}{4\pi\epsilon_0\epsilon_r}\frac{1}{|\mathbf{r}-\mathbf{r}_e|} \tag{C.2}$$

where $\Phi_{\mathrm{im}}(\mathbf{r})$ is the potential the electron feels due to image charges induced in the bounding surface S. This yields for the total potential

$$\Delta\Phi(\mathbf{r}) = \Delta\Phi_{\mathrm{im}}(\mathbf{r}) - \frac{q}{\epsilon_0\epsilon_r}\delta(\mathbf{r}-\mathbf{r}_e) \tag{C.3}$$

such that the image potential is governed by a Laplace equation

$$\Delta\Phi_{\mathrm{im}}(\mathbf{r}) = 0 \tag{C.4}$$

with surface boundary conditions

$$\Phi_{\text{im}}(\mathbf{r} \in S) = \Phi(\mathbf{r} \in S) - \frac{q}{4\pi\epsilon_0\epsilon_r}\frac{1}{|\mathbf{r}-\mathbf{r}_e|} = -\frac{q}{4\pi\epsilon_0\epsilon_r}\frac{1}{|\mathbf{r}-\mathbf{r}_e|} \tag{C.5}$$

Analytic solutions for $\Phi_{\text{im}}(\mathbf{r})$ in general do not exist for all but the simplest bounding geometries. We can, however, find solutions for the effective potential numerically using the following algorithm:

1. Define a geometry and the electrostatic potentials on the different surfaces $\mathcal{S} = \{S_1, S_2, \ldots, S_N\}$. For a surface with an applied voltage, the boundary condition reads
$$\Phi_{\text{im}}(\mathbf{r} \in S_j) = V - \frac{q}{4\pi\epsilon_0\epsilon_r}\frac{1}{|\mathbf{r}-\mathbf{r}_e|} \tag{C.6}$$
2. Solve the system numerically using a PDE solver:
$$\Delta\Phi_{\text{im}}(\mathbf{r}) = 0 \quad , \quad \Phi_{\text{im}}(\mathbf{r} \in \mathcal{S}) = -\frac{q}{4\pi\epsilon_0\epsilon_r}\frac{1}{|\mathbf{r}-\mathbf{r}_e|} \tag{C.7}$$
3. Recover the full potential $\Phi(\mathbf{r})$ using eq. (C.2).

The software package *FlexPDE* has a numerical PDE solver that allows specification of the equations and arbitrary boundary conditions on a modeled surface using finite-element methods. Extending the above calculations to multiple discrete charges is straightforward. Let $\rho(\mathbf{r})$ denote the charge density corresponding to n electrons at positions $\mathbf{r}_i, i = 1n \ldots, n$ such that

$$\Delta\Phi(\mathbf{r}) = -\frac{\rho(\mathbf{r})}{\epsilon_0\epsilon_r} = -\frac{q}{\epsilon_0\epsilon_r}\sum_{i=1}^{n}\delta(\mathbf{r}-\mathbf{r}_i) \quad , \quad \Phi(\mathbf{r} \in S) = 0 \tag{C.8}$$

Due to the linearity of the equations we find in analogy to the single electron case

$$\Phi(\mathbf{r}) = \Phi_{\text{im}}(\mathbf{r}) + \frac{q}{4\pi\epsilon_0\epsilon_r}\sum_i \frac{1}{|\mathbf{r}-\mathbf{r}_i|} \tag{C.9}$$

and

$$\Delta\Phi_{\text{im}}(\mathbf{r}) = 0 \quad , \quad \Phi_{\text{im}}(\mathbf{r} \in \mathcal{S}) = -\frac{q}{4\pi\epsilon_0\epsilon_r}\sum_i \frac{1}{|\mathbf{r}-\mathbf{r}_i|} \tag{C.10}$$

Bibliography

[1] R. P. Feynman, "Simulating physics with computers," *International Journal of Theoretical Physics*, vol. 21, no. 6-7, pp. 467–488, 1982.

[2] D. Deutsch, "Quantum theory, the Church-Turing principle and the universal quantum computer," *Proceedings of the Royal Society of London. A. Mathematical and Physical Sciences*, vol. 400, pp. 97–117, 07 1985.

[3] P. Shor, "Algorithms for quantum computation: Discrete logarithms and factoring," in *Proc. 35nd Annual Symposium on Foundations of Computer Science* (S. Goldwasser, ed.), pp. 124–134, IEEE Computer Society Press, 1994.

[4] L. K. Grover, "Quantum mechanics helps in searching for a needle in a haystack," *Physical Review Letters*, vol. 79, pp. 325–328, 07 1997.

[5] A. W. Harrow, A. Hassidim, and S. Lloyd, "Quantum algorithm for linear systems of equations," *Physical Review Letters*, vol. 103, pp. 150502–, 10 2009.

[6] N. Wiebe, D. Braun, and S. Lloyd, "Quantum algorithm for data fitting," *Physical Review Letters*, vol. 109, pp. 050505–, 08 2012.

[7] J. A. Jones, M. Mosca, and R. H. Hansen, "Implementation of a quantum search algorithm on a quantum computer," *Nature*, vol. 393, pp. 344–346, 05 1998.

[8] I. L. Chuang, L. M. K. Vandersypen, X. Zhou, D. W. Leung, and S. Lloyd, "Experimental realization of a quantum algorithm," *Nature*, vol. 393, pp. 143–146, 05 1998.

[9] D. Loss and D. P. DiVincenzo, "Quantum computation with quantum dots," *Physical Review A*, vol. 57, pp. 120–126, 01 1998/01/01/.

[10] F. Jelezko, T. Gaebel, I. Popa, A. Gruber, and J. Wrachtrup, "Observation of coherent oscillations in a single electron spin," *Physical Review Letters*, vol. 92, pp. 076401–, 02 2004.

[11] M. V. G. Dutt, L. Childress, L. Jiang, E. Togan, J. Maze, F. Jelezko, A. S. Zibrov, P. R. Hemmer, and M. D. Lukin, "Quantum register based on individual electronic and nuclear spin qubits in diamond," *Science*, vol. 316, pp. 1312–1316, 06 2007.

[12] B. E. Kane, "A silicon-based nuclear spin quantum computer," *Nature*, vol. 393, pp. 133–137, 1998.

[13] J. I. Cirac and P. Zoller, "Quantum computations with cold trapped ions," *Physical Review Letters*, vol. 74, pp. 4091–4094, 05 1995.

[14] R. Blatt and D. Wineland, "Entangled states of trapped atomic ions," *Nature*, vol. 453, pp. 1008–1015, 06 2008.

[15] H. Häffner, C. F. Roos, and R. Blatt, "Quantum computing with trapped ions," *Physics Reports*, vol. 469, p. 155, 2008.

[16] R. J. Schoelkopf and S. M. Girvin, "Wiring up quantum systems," *Nature*, vol. 451, pp. 664–669, 02 2008.

[17] J. Clarke and F. K. Wilhelm, "Superconducting quantum bits," *Nature*, vol. 453, pp. 1031–1042, 06 2008.

[18] M. H. Devoret and R. J. Schoelkopf, "Superconducting circuits for quantum information: An outlook," *Science*, vol. 339, pp. 1169–1174, 03 2013.

[19] P. W. Shor, "Scheme for reducing decoherence in quantum computer memory," *Physical Review A*, vol. 52, pp. R2493–R2496, 10 1995.

[20] A. Steane, "Multiple-particle interference and quantum error correction," *Proceedings of the Royal Society of London. Series A: Mathematical, Physical and Engineering Sciences*, vol. 452, pp. 2551–2577, 11 1996.

[21] E. Knill and R. Laflamme, "Theory of quantum error-correcting codes," *Physical Review A*, vol. 55, pp. 900–911, 02 1997.

[22] M. A. Nielsen and I. L. Chuang, *Quantum Computation and Quantum Information*. Cambridge University Press, 2000.

[23] C. Sayrin, I. Dotsenko, X. Zhou, B. Peaudecerf, T. Rybarczyk, S. Gleyzes, P. Rouchon, M. Mirrahimi, H. Amini, M. Brune, J.-M. Raimond, and S. Haroche, "Real-time quantum feedback prepares and stabilizes photon number states," *Nature*, vol. 477, pp. 73–77, 09 2011.

[24] M. D. Reed, L. DiCarlo, S. E. Nigg, L. Sun, L. Frunzio, S. M. Girvin, and R. J. Schoelkopf, "Realization of three-qubit quantum error correction with superconducting circuits," *Nature*, vol. 482, pp. 382–385, 02 2012.

[25] D. Ristè, C. C. Bultink, K. W. Lehnert, and L. DiCarlo, "Feedback control of a solid-state qubit using high-fidelity projective measurement," *Physical Review Letters*, vol. 109, pp. 240502–, 12 2012.

[26] J. Chiaverini, D. Leibfried, T. Schaetz, M. D. Barrett, R. B. Blakestad, J. Britton, W. M. Itano, J. D. Jost, E. Knill, C. Langer, R. Ozeri, and D. J. Wineland, "Realization of quantum error correction," *Nature*, vol. 432, pp. 602–605, 12 2004.

[27] P. Schindler, J. T. Barreiro, T. Monz, V. Nebendahl, D. Nigg, M. Chwalla, M. Hennrich, and R. Blatt, "Experimental repetitive quantum error correction," *Science*, vol. 332, no. 6033, pp. 1059–1061, 2011.

[28] D. G. Cory, M. D. Price, W. Maas, E. Knill, R. Laflamme, W. H. Zurek, T. F. Havel, and S. S. Somaroo, "Experimental quantum error correction," *Physical Review Letters*, vol. 81, pp. 2152–2155, 09 1998.

[29] D. P. DiVincenzo, "The physical implementation of quantum computation," *Fortschritte der Physik*, vol. 48, no. 9-11, pp. 771–783, 2000.

[30] J. M. Raimond, M. Brune, and S. Haroche, "Manipulating quantum entanglement with atoms and photons in a cavity," *Rev. Mod. Phys.*, vol. 73, pp. 565–582, Aug 2001.

[31] S. Haroche and J. Raimond, *Atoms, Cavities, And Photons*. Oxford University Press, 2006.

[32] R. J. Thompson, G. Rempe, and H. J. Kimble, "Observation of normal-mode splitting for an atom in an optical cavity," *Physical Review Letters*, vol. 68, p. 1132, 1992.

[33] G. Rempe, H. Walther, and N. Klein, "Observation of quantum collapse and revival in a one-atom maser," *Physical Review Letters*, vol. 58, pp. 353–356, 1987.

[34] M. Brune, J. M. Raimond, P. Goy, L. Davidovich, and S. Haroche, "Realization of a two-photon maser oscillator," *Phys. Rev. Lett.*, vol. 59, pp. 1899–1902, Oct 1987.

[35] D. Englund, D. Fattal, E. Waks, G. Solomon, B. Zhang, T. Nakaoka, Y. Arakawa, Y. Yamamoto, and J. Vučković, "Controlling the spontaneous emission rate of single quantum dots in a two-dimensional photonic crystal," *Phys. Rev. Lett.*, vol. 95, p. 013904, Jul 2005.

[36] T. Yoshie, A. Scherer, J. Hendrickson, G. Khitrova, H. M. Gibbs, G. Rupper, C. Ell, O. B. Shchekin, and D. G. Deppe, "Vacuum Rabi splitting with a single quantum dot in a photonic crystal nanocavity," *Nature*, vol. 432, pp. 200–203, 11 2004.

[37] K. D. Petersson, L. W. McFaul, M. D. Schroer, M. Jung, J. M. Taylor, A. A. Houck, and J. R. Petta, "Circuit quantum electrodynamics with a spin qubit," *Nature*, vol. 490, pp. 380–383, 10 2012.

[38] J. D. Thompson, B. M. Zwickl, A. M. Jayich, F. Marquardt, S. M. Girvin, and J. G. E. Harris, "Strong dispersive coupling of a high-finesse cavity to a micromechanical membrane," *Nature*, vol. 452, pp. 72–75, 03 2008.

[39] A. D. OĆonnell, M. Hofheinz, M. Ansmann, R. C. Bialczak, M. Lenander, E. Lucero, M. Neeley, D. Sank, H. Wang, M. Weides, J. Wenner, J. M. Martinis, and A. N. Cleland, "Quantum ground state and single-phonon control of a mechanical resonator," *Nature*, vol. 464, pp. 697–703, 04 2010.

[40] D. Englund, B. Shields, K. Rivoire, F. Hatami, J. Vučković, H. Park, and M. D. Lukin, "Deterministic coupling of a single nitrogen vacancy center to a photonic crystal cavity," *Nano Letters*, vol. 10, no. 10, pp. 3922–3926, 2010.

[41] A. Faraon, P. E. Barclay, C. Santori, K.-M. C. Fu, and R. G. Beausoleil, "Resonant enhancement of the zero-phonon emission from a colour centre in a diamond cavity," *Nat Photon*, vol. 5, pp. 301–305, 05 2011.

[42] A. Blais, R.-S. Huang, A. Wallraff, S. M. Girvin, and R. J. Schoelkopf, "Cavity quantum electrodynamics for superconducting electrical circuits: An architecture for quantum computation," *Phys. Rev. A*, vol. 69, p. 062320, Jun 2004.

[43] A. Wallraff, D. I. Schuster, A. Blais, L. Frunzio, R. S. Huang, J. Majer, S. Kumar, S. M. Girvin, and R. J. Schoelkopf, "Strong coupling of a single photon to a superconducting qubit using circuit quantum electrodynamics," *Nature*, vol. 431, pp. 162–167, 09 2004.

[44] D. Schuster, *Circuit Quantum Electrodynamics*. PhD thesis, Yale University, 2007.

[45] M. Goppl, A. Fragner, M. Baur, R. Bianchetti, S. Filipp, J. M. Fink, P. J. Leek, G. Puebla, L. Steffen, and A. Wallraff, "Coplanar waveguide resonators for circuit quantum electrodynamics," *Journal of Applied Physics*, vol. 104, no. 11, p. 113904, 2008.

[46] H. Paik, D. I. Schuster, L. S. Bishop, G. Kirchmair, G. Catelani, A. P. Sears, B. R. Johnson, M. J. Reagor, L. Frunzio, L. I. Glazman, S. M. Girvin, M. H. Devoret, and R. J. Schoelkopf, "Observation of high coherence in Josephson junction qubits measured in a three-dimensional circuit QED architecture," *Phys. Rev. Lett.*, vol. 107, p. 240501, Dec 2011.

[47] M. Reagor, H. Paik, G. Catelani, L. Sun, C. Axline, E. Holland, I. Pop, N. Masluk, T. Brecht, L. Frunzio, M. Devoret, L. Glazman, and R. J. Schoelkopf, "Ten milliseconds for aluminum cavities in the quantum regime," *arXiv:1302.4408*, 2013.

[48] D. I. Schuster, A. A. Houck, J. A. Schreier, A. Wallraff, J. M. Gambetta, A. Blais, L. Frunzio, J. Majer, B. Johnson, M. H. Devoret, S. M. Girvin, and R. J. Schoelkopf, "Resolving photon number states in a superconducting circuit," *Nature*, vol. 445, pp. 515–518, 02 2007.

[49] A. A. Houck, D. I. Schuster, J. M. Gambetta, J. A. Schreier, B. R. Johnson, J. M. Chow, L. Frunzio, J. Majer, M. H. Devoret, S. M. Girvin, and R. J. Schoelkopf, "Generating single microwave photons in a circuit," *Nature*, vol. 449, pp. 328–331, 09 2007.

[50] L. S. Bishop, J. M. Chow, J. Koch, A. A. Houck, M. H. Devoret, E. Thuneberg, S. M. Girvin, and R. J. Schoelkopf, "Nonlinear response of the vacuum Rabi resonance," *Nature Physics*, vol. 5, pp. 105–109, 02 2009.

[51] J. M. Fink, M. Goppl, M. Baur, R. Bianchetti, P. J. Leek, A. Blais, and A. Wallraff, "Climbing the Jaynes-Cummings ladder and observing its nonlinearity in a cavity QED system," *Nature*, vol. 454, pp. 315–318, 07 2008.

[52] G. Kirchmair, B. Vlastakis, Z. Leghtas, S. E. Nigg, H. Paik, E. Ginossar, M. Mirrahimi, L. Frunzio, S. M. Girvin, and R. J. Schoelkopf, "Observation of quantum state collapse and revival due to the single-photon Kerr effect," *Nature*, vol. 495, pp. 205–209, 03 2013.

[53] L. DiCarlo, J. M. Chow, J. M. Gambetta, L. S. Bishop, B. R. Johnson, D. I. Schuster, J. Majer, A. Blais, L. Frunzio, S. M. Girvin, and R. J. Schoelkopf, "Demonstration of two-qubit algorithms with a superconducting quantum processor," *Nature*, vol. 460, pp. 240–244, 07 2009.

[54] M. Ansmann, H. Wang, R. C. Bialczak, M. Hofheinz, E. Lucero, M. Neeley, A. D. O'Connell, D. Sank, M. Weides, J. Wenner, A. N. Cleland, and J. M. Martinis, "Violation of Bell's inequality in Josephson phase qubits," *Nature*, vol. 461, pp. 504–506, 09 2009.

[55] L. DiCarlo, M. D. Reed, L. Sun, B. R. Johnson, J. M. Chow, J. M. Gambetta, L. Frunzio, S. M. Girvin, M. H. Devoret, and R. J. Schoelkopf, "Preparation and measurement of three-qubit entanglement in a superconducting circuit," *Nature*, vol. 467, pp. 574–578, 09 2010.

[56] M. Neeley, R. C. Bialczak, M. Lenander, E. Lucero, M. Mariantoni, A. D. O/'Connell, D. Sank, H. Wang, M. Weides, J. Wenner, Y. Yin, T. Yamamoto, A. N. Cleland, and J. M. Martinis, "Generation of three-qubit entangled states using superconducting phase qubits," *Nature*, vol. 467, pp. 570–573, 09 2010.

[57] M. Mariantoni, H. Wang, T. Yamamoto, M. Neeley, R. C. Bialczak, Y. Chen, M. Lenander, E. Lucero, A. D. O'Connell, D. Sank, M. Weides, J. Wenner, Y. Yin, J. Zhao, A. N. Korotkov, A. N. Cleland, and J. M. Martinis, "Implementing the quantum Von Neumann architecture with superconducting circuits," *Science*, vol. 334, pp. 61–65, 10 2011.

[58] A. Fedorov, L. Steffen, M. Baur, M. P. da Silva, and A. Wallraff, "Implementation of a Toffoli gate with superconducting circuits," *Nature*, vol. 481, pp. 170–172, 01 2012.

[59] A. Andre, D. DeMille, J. M. Doyle, M. D. Lukin, S. E. Maxwell, P. Rabl, R. J. Schoelkopf, and P. Zoller, "A coherent all-electrical interface between polar molecules and mesoscopic superconducting resonators," *Nature Physics*, vol. 2, pp. 636–642, 09 2006.

[60] P. Rabl, D. DeMille, J. M. Doyle, M. D. Lukin, R. J. Schoelkopf, and P. Zoller, "Hybrid quantum processors: Molecular ensembles as quantum memory for solid state circuits," *Phys. Rev. Lett.*, vol. 97, p. 033003, Jul 2006.

[61] D. I. Schuster, L. S. Bishop, I. L. Chuang, D. DeMille, and R. J. Schoelkopf, "Cavity QED in a molecular ion trap," *Phys. Rev. A*, vol. 83, p. 012311, Jan 2011.

[62] A. Imamoğlu, "Cavity QED based on collective magnetic dipole coupling: Spin ensembles as hybrid two-level systems," *Phys. Rev. Lett.*, vol. 102, p. 083602, Feb 2009.

[63] J. H. Wesenberg, A. Ardavan, G. A. D. Briggs, J. J. L. Morton, R. J. Schoelkopf, D. I. Schuster, and K. Mølmer, "Quantum computing with an electron spin ensemble," *Phys. Rev. Lett.*, vol. 103, p. 070502, Aug 2009.

[64] D. Schuster, A. Fragner, M. Dykman, S. Lyon, and R. Schoelkopf, "Proposal for manipulating and detecting spin and orbital motion of trapped electrons on helium using cavity quantum electrodynamics," *Physical Review Letters*, vol. 105, p. 040503, 2010.

[65] Y. Kubo, F. R. Ong, P. Bertet, D. Vion, V. Jacques, D. Zheng, A. Dréau, J.-F. Roch, A. Auffeves, F. Jelezko, J. Wrachtrup, M. F. Barthe, P. Bergonzo, and D. Esteve, "Strong coupling of a spin ensemble to a superconducting resonator," *Phys. Rev. Lett.*, vol. 105, p. 140502, Sep 2010.

[66] R. Amsüss, C. Koller, T. Nöbauer, S. Putz, S. Rotter, K. Sandner, S. Schneider, M. Schramböck, G. Steinhauser, H. Ritsch, J. Schmiedmayer, and J. Majer, "Cavity QED with magnetically coupled collective spin states," *Phys. Rev. Lett.*, vol. 107, p. 060502, Aug 2011.

[67] E. Andrei, ed., *Two-Dimensional Electron Systems on Helium and Other Cryogenic Substrates*. Kluwer, 1997.

[68] Y. Monarkha and K. Kono, *Two-Dimensional Coulomb Liquids and Solids*. Springer, 2004.

[69] A. Chaplik *Sov. Phys. JETP*, vol. 35, p. 395, 1972.

[70] H. V. Horn, "Instability and melting of the electron solid," *Physical Review*, vol. 157, p. 342, 1967.

[71] W. Sommer and D. Tanner, "Mobility of electrons on the surface of liquid helium," *Physical Review Letters*, vol. 27, no. 20, p. 1345, 1971.

[72] M. Cole and M. Cohen, "Image-potential-induced surface bands in insulators," *Physical Review Letters*, vol. 23, p. 1238, 1969.

[73] R. Williams, R. Crandall, and A. Willis, "Surface states of electrons on liquid helium," *Physical Review Letters*, vol. 26, p. 7, 1971.

[74] R. Mehrotra, C. Guo, Y. Ruan, D. Mast, and A. Dahm, "Density-dependent mobility of a two-dimensional electron fluid," *Physical Review B*, vol. 29, no. 9, p. 5239, 1984.

[75] K. Shirahama, S. Ito, H. Suto, and K. Kono, "Surface study of liquid ^{3}He using surface state electrons," *Journal of Low Temperature Physics*, vol. 101, no. 3, p. 439, 1995.

[76] S. Lyon, "Spin-based quantum computing using electrons on liquid helium," *Physical Review A*, vol. 74, p. 052338, 2006.

[77] A. C. Johnson, J. R. Petta, J. M. Taylor, A. Yacoby, M. D. Lukin, C. M. Marcus, M. P. Hanson, and A. C. Gossard, "Triplet-singlet spin relaxation via nuclei in a double quantum dot," *Nature*, vol. 435, pp. 925–928, 06 2005.

[78] P. Platzman and M. Dykman, "Quantum computing with electrons floating on liquid helium," *Science*, vol. 284, p. 1967, 1999.

[79] M. Dykman, P. M. Platzman, and P. Seddighrad, "Qubits with electrons on liquid helium," *Physical Review B*, vol. 67, p. 155402, 2003.

[80] W. Sommer, "Liquid helium as a barrier to electrons," *Physical Review Letters*, vol. 12, no. 11, p. 271, 1964.

[81] W. T. Sommer, *The Interaction of Free Electrons with Liquid Helium*. PhD thesis, Stanford University, 1965.

[82] M. Cole, "Properties of image-potential-induced surface states of insulators," *Physical Review B*, vol. 2, p. 4239, 1970.

[83] N. Kestner, J. Jortner, M. Cohen, and S. Rice, "Low-energy elastic scattering of electrons and positrons from helium atoms," *Physical Review*, vol. 140, no. 1A, p. A56, 1965.

[84] M. A. et al. *IEEE Trans. Nucl. Sci.*, vol. 16, pp. 1009–1012, 1969.

[85] C. Grebenkemper and J. Hagen, "The dielectric constant of liquid helium," *Physical Review*, vol. 80, no. 1, p. 89, 1950.

[86] C. Chase, E. Maxwell, and W. Millett, "The dielectric constant of liquid helium," *Physica*, vol. 27, p. 1129, 1961.

[87] W. Hartung, J. Bierwagen, S. Bricker, C. Compton, T. Grimm, M. Johnson, D. Meidlinger, D. Pendell, J. Popielarksi, L. Saxton, and R. York, "RF performance of a superconducting s-band cavity filled with liquid helium," *Proc. LINAC*, p. 755, 2006.

[88] B. Burdick, "Negative ions in liquid helium II," *Physical Review Letters*, vol. 14, no. 1, p. 11, 1964.

[89] L. Tankersley, "Energy barrier for electron penetration into helium," *Journal of Low Temperature Physics*, vol. 11, p. 451, 1973.

[90] M. Woolf and G. Rayfield, "Energy of negative ions in liquid helium by photoelectric injection.," *Physical Review Letters*, vol. 15, p. 235, 1965.

[91] C. Grimes, T. Brown, M. Burns, and C. Zipfel, "Spectroscopy of electrons in image-potential-induced surface states outside liquid helium," *Physical Review B*, vol. 13, p. 140, 1976.

[92] O. Hipolito, J. D. Felicio, and G. Farias *Solid State Communications*, vol. 28, p. 365, 1978.

[93] E. Cheng, M. Cole, and M. Cohen, "Binding of electrons to the surface of liquid helium," *Physical Review B*, vol. 50, p. 1136, 1994.

[94] A. Messiah, *Quantum Mechanics*. Dover, New York, 1999.

[95] M. Nieto, "Electrons above a helium surface and the one-dimensional Rydberg atom," *Physical Review A*, vol. 61, p. 034901, 2000.

[96] T. Sanders and G. Weinreich, "Energies of external electron surface states on liquid helium," *Physical Review B*, vol. 13, p. 4810, 1976.

[97] C. Grimes and T. Brown, "Direct spectroscopic observation of electrons in image-potential states outside liquid helium," *Physical Review Letters*, vol. 32, p. 280, 1974.

[98] H. Huang, Y. Shih, and C. Woo, "Electronic surface states on liquid helium.," *Journal of Low Temperature Physics*, vol. 14, p. 413, 1974.

[99] M. Saitoh *J. Phys. Soc. Jpn.*, vol. 42, p. 201, 1977.

[100] Y. Monarkha *Sov. J. Low Temp. Phys.*, vol. 5, p. 470, 1979.

[101] E. Rousseau, D. Ponarin, L. Hristakos, O. Avenel, E. Varoquaux, and Y. Mukharsky, "Addition spectra of Wigner islands of electrons on superfluid helium," *Physical Review B*, vol. 79, pp. 045406–, 01 2009/01/12/.

[102] F. R. Bradbury, M. Takita, T. M. Gurrieri, K. J. Wilkel, K. Eng, M. S. Carroll, and S. A. Lyon, "Efficient clocked electron transfer on superfluid helium," *Physical Review Letters*, vol. 107, pp. 266803–, 12 2011.

[103] R. Crandall, "Colletive modes of a two-dimensional Wigner crystal," *Physical Review A*, vol. 8, no. 4, p. 2136, 1973.

[104] N. Ashcroft and N. Mermin, *Solid State Physics*. Brooks/Cole Publishing, 1976.

[105] P. Platzman and H. Fukuyama, "Phase diagram of the two-dimensional electron liquid," *Physical Review B*, vol. 10, p. 3150, 1974.

[106] R. Hockney and T. Brown *Journal of Physics C: Solid State Phys.*, vol. 8, p. 1813, 1975.

[107] D. Fisher, B. Halperin, and P. Platzman, "Phonon-ripplon coupling and the two-dimensional electron solid on a liquid-helium surface," *Physical Review Letters*, vol. 42, p. 798, 1979.

[108] B. Tanatar and D. Ceperley, "Ground state of the two-dimensional electron gas," *Physical Review B*, vol. 39, p. 5005, 1989.

[109] F. Gallet, G. Deville, A. Valdes, and F. Williams, "Fluctuations and shear modulus of a classical two-dimensional electron solid: Experiment," *Physical Review Letters*, vol. 49, p. 212, 1982.

[110] F. Peeters, *Two-Dimensional Electron Systems*. Kluwer, 1997.

[111] C. Grimes and G. Adams, "Evidence for a liquid-to-crystal phase transition in a classical, two-dimensional sheet of electrons," *Physical Review Letters*, vol. 42, p. 795, 1979.

[112] D. Rode, R. Willardson, and A. Beer, *Semiconductors and Semimetals*. Academic Press, N.Y., 1975.

[113] C. Grimes and G. Adams, "Observation of two-dimensional plasmons and electron-ripplon scattering in a sheet of electrons on liquid helium," *Physical Review Letters*, vol. 36, p. 145, 1976.

[114] A. Rybalko, Y. Kovdrya, and B. Eselson *Sov. Phys. JETP Lett.*, vol. 22, p. 280, 1975.

[115] E. Wigner, "On the interaction of electrons in metals," *Physical Review*, vol. 46, p. 1002, 1934.

[116] W. J. Carr, "Energy, specific heat, and magnetic properties of the low-density electron gas," *Physical Review*, vol. 122, p. 1437, 1961.

[117] R. Crandall and R. Williams, "Crystallization of electrons on the surface of liquid helium," *Physics Letters*, vol. 34A, no. 7, p. 404, 1971.

[118] V. Shikin *JETP Lett.*, vol. 19, p. 335, 1974.

[119] R. Mehrotra, B. M. Guenin, and A. J. Dahm, "Ripplon-limited mobility of a two-dimensional crystal of electrons: Experiment," *Physical Review Letters*, vol. 48, p. 641, 1982.

[120] K. Kajita, "Wigner crystallization of two dimensional electrons formed on the surface of solid neon," *J. Phys. Soc. Jpn.*, vol. 54, p. 4092, 1985.

[121] A. Rybalko, B. Eselson, and Y. Kovdrya *Sov. J. Low Temp. Phys.*, vol. 5, p. 450, 1979.

[122] K. Shirahama and K. Kono, "Dynamical transition in the Wigner solid on a liquid helium surface," *Physical Review Letters*, vol. 74, p. 781, 1995.

[123] Y. E. Lozovik and V. I. Yudson *JETP Letters*, vol. 22, no. 11, 1975.

[124] L. Bonsall and A. Maradudin, "Some static and dynamical properties of a two-dimensional Wigner crystal," *Physical Review B*, vol. 15, p. 1959, 1977.

[125] F. Pobell, *Matter and Methods at Low Temperatures*. Springer, 3rd ed., 2006.

[126] M. Mukhopadhyay, *Fundamentals of Cryogenic Engineering*. PHI Learning, 2010.

[127] M. Tinkham, *Introduction to Superconductivity*. Dover, New York, 2004.

[128] L. Gorkov and D. Chernikova, "Concerning the structure of a charged surface of liquid helium," *JETP Letters*, vol. 18, no. 68, 1973.

[129] D. Marty, "Stability of two-dimensional electrons on a fractionated helium surface," *Journal of Physics C: Solid State Phys.*, vol. 19, p. 6097, 1986.

[130] Y. Kovdrya and A. Rybalko *Fiz. Niz. Temp*, vol. 1, p. 1037, 1975.

[131] S. Sokolov and N. Studart, "Electron transport in a quasi-one-dimensional channel on suspended helium films," *Physical Review B*, vol. 66, p. 075424, 2002.

[132] F. Williams, "Collective aspects of charged-particle systems at helium interfaces," *Surface Science*, vol. 113, p. 371, 1982.

[133] R. Donnelly, J. Donnelly, and R. Hills *Journal of Low Temperature Physics*, vol. 44, p. 471, 1981.

[134] H. Lauter, H. Godfrin, V. Frank, and P. Leiderer, "Ripplons in ^{4}He films observed by neutron scattering," *Physical Review Letters*, vol. 68, no. 16, p. 2070, 1992.

[135] V. Shikin and Y. Monarkha, "On the interaction of surface electrons in liquid helium with oscillations of the vapor-liquid interface," *Journal of Low Temperature Physics*, vol. 16, p. 193, 1974.

[136] A. Volodin and V. Edelman *JETP Letters*, vol. 30, p. 633, 1979.

[137] V. Edelman *JETP Letters*, vol. 26, p. 492, 1977.

[138] A. Troyanovskii and M. Khaikin *Sov. Phys. JETP*, vol. 54, p. 214, 1981.

[139] V. Edelman and M. Faley *Journal of Low Temperature Physics*, vol. 52, p. 301, 1983.

[140] K. Kono, U. Albrecht, and P. Leiderer *Journal of Low Temperature Physics*, vol. 82, p. 279, 1991.

[141] A. Troyanovskii, A. Volodin, and M. Khaikin *JETP Letters*, vol. 29, p. 382, 1979.

[142] C. J. Hood, T. W. Lynn, A. C. Doherty, A. S. Parkins, and H. J. Kimble, "The atom-cavity microscope: Single atoms bound in orbit by single photons," *Science*, vol. 287, pp. 1447–1453, 02 2000.

[143] M. A. Sillanpaa, J. I. Park, and R. Simmonds, "Coherent quantum state storage and transfer between two phase qubits via a resonant cavity," *Nature*, vol. 449, pp. 438–442, 09 2007.

[144] M. Hofheinz, E. M. Weig, M. Ansmann, R. C. Bialczak, E. Lucero, M. Neeley, A. D. O'Connell, H. Wang, J. M. Martinis, and A. N. Cleland, "Generation of fock states in a superconducting quantum circuit," *Nature*, vol. 454, pp. 310–314, 07 2008.

[145] K. Hennessy, A. Badolato, M. Winger, D. Gerace, M. Atature, S. Gulde, S. Falt, E. L. Hu, and A. Imamoglu, "Quantum nature of a strongly coupled single quantum dot-cavity system," *Nature*, vol. 445, pp. 896–899, 02 2007.

[146] T. A. Palomaki, J. W. Harlow, J. D. Teufel, R. W. Simmonds, and K. W. Lehnert, "Coherent state transfer between itinerant microwave fields and a mechanical oscillator," *Nature*, vol. 495, pp. 210–214, 03 2013.

[147] K. Sandner, H. Ritsch, R. Amsüss, C. Koller, T. Nöbauer, S. Putz, J. Schmiedmayer, and J. Majer, "Strong magnetic coupling of an inhomogeneous nitrogen-vacancy ensemble to a cavity," *Phys. Rev. A*, vol. 85, p. 053806, May 2012.

[148] A. Fragner, M. Göppl, J. M. Fink, M. Baur, R. Bianchetti, P. J. Leek, A. Blais, and A. Wallraff, "Resolving vacuum fluctuations in an electrical circuit by measuring the Lamb shift," *Science*, vol. 322, pp. 1357–1360, 11 2008.

[149] M. Hofheinz, H. Wang, M. Ansmann, R. C. Bialczak, E. Lucero, M. Neeley, A. O'Connell, D. Sank, J. Wenner, J. Martinis, and A. Cleland, "Synthesizing arbitrary quantum states in a superconducting resonator," *Nature*, vol. 459, pp. 546–549, 05 2009.

[150] J. M. Fink, R. Bianchetti, M. Baur, M. Göppl, L. Steffen, S. Filipp, P. J. Leek, A. Blais, and A. Wallraff, "Dressed collective qubit states and the Tavis-Cummings model in circuit QED," *Phys. Rev. Lett.*, vol. 103, p. 083601, Aug 2009.

[151] J. Verdú, H. Zoubi, C. Koller, J. Majer, H. Ritsch, and J. Schmiedmayer, "Strong magnetic coupling of an ultracold gas to a superconducting waveguide cavity," *Phys. Rev. Lett.*, vol. 103, p. 043603, Jul 2009.

[152] D. Walls and G. Milburn, *Quantum Optics*. Springer, Berlin, 2008.

[153] L. Mandel and E. Wolf, *Optical Coherence and Quantum Optics*. Cambridge University Press, 1995.

[154] J. Chow, *Quantum Information Processing with Superconducting Qubits*. PhD thesis, Yale University, 2010.

[155] B. Johnson, *Controlling Photons in Superconducting Electrical Circuits*. PhD thesis, Yale University, 2010.

[156] J. Koch, T. M. Yu, J. Gambetta, A. A. Houck, D. I. Schuster, J. Majer, A. Blais, M. H. Devoret, S. M. Girvin, and R. J. Schoelkopf, "Charge-insensitive qubit design derived from the Cooper pair box," *Physical Review A*, vol. 76, p. 042319, 10 2007.

[157] D. I. Schuster, A. P. Sears, E. Ginossar, L. DiCarlo, L. Frunzio, J. J. L. Morton, H. Wu, G. A. D. Briggs, B. B. Buckley, D. D. Awschalom, and R. J. Schoelkopf, "High-cooperativity coupling of electron-spin ensembles to superconducting cavities," *Phys. Rev. Lett.*, vol. 105, p. 140501, Sep 2010.

[158] D. Pozar, *Microwave Engineering*. Wiley, NY, 3rd ed., 2005.

[159] M. Devoret, *Quantum Fluctuations*. Elsevier, Amsterdam, 1996.

[160] M. Devoret, A. Wallraff, and J. Martinis, "Superconducting qubits: A short review," *cond-mat/0411174*, 2004.

[161] R. N. Simons, *Coplanar Waveguide Circuits, Components and Systems*. Wiley, NY, 2001.

[162] R. C. Ashoori, "Electrons in artificial atoms," *Nature*, vol. 379, pp. 413–419, 02 1996/02/01/print.

[163] R. Hanson, L. P. Kouwenhoven, J. R. Petta, S. Tarucha, and L. M. K. Vandersypen, "Spins in few-electron quantum dots," *Reviews of Modern Physics*, vol. 79, pp. 1217–1265, 10 2007/10/01/.

[164] A. Tartakovskii, ed., *Quantum Dots Quantum Dots: Optics, Electron Transport and Future Applications*. Cambridge University Press, 2012.

[165] J. M. Elzerman, R. Hanson, L. H. Willems van Beveren, B. Witkamp, L. M. K. Vandersypen, and L. P. Kouwenhoven, "Single-shot read-out of an individual electron spin in a quantum dot," *Nature*, vol. 430, pp. 431–435, 07 2004/07/22/print.

[166] J. R. Petta, A. C. Johnson, J. M. Taylor, E. A. Laird, A. Yacoby, M. D. Lukin, C. M. Marcus, M. P. Hanson, and A. C. Gossard, "Coherent manipulation of coupled electron spins in semiconductor quantum dots," *Science*, vol. 309, pp. 2180–2184, 09 2005/09/30.

[167] F. H. L. Koppens, C. Buizert, K. J. Tielrooij, I. T. Vink, K. C. Nowack, T. Meunier, L. P. Kouwenhoven, and L. M. K. Vandersypen, "Driven coherent oscillations of a single electron spin in a quantum dot," *Nature*, vol. 442, pp. 766–771, 08 2006/08/17/print.

[168] G. Papageorgiou, P. Glasson, K. Harrabi, V. Antonov, E. Collin, P. Fozooni, P. G. Frayne, M. J. Lea, D. G. Rees, and Y. Mukharsky, "Counting individual trapped electrons on liquid helium," *Applied Physics Letters*, vol. 86, pp. 153106–3, 04 2005/04/11/.

[169] J. R. Petta, A. C. Johnson, C. M. Marcus, M. P. Hanson, and A. C. Gossard, "Manipulation of a single charge in a double quantum dot," *Physical Review Letters*, vol. 93, pp. 186802–, 10 2004.

[170] P. Gosh, *Ion Traps*. Oxford University Press, 1995.

[171] J. Liang and H. Müller-Kirsten, "Anharmonic oscillator equations: Treatment parallel to Mathieu equation," *arxiv.org/quant-ph/0407235v2*, 2004.

[172] J. A. Schreier, A. A. Houck, J. Koch, D. I. Schuster, B. R. Johnson, J. M. Chow, J. M. Gambetta, J. Majer, L. Frunzio, M. H. Devoret, S. M. Girvin, and R. J. Schoelkopf, "Suppressing charge noise decoherence in superconducting charge qubits," *Physical Review B*, vol. 77, pp. 180502–, 05 2008.

[173] L. Childress, A. S. Sorensen, and M. D. Lukin, "Mesoscopic cavity quantum electrodynamics with quantum dots," *Physical Review A*, vol. 69, pp. 042302–, 04 2004.

[174] A. Abragam, *Principles of Nuclear Magnetism*. Oxford University Press, 1961.

[175] R. J. Schoelkopf, A. A. Clerk, S. M. Girvin, K. W. Lehnert, and M. H. Devoret, *Qubits as Spectrometers of Quantum Noise*. Springer, 2003.

[176] G. Wentzel, "Über strahlungslose Quantensprünge," *Zeitschrift für Physik*, vol. 43, no. 8, p. 524, 1927.

[177] E. Purcell *Phys. Rev.*, vol. 69, p. 681, 1946.

[178] A. A. Houck, J. A. Schreier, B. R. Johnson, J. M. Chow, J. Koch, J. M. Gambetta, D. I. Schuster, L. Frunzio, M. H. Devoret, S. M. Girvin, and R. J. Schoelkopf, "Controlling the spontaneous emission of a superconducting transmon qubit," *Physical Review Letters*, vol. 101, pp. 080502–, 08 2008.

[179] *Semiconductor Physics: An Introduction*. Springer-Verlag, Berlin, 9th ed., 2004.

[180] J. M. Martinis, S. Nam, J. Aumentado, K. M. Lang, and C. Urbina, "Decoherence of a superconducting qubit due to bias noise," *Physical Review B*, vol. 67, pp. 094510–, 03 2003.

[181] Y. A. Bychkov and E. I. Rashba, "Oscillatory effects and the magnetic susceptibility of carriers in inversion layers," *J. Phys. C: Solid State Phys.*, vol. 17, p. 6039, 1984.

[182] P. C. Hendry and P. V. E. McClintock *Cryogenics*, vol. 27, p. 131, 1988.

[183] R. H. Koch, J. Clarke, W. M. Goubau, J. M. Martinis, C. M. Pegrum, and D. J. van Harlingen, "Flicker (1/f) noise in tunnel junction dc squids," *J. Low Temp. Phys.*, vol. 51, p. 207, 1983.

[184] H. Naegerl, D. Leibfried, H. Rhode, G. Thalhammer, J. Eschner, F. Schmidt-Kaler, and R. Blatt, "Laser addressing of individual ions in a linear ion trap," *Physical Review A*, vol. 60, p. 145, 1999.

[185] D. James, "Quantum dynamics of cold trapped ions with application to quantum computation," *Applied Physics B*, vol. 66, p. 181, 1998.

[186] A. Garg, "Decoherence in ion trap quantum computers," *Physical Review Letters*, vol. 77, pp. 964–967, 07 1996.

[187] J. P. Schiffer, "Phase transitions in anisotropically confined ionic crystals," *Physical Review Letters*, vol. 70, pp. 818–821, 02 1993.

[188] Y. Kovdrya, "One-dimensional and zero-dimensional electron systems on liquid helium," *Low Temperature Physics*, vol. 29, no. 2, p. 77, 2003.

[189] K. Uhlig *Cryogenics*, vol. 42, no. 73, 2002.

[190] K. Uhlig and C. Wang *AIP Conf. Proc.*, vol. 823, p. 939, 2006.

[191] D. F. Santavicca and D. E. Prober, "Impedance-matched low-pass stripline filters," *Meas. Sci. Technol.*, vol. 19, p. 087001, 2008.

[192] J. R. Clow and J. D. Reppy, "Temperature dependence of superfluid critical velocities near t_λ," *Phys. Rev. Lett.*, vol. 19, pp. 291–293, 1967.

[193] M. Savard, G. Dauphinais, and G. Gervais, "Hydrodynamics of superfluid helium in a single nanohole," *Phys. Rev. Lett.*, vol. 107, p. 254501, Dec 2011.

[194] C. Lim, "Indium seals for low-temperature and moderate pressure applications," *Rev. Sci. Instrum.*, vol. 57, no. 1, p. 108, 1986.

[195] A. Kent, *Experimental Low-Temperature Physics*. Springer Verlag, 1993.

[196] L. Wilen and R. Giannetta, "Cryogenic photoemissive electron source," *Review of Scientific Instruments*, vol. 56, p. 2175, 1985.

[197] R. H. Fowler and L. Nordheim, "Electron emission in intense electric fields," *Proceedings of the Royal Society of London. Series A*, vol. 119, pp. 173–181, 05 1928.

[198] L. Loeb, *Electrical Coronas, Their Basic Physical Mechanisms*. University of California Press, 1965.

[199] G. E. Spangler and F. L. Hereford, "Injection of electrons into He II from an immersed tungsten filament," *Phys. Rev. Lett.*, vol. 20, p. 1229, 1968.

[200] K. Okuda, Y. Inaba, and M. Date, "Size of gas sheath around a hot filament in liquid He II," *J. Phys. Soc. Jpn.*, vol. 34, p. 1425, 1973.

[201] I. Silvera and J. Tempere, "Electron emission in superfluid and low temperature vapor phase helium," *Physical Review Letters*, vol. 100, p. 117602, 2008.

[202] J. Fang, A. E. Dementyev, J. Tempere, and I. Silvera, "Thermionic emission and a novel electron collector in a liquid helium environment," *Rev. Sci. Instrum.*, vol. 80, no. 043901, 2009.

[203] L. Frunzio, A. Wallraff, D. Schuster, J. Majer, and R. Schoelkopf, "Fabrication and characterization of superconducting circuit QED devices for quantum computation," *IEEE Trans. Appl. Supercond.*, vol. 15, no. 2, p. 860, 2005.

[204] J. Klier, I. Diocescu, and P. Leiderer, "First dc measurements of electrons on liquid helium: the helium-FET," *J. Low Temp. Phys.*, vol. 121, no. 5/6, p. 603, 2000.

[205] J. Klier, I. Doicescu, P. Leiderer, and V. Shikin, "Electron conductivity in helium films," *J. Low Temp. Phys.*, vol. 150, p. 212, 2008.

[206] P. Glassom, V. Dotsenko, P. Fozooni, M. Lea, W. Bailey, and G. Papageorgiou, "Observation of dynamical ordering in a confined Wigner crystal," *Physical Review Letters*, vol. 87, no. 17, p. 176802, 2001.

[207] D. G. Rees, I. Kuroda, C. A. Marrache-Kikuchi, M. Höfer, P. Leiderer, and K. Kono, "Point-contact transport properties of strongly correlated electrons on liquid helium," *Physical Review Letters*, vol. 106, pp. 026803–, 01 2011.

[208] D. Berkeland, J. Miller, J. Bergquist, W. Itano, and D. Wineland, "Minimization of ion micromotion in a paul trap," *Journal of Applied Physics*, vol. 83, no. 10, p. 5025, 1998.

[209] S. Narayanan, N. Daniilidis, S. Moeller, R. Clark, F. Ziesel, K. Singer, F. Schmidt-Kaler, and H. Häffner, "Electric field compensation and sensing with a single ion in a planar trap," *Journal of Applied Physics*, vol. 110, p. 114909, 2011.

[210] R. Behunin, Y. Zang, D. Dalvit, and S. Reynaud, "Electrostatic patch effects in Casimir force experiments performed in the sphere-plane geometry," *Phys. Rev. A*, vol. 86, p. 052509, 2012.

[211] D. G. Rees, H. Totsuji, and K. Kono, "Commensurability-dependent transport of a Wigner crystal in a nanoconstriction," *Physical Review Letters*, vol. 108, pp. 176801–, 04 2012.

[212] R. Severens, H. Verhoeven, M. Schaepkens, M. van de Sanden, and D. Schram, "Electrodeless thin film conductance measurements using the Sommer-Tanner method," *Rev. Sci. Instrum.*, vol. 67, no. 10, p. 3624, 1996.

[213] M. A. Stan and A. J. Dahm, "Two-dimensional melting: Electrons on helium," *Physical Review B*, vol. 40, pp. 8995–9005, 11 1989.

[214] M. Lea, A. Stone, P. Fozooni, and J. Frost, "The ac response of a 2-d electron gas on liquid helium in a magnetic field," *Journal of Low Temperature Physics*, vol. 85, no. 1, p. 67, 1991.

[215] R. Mehrotra and A. Dahm, "Analysis of the Sommer technique for measurement of the mobility for charges in two dimensions," *J. Low Temp. Phys.*, vol. 67, no. 1, p. 115, 1987.

[216] M. Ashari, D. G. Rees, K. Kono, E. Scheer, and P. Leiderer, "The helium field effect transistor (i): Storing surface state electrons on helium films," vol. 167, no. 1-2, pp. 15–25, 2012.

[217] G. Sabouret and S. Lyon, "Measurement of the charge transfer efficiency of electrons clocked on superfluid helium," *Applied Physics Letters*, vol. 88, p. 254105, 2006.

[218] D. C. Rapaport, *The art of molecular dynamics simulation*. Cambride University Press, 1995.

[219] P. Bugnion, "Modelling of electron spin interactions for qip," Master's thesis, Oxford University, 2009.

[220] M. Tavis and F. W. Cummings, "Exact solution for an n-molecule radiation-field Hamiltonian," *Phys. Rev.*, vol. 170, pp. 379–384, Jun 1968.

[221] M. Tavis and F. W. Cummings, "Approximate solutions for an n-molecule-radiation-field Hamiltonian," *Physical Review*, vol. 188, pp. 692–695, 12 1969.

[222] F. Bradbury, *Cold electrons in silicon and on superfluid helium*. PhD thesis, Princeton University, 2010.

[223] R. Hughes, D. James, E. Knill, R. Laflamme, and A. Petschek, "Decoherence bounds on quantum computation with trapped ions," *Phys. Rev. Lett.*, vol. 77, no. 15, p. 3241, 1996.

[224] H. Goldstein, C. Poole, and J. Safko, *Classical Mechanics*. Addison-Wesley, 3rd ed., 2002.